The characterisation of epitaxial layers of the dilute magnetic semiconductor Hg(_1-x)Mn(_x)Te

T.D. Hallam

The Characterisation of Epitaxial Layers of the Dilute Magnetic Semiconductor $Hg_{1-x}Mn_xTe$

by

T.D. Hallam

This thesis is presented in canditature for the degree of

Doctor of Philosophy

in the

University of Durham

July 1995

Abstract

This work is concerned with the characterisation of epitaxial (Hg,Mn)Te, and in particular the assessment of the structural and transport properties of the layers.

Direct alloy growth (DAG) of (Hg,Mn)Te on buffered GaAs and unbuffered (Cd,Zn)Te substrates in a horizontal MOVPE reactor resulted in poor surface compositional and thickness uniformity. This was attributed to the differences in the pyrolysis rates of the Te and Mn precursors. Double crystal x-ray diffraction was used to determine accurately layer thickness, composition and quality. Analysis of the symmetric and asymmetric rocking curves revealed that for thickness over 1μm (Hg,Mn)Te was almost 100% relaxed. A reduction in the dislocation density, as inferred from the x-ray rocking curve width, was observed with increasing layer thickness and was considered in terms of the Gay model. A sub-grain structure was seen using double crystal x-ray topography, where grain diameter decreased in a linear manner with inverse layer thickness. Triple axis x-ray diffraction revealed that tilts between the sub-grains were the primary cause of the rocking curve broadening.

Hall and resistivity measurements were made in the temperature range 4K to 290K. The majority of the layers exhibited n-type behaviour, with carrier concentrations and mobilities dependent on layer thickness. Modelling of the temperature dependence of the carrier mobility was attempted for various lattice and impurity scattering mechanisms. Attempts were also made to explain the temperature dependence of the carrier concentration using a two band model and estimates for the bandgaps obtained from intrinsic Hall data.

The interdiffused multilayer process (IMP) was then employed, resulting in layers with superior lateral compositional and thickness uniformities. Improved crystalline quality to that seen in comparable DAG layers was also obtained. The electron mobilities were higher in IMP layers than in comparable DAG ones and analysis of the mobility data indicated that several scattering mechanisms were operative, including ionised and neutral impurity, optical phonon and piezoelectric (in Mn rich layers) scattering. Layers grown by IMP appeared to be more stable and changes in transport properties over a period of a few months were less pronounced than for comparable DAG layers.

Acknowledgements

I wish to thank my supervisor Dr Andy Brinkman for all his guidance during this study, Minoru Funaki for his tireless growth of the layers and Professor Brian Tanner for allowing me to use the x-ray diffraction equipment. During the course of this work I have had the pleasure of knowing the following people: John Hudson, Caroline Moore, Ian Pape, Chaorong Li, Dr Halder, Debbie Hales, Ruth Port, Ken Durose, John Lewis, Sener Oktik and Haider Al-Allak.

None of this would have been possible without the support of my Mum, Dad, Valerie and sister Liz who have done so much for me over the years.

Special thanks go to John Kelly and Sarah Phillips for their hospitality and humour. Also instrumental in my life have been: Nathan Garside, Peter Powner, Dr Blamey, Tony Wells, John Parkinson, Andy Cross and Pete Mc Cullough. All of whom have dragged me through caves and shipwrecks or tried to break my legs on the football pitch.

I am eternally gratefully to Bede Scientific Instruments Ltd and ESPRC for the financial support which they have given me.

This thesis is dedicated to my fiancée Mhairi Elliott, for all her love and devotion.

Contents

Chapter Three

Experimental Methods

Chapter Four

Analysis of Electrical Transport Data

Chapter Five

Assessment of Structural and Defect Properties

Chapter Six

Transport Properties

Chapter Seven

The Interdiffused Multilayer Process

Chapter Eight

Electrical Characterisation of Epitaxial (Hg,Mn)Te Grown by the Interdiffused Multilayer Process

Chapter Nine

Summary and Conclusions

Chapter One

Properties of (Hg,Mn)Te

1.1 Introduction

Mercury manganese telluride is of considerable potential interest to the device market due to it's novel magneto-optic and magneto-transport properties, which result from the spin-spin exchange interaction between band carriers and the localised moments of the magnetic ions [1]. This gives rise to a large Faraday rotation and (Hg,Mn)Te has been proposed as a suitable material for use in isolators [2], optical switches, modulators and optical magnetometers [3]. Other possible applications include x-ray detectors, where the high atomic mass number of mercury makes (Hg,Mn)Te a good x-ray absorber, and tunable infra-red detectors since mercury rich compositions are narrow gap [4].

Mercury manganese telluride belongs to a class of materials referred to as dilute magnetic semiconductors (DMS). In these materials some proportion of the cation sites in the host (in this case HgTe) lattice are substituted by a magnetic species (i.e. Mn). By Hund's rule all five spins in the 3d orbital of the manganese ion are parallel and it would require considerable energy for an electron to have opposite spin in the atom. In this sense the $3d^5$ orbital is complete and thus the manganese ion resembles a group II element [5].

Mercury manganese telluride was first grown in bulk crystal form by Delves and Lewis in 1963 [6] using the vertical Bridgman technique and most of the physical properties of this material have been discovered using such bulk material. Epitaxial layers have been grown by liquid phase epitaxy, over the composition range 10% to 30% manganese, using a

tipping system with a Te rich solution in a closed ampoule [7]. The first reported epitaxial growth of (Hg,Mn)Te by molecular beam epitaxy (MBE) was in 1985 [8] and superlattices of (Hg,Mn)Te and HgTe were deposited using MBE by Harris et al [9] in 1986, who reported electron mobilities of around 10 $m^2V^{-1}s^{-1}$. The growth of epitaxial layers by metal organic vapour phase epitaxy (MOVPE) was first reported by Durham in 1990 [10-12].

The advantages of epitaxial growth over bulk growth and LPE techniques include a lower growth temperature, growth of hetero-structures and, in principle, selective area doping. In MOVPE, a carrier gas (usually hydrogen) is bubbled through the precursors and the reactant vapours mixed at a manifold, before entering a heated reactor, where they react to form the desired layer on a heated substrate. For mercury containing layers the mercury is usually held in an independently heated boat upstream of the susceptor, but within the reactor.

Dilute magnetic semiconductors are predominantly II-VI compounds in which manganese ions have been substituted on cation sites in the lattice. The group II elements mercury, cadmium and zinc and the group VI elements sulphur, selenium and tellurium have been the most commonly studied. However research has begun on $A^{II}B^{VI}$-Fe alloys and $A^{IV}B^{VI}$-Mn although as yet, relatively little work has been published on these compounds [14-16].

1.2 The Structural Properties of (Hg,Mn)Te

Delves and Lewis [6] constructed the phase diagram for the growth of (Hg,Mn)Te, Fig 1.1. They found that at temperatures below 650°C (Hg,Mn)Te exists in the α phase (the zinc blende structure) up to 35% manganese,

beyond which $MnTe_2$ co-exists as a separate phase and in specimens containing in excess of 78% manganese, the additional MnTe phase becomes evident. The zinc blende structure adopted by the (Hg,Mn)Te component can be represented as two interpenetrating fcc lattices, one occupied by anions and the other by cations and separated by one quarter of a body diagonal, Fig 1.2.

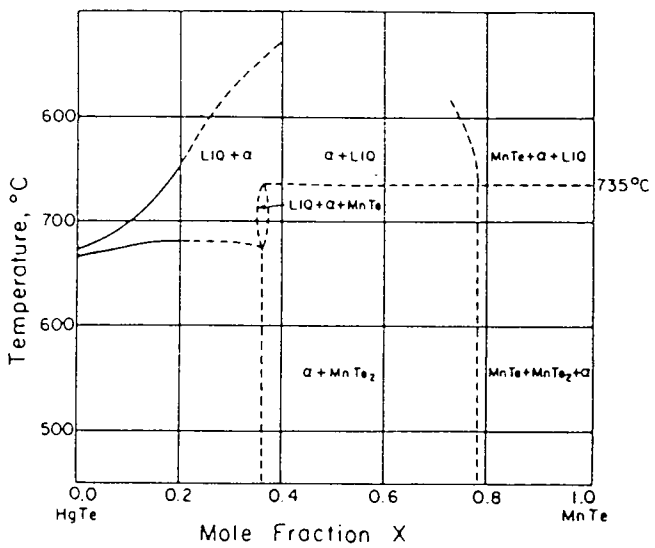

Fig 1.1 The phase diagram for the growth of (Hg,Mn)Te [6].

Close packing of ions exists on the {111} planes of zinc blende which are polar, comprising either cations or anions, and are denoted by using labels of A or B respectively. In the zinc blende phase, $s\text{-}p^3$ bonding exists between the anions and cations, involving two valence electrons from the group II element and six valence electrons from the group VI element.

The limit of manganese solubility in the zinc blende structure arises

because MnTe does not normally crystalise in the zinc blende or related wurtzite structures but adopts a nickle arsenide type structure, Fig 1.2, where the manganese ions take the nickel sites. The $MnTe_2$ phase usually crystalises in the pyrites type structure [6] with the manganese ions occupying the iron sites.

Like the majority of DMS's, the lattice parameter of (Hg,Mn)Te obeys Vegard's law in that it varies linearly with composition up to the point where the zinc blende structure is lost, Fig 1.3. The variation of lattice parameter with composition is given by the line of best fit, equation 1.1, and when extrapolated to the limit of no mercury, gives a lattice parameter of 6.334Å for cubic MnTe.

$$a = 6.46 - 0.126x \qquad 1.1.$$

where a is the lattice parameter (in Å) and x is the mole fraction of manganese.

Manganese telluride with the *zinc blende structure* has been grown using ionized-cluster beam deposition on GaAs (100) and sapphire (0001) substrates by H. Anno et al in 1991 [17] and was found by x-ray diffraction to have a lattice parameter of "around 6.34Å", as expected from the extrapolation of Vegard's law.

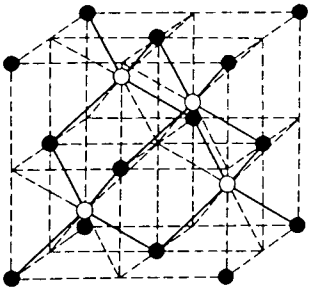

(a)

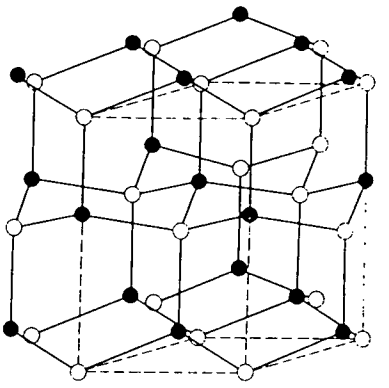

(b)

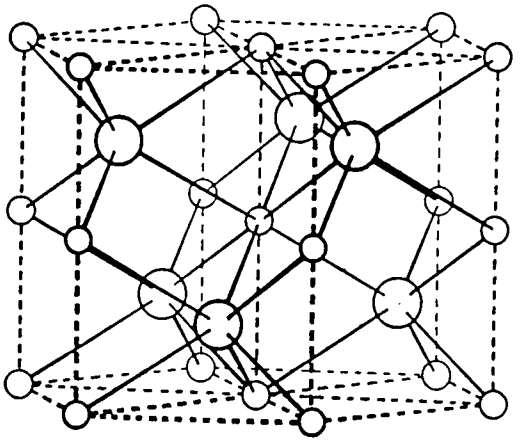

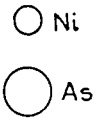

(c)

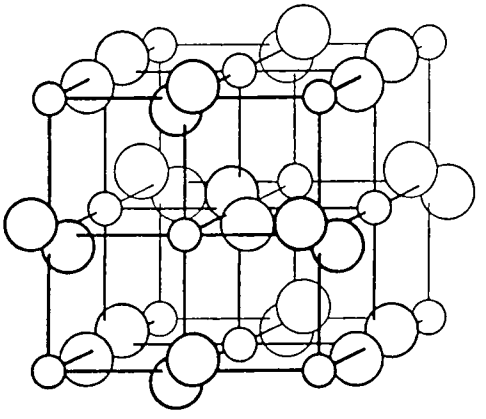

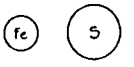

(d)

Fig 1.2 Structures adopted by MnTe and $MnTe_2$; (a) zinc blende [17], (b) wurtzite [17], (c) NiAs [18] , (d) pyrite, FeS_2 [19].

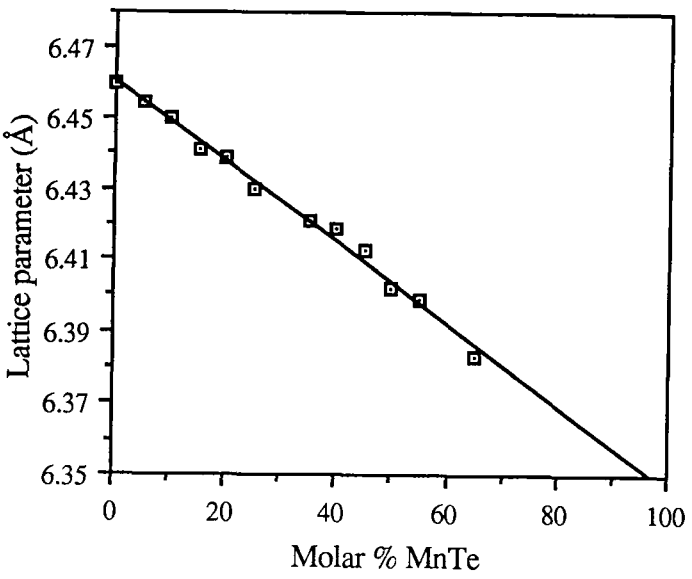

Fig 1.3 Lattice parameter variation of (Hg,Mn)Te with composition [6].

However, it should be noted that the lattice parameter discussed here is the average lattice parameter over a large volume of the lattice. When the microscopic structure of (Cd,Mn)Te was investigated using Extended X-ray Absorption Fine Structure Studies (EXAFS) the results suggested that while the cation lattice, to a first approximation does not distort on introducing manganese ions, the anion, tellurium, lattice does, creating an anion sub-lattice which no longer has the fcc structure [21]. Since the Mn-Te bond length is considerably less than that of the Cd-Te bond, on distortion the tellurium ion move towards the manganese and away from the cadmium. Balzarotti [21] suggested that this will probably be the case for other Mn-based DMS's, which would include (Hg,Mn)Te.

In heteroepitaxy the epitaxial film generally has a different lattice parameter to that of the substrate and this is the case for the MOVPE growth of (Hg,Mn)Te. The effective mismatch, f, between substrate and layer is given by the ratio of the difference between substrate lattice parameter,

a_{sub}, and that of the layer, a_{lay}, to the substrate lattice parameter.

$$f = \frac{a_{lay} - a_{sub}}{a_{sub}} \qquad 1.2$$

For layer thicknesses less than some critical thickness, which is dependant on the effective mismatch and the elastic constants of the constituents, a layer coherent with the substrate may be grown. This results in an in-plane lattice parameter equal to that of the substrate and a distorted lattice parameter perpendicular to the surface which is dependant on the Poisson ratio of the material.

For layer thicknesses greater than the critical thickness, relaxation occurs by the creation of misfit dislocations at the interface, which proceed through the crystal until anhilated or until they reach the surface. The relaxed layer will have a lattice parameter similar to that of the bulk crystal but the quality of the layer will be affected by the dislocations.

The variation in lattice parameter of (Hg,Mn)Te over the composition range from HgTe to cubic MnTe is around 2%, which is considerably greater than that of (Hg,Cd)Te, 0.3%. This implies that the epitaxial growth of (Hg,Mn)Te will be technologically more challenging since the effective mismatch between substrate and layer will be more dependant on composition than that of (Hg,Cd)Te.

1.3 Bandstructure

The bandstructure of (Hg,Mn)Te at 4K was investigated by Bastard in 1977 [22] and is shown in Fig 1.4. Both the minimum in the conduction band and the maximum of the valence band occur at the central point of the Brillouin zone, thus giving a direct bandgap. Hence (Hg,Mn)Te is a

candidate for optical device applications, particularly infrared detection, for which the magnitude of the bandgap is most suited. There are three bands of similar energy, a fourfold degenerate band of Γ_8 symmetry and two doubly degenerate bands of Γ_6 and Γ_7 symmetry.

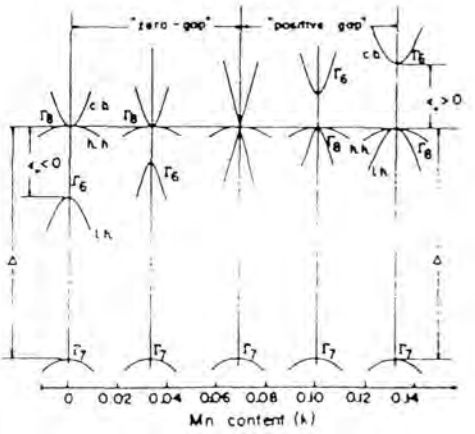

Fig 1.4 The bandstructure of (Hg,Mn)Te at 4K for varying compositions [22].

Increasing the manganese content of (Hg,Mn)Te widens the bandgap as shown in Fig 1.5. Increasing the temperature also widens the bandgap at low manganese concentrations, but has little effect at higher concentrations (~20%). Below 6.5% manganese at 4K, and 4% manganese at 295K, band overlap occurs between Γ_8 and Γ_6 and a "negative bandgap" results. This corresponds to a semimetallic state since the concentration of carriers in the region of overlap is low.

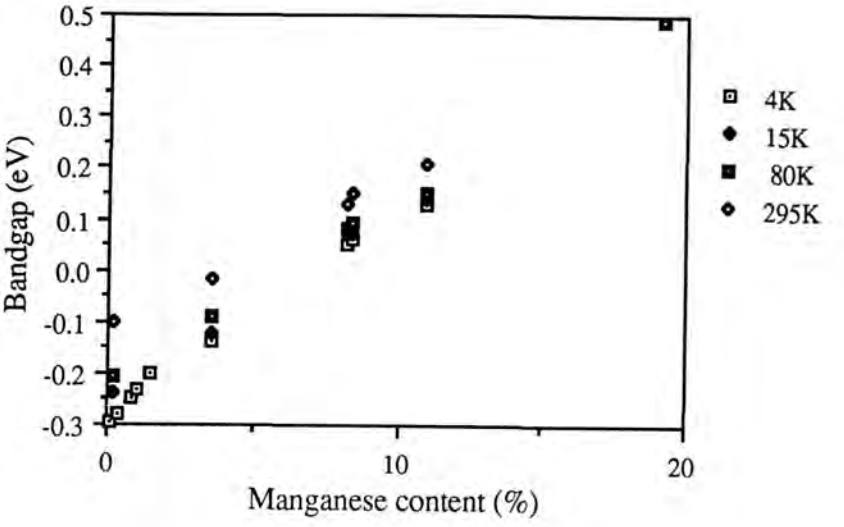

Fig 1.5 Temperature dependence of the bandgap for (Hg,Mn)Te [4,22].

$$Eg = -0.253 + 3.446x + 4.9X10^{-4}T - 2.55X10^{-3}xT \qquad 1.3.$$

where Eg is the bandgap in eV and T is the absolute temperature [4].

The effective masses of the conduction band electrons in (Hg,Mn)Te have been determined by Jaczynski et al [23] from Shubnikov-de Haas oscillations. They discovered that there was a minimum in the effective mass at compositions corresponding to band overlap, Fig 1.6, and that the values at all compositions were proportional to the cube root of the carrier concentration.

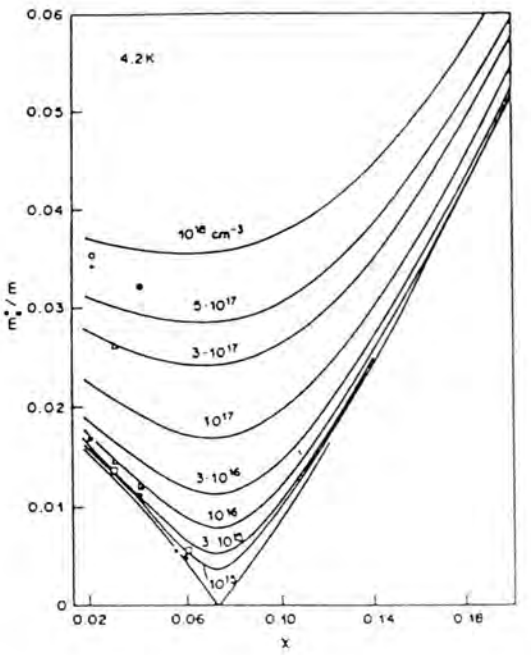

Fig 1.6 The dependence of electron effective mass at a temperature of 4.2K, on (Hg,Mn)Te composition [23].

1.4 Magnetic properties

The band structure of (Hg,Mn)Te is qualitively similar to that of (Hg,Cd)Te in the absence of a magnetic field. However on the application of a magnetic field the exchange interaction of band carriers with the Mn^{2+} paramagnetic ions alters the energy spectrum. The manganese ions have partially filled 3d orbitals giving a spin of 5/2 and thus a relatively large magnetic moment of $5\mu_B$. An applied magnetic field aligns the localised magnetic moments of the manganese ions thus creating a non zero average component of the spins along its direction. At manganese concentrations of less than one percent the influence of manganese on the bandstructure can be disregarded and the manganese interaction with carriers neglected. At larger concentrations interesting effects due to spin-spin exchange interactions between band electrons and localised moments of the magnetic ions occur. The presence of a strong magnetic field lifts the degeneracy of

the conduction and heavy hole bands in negative bandgap semiconductors. In dilute magnetic semiconductors the uppermost heavy hole subband is shifted upwards [24].

Giant negative magnetoresistance has been observed in p-type (Hg,Mn)Te containing 8% manganese at low temperatures, typically 4.2K, using magnetic fields of the order of 7 Tesla [25]. This has been explained in terms of the boil off effect where the transverse mass decreases thus lowering the acceptor binding energy, Fig 1.7, as the magnetic field is increased. Reductions of up to seven orders of magnitude in resistivity have been observed, Fig 1.8.

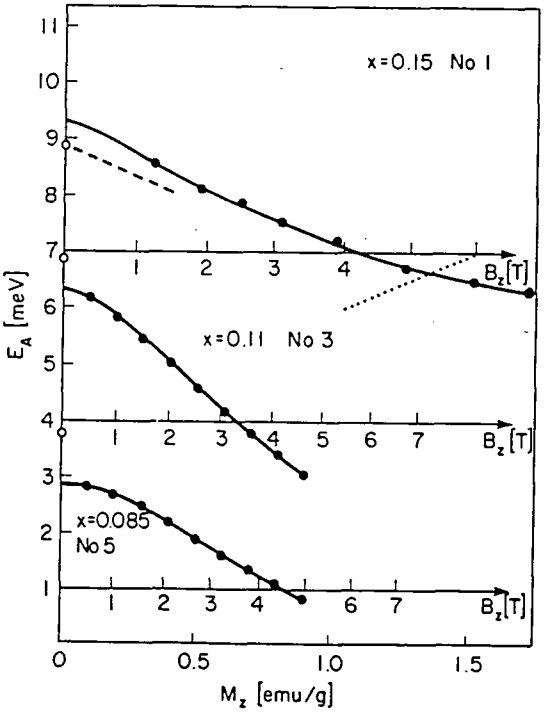

Fig 1.7 Effect of an applied magnetic field on the acceptor activation energy [26].

The decrease in activation energy with increasing magnetisation may be so strong for layers with a low manganese content and high acceptor concentrations that the concentration of free holes will increase in the extrinsic range with decreasing temperature [26]. As stated previously a

seven orders of magnitude reduction in resistivity has been observed in (Hg,Mn)Te under these conditions of low temperatures and large magnetic fields.

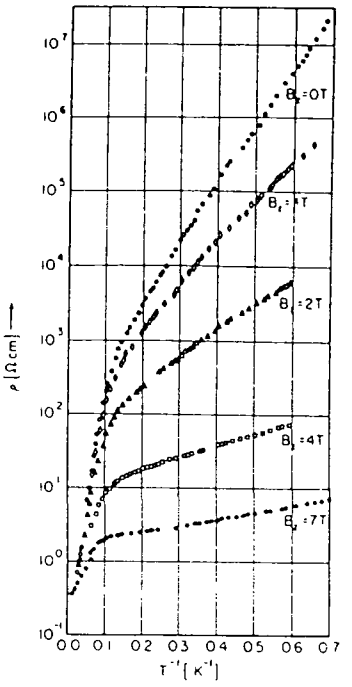

Fig 1.8 Giant negative magnetoresistance [25].

A secondary effect of increasing the magnetic field is that the conduction becomes anistropic due to the induced anistropy of the overlap integral of neighbouring acceptors. This has been observed in p-type (Hg,Mn)Te with manganese compositions between 12 and 17% and with acceptor concentrations around 10^{22} m^{-3}. Ultimately an increase of resistivity at very large magnetic fields is observed as the ultraquantum limit is approached and the acceptor radius begins to decrease with increasing magnetic field.

Germarienko et al [27] found that the application of uniaxial deformation, of up to 1.5Kbar, to p-type (Hg,Mn)Te with negative bandgaps altered the energy spectrum, by separating the light and heavy hole bands, Fig 1.9. In the absence of an external magnetic field the energy spectrum of

(Hg,Mn)Te is similar to (Hg,Cd)Te and for low (less than 7%) manganese concentrations acceptor levels appear within the conduction band. Under these conditions the effect of uniaxial compression upon the energy spectra of (Hg,Mn)Te and (Hg,Cd)Te appear similar and a bandgap is created on increasing the compression. This has the effect of lowering the Fermi level from the bottom of the conduction band and hence reducing the electron density and mobility.

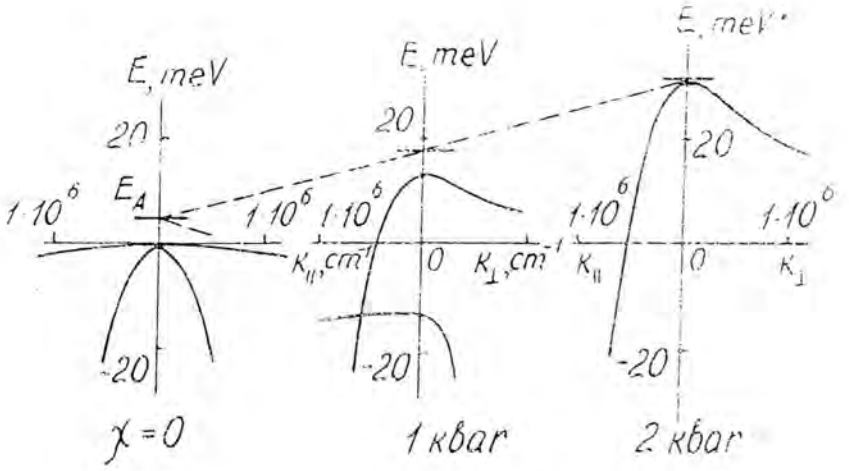

Fig 1.9 Effect of unaxial deformation on the energy spectrum [27].

The changes in transport measurements on the application of pressures, Fig 1.10 and 1.11 were reversible thus showing the elastic nature of the material. Changing the orientation of the (Hg,Mn)Te did not make any difference to the dependence of transport properties on deformation.

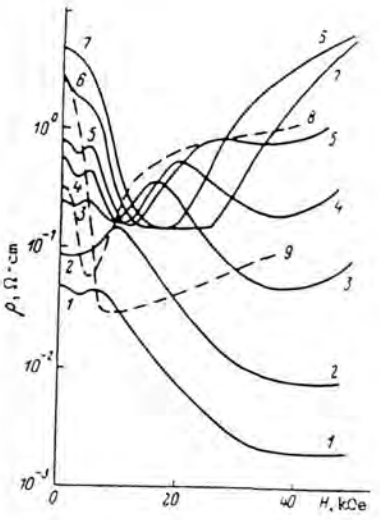

Fig 1.10 Effect of unaxial deformation on the magnetoresistance of $Hg_{0.975}Mn_{0.025}Te$ (p-type) at 1.8K for different pressures (in Kbar): 1) 0; 2) 0.3; 3) 0.5; 4) 0.6; 5) 0.7 6) 0.9 7) 1.1 8) 1 9) 1.36 [27].

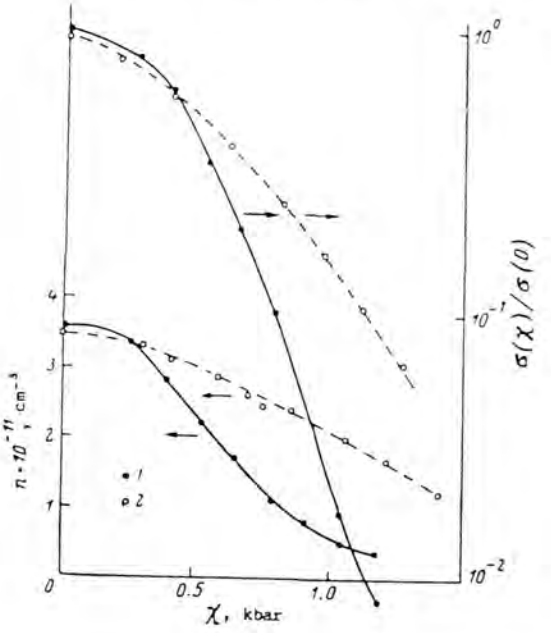

Fig 1.11 Influence of uniaxial deformation on carrier concentration and conductivity of (1) p-type $Hg_{0.935}Mn_{0.065}Te$, (2) p-type $Hg_{0.935}Cd_{0.065}Te$ [27],

The Faraday rotation of (Hg,Mn)Te, for compositions between 30% and 50% manganese at temperatures in the range 4.2K to 60K have been reported [2]. Bulk crystals with a compositional uniformity of 0.2%/cm in the growth direction were analysed using 45° linear crossed polarisers and radiation of energy in the range 70% to 90% of the bandgap. The Faraday rotation was then determined from the intensity of the transmitted radiation as a function of applied magnetic fields up to 0.1 Tesla. The results are given in Fig 1.12 which is reproduced from reference 2.

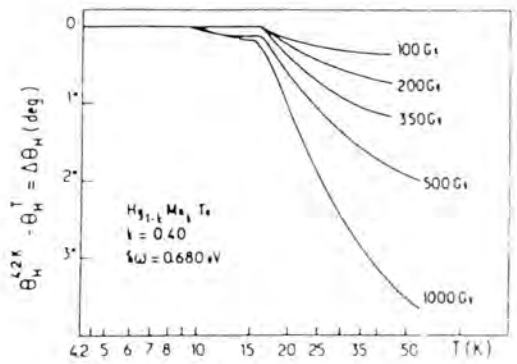

Fig 1.12 Faraday rotation in (Hg,Mn)Te [2].

1.5 Present work at Durham.

This thesis concentrates on analysis of the structural and carrier transport properties of MOVPE grown (Hg,Mn)Te epitaxial films. The overall aim of the programme was to develop high quality, uniform material suitable for device applications.

Chapter Two describes the MOVPE equipment and operation, including characterisation of temperature profiles. A systematic analysis is presented of the effects of growth conditions on the properties of the grown films. The mechanisms of the precursor pyrolysis and the

influence on the uniformity of growth are discussed.

Analysis techniques implemented in subsequent chapters are discussed in Chapter Three and their merits and limitations described. Layer structural quality was assessed using double crystal x-ray diffraction, x-ray topography and triple axis x-ray diffraction techniques. A scanning electron microscope fitted with EDAX was used to assess surface morphology and to determine (Hg,Mn)Te composition. Transport data was collected from temperature dependent resistivity and Hall measurements, using a cryostat capable of liquid helium temperatures.

An account of the interpretation of transport data is presented in Chapter Four and models to describe the Hall temperature measurements examined. Mobility data is used to determine the types of scattering present in (Hg,Mn)Te at various temperatures.

In Chapter Five the results of the double crystal x-ray diffraction (DCXRD) studies are presented and used to assess the dependence of layer quality on layer thickness. Data from double crystal x-ray topography and TEM are also given and used to discuss the results in terms of dislocation behaviour. Models for this behaviour are compared and contrasted. Measurements of composition, thickness and uniformity were made using an x-y scanning stage in the DCXRD arrangement. Analysis of x-ray scattering mechanisms was made using triple axis x-ray diffraction, and the influence of differing substrates was investigated. Surface morphology was studied as a function of substrate type and orientation and growth temperature.

In Chapter Six Hall and resistivity measurements are reported and used to determine carrier concentrations and mobilities, and the influence of layer thickness and composition upon them. Modelling of mobility - temperature data is used in the analysis of scattering mechanisms. Small

field (0.38T) magnetoresistance measurements were undertaken at various temperatures, layer thicknesses and layer compositions and thus are also described here. For successful device fabrication (Hg,Mn)Te must have electrical properties which do not alter significantly with time and so the final part of chapter six reports on an investigation of the stability of carrier behaviour over a period of months.

In an attempt to improve the uniformity of growth the interdiffused multilayer process (IMP) was adopted and Chapter Seven describes the growth and analyses the structural properties of the grown layers.

Chapter Eight is an account of the investigation of carrier mobility and behaviour in IMP layers, using Hall and resistivity measurements. Magnetoresistance and stability were measured and comparisons made with layers grown by the direct alloy growth method.

Chapter Nine brings together all the results and ideas generated by this work and discusses the future of (Hg,Mn)Te.

References

[1] G. Bastard, C. Rigaux, Y. Guilder, J. Mycielski and A. Myielski. (1978) Le J. de Physique **39** 87.

[2] A. Mycielski, C. Rigaux and M. Menant (1984) Sol. Stat. Commun. **50** 257.

[3] N. Kullendorf and B. Hok (1985) Appl. Phys. Lett **46**(11) 1016.

[4] J. Kaniewski and A. Mycielski (1982) Sol. Stat. Comm. **41**(12) 959.

[5] "The Physical Principles of Magnetism" by A.H. Morris (1956) Pub. John Wiley and Sons London.

[6] R.T. Delves and B. Lewis (1963) J. Phys. Chem. Solids **24** 549.

[7] P. Becla, P.A. Wolff, R.L. Aggarwal and S.Y. Yuen (1985) J. Vac. Sci. Technol. **A3**(1) 116.

[8] J. Reno, I.K. Sou, P.S. Wijewarnasuriya and J.P. Faurie (1985) Appl. Phys. Lett 47 1168.

[9] K.A. Harris, S. Hwang, Y. Lansari, J.W. Cook Jr and J.F. Schetzina (1986) Appl. Phys. Lett. **49**(12) 713.

[10] P.A. Clifton, A.W. Brinkman and H.M. Al-Allak (1990) Semicon. Sci. Technol. **5** 1067.

[11] H.M. Al-Allak, A.W. Brinkman, P.A. Clifton and P.D. Brown (1991) Mater. Res. Soc. Symp. Proc. **216** 35.

[12] M. Funaki, J.E. Lewis, T.D. Hallam, Chaorang Li, S.K. Halder, A.W. Brinkman and B.K. Tanner (1993) Semicon. Sci. Technol. **8** 200.

[13] R. Korenstein, P. Hallock and B. MacLeod (1990) J. Vac. Sci. Technol. **B9** 1630.

[14] M. Vaziri, V. Dedska and R. Reifenberger (1985) Appl. Phys. Lett. **47** 407.

[15] Y. Guldner, C. Rigaux, M. Menant, D.P. Mullins and J.K. Furdyna (1980) Sol. Stat. Commun. **33** 133.

[16] G. Karczewski, M.von Ortenberg, Z. Wilamowski, W. Dodrowolski and J. Niewodniczanska-Zawadzka (1985) Sol. Stat. Commun. **55** 249.

[17] "The Crystal Structure of Solids" by Brown and Forsyth (1973), pub Edward Arnold, London.

[18] "Crystal Structure of Minerals" by Bragg and Claringbull (1965), pub University press, Glasgow.

[19] "Crystal Structures" by H.D. Megaw (1973), pub W.B. Saunders, London.

[20] H. Anno, T. Koyanagi and K. Matsubara (1992) J. Crystal Growth **117** 816.

[21] A. Balzariott, M. Czyzyk, A. Kisiel, N. Motta, M. Podgorny and M. Zimnal-Starnawska (1984) Phys. Rev. **B30** 2295.

[22] G. Bastard, C. Rigaux and A. Mycielski (1977) Physica Status Solidi **B79** 585.

[23] M. Jaczynski and W. Dobrowolski (1980) Physica Status Solidi **B102** 195.

[24] M. Dobrowolska, W. Dobrowolski, R.R. Galazka and T. Kossut (1979) Sol. Stat. Comm. **30** 25.

[25] A. Mycielski and J. Mycielski (1980) J. Phys. Soc. Japan **49** 809.

[26] Wojtowicz and Mycielski (1984) Acta Physica Polonica **A67** 363.

[27] A.V. Germarienko, G.M. Min'kov, E.L. Rumyantsey, O.E. Rut, N.P. Gavaleshko and V.M. Frasunyak. (1989) Sov. Phys. Semicond. **23**(1) 71.

Chapter Two

Growth of (Hg,Mn)Te Crystals by MOVPE Using Direct Alloy Growth

2.1 Introduction

The first bulk crystals of (Hg,Mn)Te [1] were grown by the Bridgman technique from milled ingots of HgTe and MnTe. The latter were prepared from electrolytic flakes of manganese, elemental mercury and powered tellurium, heated to 450°C in an argon atmosphere for three days. From these bulk crystals the phase diagram was constructed, which showed that below 650°C, (Hg,Mn)Te had the zincblende structure up to 35% manganese, beyond this the MnTe complex was present, while specimens containing in excess of 78% manganese included the additional $MnTe_2$ complex. Bulk crystal (Hg,Mn)Te has been produced by a number of techniques including; Bridgman, zone melting, travelling heater method, modified two phase mixtures and solid-state recrystallization [2]. The latter technique appears to produce the best compositional uniformity although large diameter (several centimetres) crystals have been obtained using all these methods.

Epitaxial growth of (Hg,Mn)Te has been successfully achieved by LPE [3], MBE [4] and MOVPE [5-7], although comparatively little epitaxial work has been reported. In MOVPE the layer is deposited from the metalorganic species of the required elements in a vapour phase transferred from the bubblers to the heated substrate using a carrier gas (usually hydrogen). In the growth of solid solutions, if all the reactants are transported to the reactor simultaneously and reacted directly to form the compound, the

MOVPE process is referred to as Direct Allow Growth (DAG).

This chapter discusses the MOVPE growth of (Hg,Mn)Te and examines some of the particular problems associated with the growth of this material.

2.2 Growth Technique

2.2.1 Growth System

The epitaxial (Hg,Mn)Te films used in this study were grown by M.Funaki at Durham, in a horizontal atmospheric pressure reactor using purified hydrogen as a carrier gas. The MOVPE system was constructed at Durham university in 1985, originally for the deposition of (Hg,Cd)Te, and has the layout shown in Fig 2.1. Hydrogen gas and vapour flows were controlled using Brook Instruments 5850R mass flow controllers (MFC) which have an accuracy of ±1%. The reactants were entrained in the carrier gas by bubbling the hydrogen through bubblers containing the precursor compounds; di-isopropyl telluride (DIPTe), tricarbonyl methylcyclopentadienyl manganese (TCMn), dimethylcadmium (DMCd) and dimethylzinc (DMZn) obtained from Epichem Ltd and Morton Ltd. Mercury was provided from an elemental source located in the reactor. The precursor vapours were mixed at a vent/run manifold and a constant pressure was maintained in the reactor. Pipes leading from the TCMn bubbler were electrically heated to 100°C in order to prevent condensation and entered the reactor via a side arm. Bypass lines were included to divert the carrier gas around the bubblers when they were not required. The system was fully automated using an Archimedes computer programmed in BASIC.

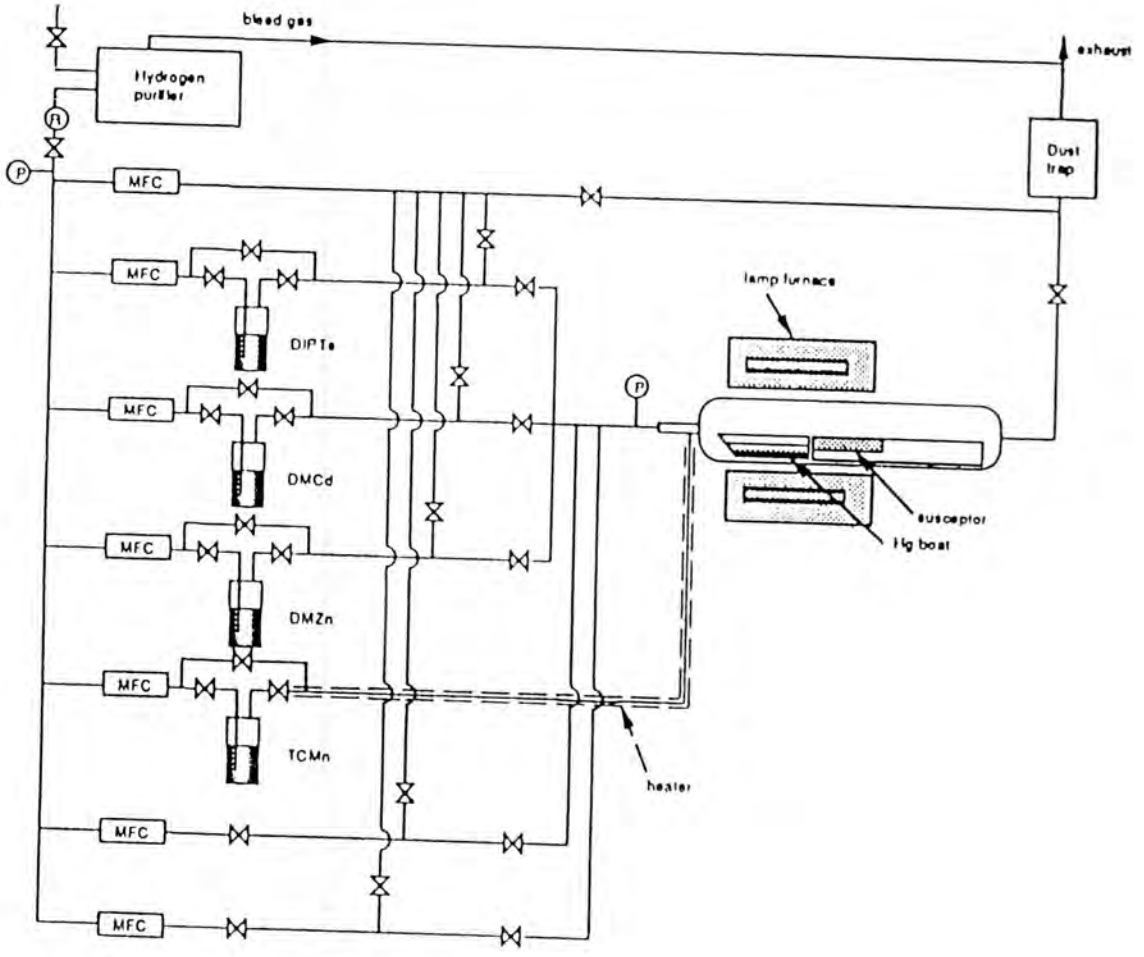

Fig 2.1 A diagram illustrating the MOVPE system used in this study.

2.2.2 Temperature Control

The original graphite susceptor was replaced by one engineered from stainless steel, which was easier to clean as it did not absorb the reactants to the same extent as graphite. The susceptor was heated resistively by a Mo wire. Temperature profiles along the direction of gas flow for a set point temperature of 380°C are shown in Fig 2.2, for the susceptor surface and on top of a GaAs wafer placed on the susceptor. The profiling was performed using six independent thermocouples attached to the susceptor and/or the substrate using quick drying silver paint. The rate of change of temperature with position on the susceptor was greatest near the front or rear edge and the flatest part was obtained between 20 and 30mm from the upstream edge. Substrates were subsequently positioned in the centre of the susceptor where the minimum variation of temperature with position occurred.

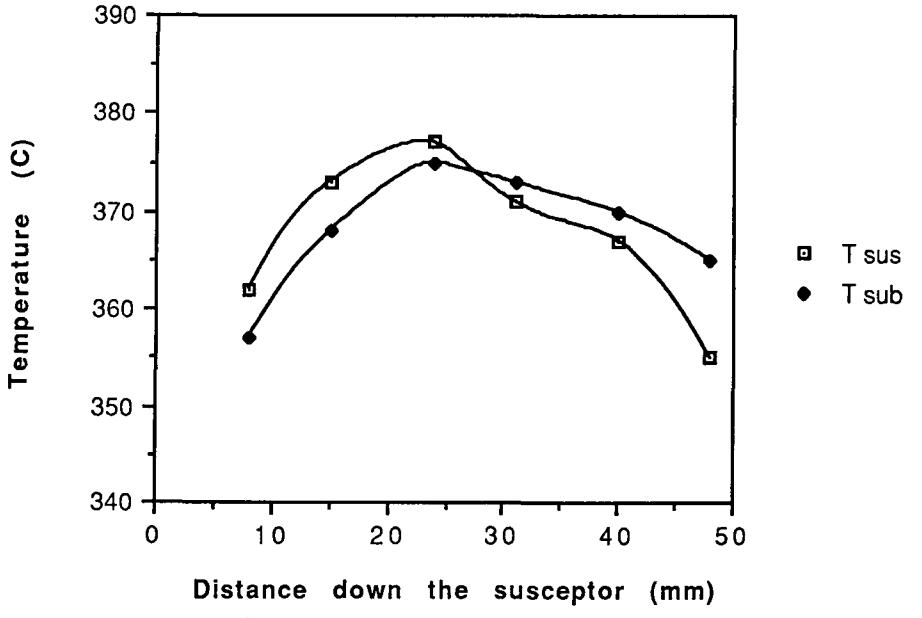

Fig 2.2 Temperature profiles along the susceptor (T_{sus}) and on GaAs substrates placed on it (T_{sub}) along the gas flow direction, for a set point temperature of 380°C.

A cross-over in the susceptor and substrate temperature profile were observed at ~27mm from the upstream edge. The reason for this was unclear but may indicate that the GaAs was introducing some turbulence with a consequent reduction in heat loss.

2.2.3 Precursor Pressures

Typical vapour pressures of the precursors used during growth and the temperatures required are presented in Table 2.1 as calculated using the equations 2.1 to 2.5 [8].

Precursor	Bubbler Temperature (°C)	Vapour pressure (Torr)
DIPTe	15	2.05
TCMn	75	1.89
DMCd	0	9.72
DMZn	-12	66.8
Hg	215	27.9

Table 2.1 Temperatures and associated vapour pressures of the precursors used for the growth of the (Hg,Mn)Te and the buffer layers.

$$\log_{10} P_{DIPTe}(\text{Torr}) = 8.125 - \frac{2250}{T(K)} \qquad 2.1$$

$$\log_{10} P_{DMCd}(\text{Torr}) = 7.764 - \frac{1850}{T(K)} \qquad 2.2$$

$$\log_{10} P_{DMZn}(\text{Torr}) = 7.802 - \frac{1560}{T(K)} \qquad 2.3$$

$$\log_{10} P_{TCMn}\,(\text{Torr}) = 8.632 - \frac{2908}{T\,(K)} \qquad 2.4$$

$$\log_{10} P_{Hg}\,(\text{Torr}) = 10.355 - \frac{3305}{T\,(K)} - 0.795\left[\log_{10} T\,(K)\right] \qquad 2.5$$

The temperature of the precursors were controlled by emersing them in temperature controlled baths. Elemental mercury was chosen since it provides an adequate vapour pressure at the (Hg,Mn)Te growth temperatures, can be obtained in a highly pure form, is inexpensive and is less toxic than many of its organic compounds. The mercury was placed in a quartz-silica boat upstream of the susceptor in the reactor and was heated using four 750 Watt quartz halogen lamps. The lamps also heated the reactor walls thus preventing any unwanted mercury condensation. Heating of the mercury was investigated using a thermocouple immersed in the mercury and comparisons made with the control thermocouple which was located under the mercury boat, Fig 2.3. A stabilisation time of 15 minutes was required to heat the mercury to 215°C from room temperature.

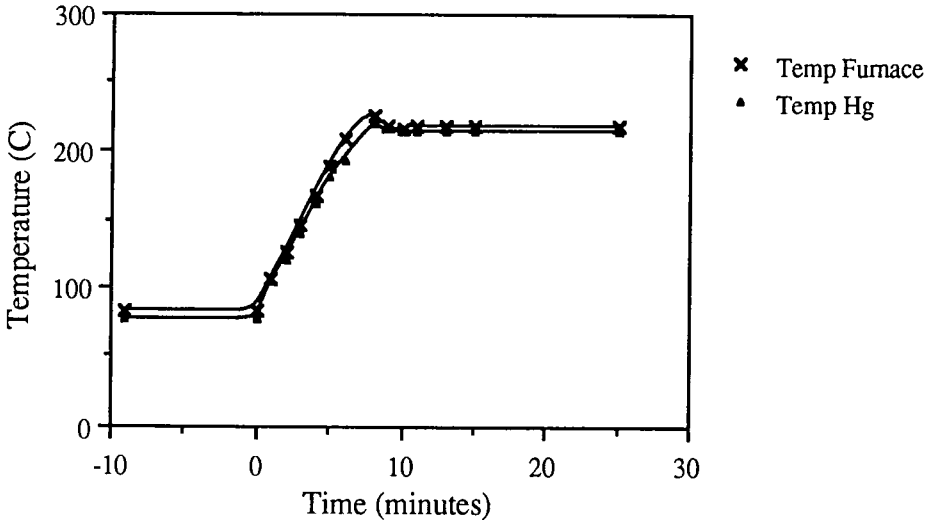

Fig 2.3 Calibration of the mercury temperature controller.

Assuming that the total pressure inside the reactor was 760 torr the feed rate of each precursor could be calculated by considering the partial pressure contribution from that precursor, equation 2.6.

$$\text{Feed Rate [moles/hour]} = \frac{P \cdot v \cdot 60}{22.4(760)} \qquad 2.6$$

where P is the vapour pressure of a precursor in torr and v is the flow rate of the carrier gas in $L.min^{-1}$.

2.2.4 Substrates

Layers were grown on a variety of substrates including: GaAs (100) and $Cd_{0.96}Zn_{0.04}Te$ (100) 2° off to nearest (110), (111)B and (211)B substrates provided by Japan Energy Corp (formally Nippon Mining). The substrates were scribed into pieces 10mm by 10mm for GaAs, or 15mm by 15mm for $Cd_{0.96}Zn_{0.04}Te$ and were degreased and cleaned using the procedure shown in Fig 2.4. Usually the substrates were heat cleaned by heating in the reactor, in a flow of hydrogen, to 400°C (growth temperature) for GaAs for 15 minutes, and 530°C for 40 minutes in the case of $Cd_{0.96}Zn_{0.04}Te$.

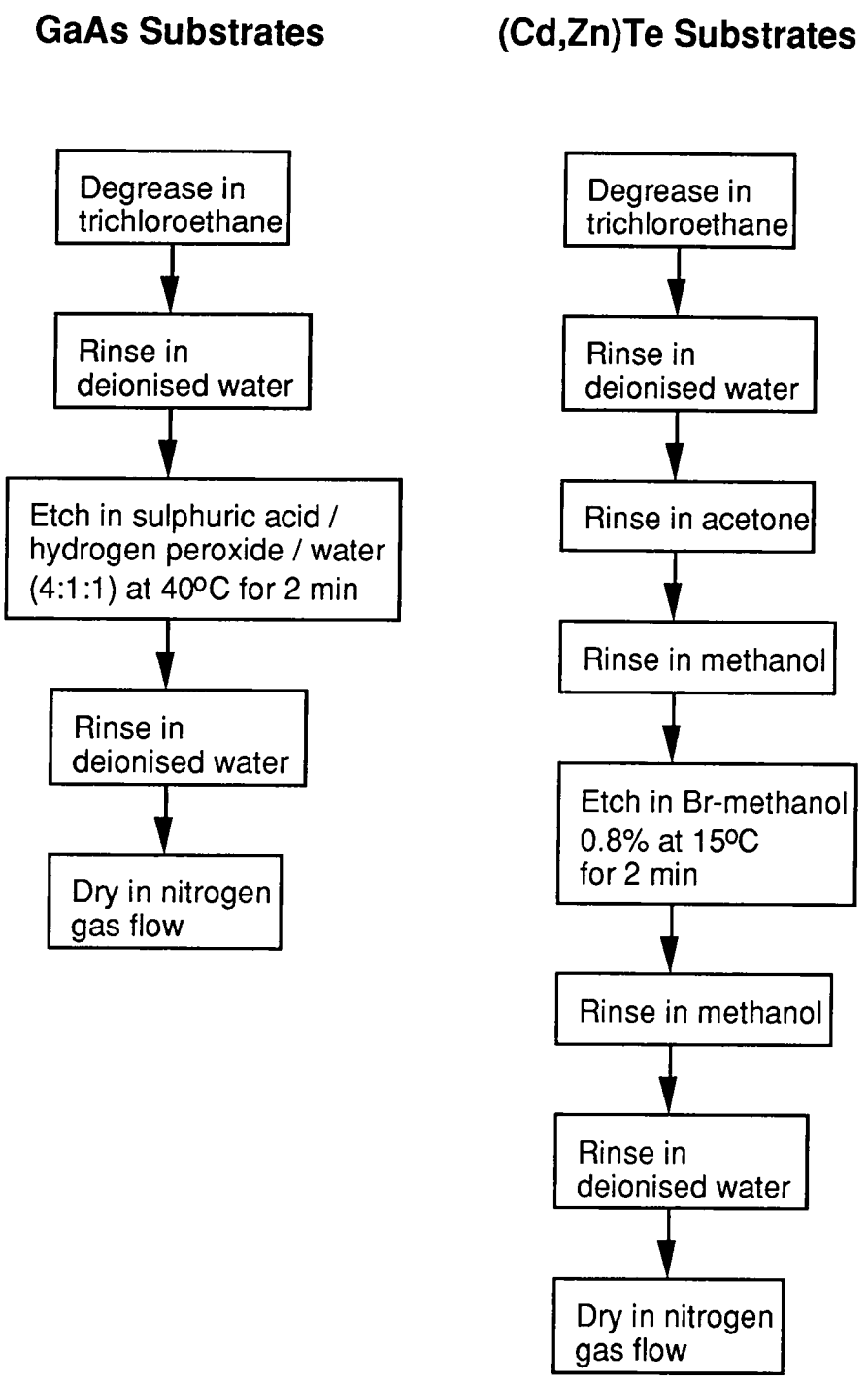

Fig 2.4 Cleaning procedures for the substrates.

2.3 Growth Conditions

A buffer layer structure was required for growth on GaAs substrates to accommodate the mismatch and to minimise cross-diffusion of Ga and As into the layer. The structure consisted of a ZnTe layer of approximately

0.1μm thickness, which ensured that the layers grew in the (100) orientation [9]. This was followed by a second buffer layer consisting of a 1μm thick CdTe layer to reduce the lattice mismatch experienced by the (Hg,Mn)Te layer and hence the dislocation density [6].

DIPTe was chosen as a precursor as it allows CdTe to be grown at lower temperatures (300°C instead of 390°C for diethyl telluride) reducing gallium and arsenic outdiffusion from the substrate and stress due to differential contraction between the substrate and the layer on cooling. Finally the (Hg,Mn)Te is deposited with growth times of 1 to 2 hours and without any annealing or a cap layer.

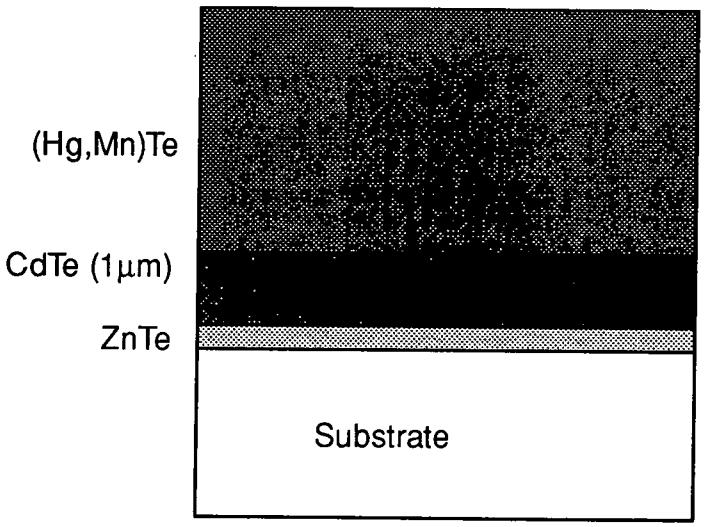

Fig 2.5 Typical layer structure grown on GaAs (100) substrates. Typical growth conditions are given in Table 2.2.

Layer	ZnTe	CdTe	(Hg,Mn)Te
Susceptor temperature (°C)	350	350	350-410
Total flow rate (cc/min)	7200	7200	1400
DIPTe feed rate (mmol/hr)	1.3	1.3	3.69
DMZn feed rate (mmol/hr)	3.1		
DMCd feed rate (mmol/hr)		1.94	
TCMn feed rate (mmol/hr)			2.67
Hg temperature (°C)			215

Table 2.2 Growth conditions used for the (Hg,Mn)Te/CdTe/ZnTe/GaAs system.

2.4 The Effect of the MOVPE Conditions on the Growth of (Hg,Mn)Te Epitaxial Films.

2.4.1 Susceptor Temperature Dependence

By varying the susceptor temperature between 350°C and 410°C while the other conditions were kept constant (as listed in Table 2.2), the effect on the composition of a layer grown on a centrally positioned substrate was found to be pronounced. Fig 2.6 shows the manganese content of the layers at positions near the downstream and upstream edges of the layer, giving some indication of the compositional uniformity.

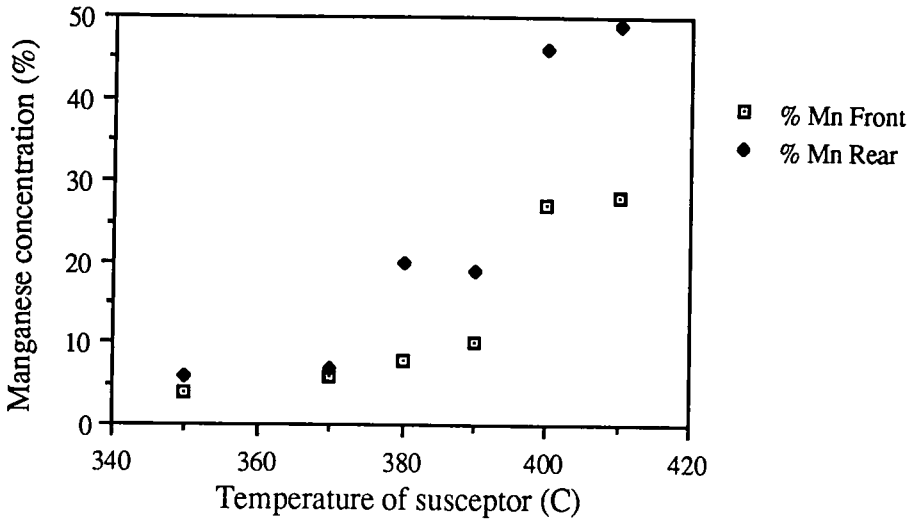

Fig 2.6 The dependence of layer composition on the susceptor temperature.

At a susceptor temperature of 380°C the manganese incorporation in the layers increased dramatically, due to the onset of TCMn pyrolysis at ~370°C [10]. The chemical structure of TCMn is illustrated in Fig 2.7 and consists of a π-methylcyclopentadienyl ring with a manganese atom covalently bonded to the ring and equidistant from the carbon atoms in the ring. Sang et al [11] have investigated the pyrolysis of TCMn in the MOVPE process using a quadrupole mass spectrometer and a capillary tube to collect the species. It was found that the π bonds connecting the carbonyl groups to the manganese atom were broken first since the bond energies are 97.5 $KJ.mol^{-1}$ compared to 236 $KJ.mol^{-1}$ for the manganese-ring covalent bond. The manganese atom was then released from the cyclopentadienyl ring afterwards.

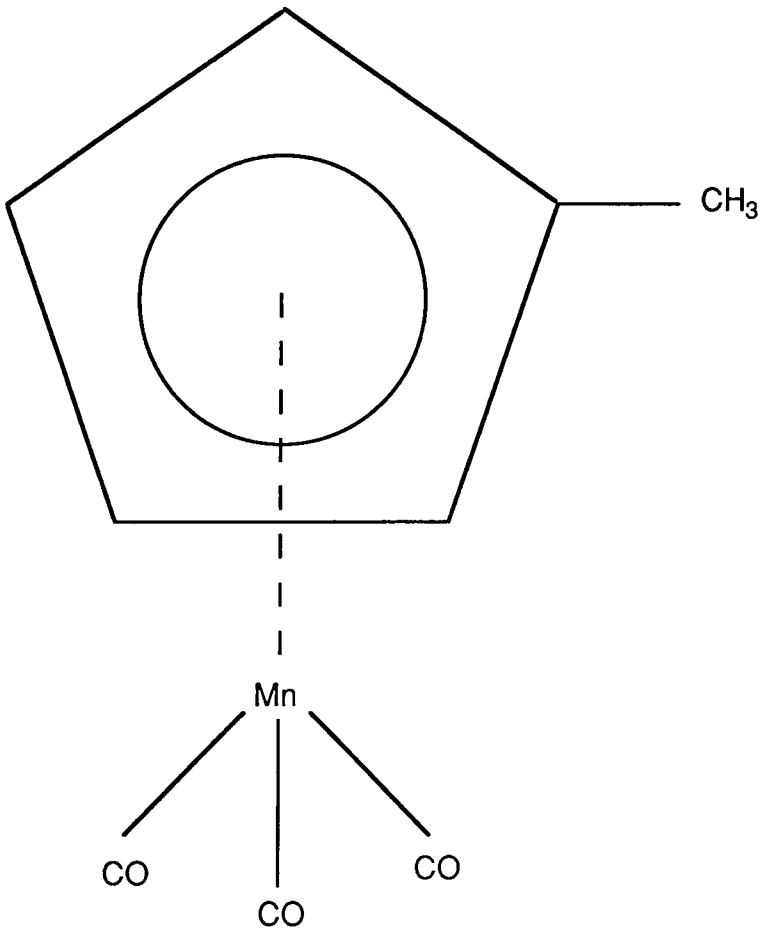

Fig 2.7 Chemical structure of TCMn

In the absence of any other precursors TCMn starts to pyrolyse at 410°C but if DIPTe is introduced the onset of pyrolysis occurs at a lower temperature. For a TCMn/DIPTe feed rate ratio of 0.55 at a flow rate of 1400 cc.min^{-1} the thermal activation energy of TCMn (the ring-Mn bond strength) is reduced from 236 KJ.mol^{-1} to 165 KJ.mol^{-1} and the corresponding onset of pyrolysis from 410°C to 350°C. Also it was found that the presence of TCMn increases the onset of pyrolysis of DIPTe from 210°C to 230°C [11]. The change in the activation energies in the precursors has been attributed to the formation of donor-acceptor adducts [10,12].

At higher temperatures (410°C) $MnTe_2$ and MnTe complexes were thought to occur in the layers.

2.4.2 The Mercury Vapour Pressure Dependence

To investigate the influence of the mercury vapour pressure upon the layer composition a series of growth trails were carried out in which the mercury temperature was varied from 215°C to 250°C, with the other growth conditions remained constant as shown in Table 2.3. The growth trials were performed using $Cd_{0.096}Zn_{0.04}Te$ (211)B substrates. The mercury content of the layers (1-x) was found to be approximately exponentially dependent on the mercury vapour pressure, Fig 2.8. As the mercury vapour pressure approached the equilibrium vapour pressure, adsorbed mercury atoms have a longer lifetime on the layer surface, increasing the probability of the mercury atom bonding to a tellurium atom before re-evaporation occurred. An increase in the mercury content in the layer would then be expected since the mercury and manganese atoms are competing for sites in the lattice.

Layer	ZnTe	CdTe	(Hg,Mn)Te
Susceptor temperature (°C)	350	350	400
Total flow rate (cc/min)	7200	7200	2000
DIPTe feed rate (mmol/hr)	1.3	1.3	3.69
DMZn feed rate (mmol/hr)	3.1		
DMCd feed rate (mmol/hr)		1.94	
TCMn feed rate (mmol/hr)			2.67
Hg temperature (°C)			215-250

Table 2.3. The growth conditions used in the study of the effect of mercury vapour pressure on layer composition.

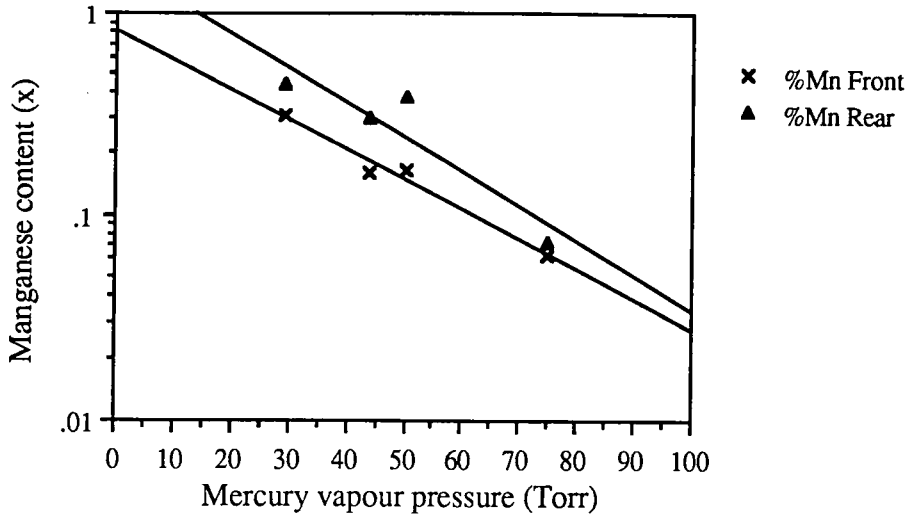

Fig 2.8 The mercury content in (Hg,Mn)Te layers, grown at a susceptor temperature of 400°C, as a function of mercury vapour pressure.

An analysis of the mercury vapour species present in the Durham MOVPE reactor at a mercury temperature of 200°C was made by Lovergine et al [13]. They detected both singly (Hg^+) and doubly ionised (Hg^{2+}) ions as well as a relatively small amount of mercury hydride $(HgH)^+$. This was achieved using a quadrupole mass spectrometer with a capillary tube electrically heated to a temperature greater than that of the mercury boat to avoid mercury condensation.

2.4.3 TCMn/DIPTe Feed Rate Ratio Dependence

To investigate the effect of the TCMn/DIPTe feed rate ratio on the composition of the layers a number of layers were grown with differing flow rates of the DIPTe carrier gas. The growth conditions used are shown in Table 2.4. Layers were grown on GaAs (100) substrates. Assessment of composition was done by EDAX at three positions 5mm apart along the direction of gas flow, Fig 2.9.

Layer	ZnTe	CdTe	(Hg,Mn)Te
Susceptor temperature (°C)	350	350	380
Total flow rate (cc/min)	7200	7200	1750
DIPTe feed rate (mmol/hr)	1.3	1.3	1.09 to 3.26
DMZn feed rate (mmol/hr)	3.1		
DMCd feed rate (mmol/hr)		1.94	
TCMn feed rate (mmol/hr)			2.67
Hg temperature (°C)			250

Table 2.4 The growth conditions used in the experiments to assess the effect the TCMn/DIPTe feed rate ratio had on layer composition.

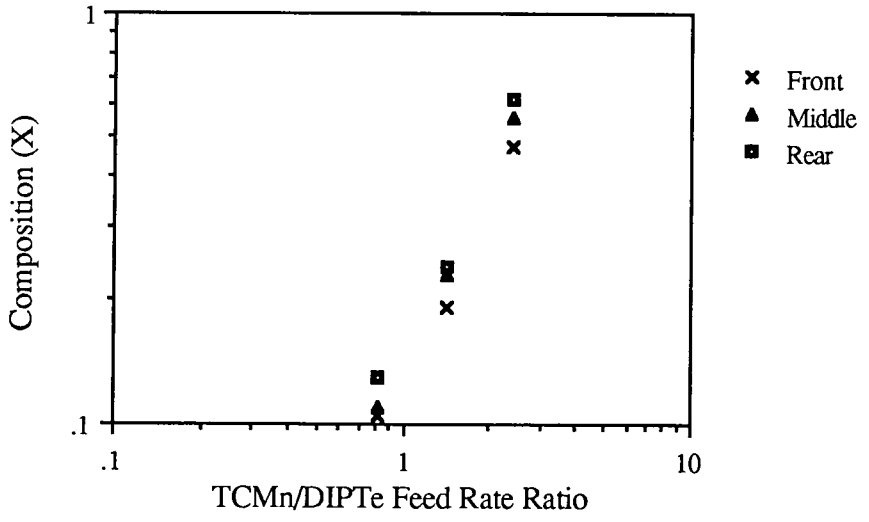

Fig 2.9 The influence of the TCMn/DIPTe feed rate ratio on layer composition.

The feed rate ratio was varied by changing the carrier gas flow rate through the DIPTe bubbler, and hence the resulting TCMn/DIPTe ratio. Fig 2.9 shows that increasing the rate of flow of the carrier gas through the DIPTe bubbler (i.e. increasing DIPTe concentration in the vapour) reduced

the manganese content of the layers. The manganese content was proportional to the TCMn/DIPTe feed rate ratio to the power of 1.3 (found from the slope of Fig 2.9).

If the composition of the layer is determined by the deposition rate of manganese atoms (R_{Mn}) compared to that of mercury (R_{Hg}) equation 2.7 is obtained.

$$x = \frac{R_{Mn}}{R_{Mn}+R_{Hg}} \qquad 2.7$$

Assuming the deposition rate of manganese atoms to be a function of the partial pressure of TCMn (P_{TCMn}) and DIPTe (P_{DIPTe}) only.

$$R_{Mn} = K_1\left(P_{TCMn}\right)^a\left(P_{DIPTe}\right)^b \qquad 2.8$$

where a and b are the power dependence of the partial pressures and K_1 is a rate constant.

Similarly the deposition rate of mercury can be given by the partial pressure of mercury (P_{Hg}) and DIPTe (P_{DIPTe}) and since the bonding energy of Hg-Te is considered to be less than that of Mn-Te the mercury atoms are only able to occupy those sites left vacant by manganese atoms (1-x).

$$R_{Hg} = K_2\left(P_{Hg}\right)^c\left(P_{DIPTe}\right)^d\left(1- x\right) \qquad 2.9$$

where c and d are the power dependences of the partial pressures and K_2 is a rate constant.

Since the mercury vapour pressure was kept constant (at around 75 torr) it can be incorporated into the rate constant.

$$R_{Hg} = K_3\left(P_{DIPTe}\right)^d(1-x) \qquad 2.10$$

where $K_3 = K_2.(P_{Hg})^c$.

From 2.7, 2.8 and 2.10 equation 2.11 is obtained.

$$x = K\left(P_{TCMn}\right)^a\left(P_{DIPTe}\right)^{b-d} \qquad 2.11$$

where $K = K_1/K_3$

Considering the TCMn/DIPTe feed rate ratio, β,

$$\beta = \frac{P_{TCMn}}{P_{DIPTe}} \qquad 2.12$$

Substituting equation 2.12 into 2.11,

$$x = K\left(P_{TCMn}\right)^{a+b-d}\beta^{d-b} \qquad 2.13$$

Since P_{TCMn} was constant a new constant, Q, can be introduced.

$$x = Q\beta^{d-b} \qquad 2.14$$

Taking the logarithm of equation 2.14 an equation for Fig 2.13 is obtained in the form of a straight line of gradient d-b.

$$\log_{10}x = \log_{10}Q+(d-b)\log_{10}\beta \qquad 2.15$$

By considering the growth rate of HgTe (x=0) a value for d of the order of 1.3 is obtained. From Fig 2.9 a slope of approximately 1.3 is obtained which implies that b is very small and the partial pressure of TCMn is the dominant variable in the incorporation of manganese into the layers.

2.4.4 Dependence of Growth on Substrate Position

To investigate the change in layer parameters grown at different positions in the gas flow, nine 5mm long GaAs (100) substrates were placed in a row, downstream of one another. The temperature profile of the susceptor for a set temperature of 380°C was given in Fig 2.2. The compositions, found by EDAX, and the thicknesses, found from x-ray diffraction, of the centre of the layers grown under the condition in Table 2.2 are given in Fig 2.10 and 2.11.

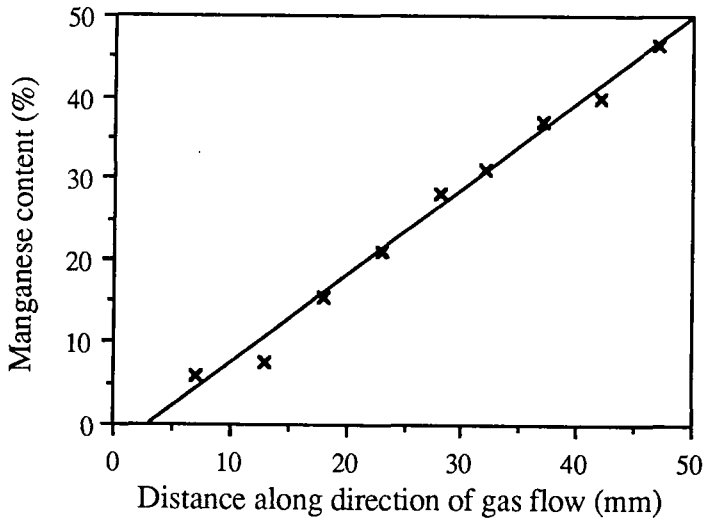

Fig 2.10 Positional dependence of layer composition along the direction of the gas flow (set conditions; susceptor temperature = 380°C and TCMn/DIPTe feed rate ratio = 0.72).

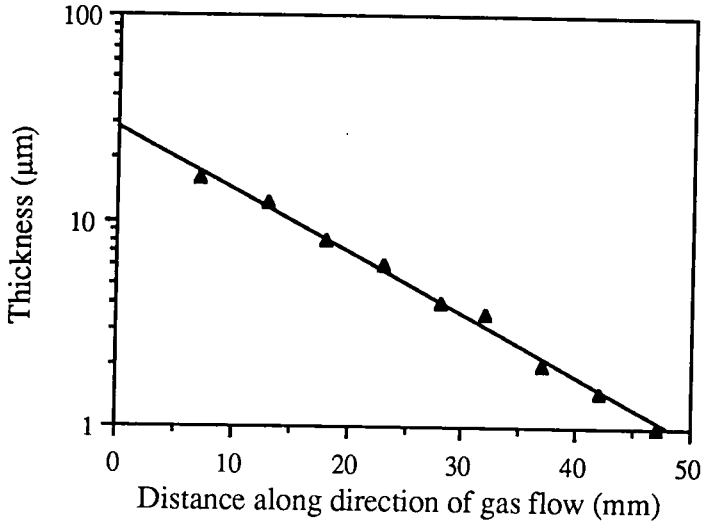

Fig 2.11 Positional dependence of layer thickness along the direction of the gas flow (set conditions; susceptor temperature = 380°C and TCMn/DIPTe feed rate ratio = 0.72).

These graphs show a linear change of composition with substrate position and an exponential dependence of thickness on substrate position. This was thought to be due to an increase in TCMn/DIPTe partial pressure ratio along the gas flow. The reduction in thickness may be a direct result of the reduction in the concentration of tellurium. In order to investigate this further a model was developed to try and understand the variation in layer parameters along the direction of the gas flow.

The concentration profiles of reactants were calculated [14] using a plug flow model [15], where the gas flow was governed by an imposed pressure gradient rather than by a diffusion mechanism. Assumptions made were that the temperature of the gas over the susceptor was constant with time, the change in the volume of the gas due to the reaction was negligible

(since the precursors occupied less than 1% of the total gas flow) and that the pyrolysis was an irreversible first order reaction where the rate constant, k, was given by equation 2.16.

$$k = A\exp\left(\frac{-E}{RT}\right) \qquad 2.16$$

where A is a constant and E, R and T are an activation energy, the universal gas constant and the absolute temperature respectively.

The mass balance geometry is shown in Fig 2.13 and may be represented by equation 2.17.

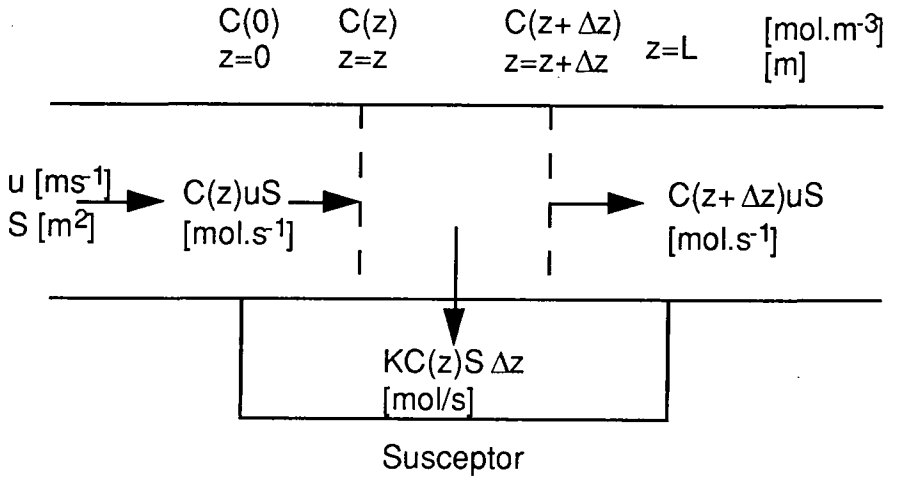

Fig 2.13 The precursor mass balance for the plug flow model.

$$C(z)uS = C(z+\Delta z)uS + kSC(z)\Delta z \qquad 2.17$$

where C(Z) is the precursor concentration at position z, the cross sectional area of the reactor is S, L is the susceptor length and u is the gas flow velocity.

In the limit $\Delta z \rightarrow 0$,

$$\frac{dc}{dz} = \frac{-k}{u}c(z) \qquad 2.18$$

and on integrating,

$$C(z) = C(0)\exp\left(\frac{-kz}{u}\right) \qquad 2.19$$

Dimensionless parameters were introduced to generalise the situation. The relative concentration, position and rate constant are defined in equations 2.20 to 2.22 respectively.

$$\Phi(z) = \frac{C(z)}{C(0)} \qquad 2.20$$

$$\eta(z) = \frac{Z}{L} \qquad 2.21$$

$$\alpha(z) = \frac{kL}{u} \qquad 2.22$$

Equation 2.19 is then reduced to;

$$\Phi(\eta) = \exp(-\alpha\eta) \qquad 2.23$$

When the total mass flow rate of the gas is constant, the gas velocity above the susceptor is directly proportional to the susceptor temperature, i.e if u_1 and u_2 are the gas velocities at temperatures T_1 and T_2 then equation 2.24 is obtained.

$$\frac{u_1}{u_2} = \frac{T_1}{T_2} \qquad 2.24$$

Using equations 2.16 and 2.22 the temperature dependence of the relative rate constant is described by equation 2.25.

$$\alpha_1 = \alpha_2 \frac{T_1}{T_2} \exp\left[\frac{E}{R}\left(\frac{1}{T_1} - \frac{1}{T_2}\right)\right] \qquad 2.25$$

The quantitative description for the pyrolysis behaviour requires the actual value of α and this can be determined experimentally from the pyrolysis behaviour of the precursors. Activation energies for the pyrolysis of TCMn and DIPTe were found to be 165 and 106KJ.mol^{-1} respectively by Wen-bin [11] from pyrolysis-temperature characteristics taken at the downstream end of the Durham reactor (including the correction in equation 2.24). Corresponding values for α for TCMn and DIPTe of 20 and 80 respectively were then calculated using equation 2.25 by a process of iteration (T=773K and total flow rate = 1.4 litres.min^{-1}).

When the precursor concentration profiles along the reactor were calculated it was discovered that TCMn decreased in a linear manner along the reactor, whereas DIPTe reduced sharply at the front of the reactor, Fig 2.13. At a susceptor temperature of 400°C the pyrolysis of DIPTe was almost complete at η~0.6, while that of the TCMn was only around 40% complete under the same conditions. This clearly indicates the large disparity in the pyrolysis rates of the two precursors and hence leads to an appreciation of the difficulty in growing uniform (Hg,Mn)Te using these precursors.

From equation 2.23 it is obvious that the relative concentration of DIPTe has an exponential dependence on position in the gas flow, which corresponds well with the observed exponential dependence of layer thickness on position, Fig 2.11. This implies that the concentration of DIPTe is the dominant factor in the determination of the (Hg,Mn)Te layer growth rate.

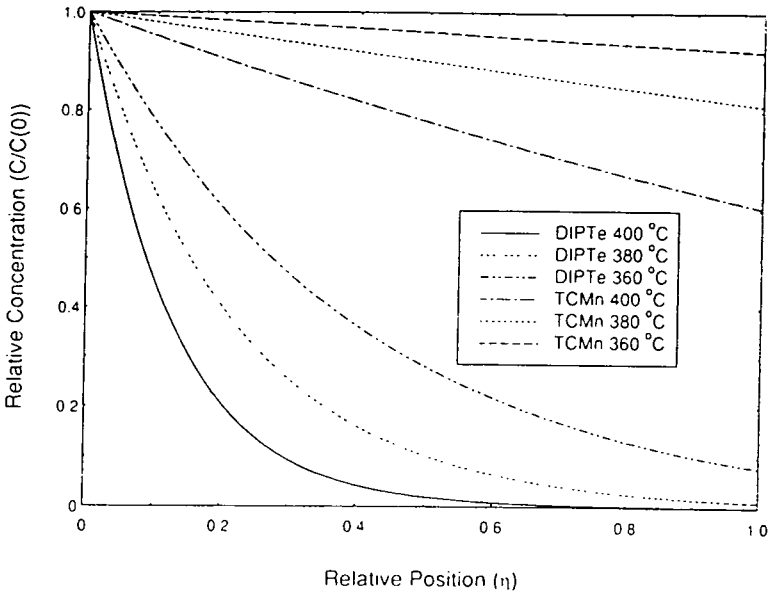

Fig 2.13 Calculated variation in TCMn and DIPTe concentration along the susceptor at a total flow rate of 1.4 litres.min^{-1}.

More precisely it is the TCMn/DIPTe pyrolysis rate ratio which is the important parameter. This ratio is given by equation 2.26.

$$\frac{\xi_{Mn}}{\xi_{Te}} = \frac{k_{Mn}C_{Mn}(0)}{k_{Te}C_{Te}(0)}\exp\left[(\alpha_{Te}-\alpha_{Mn})\eta\right] \qquad 2.26$$

where ξ denotes the pyrolysis rate of a particular precursor and C(0) is the initial concentration.

Equation 2.26 clearly indicates an exponential dependence of the pyrolysis rate ratio on susceptor position, Fig 2.14. In section 2.4.4 the manganese concentration was found to increase linearly with distance down the gas flow. This implies that the manganese incorporated into the epitaxial (Hg,Mn)Te was logarithmically dependent on the pyrolysis rate ratio as shown in Fig 2.15. This indicates that as the TCMn/DIPTe ratio becomes

very large, for a given mercury vapour pressure, the incorporation of manganese tends to saturate as the relative availability of free tellurium becomes restricted.

Although the slopes of the pyrolysis rate ratio plots increase with susceptor temperature, the variation in the ratio along the direction of gas flow can be suppressed by increasing the total flow rate through the reactor, e.g. for increasing the flow rate from 1.4 litres.min^{-1} to 6 litres.min^{-1} the variation along the length of the reactor at 380°C was reduced from two orders of magnitude to a factor of three.

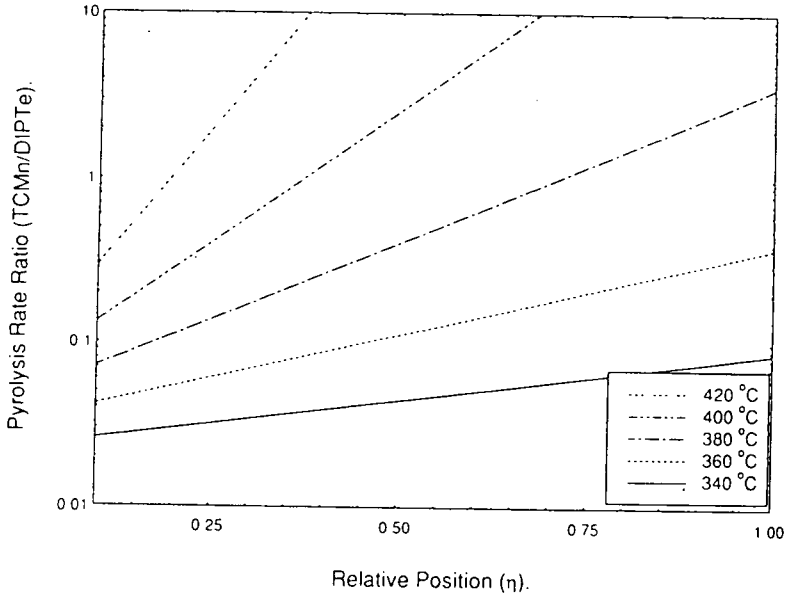

Fig 2.14 Variation in the precursor pyrolysis rate along the susceptor at a total flow rate of 1.4 litres.min^{-1}.

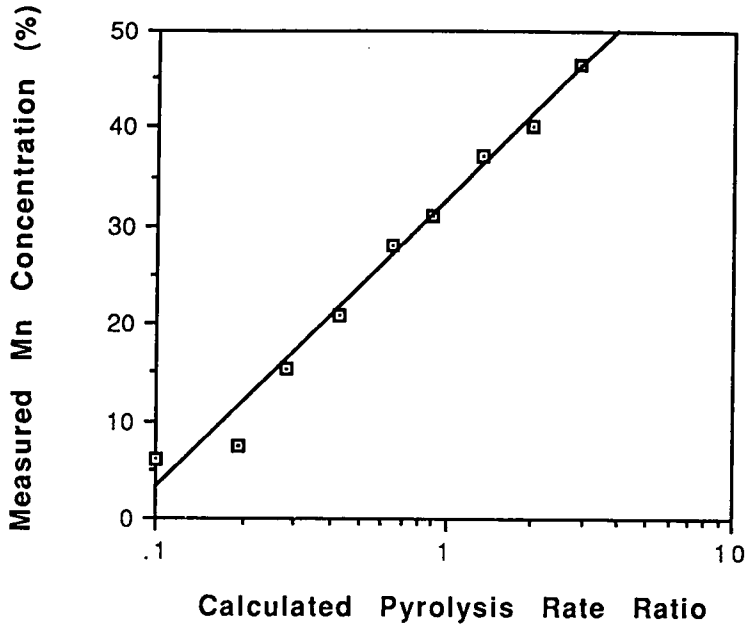

Fig 2.15 Dependence of the measured manganese concentration in (Hg,Mn)Te on the calculated pyrolysis rate ratio.

The data in Fig 2.15 was fitted by the exponential expression given in equation 2.27.

$$x = 32.4 + 29.4\log_{10}\left(\frac{\xi_{Mn}}{\xi_{Te}}\right) \qquad 2.27$$

2.5 Conclusions

Precursors of TCMn, DIPTe and elemental mercury were used to grow layers of (Hg,Mn)Te in a horizontal atmospheric pressure MOVPE reactor.

Layer composition was strongly dependent on the susceptor temperature due to the nature of the TCMn pyrolysis. However, a small percentage of manganese was still present in layers grown below the pyrolysis temperature of TCMn which suggested the possible presence of manganese species with pyrolysis temperatures lower than that of TCMn.

Mercury vapour pressure was found to a have a large effect on layer composition, by restricting the inclusion of manganese in the layer.

A semi-empirical model was proposed to explain the exponential dependence of the composition on the TCMn/DIPTe feed rate ratio. This indicated that for a given vapour pressure of mercury the pyrolysis rate ratio of TCMn/DIPTe was an important variable.

However the greatest problem, with a view to device fabrication is the non-uniformity of the composition and layer thickness. Differing pyrolysis rates of DIPTe and TCMn are the major cause of this non-uniformity in MOVPE grown (Hg,Mn)Te. To improve uniformity an alternative tellurium precursor with pyrolysis characteristics closer to that of TCMn (such as diethyl telluride) could be used for the (Hg,Mn)Te layer or the installation of a rotating susceptor, as commonly used for the MOVPE growth of (Hg,Cd)Te [16]. Another method for improving the uniformity of growth has been developed by Tunnicliffe et al (Hg,Cd)Te [17], where alternate thin layers of the binary compounds are grown then allowed to diffuse, the so called interdiffused multilayer process (IMP). This was also used to grow (Hg,Mn)Te and is discussed in Chapter Seven.

References

[1] R.T. Delves and B. Lewis (1963) J. Phys. Chem. Solids **24** 549.

[2] A. Rogalski (1991) Infrared Phys. **31** 117.

[3] P. Becla, P.A. Wolff, R.L. Aggarwal and S.Y. Yuen (1985) J. Vac. Sci. Technol. **A3**(1) 116.

[4] J. Reno, I.K. Sou, P.S. Wijewarnasuriya and J.P. Faurie (1985) Appl. Phys. Lett **47** 1168.

[5] P.A. Clifton, A.W. Brinkman and H.M. Al-Allak (1990) Semicon. Sci. Technol. **5** 1067.

[6] H.M. Al-Allak, A.W. Brinkman, P.A. Clifton and P.D. Brown (1991) Mater. Res. Soc. Symp. Proc. **216** 35.

[7] M. Funaki, J.E. Lewis, T.D. Hallam, Chaorang Li, S.K. Halder, A.W. Brinkman and B.K. Tanner (1993) Semi. Sci. Technol. **8** 200.

[8] Data Sheets, Speciality Chemical Group, Morton International Inc. (1989).

[9] H. Shtrikman (1988) J. Electron. Matter **17** 105.

[10] J.B. Mullins, S.J.C. Irvine and D.J. Ashen (1981) J. Crystal Growth **55** 92.

[11] S. Wenbin, K. Durose, A.W. Brinkman and J. Woods (1991) J. Crystal Growth **113** 1.

[12] M.R. Czerniak and B.C. Easton (1984) J. Crystal Growth **68** 128.

[13] N. Lovergine, P.A. Clifton, A.W. Brinkman and J. Woods (1991) Chemtronics **5** 11.

[14] T.D. Hallam, S. Oktik, M. Funaki, C. Moore, A.W. Brinkman, K. Durose and B.K. Tanner (1995) J. Crystal Growth **146** 604.

[15] "Organometallic Vapor Phase Epitaxy" by G.B. Stringfellow (1989) pub. Academic Press, London p226.

[16] R. Korenstein, P. Hallock and B. MacLeod (1990) J. Vac. Sci. Technol. **B9(3)** 1630.

[17] J. Tunnicliffe, S.J.C. Irvine, O.D. Dosser and J.B. Mullins (1984) J. Crystal Growth **68** 245.

Chapter Three

Experimental Methods

3.1 Introduction

This chapter describes the experimental procedures and equipment used in the assessment of the Durham grown epitaxial (Hg,Mn)Te. As discussed previously, one of the main aims of this project is to characterise the fundamental behaviour of carriers in (Hg,Mn)Te epitaxial films and their dependence on film properties such as thickness, composition and layer quality.

The transport properties were measured using Hall [1] and resistivity measurements. The van der Pauw method of resistivity measurement developed in 1958 at Philips research laboratories in Eindhoven by L.J van der Pauw [2] was adopted since only four contacts are required (as opposed to the standard five point probe technique), it requires only knowledge of the layer thickness and can be applied to any arbitrary geometry of the layer provided the thickness is constant.

The second aim was to assess the structural quality of epitaxial (Hg,Mn)Te and the effect on electrical transport. Extensive x-ray diffraction work was undertaken, since this has the major advantage of being a very precise and non-destructive technique, making it possible for other measurements to be made subsequently on the same sample. Information obtained from x-ray diffraction included layer thickness, composition and perfection (from double crystal diffraction), two dimensional maps of lattice strain (from topography) and a measure of lattice tilts and dilations (from triple axis diffraction [3]).

3.2 Transport Measurements

3.2.1 The van der Pauw Technique

This technique allows the measurement of resistivity for any geometry of layer provided the following requirements are met:

i) The contacts are placed on the periphery of the layer;

ii) That the contacts are small in relation to the sample dimensions, (in the present context this means less than ~1mm diameter);

iii) The thickness of the layer is constant;

iv) That the layer is singularly connected i.e contains no isolated holes.

Consider the plan view of a layer complete with contacts, which satisfies the above criteria (Fig 3.1). In the van der Pauw method a current is passed through contacts A and B and the resulting voltage measured across C and D, and used to calculate a resistance (Equation 3.1). The current is then passed through B and C and the resulting voltage between D and A measured, thus giving a second resistance (Equation 3.2). The process may then be repeated for the other two combinations.

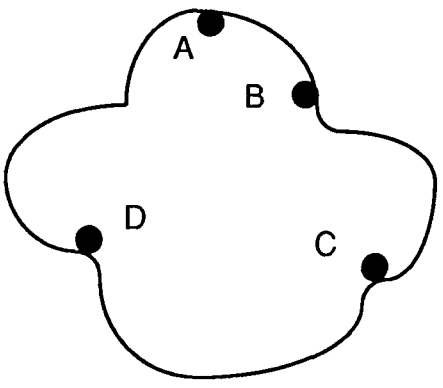

Fig 3.1 A van der Pauw electrical contact arrangement.

$$R_{AB,CD} = V_{CD}/I_{AB} \qquad 3.1$$

$$R_{BC,DA} = V_{DA}/I_{BC} \qquad 3.2$$

Knowing any pair of resistances, and the thickness of the film, the resistivity can be calculated from equation 3.3.

$$\rho = \frac{\pi d}{\log_e 2}\left[\frac{R_{AB,CD}+R_{BC,DA}}{2}\right]f \qquad 3.3$$

where ρ is the resistivity of the layer, d is the layer thickness and f is a geometric factor derived from $R_{AB,CD}$ and $R_{BC,DA}$ (and which must satisfy the condition in equation 3.4).

$$\frac{R_{AB,CD}-R_{BC,DA}}{R_{AB,CD}+R_{BC,DA}} = f\,\mathrm{arccosh}\left(\frac{\exp(\log_e 2/f)}{2}\right) \qquad 3.4$$

It is clear that this is a complex equation and for routine calculations the graph in Fig 3.2 can be used.

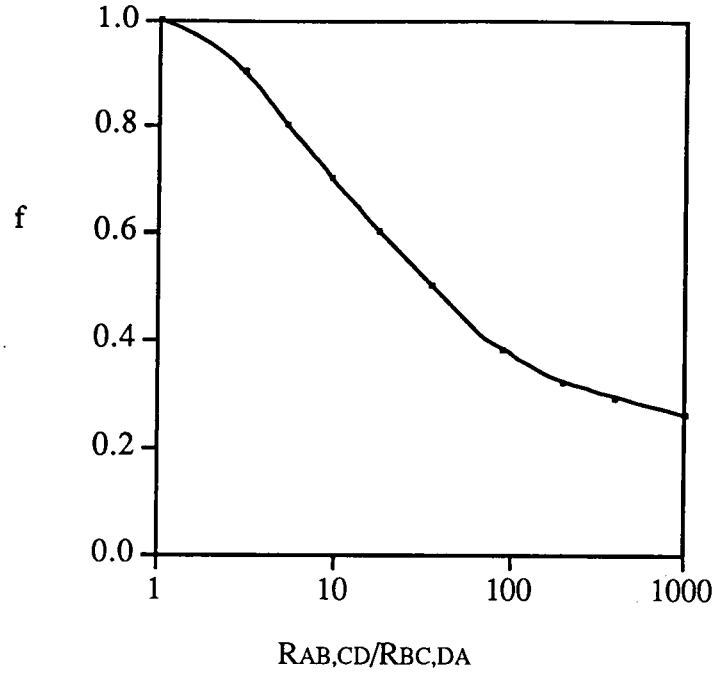

Fig 3.2 Graph of the geometric correction factor, f, as a function of the measured resistances in the van der Pauw technique.

It can be seen that for values of ($R_{AB,CD}/R_{BC,DA}$) less than three, f can be assumed to be unity without significant error.

3.2.2 Electrical Measurements

To implement the electrical characterisation of (Hg,Mn)Te over a temperature range of 4.2K to 290K, an Oxford Instruments MD3 cryostat together with an ITC4 temperature controller and a rotatable magnet was used in the arrangement shown in fig 3.3. Electrical contacts were made to the layers by evaporating gold or indium contact pads through a mask and carefully attaching copper wires to the pads with silver paint. The sample support rod allowed two samples to be characterised in the same run and had a gold/chrome thermocouple positioned on the sample stage for accurate temperature measurement. A Durham built constant current source capable of supplying currents from 0.1μA to 1 A was used together

with an HP 3456A digital voltmeter. For ease of operation, external electrical connection to the (Hg,Mn)Te layers were controlled via a system of relays, designed to provide the required configurations of currents and voltages in a simple manner. The current passing through the coils of a Newport type A magnet (up to 10 Amps), was supplied by a Newport Instruments type D104 power supply, to give magnetic fields up to 0.38T between the polepieces of the magnet.

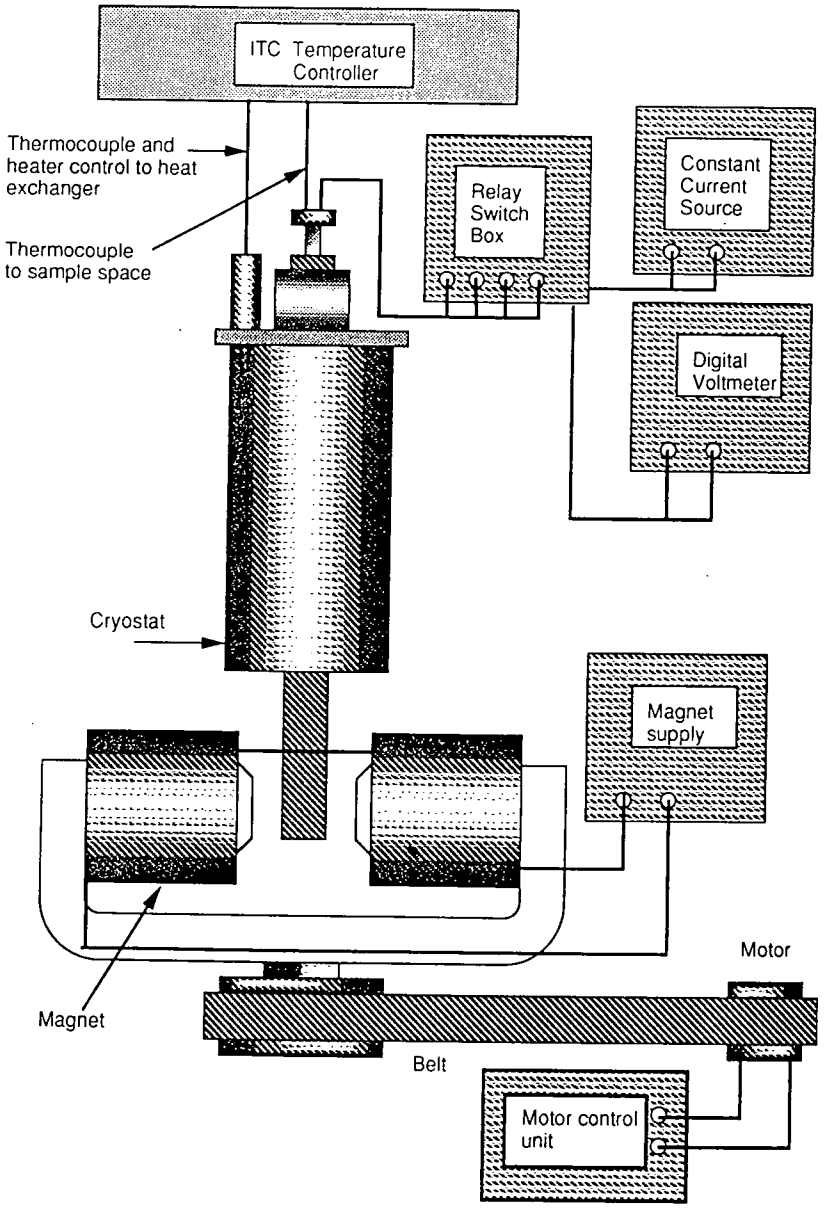

Fig 3.3 The system used to perform variable temperature measurements.

The horizontal and vertical profiles of the magnetic field between the magnet pole pieces were measured using a TET model 3103A teslameter and are shown in figs 3.4 and 3.5. The magnetic field strength is greatest along the axis of the pole pieces and directly next to one or other of them.

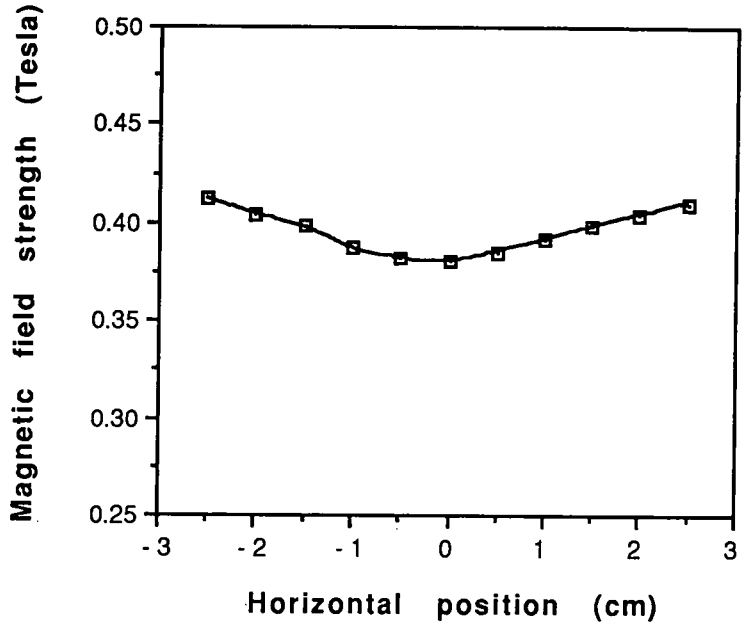

Fig 3.4 The magnetic field profile taken along the axis of the magnet polepieces.

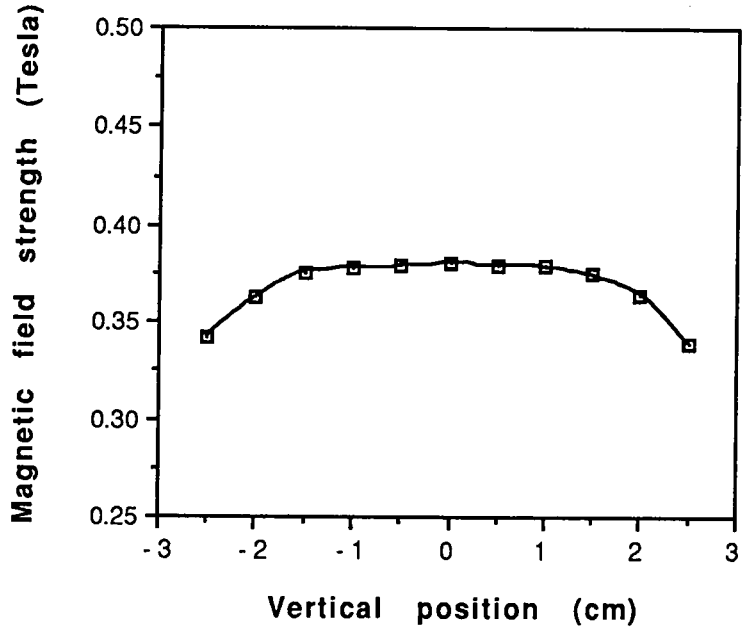

Fig 3.5 The magnetic field profile taken perpendicular to the axis of the polepieces in the centre of the gap.

The relationship between the magnetic field in the centre of the polepieces (where the (Hg,Mn)Te layers were positioned) and the current through the coils was measured and is shown in Fig 3.6. The B-I characteristic could be represented by the quadratic relationship given in equation 3.5.

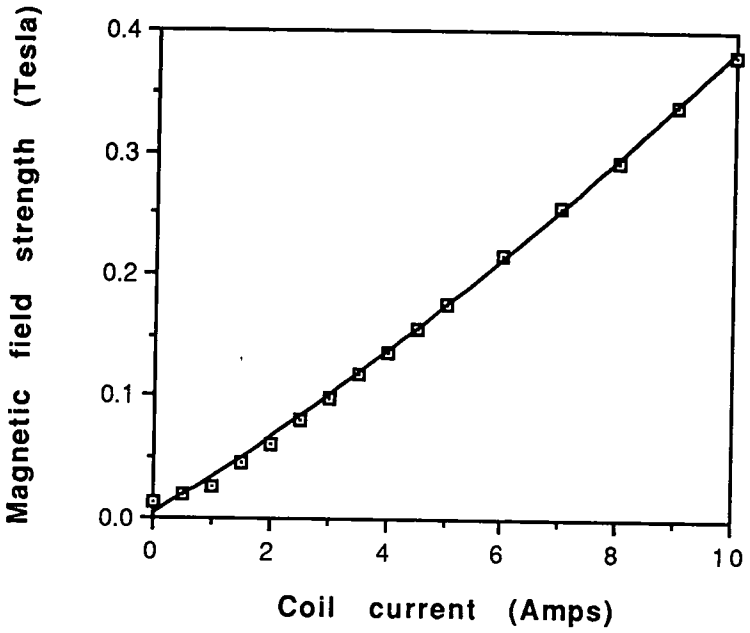

Fig 3.6 Calibration curve for the magnet.

$$B = 0.001I^2 + 0.030I + 0.003 \qquad 3.5$$

where B was the magnetic field strength in the centre of the polepieces in Teslas and I was the current in Amps passing through the coils.

To reverse the direction of the magnetic field the magnet was rotated about the cryostat by 180^{o}. A potentiometer mounted on the base of the stage allowed accurate positioning of the magnet (Fig 3.7).

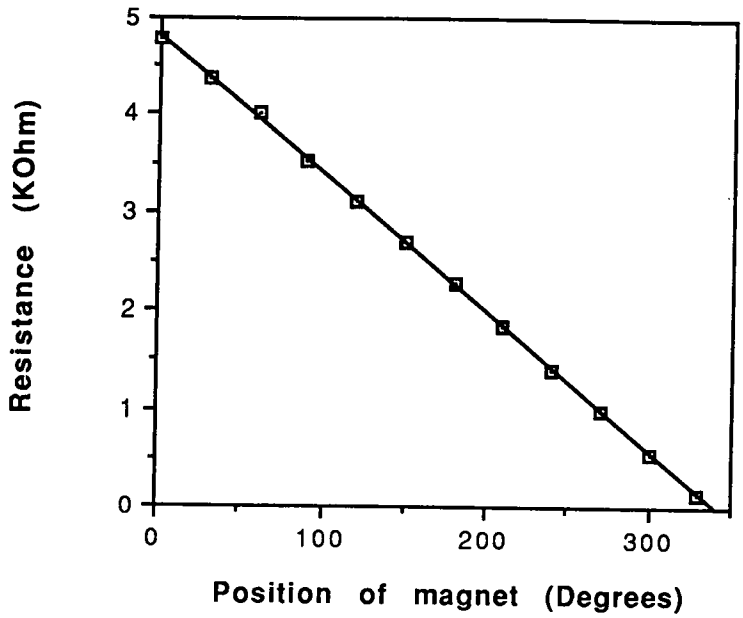

Fig 3.7 Calibration curve for the potentiometer mounted on the base of the magnet to indicate angular position.

The cryostat consisted of two chambers, the outer vacuum case (OVC) was evacuated using a diffusion pumped system to ~10^{-5} mbar to ensure good thermal insulation. The reservoir and sample space had first to be thoroughly flushed with dry helium before the system was pre-cooled by filling the reservoir with liquid nitrogen. The system was then left to stand for 24 hours, when the remaining liquid nitrogen was blown out using dry helium gas and liquid helium was transferred into the reservoir.

Once the reservoir had been filled the liquid helium was pumped over the sample to obtain a temperature of 4.2K. Lower temperatures could be obtained by pumping hard on the liquid helium or by allowing liquid helium to build up at the heat exchanger then pumping on it very quickly (the single shot method) [4].

3.3 Structural Analysis

3.3.1 The Nature of X-rays

X-rays are produced when electrons are accelerated through a high (typically 40kV) potential and strike a heavy target such as copper. This is an inefficient process as 99% of the energy is lost as heat and therefore the target has to be water cooled. The spectral output of the x-ray tube consists of two components: a broadband component caused by core scattering and which has a very wide range of wavelengths from the minimum wavelength that can be excited by the applied voltage to the maximum wavelength that will pass through the windows of the tube with an appreciable intensity. The second and more important part of the emission is the line spectrum characteristic of the target element and is caused by inner shell ionisation. Filters can be used which will remove certain wavelengths, by absorption.

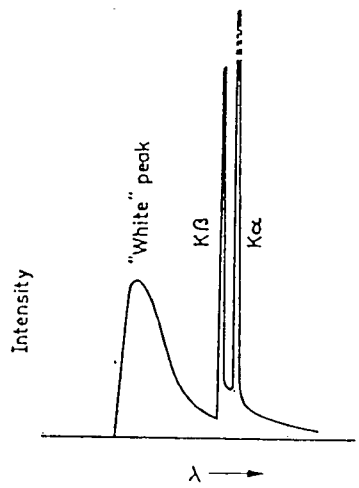

Fig 3.8 The emission spectrum of an x-ray tube.

The geometrical optics of x-rays is simple compared to that of visible light, since they are not practically deviated by refraction. Whatever the medium they pass through, x-rays have virtually the same velocity as light in a vacuum and the variation in x-ray velocity in differing mediums is

less then 1 in 10^4. Consider the index of refraction (n) to be slightly less than unity. Theoretically n for a pure material is given by equation 3.6 [5]

$$n = 1-\delta = 1- [(1/2\pi)r_e N\lambda^2] \qquad 3.6$$

where r_e is the classical radius of an electron (2.818×10^{-15}m), N is the number of electrons per cubic metre and λ is the wavelength of the x-rays.

If ρ is the density of the medium and Z is the number of electrons in the atomic group (atom, unit cell etc) of relative atomic mass M then for λ in Å

$$\delta = 2.72 \times 10^{-6} (Z/M)\rho\lambda^2 \qquad 3.7$$

since Z/M is always about 0.5 then δ will be always of the order of $1.3 \times 10^{-6}\rho\lambda^2$. Even when considering high density materials, with long wavelength x-rays, δ is still only around 10^{-4}.

The intensity of an x-ray beam is defined as the flux of energy per unit area passing a fixed point per second. For a monochromatic beam the intensity is directly proportional to the square of the amplitude. The absolute intensity measurements are made in Wm^{-2}.

A beam of x-rays passing through some material medium may be attenuated by scattering (either elastic or inelastic (Compton scattering)) or by absorption. When x-ray photons are absorbed by an atom, electrons are ejected by the photoelectric effect. The atom then returns to its ground state emitting either another electron (Auger) or another x-ray photon (fluorescence).

Consider a beam of monochromatic x-rays passing through some material, such that the incident beam has intensity I and the emerging beam has

intensity I + dI. If the material is thin and has a mass per unit area of dp then experimentally it is found that dI is directly proportional to I and dp. Therefore;

$$dI = -\mu.I.dp \qquad 3.8$$

where the constant of proportionality, μ, is the mass absorption coefficient. For a finite thickness, integration of equation 3.8 gives:

$$(I+dI)/I = \exp(-\mu p) \qquad 3.9$$

or as a function of thickness where ρ is the density of the material,

$$(I+dI)/I = \exp(-\mu\rho l) \qquad 3.10$$

where l is the thickness of the material.

The product $\mu\rho$ is often referred to as the linear absorption coefficient. The mass absorption coefficient increases with wavelength although absorption discontinuities occur when the mechanism of absorption changes as the photon energy increases sufficiently to ionise a new electronic shell. At the same time fluorescence, or the emission of characteristic x-rays from relaxation processes in the excited atom may take place.

3.3.2 X-ray Diffraction from a Single Crystal

X-rays can be scattered by two mechanisms giving coherent or incoherent (Compton) scattering. In the former x-ray photons cause tightly bound electrons to oscillate and emit x-ray photons with identical energies to the incident ones. Compton scattering occurs when x-ray photons lose energy

to the electrons thus changing the x-ray wavelength . Since Compton scattering is incoherent it does not contribute to diffraction effects. Diffraction results from two phenomena. The first being coherent scattering from individual atoms and the second being the interference between the scattered waves [6]. Consider the scattering of monochromatic x-rays from neighbouring planes of atoms in Fig 3.9.

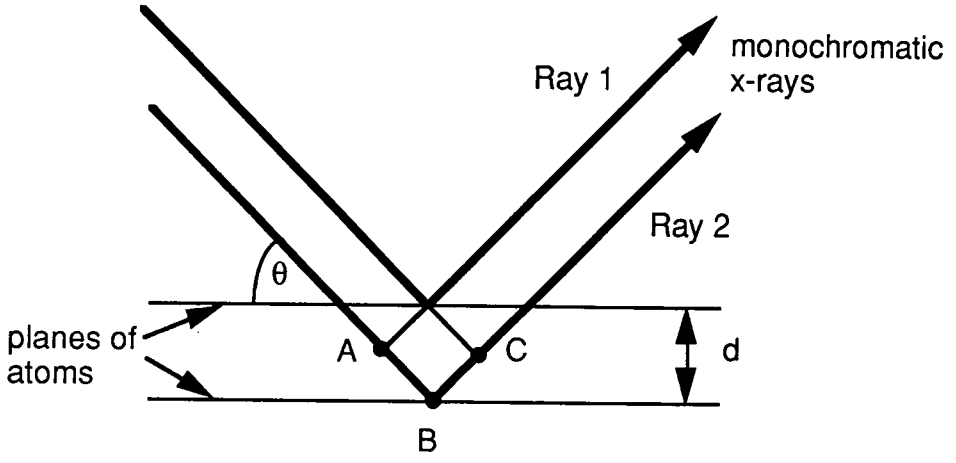

Fig 3.9 Scattering from neighbouring planes of atoms.

The additional path length ABC for the second ray, can be easily obtained from simple trigonometry to give equation 3.11.

$$ABC = 2d\sin\theta \qquad 3.11$$

where d is the interplanar spacing and θ is the angle between the incident x-rays and the planes of atoms.

For constructive interference the path length ABC must be an integral number (n) of wavelengths.

$$ABC = n\lambda \qquad 3.12$$

Hence:

$$n\lambda = 2d\sin\theta \qquad 3.13$$

3.3.3 Double Crystal X-ray Diffraction

Developed initially in the 1920's double crystal x-ray diffraction (DCXRD) was of mainly academic interest until the mid 1980's when commercial optoelectronic epitaxial structures became important and a method was required for non-destructive structural analysis.

Using a reference crystal (Fig 3.10) the width of the Bragg diffraction peak of the specimen crystal, due to the collimator and source geometry, is dramatically reduced [7]. The reference crystal conditions the beam, producing one of very narrow angular divergence but does not monochromate it.

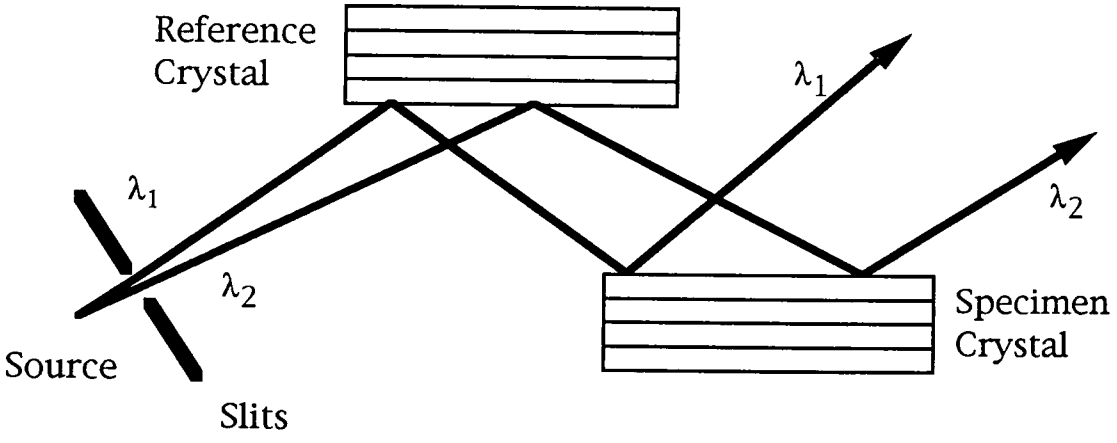

Fig 3.10 Double crystal x-ray diffraction.

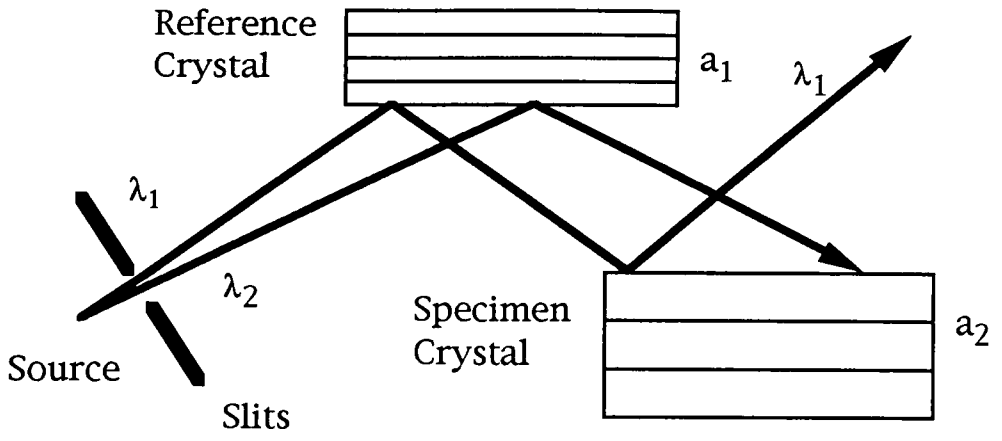

Fig 3.11 Using a reference crystal of differing lattice parameter to that of the specimen.

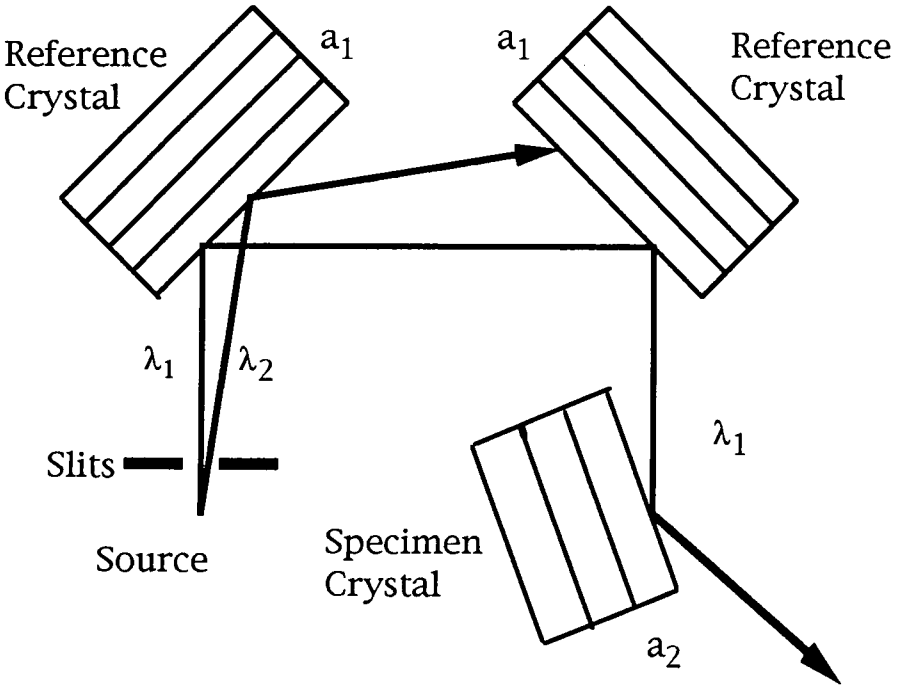

Fig 3.12 Using two reference crystals to reduce spectral dispersion.

Monochromation is achieved by using variable slits between the reference and specimen crystals. When the spectrum of x-ray emission is considered

(Fig 3.8) high intensity peaks corresponding to $K\alpha_1$ and $K\alpha_2$ are of interest in x-ray diffraction since they can easily be angularly separated and used individually. To achieve diffraction the reference and specimen crystals must be set to the appropriate Bragg angles. Small angular deviations by the specimen crystal from the Bragg angle result in a loss of diffracted intensity. It is the intensity dependence of the angular position of the specimen crystal which is referred to as the "rocking curve". Mathematically the rocking curve corresponds to the correlation of the two perfect crystal reflecting curves of the two crystals. Perfection of the layer may be assessed by the Full Width at Half Maximum (FWHM) of a particular x-ray rocking curve. Tilts and dilations in the specimen crystal are mainly responsible for rocking curve broadening. However curvature in the reference or specimen crystals will effect the FWHM [8] as well. Care must be taken when presenting results to quote the beam size, particularly if sub-grain diameters in the layer are comparable to the beam area. Differences between the lattice parameters of reference and specimen crystals can also result in a widening of the Bragg peak, due to different wavelengths satisfying the Bragg condition at different angles of specimen and reference crystals. This broadening can be calculated from equation 3.14.

$$\delta\theta = |\tan\theta_1 - \tan\theta_2|\, \delta\lambda/\lambda \qquad 3.14$$

Where $\delta\theta$ is the broadening of the Bragg peak, θ_1 and θ_2 are the angles of the specimen and reference crystals respectively and $d\lambda/\lambda$ is the fractional spread of wavelengths reaching the specimen crystal.

Note that if the reference and specimen crystals are set to the same angle then there is no broadening of the Bragg peak. If both $K\alpha_1$ and $K\alpha_2$ are used at the specimen stage then $\delta\lambda/\lambda = 2.5 \times 10^{-3}$ whereas if $K\alpha_2$ is removed

$\delta\lambda/\lambda$ is reduced to 2.6 x 10^{-4} which is the intrinsic width of the $K\alpha_1$ peak.

Adding a second reference crystal can reduce dispersion and commercial machines often use one or two additional reflections to reduce the "tails" of the Bragg peaks (Fig 3.13) and allow the use of a variety of specimens without the need for resetting the arrangement [9].

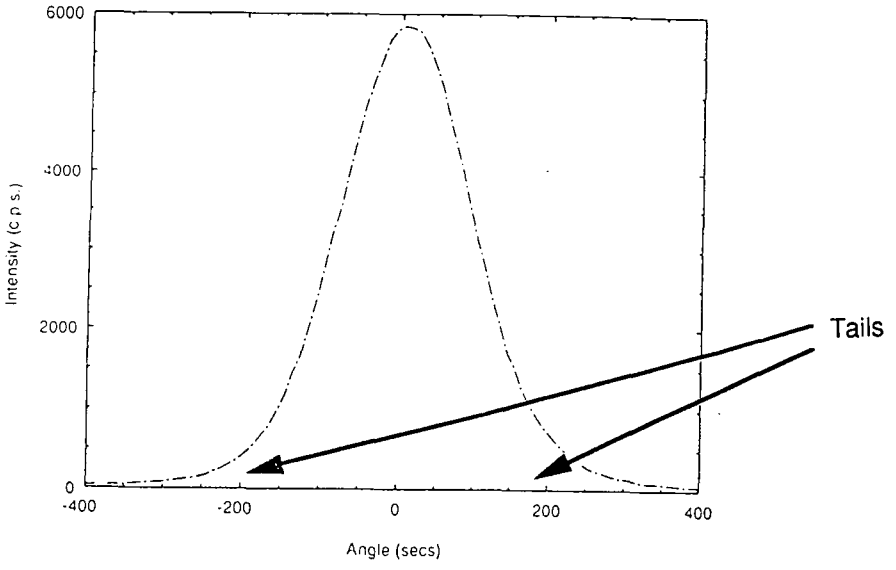

Fig 3.13 A typically double crystal x-ray rocking curve.

In the present study a Bede model 150 diffractometer (so called because the distance between first and second axes is 150mm) equipped with a GaAs (100) reference crystal was used with $CuK\alpha_1$ radiation, the $CuK\alpha_2$ being removed by a set of slits between the reference and specimen crystals. Tangent arms were used to drive the axes angularly, these were controlled by micrometer screws which were, in turn, driven by four phase stepper motors via gearboxes using a 10 to 1 gear ratio. Angular resolution of the axes of the Durham diffractometer was determined to be better than one arc.second by A.Turnbull [10]. Bede DCC (Double Crystal Control) software was used in conjunction with an Elonex 286 M-120 computer and IEEE boards in a MINICAM interface to control the motors and process the x-ray

detector output. The x-ray detector used was a Nuclear Enterprises DM 1-1 sodium iodide scintillation counter with a window diameter of 20mm. This allowed easy detector positioning since the x-ray beam had a diameter of 1mm. A Hilton Brooks model DG2 x-ray generator was used with a copper or cobalt tube. To prolong the lives of the x-ray tubes they were operated at a setting of 40kV and 30mA (1.2kW) or 80% of the maximum power rating of 1.5 kW specified by the manufacturer.

3.3.4 Triple Axis X-ray Diffraction

Although double crystal diffraction techniques provide a good general measure of crystal quality, they do not provide any means of distinguishing between the causes of line broadening. For example, local variations in lattice parameter (dilations) due to an uneven distribution of strain in the layer would lead to correspondingly small shifts in the Bragg angle and as a result some broadening of the x-ray rocking curve. Alternatively tilts between any subgrains present in the layer would also broaden the rocking curve.

In order to examine the degree of scattering from different sources an analyser crystal may be placed between the specimen and the detector (Fig 3.14) [3]. This analyser consists of a block of Si(111) with a channel cut into it to allow for, typically, four reflections of the diffracted x-ray (Fig 3.15). In the double axis arrangement an open detector is employed which integrates scattering from all angles falling onto the detector window. By adding an analyser and independent scanning of the specimen and analyser, the direction of radiation scattered by the specimen can be investigated. Complications of bent or mosaic specimens are eliminated by employing the triple axis method and scattering from different sources can be investigated.

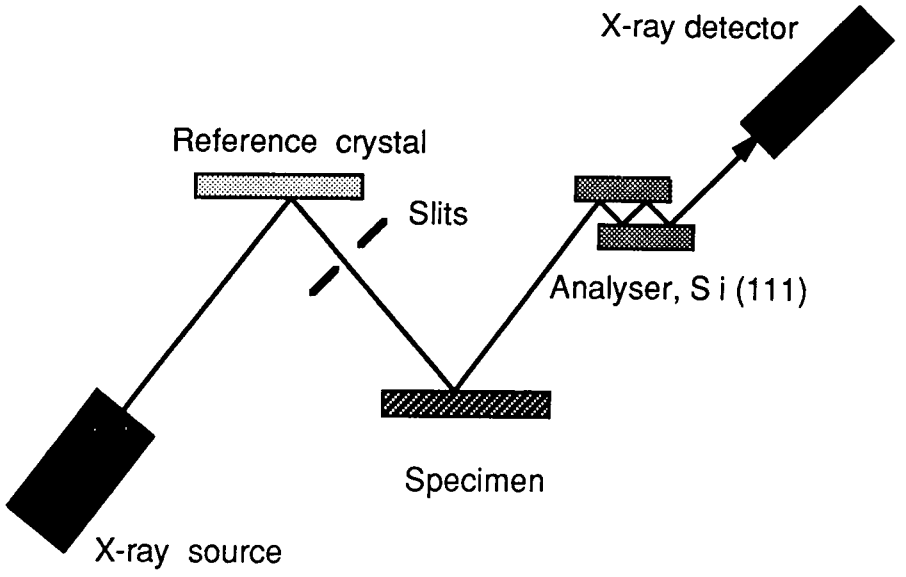

Fig 3.14 Triple axis x-ray diffraction

The degree of tilt in a specimen is measured by keeping the analyser fixed to satisfy the Bragg conditions for x-rays diffracted from the specimen. Only the specimen is scanned thus bringing tilted sub-grains into the diffracting conditions. Regions of lattice parameter which differ from those for which the analyser was set will never diffract strongly since the Bragg condition at the analyser will not be satisfied.

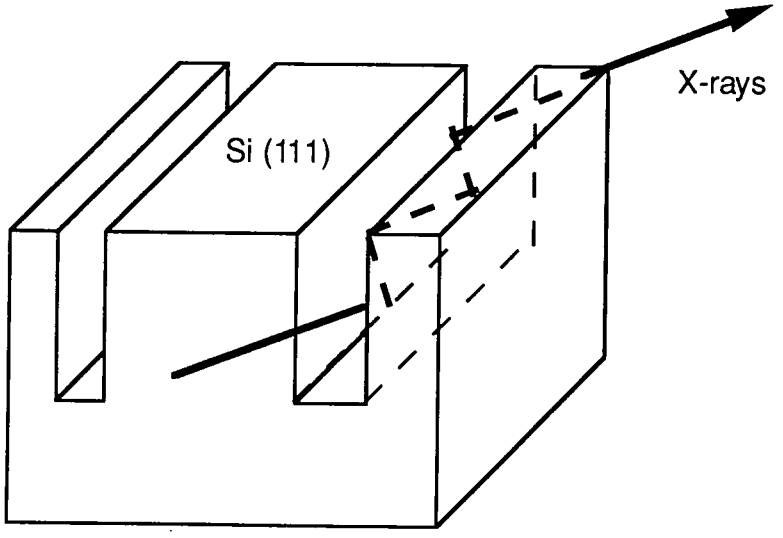

Fig 3.15 A typical analyser used in triple axis diffractometry.

To measure the dilation (lattice parameter distribution) independently of the effect of tilts a θ-2θ scan must be implemented. This involves scanning the analyser at twice the rate of the specimen crystal thus keeping the diffraction conditions satisfied for differing lattice parameters within the specimen. Tilted sub-grains will not scatter onto the detector since the Bragg angle subtended by the analyser by tilt scatter x-rays will not be that required to diffract.

A complete map of the scattering for the specimen can be plotted in reciprocal space by measuring the diffracted intensity from a series of specimen and analyser positions. Reciprocal space isointensity contour plots, an example of which is shown in Fig 3.16, provide the crystallographer with much information such as measures of tilts and dilations. A broad central hill on the plot represents the diffuse scattering and from this misorientation and phase changes can be investigated in detail. In order to fully extract data from reciprocal space isointensity contour plots the diffraction theory behind it must first be understood.

The two vectors which constitute the scattering angle are defined by the angular positions of the incident beam and of the analyser. The diffracting planes whose scattering is measured by the scattering angle are defined by the specimen angle. Consider point *h* in Fig 3.16 to be the diffraction planes in reciprocal space, the origin to be O and the scattering measured in a small volume represented by $[\Delta Q_y, \Delta Q_z]$.

Then:

$$\mathbf{K} = \mathbf{h} + \Delta\mathbf{Q} \qquad 3.15$$

Where $\mathbf{K}$ is the scattering vector (not shown in Fig 3.16), $\mathbf{h}$ is the "ideal" scattering vector from the origin, O, to h and $\Delta\mathbf{Q}$ is the deviation.

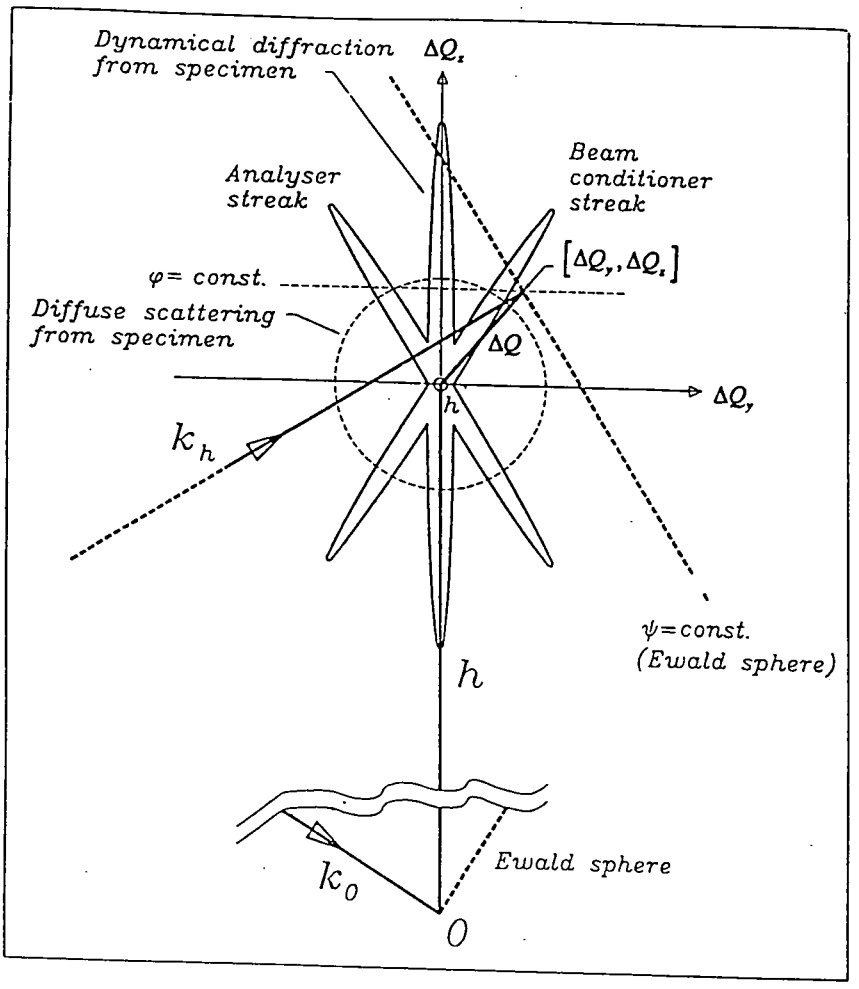

Fig 3.16 A Triple Axis Scattering Map in Reciprocal Space [11].

The deviation can be resolved into horizontal, ΔQ_y, and vertical, ΔQ_z, components. Geometrically it can be shown from Fig 3.16 that there is a clear relationship between ΔQ_y and ΔQ_z and the deviations of specimen and analyser, $\Delta\varphi$ and $\Delta\phi$, from the Bragg condition, thus,

$$\Delta Q_z = \Delta\phi \cos\theta_B/\lambda \qquad 3.16$$

$$\Delta Q_y = (2\,\Delta\varphi - \Delta\phi)\sin\theta_B/\lambda \qquad 3.17$$

Hence scanning the specimen ($\Delta\varphi$) affects ΔQ_y only and in reciprocal space sweeps from left to right, whereas scanning the analyser affects both ΔQ_y and ΔQ_z sweeping along the Ewald sphere (fig 3.16). To obtain the trace of

ΔQ_z alone, a θ-2θ scan must be performed where the analyser is swept at twice the rate of the specimen thus giving equation 3.18.

$$2\,\Delta\varphi - \Delta\phi = 0 \qquad 3.18$$

It is along the ΔQ_z direction which the main scattering from the specimen occurs and for a high quality crystal, little extension in the ΔQ_y should be observed. In the centre of the map diffuse scattering will appear as a broad, weak region of scatter. Streaks appearing inclined at the Bragg angle to the vertical are due to the finite angular resolution of the beam conditioner and analyser and can be reduced by utilising multiple reflections in the beam conditioner and analyser [12]. It should be noted that a double crystal experiment without an analyser corresponds to a horizontal scan through reciprocal space and integrating all intensities along the Ewald sphere.

Triple axis diffraction was performed on a Bede model 200 diffractometer equipped with a triple-axis stage on the detector axis. Beam conditioning was obtained by using an InP (001) reference crystal and a Si (111) analyser between the specimen and a gas-filled proportional counter, which had linear characteristics over the intensity range studied.

3.3.5 Single Crystal X-ray Topography

The aim of x-ray topography is to image the defects in crystals in either reflection or transmission. Although single crystal topography was not used to analyse Durham grown (Hg,Mn)Te layers (double crystal topography was used instead), it is instructive to look at this simpler method first. In x-ray topography there are two sources of contrast;

orientation and extinction.

The former occurs if the angle of tilt of different regions of the crystal is greater than the beam divergence, thus some regions will not satisfy the diffraction conditions (Fig 3.17).

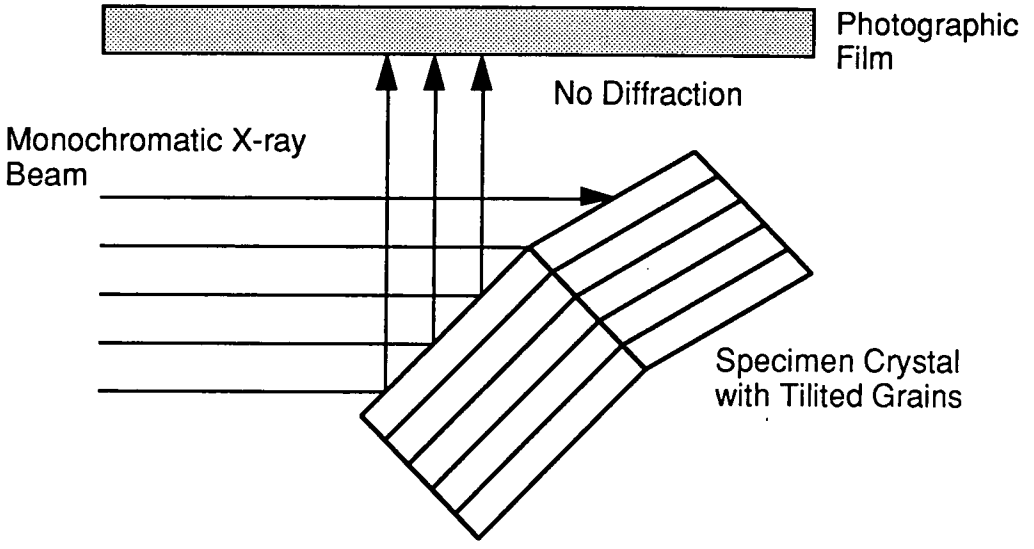

Fig 3.17 Diffraction of a monochromatic x-ray beam from a specimen containing tilted grains.

Extinction contrast results from distortion of the lattice around a defect and the nature of the image is gained from a knowledge of x-ray dynamical diffraction theory.

Berg first experimented with the idea of x-ray topography in 1931 [13] and Barrett developed the method still further in 1945 [14]. The technique is simple and cheap to apply, since no precision components are required. Often this is the first assessment used on newly grown materials, which may have high dislocation densities. The specimen crystal is set to diffract directly onto a closely placed film (Fig 3.18).

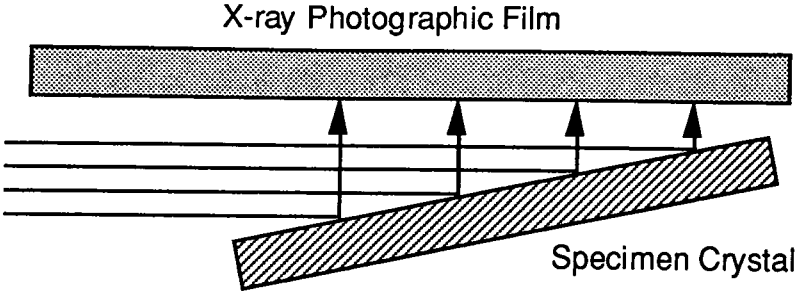

Fig 3.18 Basic x-ray topography

Since the specimen-film distance is small and the source is extended the method is insensitive to orientation contrast although orientations greater than about one degree will yield no diffraction. Having a wide source of x-rays assists in the easy positioning of the specimen and the inherently large FWHM provides easy setting up. There is a loss of resolution if a polychromatic beam is used, which was overcome by Barrett by limiting the source to a width of 1mm and cutting the crystal so its diffracting planes were not parallel to its surface, thus ensuring a strong asymmetric reflection. This enables a wide diffracted beam to be obtained from a narrow incident one, allowing the film to be placed close to the specimen and divergence of the $K\alpha_1$ and $K\alpha_2$ lines avoided. However, with a small specimen-film distance it was difficult to position the film so that it was perpendicular to the diffracted beam and as a result spatial resolution was limited. The use of thin (10μm) photographic emulsions did reduce this problem. Soft radiation creates a small extinction distance and so only a small specimen depth is sampled.

For transmission topography (Barth-Hosemann Geometry) [15] the geometry in Fig 3.19 is used to separate the diffracted beam from the generally stronger direct beam. Normally the crystals used must be thin and the specimen-film distance should be sufficiently large to allow removal of the direct beam by a slit.

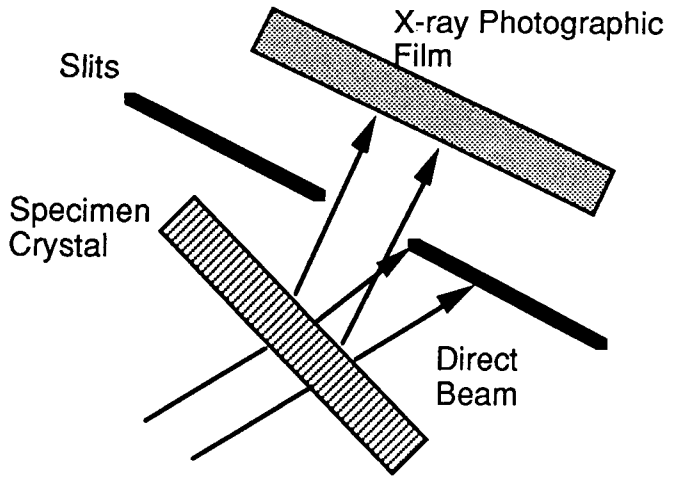

Fig 3.19 Transmission x-ray topography.

The two main disadvantages of this method are the danger to the operator from the large quantity of scatter and the amount of noise this scatter causes on the image. The former can be reduced by effective lead shielding but the latter is harder to rectify. However transmission is simple and due to its low orientation sensitivity can be used successfully with bent crystals.

Lang Topography [16] is the most popular transmission x-ray topography technique and is sensitive to both extinction and orientation (5×10^{-4} rad). The arrangement is shown in Fig 3.20 which differs from the basic transmission technique in that both specimen and slits are scanned to provide 100% coverage of the specimen surface.

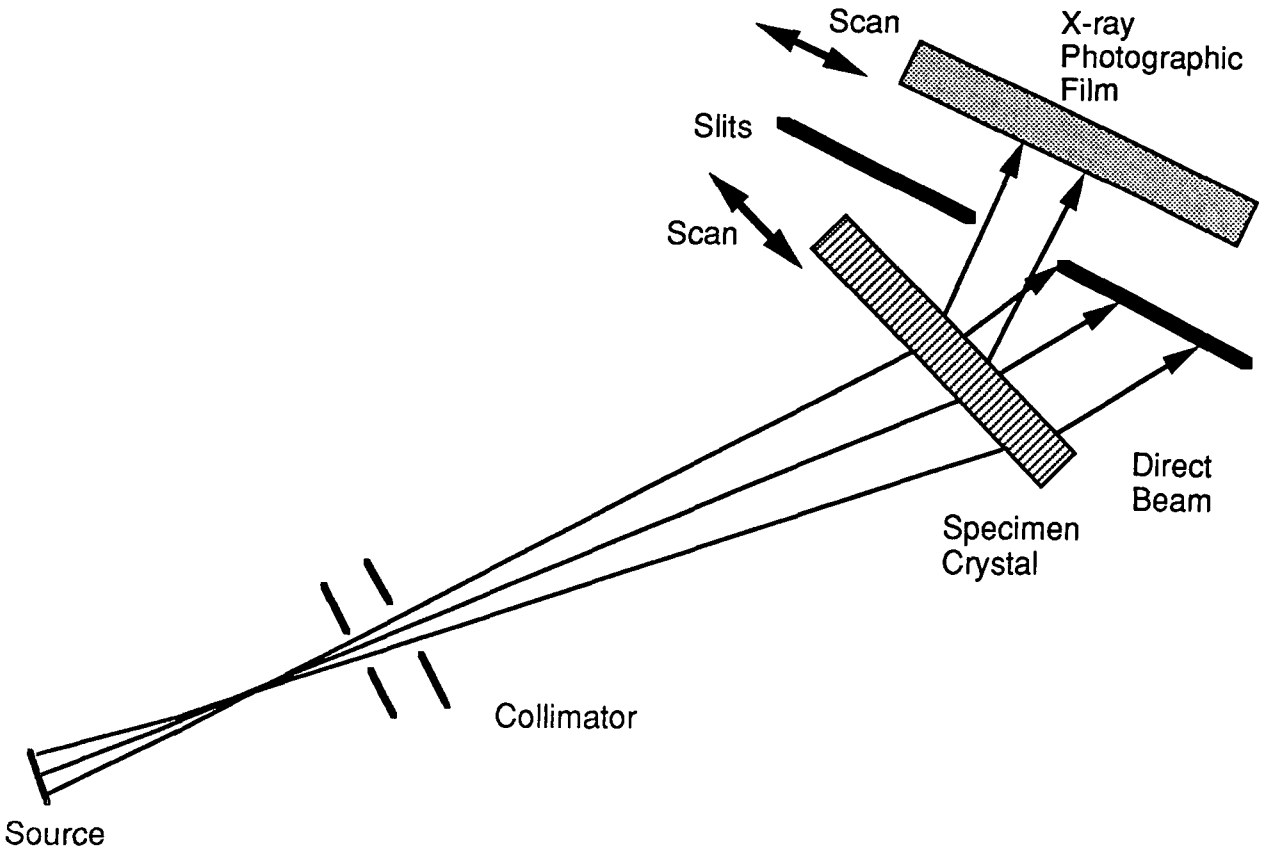

Fig 3.20 Lang transmission topography.

Double images are avoided by collimating the beam to allow only $K\alpha_1$ or $K\alpha_2$ through. $K\alpha_1$ is usually selected since it has the greater intensity. Beam divergence in the Lang arrangement is usually of the order of 5×10^{-4} rad. Reflection methods of topography are better than transmission for high dislocation density crystals (up to 10^6 cm^{-2}) since the resolution is limited by image overlap.

The arrangement used here at Durham was based on Barrett's method but used a reference crystal to condition the beam (Fig 3.21). Topographs were taken on a Bede model 150 diffractometer with $CuK\alpha_1$ radiation using a (004) Silicon reference crystal, giving a beam size of 8mm vertically by 1mm horizontally. High order asymmetric reflections, such as (224), were used to give a grazing incidence angle of 0.55^o and a 71^o exit angle, thus

providing a large surface coverage. The images were recorded on dental film or, for high resolution, on nuclear emulsion plates. Ilford L4 nuclear emulsion plates have a grain size of 0.14μm but on developing the grains can swell and the overlap of exposed grains throughout the thickness of the plate can reduce the resolution to 1μm. Film exposure times were dependant on the x-ray tube settings, and the nature of the specimen and reflection. However a typical exposure time for (Hg,Mn)Te was of the order of six hours.

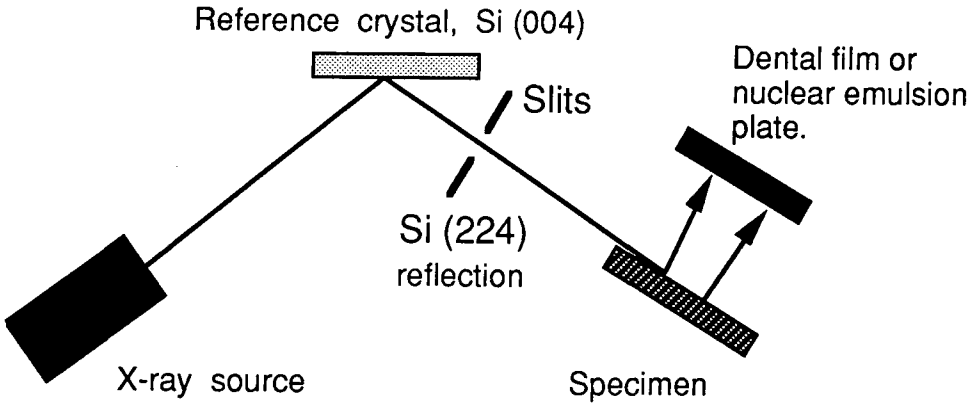

Fig 3.21 The arrangement used for x-ray topography in Durham.

3.4 The Scanning Electron Microscope

3.4.1 Electron Interaction With Matter

When an energetic electron strikes some material a variety of interactions occur. Fig 3.22 shows the "generation volume" within the specimen, which provides a model of these interactions as a function of depth into the material.

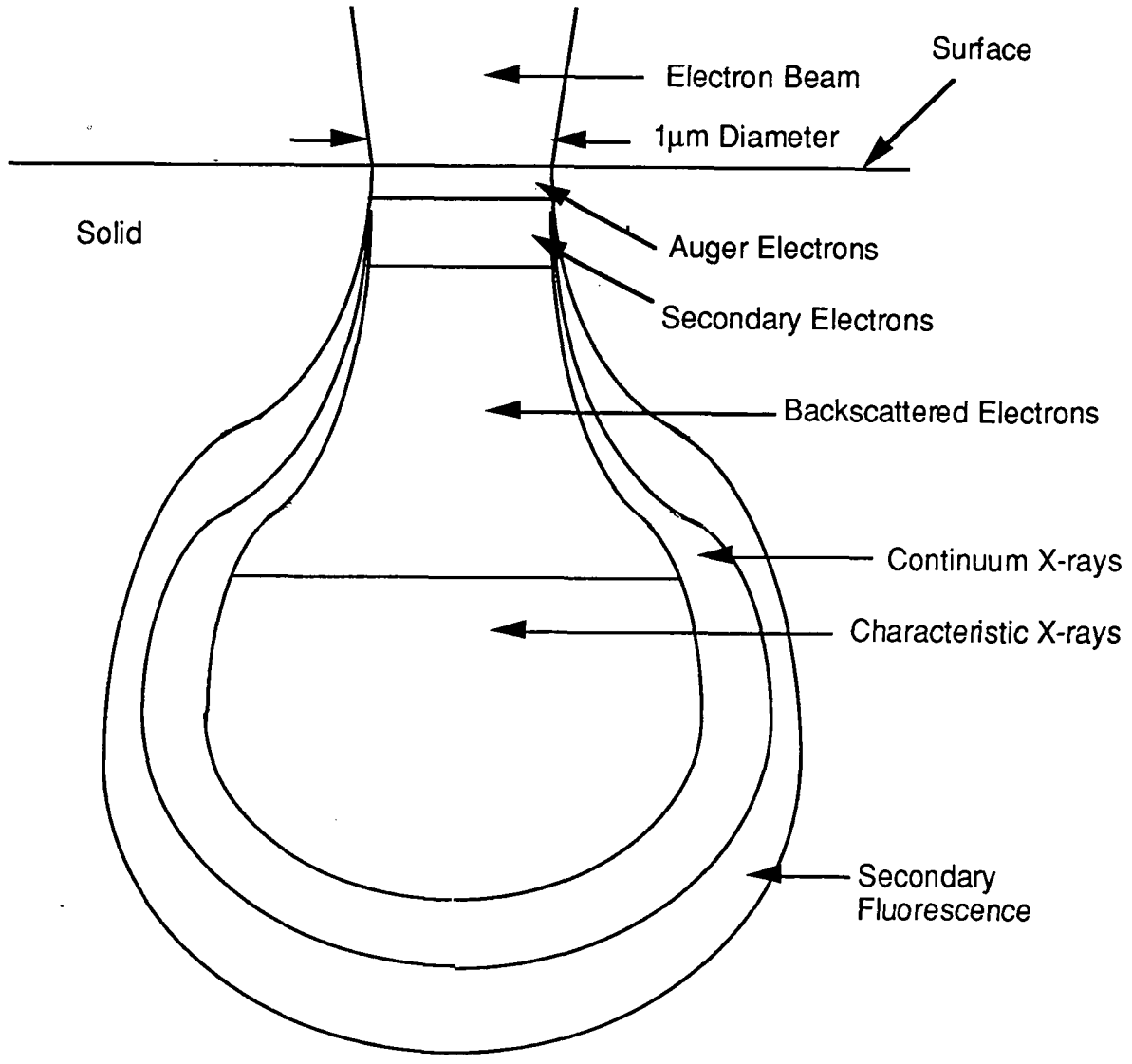

Fig 3.22 The generation volume of electron-specimen interactions.

Due to the large variety of electron-solid interactions, the SEM has a wide range of uses to the material scientist, and typically offers the following techniques;

i) Secondary electron imaging, ii) Elemental analysis using emitted x-rays, iii) Photoluminescence, iv) Cathodoluminescence, v) Backscattering of primary electrons, vi) Auger electron analysis, vii) Electron beam induced currents.

Only the first two techniques were used here at Durham on (Hg,Mn)Te,

although some of the remaining techniques are under development.

3.4.2 Basic Principle of Operation of an SEM.

Electrons are ejected from a cathode and accelerated using a high voltage (typically 25kV). Electro-magnetic lenses are used to focus the beam onto the specimen surface and spot sizes down to 0.01μm may be achieved. Coils are used to synchronise scanning of the electron beam and that in the cathode ray tube on a monitor to trace a series of lines providing full coverage of the examined area. Magnification of up to 100,000 is possible. A proportion of the current leaving the sample is collected by plate p (Fig 3.23), amplified and used to modulate the electrode of the cathode ray tube, i.e alters the brightness of the spot on the screen. The current collected on plate p will be dependent on the nature of the surface (shape, magnetism etc).

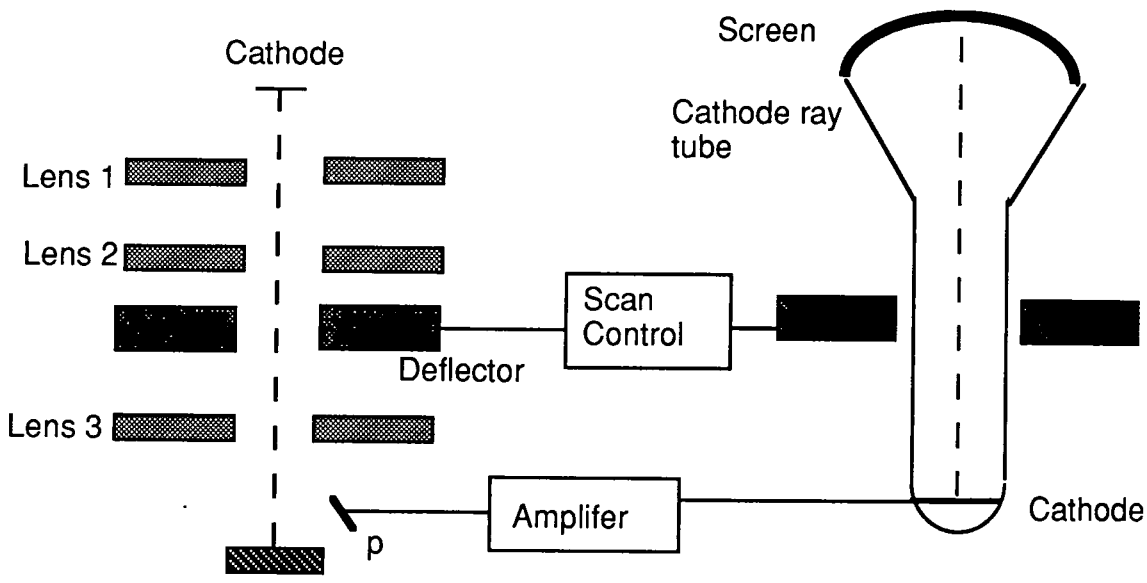

Fig 3.23 The basic layout of a scanning electron microscope [16]

Evacuation of the system is required to around 10^{-4} Torr in order to provide a mean free path length for the electrons of about 1-2m, the cathode to specimen distance.

The system used for analysis of the Durham grown epitaxial (Hg,Mn)Te was a Cambridge Instruments Stereoscan 600 fitted with a Link systems 860II EDAX facility. Electron acceleration voltages could be varied from 1.5kV to 25kV with a corresponding range in magnification from 20 times to 50,000 times.

Electrons (primary and secondary) generated by interaction between the solid and the electron beam are detected using an Aluminium covered scintillator biased at +10kV, producing electron-hole pairs which recombine to produce photons. A photomultiplier tube converts the light from the scintillator into a voltage which is used to modulate the intensity of the electron beam in the display cathode ray tube. Secondary electron imaging (secondary electrons have energies up to 50eV) is achieved by applying a +250V bias to the EHT grid in front of the detector system to attract both primary and secondary electrons. However since the secondary electrons vastly outnumber the primary electrons, the image obtained is predominantly due to secondary emission.

(For primary electron imaging a -50V bias is placed on the EHT grid to deflect the secondary electrons away from the detector).

The main role of secondary electron imaging is in topographic investigation of the surface of the specimen. This is due to the differing probability of secondary electron collection from different parts of the surface.

Backscattering of primary electrons is stronger for higher atomic number materials giving rise to compositional contrast. However for the (Hg,Mn)Te specimens the EDAX facility was used for compositional investigations.

3.4.3 Energy Dispersive Analysis of X-rays (EDAX)

Some of the energy of the electrons striking the specimen is used in generating characteristic x-rays from the atoms present in the material. X-ray microanalysis can be obtained by either wavelength or energy dispersive techniques. The former has greater resolution and lower detection limits but the latter is faster and easier to operate. The Link Systems 860II EDAX uses the energy dispersive mode, and is based on a liquid nitrogen cooled Li drifted Si solid state detector, behind a Be window. Electron hole pairs are created by the incident x-ray photons and are swept apart by an applied voltage. The resulting charge pulse is proportional to the energy of the incident photon. Pulse height discrimination is then used to sort the pulses in a multichannel analyser to construct the x-ray energy spectrum. Fig 3.24 shows a typical EDAX spectrum, showing peaks characteristic of the principal elements.

EDAX spectra were obtained in one of two ways, either large area mode or spot mode. In the large area mode, the electron beam is scanned over the desired region of the specimen and the resulting EDAX spectrum is then an average of the composition over the scanned area. In the spot mode, the electron beam is kept stationary at one position (typically at some surface feature). The resolution in the spot mode is limited to about 1μm by the generation volume of the electron beam.

It should also be noted that the x-ray production by electrons is inefficient and noisy hence a large beam current is required which will reduce resolution further. The Link Systems 860II EDAX used here at Durham had no ZAF correction. Hence it was necessary to calibrate the EDAX facility for (Hg,Mn)Te analysis by independently calibrating specimens of (Hg,Mn)Te using facilities kindly provided by Japan Energy Corporation (formerly Nippon Mining Ltd). The ratios of the (Hg-M)/(Te-L) and (Mn-K)/(Te-L)

characteristic lines were used, with the background intensity subtracted, in order to determine composition. The manganese compositions of various layers (x) found by Japan Energy Corporation (formerly Nippon Mining Ltd) was investigated as a function of the (Mn-K/Te-L) intensity ratios and a good linear relationship found, Fig 3.25 with the best fit line given in equation 3.20.

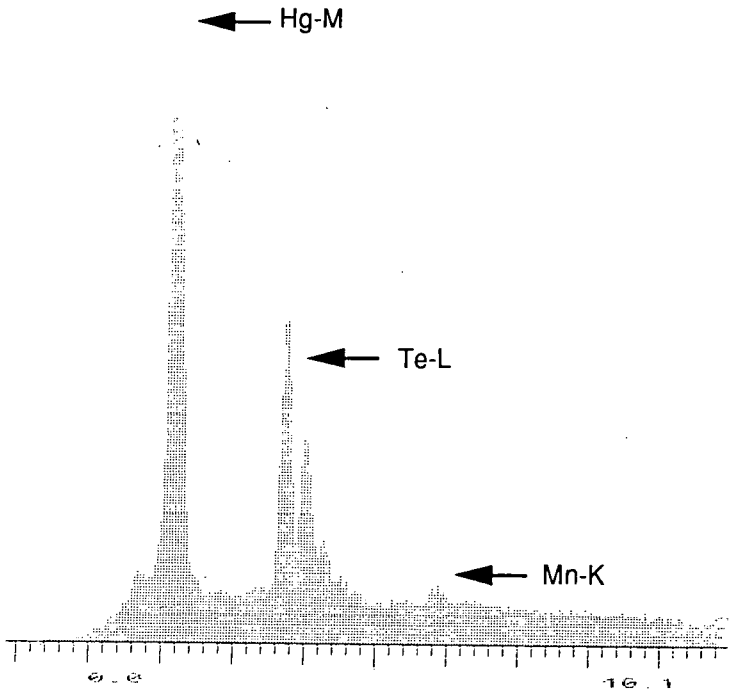

Fig 3.24 An EDAX display for (Hg,Mn)Te.

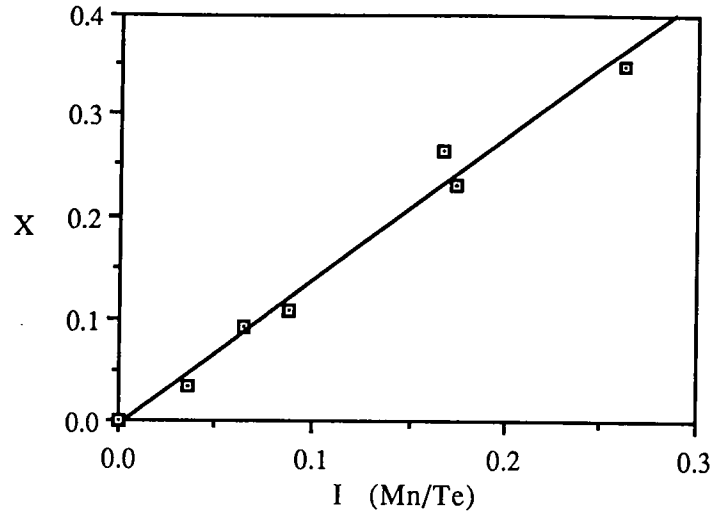

Fig 3.25 EDAX Calibration curve for Manganese concentrations in Durham grown (Hg,Mn)Te, examined using a Link Systems 860 II EDAX.

$$x = -0.0049 + 1.3738[I(Mn)/I(Te)] \qquad 3.19$$

where x is the manganese content of the (Hg,Mn)Te layer and I(Mn)/I(Te) is the ratio of the heights of the Mn-K and Te-L lines in the EDAX spectrum.

Secondary electron imaging using an SEM has a spatial resolution of the order of 200Å. However that of EDAX is around 1μm due to a greater current being required for this less efficient process. The detection limit for EDAX is ~1% of an element within a compound. However it should be noted that the efficiency of the production of characteristic x-rays falls off rather rapidly for lower atomic number elements. Also, difficulties exist in the detection of longer wavelength radiation.

3.5 Summary

The analysis of Durham grown epitaxial (Hg,Mn)Te can be classified into three distinct experimental areas;

i) Transport measurements,

ii) X-ray diffraction,

iii) Scanning electron microscopy.

Transport measurements were performed over the temperatures from liquid helium to room temperature using an Oxford Instruments cryostat. For measurements of resistivity the van der Pauw technique was adopted, since it can be applied to any sample geometry. Carrier concentrations and mobilities were calculated from the Hall effect using a calibrated electromagnet on a rotatable base.

Three main X-ray diffraction techniques were used. Firstly, double crystal x-ray diffraction which allowed quick and easy measurements of thickness, composition and layer quality to be made. By using an x-y scanning stage in the double crystal arrangement studies of layer uniformity were made. Secondly, double crystal topography was used to map the strain within layers, due to dislocations or due to wafer curvature etc. Triple axis diffraction, where the insertion of an analyser crystal between the specimen and detector enabled the sources of scattering to be identified, was also used to determine the degree of tilt and dilation.

For investigations of surface morphology and layer composition a Cambridge 600 SEM was used with a Link Systems 860II EDAX facility.

References

[1] "Electrons and Holes in Semiconductors" by Schockley (1951), pub D. Van Nostrand, London p203.

[2] L.J. van der Pauw, (1958) Philips Res. Reports **13**, 1-9.

[3] B.K. Tanner and D.K. Bowen, (1993) J. Crystal Growth **126** 1.

[4] Oxford Instruments Manual for MD4 cryostat.

[5] "Optical Properties of X-ray Diffraction" by R.W. James (1948) , pub. Bell, London p53.

[6] W.L. Bragg (1913) Proc. Camb. Phil. Soc **17** 43-52.

[7] B.K. Tanner, (1990) Advan. X-ray Anal. **33** 1.

[8] M.A.G. Halliwell, M.H. Lyons and M.J. Hill, (1984) J. Crystal Growth **68** 523.

[9] N. Loxley, D.K. Bowen and B.K. Tanner, (1991) Mater. Res. Soc. Symp. Proc. **208** 107.

[10] A.G. Turnbull (1992) PhD Thesis, Durham.

[11] A. Lida and K. Kohra (1979), Phys. Status. Solidi (a) **51** 533.

[12] P. Zaumseil and U. Winter (1982), Phys. Status. Solidi (a) **70** 497.

[13] W.F. Berg (1931), Naturwissenscaften **19** 391.

[14] C.S. Barrett (1945), Trans. AIME **161** 15.

[15] H. Barth and R. Hosemann (1958), Z. Naturforschung **13**a 792.

[16] A.R. Lang (1959), Acta. Cryst. **12** 249.

[17] "Practical scanning electron microscopy" by J.I. Goldstein and H. Yakowitz (1975), pub. Plenum press, London.

Chapter Four

Analysis of Electrical Transport Data

4.1 Introduction

Transport measurements, and in particular the dependence of transport data on temperature, can provide an insight into the band structure, lattice defects and impurity levels of a semiconducting crystal. In Chapter One the dependence of the bandgap of (Hg,Mn)Te on composition was discussed. When the manganese content is less than 4% then semimetallic behaviour is exhibited at room temperature due to an overlap of the conduction and valence bands [1]. For manganese compositions between 4% and ~15% (the bandgap energy ranges from 0 to 300 meV) narrow gap behaviour is observed, where intrinsic electrons contribute to conduction at room temperatures. For manganese concentrations greater than 15%, when the band gap exceeds ~300meV, the probability of thermal excitation of electrons from the valence to the conduction band at room temperatures is negligible and the material behaves extrinsically with conduction controlled by defect or impurity levels.

Hence it is the intention of this chapter to discuss the carrier behaviour of semimetallic and narrow bandgap semiconductors, since the compositions of (Hg,Mn)Te considered correspond to these regimes. For positive band gap semiconductors only the upper edge of the valence band and the lower edge of the conduction band are of importance for transport processes. However the curvature of the bands at the zone centre is important in determining the respective effective masses. These have been obtained for (Hg,Mn)Te from Shubnikov-de Haas oscillations by Jacznski et al [2]. They found the effective masses to be directly proportional to the bandgap for

manganese concentrations in excess of 10%.

4.2 Semimetallic Behaviour

In 1958 Harman et al [3] prepared bulk crystals of HgTe and obtained a positive bandgap of 0.02eV at temperatures close to absolute zero from analysis of the transport data. Three years later in 1961 whilst considering (Hg,Se)Te alloys Harman obtained Hall data which could not be explained by a two band model [4]. Instead he proposed that HgTe was a semimetal and that previous analysis of Hall data of HgTe should be reconsidered. This discovery was supported by subsequent magnetoabsorption experiments carried out by G.Bastard [5] which gave a negative bandgap of the order of -300meV.

Although in 1961 Harman did not investigate the bandstructure of HgTe in detail, the methods he introduced for calculating the free electron concentration in HgSe were of interest since HgSe has a similar bandstructure to that of HgTe [6].

The free electron concentration, n, of HgSe was obtained from the Hall data using the standard semiconductor equation for one carrier conduction (see later):

$$R_H = \frac{r_H}{n|q|} \qquad 4.1$$

where R_H is the Hall coefficient, q is the electronic charge and r_H depends on the degree of degeneracy, scattering, the bandstructure and the product of the electron mobility and magnetic field. For HgSe Harman determined from galvanomagnetic and thermomagnetic data that r_H could be assumed to be unity.

The electron to hole mobility ratio, b, was determined by Harman et al [4] from the Hall coefficient in the extrinsic region, R_{Hext}, and the maximum Hall coefficient, R_{Hmax}, equation 4.2.

$$\frac{R_{Hmax}}{R_{Hext}} = \frac{(1 - b)^2}{4b} \qquad 4.2$$

For HgSe and HgTe, b was found to be 85 and 100 respectively [7]. The Hall mobility of electrons in HgSe and HgTe was claimed to be the same to within 25% by Harman et al [4].

To calculate theoretically the free electron concentration in HgSe, Harman et al considered a model where one valence band overlaps the conduction band and one other valence band lies below the conduction band, Fig 4.1a. The energy gap between the conduction band and V_2 in Fig 4.1a was indirect; however subsequent work revealed that for semimetallic HgTe this was a direct energy gap [5]. The free electrons were considered as being in the conduction band but free holes were assumed to be present only in valence band V_2 (i.e the overlapping band) and not V_1. In order to obtain carrier concentrations as a function of temperature Harman considered equation 4.3, the general equation for the concentration of free carriers in a band.

$$n = \frac{1}{4\pi}\int f_0 d^3K \qquad 4.3$$

where n, f_0 and K are the free electron concentration, the equilibrium distribution function and the wave vector respectively.

The exact values of the conduction band parameters were known to Harman

and his consideration of the magnetoresistance as a function of the angle between the current and the applied magnetic field revealed that the conduction band of HgSe was spherically symmetrical. Seebeck and infrared reflectivity measurements showed that the electron energy with respect to the bottom of the conduction band did not have a simple quadratic dependence on the wave vector.

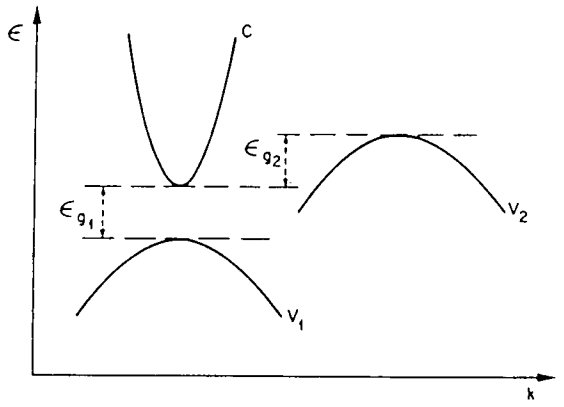

Fig 4.1a Band diagram model used to calculate the free electron concentration in HgSe by Harman et al [4].

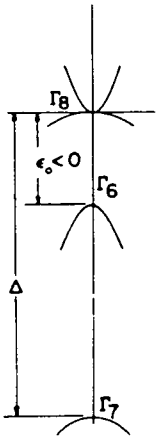

Fig 4.1b Band diagram of HgSe as reported by Carlson [5].

Kane [8] proposed an expression for the electron energy, ε, relative to the bottom of the conduction band:

$$\varepsilon = \frac{-\epsilon_{g1}}{2} + \frac{\sqrt{\epsilon_{g1}^2 + 8P^2K^2}}{2\sqrt{q}} \qquad 4.4$$

where P is a matrix element and K is the wave vector.

When the integral in equation 4.3 is evaluated using Fermi-Dirac statistics and equation 4.4, the equation obtained for the free electron concentration, n, is given by equation 4.5.

$$n = \frac{3}{4\pi^2}\sqrt{\frac{3}{2}}\left(\frac{\kappa T}{P}\right)^3 \int_0^{\infty} \frac{\sqrt{X(X+\phi)}\,(2X+\phi)}{1+\exp(X-\Re)}\,dX \qquad 4.5$$

where κ is Boltzmann's constant and X, ϕ and $\Re$ are defined as:

$$X \equiv \frac{\varepsilon}{\kappa T}\,,\quad \phi \equiv \frac{\epsilon_{g1}}{\kappa T} \quad \text{and} \quad \Re \equiv \frac{E_f}{\kappa T}$$

where E_f is the Fermi energy.

For the conduction band of HgSe, values of P, ϵ_{g1} and m^*_e were calculated by Harman to be 9 x 10^{-8} eV.cm^{-1}, 0.1eV and 0.014m_0 respectively in order to give results which were in good agreement with experimentally measured values of the Seebeck effect. The value of the matrix element was very similar to that of InSb, InAs, GaSb, InP and GaAs [4].

Similar treatment of the valence bands by Harman gave values of E_{g2} and the effective mass of holes to be -0.07eV and 0.17m_0 respectively. The concentration of free holes, p, is given by equation 4.6 by assuming that V_2 is a simple parabolic band.

$$p = 4\pi\left(\frac{2\kappa}{h^2}\right)^{3/2}\left(m^*_p\right)F_{1/2}\left[-(\Re+\phi)\right] \qquad 4.6$$

where m^*_p is the density of states effective mass for holes and $F_{1/2}$ is the Fermi integral.

For single carrier n-type conduction, where the concentration of electrons is considerably greater than the concentration of free holes, a value of the Fermi level was chosen to give:

$$n = p + N_D \qquad 4.7$$

where N_D is the excess donor concentration.

Equation 4.7 is only applicable where the excess donors are fully ionised. This was shown to be the case for HgSe over the entire temperature range since the Hall coefficient reached a constant value at low temperatures. The determination of the free electron concentration using equations 4.5 to 4.7 for various donor concentrations for HgSe is shown in Fig 4.2.

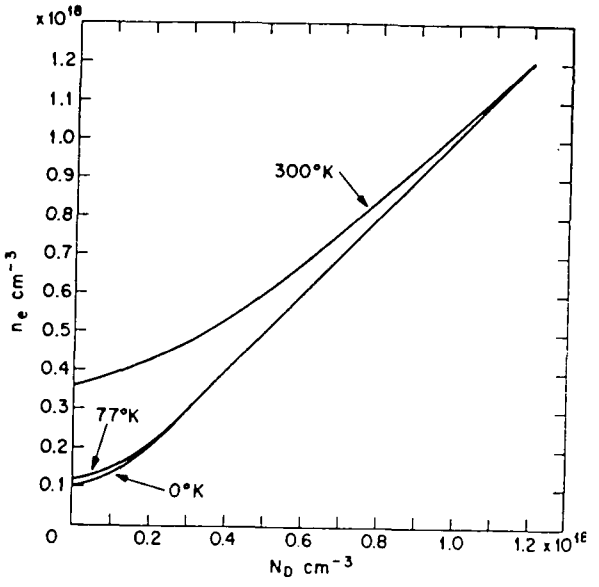

Fig 4.2 Theoretical dependence of the free electron concentration, n, on donor concentration, N_D, and temperature [4].

4.3 Narrow Gap Conduction

4.3.1 Semiconductor Statistics

In this category, which covers the range of bandgaps from 0 to 300meV, intrinsic electrons contribute significantly to conduction at room temperature, and models for carrier behaviour must take this into account.

Considering the number of free electrons in the conduction band, N_{CB}, to be the product of the density of states, S(E), and the probability of each state being filled i.e. the Fermi Dirac function, F(E), for all energies in the band.

$$N_{CB} = \int_{E=Ec}^{Ec,Top} S(E)\,F(E)\,dE \qquad 4.8$$

where E_c is the conduction band energy.

The density of states may be determined from the effective mass of the carrier, m^*, and the energy of the relevant band edge, E_c for the conduction band.

$$S(E) = \frac{4\pi}{h^3}\left(2m^*_e\right)^{3/2}\left(E-E_c\right)^{1/2} \qquad 4.9$$

where E is the energy of the state and h is Planck's constant.

The probability of a state being occupied by an electron is given by the Fermi-Dirac function, equation 4.10.

$$F(E) = \frac{1}{\exp\left(\frac{E-E_f}{\kappa T}\right)+1} \qquad 4.10$$

where E_f is the Fermi energy.

For $(E-E_f)>>\kappa T$ the 1 in the denominator can be ignored and the function is reduced to a Maxwell-Boltzmann distribution. Since F(E) diminishes rapidly with increasing energy above the Fermi energy, the top energy level of the conduction band can be regarded as infinity, equation 4.11.

$$n = \frac{4\pi}{h^3}\left(2m^*_e\right)^{3/2}\int_{E=E_c}^{\infty}\frac{\left(E-E_C\right)^{1/2}}{\exp\left(\frac{E-E_f}{\kappa T}\right)}dE \qquad 4.11$$

Evaluating the integral gives equation 4.12.

$$n = N_c\exp\left(\frac{-(E_c-E_f)}{\kappa T}\right) \qquad 4.12$$

where,

$$N_c = 2\left[\frac{2\pi.m^*_e \kappa T}{h^3}\right]^{3/2} \qquad 4.13$$

N_c is the effective density of states in the conduction band.

The same argument can be applied to conduction by holes in the valence band where the fraction of states occupied by holes is 1-F(E):

$$p = N_v \exp\left(\frac{-(E_f - E_v)}{\kappa T}\right) \qquad 4.14$$

where p is the free hole concentration and N_v is the effective density of states in the valence band:

$$N_v = 2\left[\frac{2\pi.m^*_e \kappa T}{h^3}\right] \qquad 4.15$$

For intrinsic conduction each electron promoted to the conduction band leaves behind a hole in the valence band. Therefore the Fermi level can be obtained using this relation with equations 4.12 to 4.14.

$$E_f = \left[\frac{E_c + E_v}{2}\right] + \frac{3}{4}\kappa T \log_e\left[\frac{m^*_h}{m^*_e}\right] \qquad 4.16$$

Also by combining the number of electrons in the conduction band and the number of holes in the valence band the intrinsic carrier concentration, n_i, may be determined:

$$n.p = n_i^2 = N_c N_v \exp\left(\frac{E_v - E_c}{\kappa T}\right) \qquad 4.17$$

For low temperatures (less than 100K) conduction is predominantly determined by defects or impurities which produce levels within the band gap. Shallow levels are those lying ~κT from the band edges to which they will accept or donate carriers when thermally activated. Deep levels are those for which the activation energy is too great in relation to κT for ionisation to occur. Deep levels can either trap carriers where they may be re-excited to the free state (traps) or may recombine with oppositely charged carriers (recombination centres).

If all the donors and acceptors are ionised, then at low temperatures where intrinsic carriers are negligible, the number of free electrons is the difference in ionised donor (N_D^+) and ionised acceptor (N_A^-) concentrations.

$$n = N_D^+ - N_A^- \qquad 4.18$$

The concentration of ionised donors, N_D^+, is given by the product of the concentration of donors, n_d, and the Fermi function.

$$N_D^+ = \frac{n_d}{\frac{1}{g}\exp\left[\frac{(E_D - E_f)}{\kappa T} + 1\right]} \qquad 4.19$$

where g is the degeneracy factor for that donor. Since the (Hg,Mn)Te conduction band is two fold degenerate a value of two was taken for g.

Since:

$$N_D^+ = n - p \qquad 4.20$$

and for non degenerate semiconductors,

$$p = n_i^2/n \qquad 4.21$$

hence,

$$N_D^+ = n - \frac{n_i^2}{n} \qquad 4.22$$

Combining 4.12, 4.19 and 4.22 a relation between the electron concentration in the conduction band and the donor levels is obtained.

$$n = \frac{n_d}{1+\frac{n}{2N_c}2\exp\left(\frac{E_D}{\kappa T}\right)} + \frac{n_i^2}{n} \qquad 4.23$$

Hence if a plot of $\log_e(n)$ as a function of reciprocal temperature is made and the $T^{3/2}$ dependence of N_c is ignored then the donor activation energy can be obtained from the gradient of the graph.

At high temperatures the activation energies of donors and acceptor are very much less than κT and the effective density of states is greater than the concentration of carriers in the conduction and valence bands. Thus solving equation 4.22 for n,

$$n \approx \frac{N_D^+ + \sqrt{\left(N_D^+\right)^2 + 4n_i^2}}{2} \qquad 4.24$$

and similarly for the hole density,

$$p \approx \frac{N_A^- + \sqrt{\left(N_A^-\right)^2 + 4n_i^2}}{2} \qquad 4.25$$

where N_A^- is the ionised acceptor concentration.

The measurement of resitivity, ρ, was described in detail in Chapter Three and can be obtained from fundamental carrier quantities using equation 4.26 to 4.28.[9]

$$\rho = \frac{1}{\sum_j n_j |q_j| \mu_j} \qquad 4.26$$

where n, q and μ are the carrier concentration, electronic charge and carrier mobility respectively.

Thus for conduction by electrons and holes equation 4.27 applies.

$$\rho = \frac{1}{p|q|\mu_h + n|q|\mu_e} \qquad 4.27$$

Note that for $n\mu_e >> p\mu_h$ equation 4.27 reduces to the single carrier case and thus:

$$\rho = \frac{1}{n|q|\mu_e} \qquad 4.28$$

4.3.2 Hall Effect

When a magnetic field, B_z, is applied perpendicular to the direction of current passing through a material, I_x, the carriers are deflected in a third orthogonal direction by the Lorentz force, F, Fig 4.3.

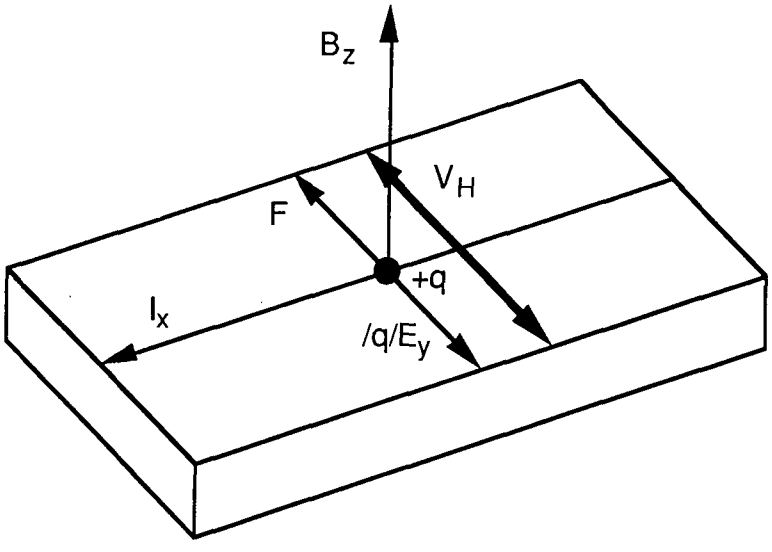

Fig 4.3 Hall effect geometry.

The resulting accumulation of charge on one side of the material (and depletion on the other) continues until an equilibrium is obtained. This occurs when the force due to the electric field, E_y, produced by the charge distribution is equal to the Lorentz force deflecting the carriers [9].

For n-type material:

$$|B_z q \upsilon_x| = |E_y q| \qquad 4.29$$

where υ_x is the electron drift velocity.

The current density, J_x, is the quantity of charge passing through a unit area per second:

$$J_x = q\upsilon_x n \qquad 4.30$$

which when combined with equation 4.29 gives the relationship for E_y in equation 4.31.

$$E_y = \frac{J_x}{n|q|}B_z \qquad 4.31$$

The Hall coefficient (R_H) is defined as the electric field produced by unit magnetic field and unit current density:

$$R_H = \frac{E_y}{J_x B_z} = \frac{V_y t}{I_x B_z} \qquad 4.32$$

where t is the thickness of the specimen in the z direction.

Thus the calculation of the Hall coefficient for a single carrier system from transport data requires knowledge of the layer thickness, Hall voltage, magnetic field and current only.

However for a multicarrier system the contribution from each group of carriers must be considered [9].

$$\frac{V_y}{I_x B_z} = \frac{\sum_j A_j}{\left(\sum_j C_j\right)^2 + \left(\sum_j A_j\right)^2} \qquad 4.33$$

where:

$$A_j = \frac{n_j|q_j|\mu_j^2 B}{1+B^2\mu^2_j} \qquad 4.34$$

and

$$C_j = \frac{n_j|q_j|\mu_j}{1+B^2\mu^2_j} \qquad 4.35$$

If the field mobility product is very much less than unity as is the case for the small fields (0.38T) used in the present study with (Hg,Mn)Te, then $B^2\mu^2 << 1$ and:

$$\left(\Sigma A_j\right)^2 << \left(\Sigma C_j\right)^2 \qquad 4.36$$

Under this low field approximation the Hall coefficient for a two carrier system of electrons and holes equation becomes:

$$R_H = \frac{p|q|\mu_h^2 - n|q|\mu_e^2}{\left(p|q|\mu_h + n|q|\mu_e\right)^2} \qquad 4.37$$

For a one carrier system the above relation reduces to the usual equation, 4.38.

$$R_H = \frac{1}{n|q|} \qquad 4.38$$

Strictly, the terms in the numerator of equation 4.38 should be weighted by the relative scattering factors, r_H, but since these are generally of order unity, these are generally neglected. For the purpose of processing transport data in this report, the scattering factor will be assumed to be unity, since many different scattering processes were found to limit the carrier mobility.

Hall mobility, μ_H, for a single carrier system is simply the ratio of the Hall coefficient to the resistivity and is also the product of the scattering factor and the mobility of conductivity, μ_C.

$$\mu_H = \frac{R_H}{\rho} \qquad 4.39$$

$$\mu_H = r_H \mu_c \qquad 4.40$$

4.4 Scattering Processes in Semiconductors

Carrier transport in semiconductors (as in all solids) is limited by carrier scattering processes. These scattering mechanisms fall into two main categories, either lattice related or defect/impurity related. For temperatures typically over 150K lattice deformations or phonons are usually the most dominant effect, whereas for temperatures below 100K defects or impurities become increasingly important for the scattering of carriers.

Scattering reduces the mean free time between collisions (τ) and hence the mobility:

$$\mu = \frac{|q|\tau}{m^*_e} \qquad 4.41$$

4.4.1 Lattice scattering

This is due to interaction between electrons and phonons and can take various forms. The main types of interaction in II-VI semiconductors, where ionic bonding is important in the lattice, are listed below.

a) Optical phonon scattering

b) Piezoelectric scattering

c) Alloy scattering

4.4.1.1 Optical Phonon Scattering

Two atoms vibrating in anti-phase in a unit cell produces an optical phonon. In compound semiconductors, adjacent atoms are oppositely charged and this allows an electrostatic potential to be associated with an optic phonon. For II-VI semiconductors the potential is a function of the ionicity of the bonding. Hence the charge on each ion affects the interaction between electrons and the lattice and can be expressed in terms of the static and optical dielectric constants. The interaction between an electron and the optical modes is characterised by a coupling constant (α).

$$\alpha = \frac{q^2 m^*_e}{2\hbar^2 \omega_l}\left[\frac{\varepsilon'_s - \varepsilon_\infty}{\varepsilon'_s \varepsilon_\infty}\right] \qquad 4.42$$

where the energy of the optical mode is given by the product $h\omega_l$ and ε'_s and ε_∞ are the static and high frequency dielectric constants respectively.

In non-polar crystals the coupling constant is very much less than unity

whereas in polar crystals it has a value just less than unity.

The effect which optical scattering has upon carrier mobility was investigated by D. Howarth et al [10] who proposed equation 4.43.

$$\mu_{opt} = \frac{8|q|}{6\alpha\omega_1 m^*_e \sqrt{\pi Z}} \psi(Z)\left(e^z - 1\right) \qquad 4.43$$

where Z is the ratio of the Debye temperature to that of the lattice:

$$Z = \frac{h\omega_1}{\kappa T} \qquad 4.44$$

The function $\psi(Z)$ lies between 0.6 and unity for temperatures in the range 70K to 300K.

4.4.1.2 Piezoelectric Scattering

This type of scattering is usually associated with ionic or partially ionic crystals. Acoustic modes create regions of compression and rarefaction within the crystal which in turn leads to a non-uniformity in the internal electric field causing scatter. This effect is more prominent in hexagonal structures than in cubic. The mobility limited by piezoelectric scattering is given by a relation between the piezoelectric electrochemical coupling constant (C), the density of material (d), the longitudinal wave velocity (C_L) and the mobility (μ_{pie}) [11].

$$\mu_{pie} = \frac{0.044 d C_L^{\,2} \hbar^2 \varepsilon_s'^{\,2}}{qC^2\left(m^*_e{}^3 \kappa T\right)^{1/2}} \qquad 4.45$$

4.4.1.3 Alloy Scattering.

In a semiconductor solid solution alloy the scattering of free carriers due to the deviations from the perfect periodicity of the crystal lattice, caused by the random distribution of the alloy atoms on the available lattice sites, is referred to as alloy scattering. Harrison et al [12] proposed equation 4.46 for the mobility limited by alloy scattering processes.

$$\mu_{all} = \frac{4qN_{all}h^4}{3\sqrt{2}.m^*\pi x(1-x)(m^*)^{3/2}(\Delta E)^2(\kappa T)^{1/2}} \qquad 4.46$$

where N_{all}, x and ΔE are the density of the alloy sites, the alloy fraction and the depth of the scattering potential well respectively. Harrison et al considered ΔE to be the difference between the electron affinities of the two end binary compounds.

4.4.2 Impurity Scattering.

4.4.2.1 Ionised Impurity Scattering

This is due to doping of the semiconductor with impurities or by defects within the lattice, where charges on the scattering centre deflect carriers. Brookes et al [13] produced a model based on the screening of the Coulomb field of ionised impurities by free electrons, equation 4.47.

$$\mu_{II} = \left[\frac{2^7(\kappa T)^3}{\pi^3 m^*}\right]^{1/2} \frac{\varepsilon'_s{}^2}{q^3 N_I}\left\{\log_e \frac{6m^*\varepsilon'_s(\kappa T)^2}{q^2h^2n'(2-n'/N)}\right\}^{-1} \qquad 4.47$$

$N_I = z_A N_D^+ + z_B N_A^-$, where z_A and z_B are the effective charges of the acceptors and donors respectively. Also n' is the number of free carriers per unit volume and $N = N_D^+ - N_A^-$.

4.4.2.2 Neutral Impurity Scattering

This occurs at low temperatures when carriers freeze out into impurity centres. The interaction between electrons and neutral impurities is very similar to electron scattering by hydrogen atoms. Erginsoy et al [14] proposed equation 4.48.

$$\mu_{NI} = \frac{m^*}{20 N_N \varepsilon'_s}\left[\frac{q}{\hbar}\right]^3 \qquad 4.48$$

Where N_N is the number of neutral impurity atoms per unit volume.

Table 4.1 summaries the dependence of each scattering mechanism considered in this chapter and their dependence on the effective mass of the free electrons and upon temperature.

Mechanism	$\mu \alpha (m^*e)^x T^y$		r
	x	y	
Optical phonon	-3/2	Exponential	1 to 1.14
Piezoelectric	-3/2	-1/2	$45\pi/128$
Ionised Impurity	-1/2	3/2	$315\pi/512$
Neutral Impurity	1	Independent	1

Table 4.1 The dependence of mobility on temperature and effective mass for different scattering mechanisms [15].

To combine the effects of more than one scattering process Mathiessen's rule [16] must be applied, equation 4.49.

$$\frac{1}{\mu_{Total}} = \sum_j \frac{1}{\mu_j} \qquad 4.49$$

4.5 Summary

Harman's model for calculation of the free electron concentration for semimetallic HgSe was reported and it's applicability to HgTe considered. The model for HgSe was based on one valence band overlapping the conduction band and one other valence band present below the conduction band, Harman obtained the electron energy from calculations by Kane.

Semiconductor statistics for narrow gap conduction have also been reviewed and expressions obtained for the dependence of free carrier concentration on temperature and doping levels. Interpretation of resistivity and Hall data was included to aid the analysis of carrier behaviour from these techniques and the importance of the low field approximation for simplification of this analysis was emphasised.

The temperature dependence of the Hall mobility provides an insight into the free carrier scattering mechanisms. Those mechanisms which are important in II-VI compounds (optical phonon, piezoelectric, alloy, ionised impurity and neutral impurity) have been briefly discussed and the relevant equations for the associated mobilities and their dependence on effective mass and temperature given.

References.

[1] "Semiconductors and Semimetals" ed J.K. Furdyna and J. Kossut (1988) **vol 25,** pub. Academic Press Inc.

[2] M. Jaczynski and W. Dobrowolski (1980) Physica Status Solidi **102**(b) 195.

[3] T.C. Harman, M.J. Logan and H.L. Goering (1958) J. Phys. Chem. Solids **7** 228.

[4] T.C. Harman and A.J. Strauss (1961) J. Appl. Phys **32** 2265.

[5] G. Bastard, C. Rigaux, Y. Guldner, J. Mycielski and A. Mycielski. (1978) Le Journal De Physique **39** 87.

[6] "Semiconductors and Semimetals" ed. R.K. Willardson and A.C. Beer (1977) **Vol 10,** pub. Academic Press Inc p85.

[7] R.O. Carlson (1958) Phys. Rev. **111** 476.

[8] E.O. Kane (1957) J. Phys. Chem. Solids **1** 249.

[9] "Semiconductors" by R.A. Smith (1978) pub. Cambridge University Press, Cambridge p101-110.

[10] D. Howarth and E.H. Sondheimer (1953) Proc. Roy. Soc. **A219** 53.

[11] W.A. Harrison, (1956) Phys. Rev. **101** 903.

[12] J.W. Harrison and J.R. Hauser (1976) J. Appl. Phys. **47(1)** 292

[13] "Advances in Electronic and Electron Physics" by H. Brook (1976) pub. Academic press, New York pp85-182.

[14] C. Erginsoy (1950) Phys. Rev. **79** 1013.

[15] "Semiconductor Physics, An Introduction" by K. Seeger (1982) pub. Springer, London p161.

[16] "Electrons and Phonons" by J.M. Ziman (1967) pub. Oxford University Press, London p156-178.

Chapter Five

Assessment of Structural and Defect Properties

5.1 Introduction

An analysis of the crystalline properties of (Hg,Mn)Te layers in terms of uniformity, dislocation density and surface morphology was made with respect to layer thickness and composition. The determination of crystal thickness, composition and quality from high resolution double crystal x-ray diffraction (DCXRD) is discussed and models for the dependence of the rocking curve full width at half maximum (FWHM) on layer thickness are compared. Double crystal x-ray topography and transmission electron microscopy (TEM) revealed clear sub-grain structures, in (Hg,Mn)Te grown using the DAG technique, with a mean grain diameter that increased with thickness. Analysis of the x-ray scattering mechanisms by triple axis x-ray diffraction, from these layers, revealed that the degree of tilt between the sub-grains was the dominant factor in the broadening of the x-ray rocking curves and that this decreased with increasing grain size. Investigations of surface morphology indicated that the optimum morphology, again for DAG grown (Hg,Mn)Te, was obtained using (100) orientated substrates at a growth temperature of 380°C.

5.2 Determination of Crystal Parameters from X-ray Diffraction Data

In this section techniques for the determination of layer parameters (composition, thickness and quality) from double crystal diffraction are discussed.

5.2.1 X-ray Rocking Curve Full Width at Half Maximum (FWHM)

The FWHM is a measure of the perfection of a diffracting crystal and is obtained by simply measuring the width of the rocking curve at half the maximum intensity after subtracting the background countrate, as discussed in section 3.3.3.

The DCXRD spectrum for a typical (Hg,Mn)Te/GaAs structure contained two distinct symmetric Bragg peaks, Fig 5.1: one from the GaAs substrate and another from the (Hg,Mn)Te layer [1]. Typically the GaAs substrate had a FWHM of 17" which is close to that of a perfect crystal structure. However the FWHM of the (Hg,Mn)Te layer was very much broader than that of the GaAs with the smallest value obtained being 120". The CdTe buffer layer, generally appeared as a shoulder on the principal (Hg,Mn)Te rocking curve, since the lattice parameters for (Hg,Mn)Te and CdTe are close. In addition the CdTe layer was generally thinner ($\leq 1\mu m$) than the (Hg,Mn)Te layer ($\geq 1\mu m$) and was highly defected (i.e broad peak and low amplitude). The high absorption of the (Hg,Mn)Te layer also reduced the magnitude of the CdTe peak. All the (Hg,Mn)Te and CdTe rocking curves considered could be fitted to a Gaussian distribution (after allowing for the CdTe shoulder). It also should be noted that the change in angular separation between GaAs and (Hg,Mn)Te due to a maximum variation in layer composition was small (2233") compared to the separation itself (14115" GaAs to MnTe) since the difference in the lattice spacing of HgTe (6.46 Å) and cubic MnTe (6.334Å) is very much less than that between the (Hg,Mn)Te layer and GaAs (5.653Å). The lattice spacing of CdTe, which was the largest in the system, is (6.481Å). For layers over 1μm thick analysis of the asymmetric and symmetric reflections revealed that the layer lattice parameters perpendicular and parallel to the surface were very similar, implying almost 100% relaxation of the (Hg,Mn)Te in both <110> directions in the

(001) surface.

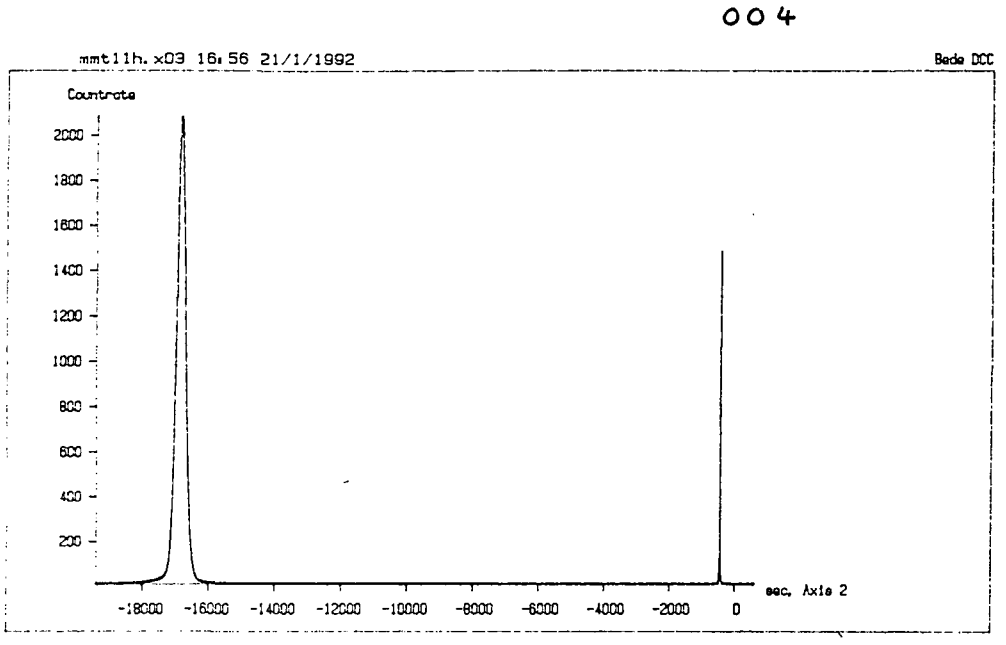

Fig 5.1 Typical rocking curves from the (Hg,Mn)Te/CdTe/GaAs system.

5.2.2 Layer Composition

The (Hg,Mn)Te layer composition was determined from the angular separation between the corresponding substrate and layer x-ray diffraction peaks. Fig 5.1. The Bragg angle of the layer was determined from the substrate Bragg angle, $\theta_{B\ Substrate}$, which for GaAs is well established, and the peak separation, S:

$$\theta_{B\ layer} = \theta_{B\ substrate} + S \qquad 5.1$$

For a symmetric reflection, where the angle of incidence on the surface is equal to the angle of exit on the surface, equations 5.2 and 5.3 enable the calculation of the lattice parameter perpendicular to the substrate surface, $a_{\perp}$. For a fully (100%) relaxed layer this can also be used to calculate the composition (see Chapter One).

$$\lambda = 2d_{hkl}.\sin\theta_B \qquad 5.2$$

$$d_{hk\ell} = \frac{a_\perp}{\sqrt{h^2+k^2+\ell^2}} \qquad 5.3$$

where h, k and l are the Miller indices of the diffracting planes.

When an epitaxial layer is grown on a crystalline substrate, the layer first grows pseudomorphically, i.e. with the same in-plane lattice parameter as the substrate. It is therefore under strain and as the layer grows the strain energy increases, until at some critical thickness (h_C), the layer relaxes to its natural bulk lattice spacing, through the formation of a network of dislocations at the interface, Thus a layer of thickness less than the critical thickness will be constrained by the in-plane substrate lattice spacing. The vertical spacing will be correspondingly distorted by Poisson's ratio and will not be a true value of the bulk (free standing) lattice parameter. The structure is illustrated in Fig 5.2. In this situation the lattice parameter parallel to the substrate surface must also be measured.

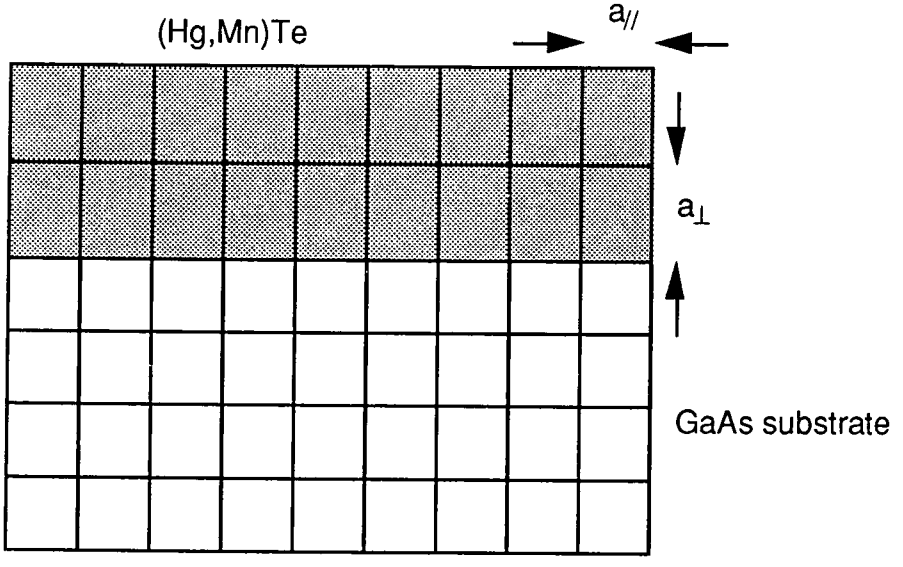

Fig 5.2 Strained lattice mismatched system (thickness < h_C).

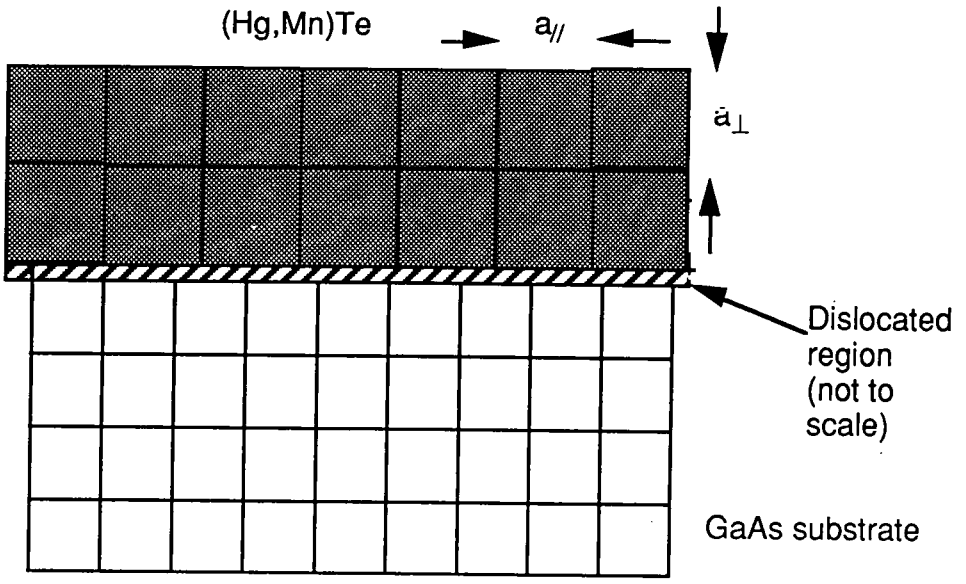

Fig 5.3 Relaxed lattice mismatched systems (thickness > h_C).

This is achieved using an asymmetric reflection where the angle of incidence on the surface is unequal to the exit angle from the surface, i.e. diffraction occurs from planes of atoms that are not parallel to the surface, Fig 5.4.

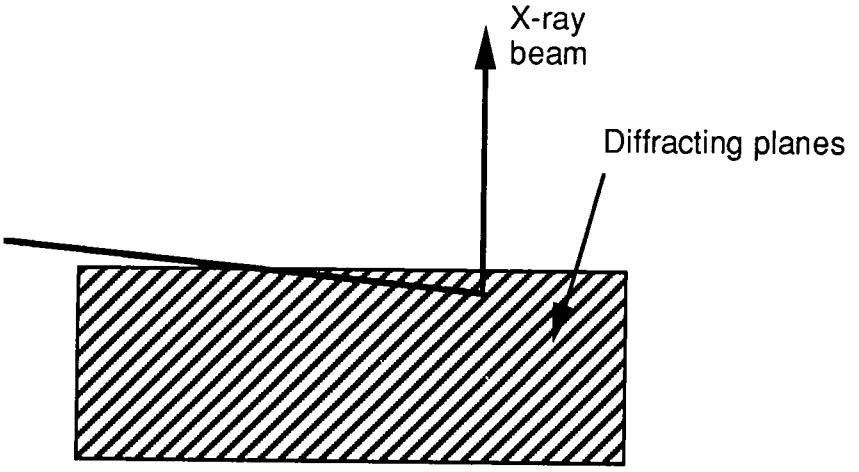

Fig 5.4 An asymmetric x-ray reflection.

To correct for any tilt of the layer with respect to the substrate (ϕ) a reflection was also taken with the sample rotated through 180° in the plane of the surface. Fewster [2] denoted this averaged angular separation

between the layer and substrate peaks for the 115 reflection to be $\Delta\theta$. From the differentiation of Bragg's law and geometrical considerations Fewster found:

$$\left(\frac{\Delta a}{a}\right)_{\perp} = -\frac{\cot\theta\,\Delta\theta}{\cos^2\phi} \qquad 5.4$$

where a is the substrate lattice parameter perpendicular to the surface and Δa is the difference between the layer and substrate lattice parameters.

Then from simple geometry Fewster related $\Delta\theta$ and $\Delta\phi$. Thus by performing one experiment equation 5.5 can be used to obtain the change in lattice spacing i.e. tetragonal distortion.

$$\left(\frac{\Delta a}{a}\right)_{\perp} = -\frac{\Delta\omega}{\cos^2\phi(\tan\theta+\tan\phi)} \qquad 5.5$$

where $\Delta\omega$ is the separation between the layer and substrate peaks with no correction for tilt made.

Alternatively if two experiments are performed then a check can be made on whether tetragonal distortion can be considered as elastic. The 'relaxed' lattice parameter is then related to that measured by:

$$\left(\frac{\Delta a}{a}\right)_{relaxed} = \left(\frac{\Delta a}{a}\right)_{\perp}\frac{1-\gamma}{1+\gamma} \qquad 5.6$$

where γ is Poisson's ratio.

Poisson's ratio in the [001] direction is obtained from the elastic constants C_{11} and C_{12} (table 5.1):

$$\gamma = \frac{C_{12}}{C_{11} + C_{12}} \qquad 5.7$$

Compound	C_{11}	C_{12}	γ	Reference
HgTe	5.36	3.66	0.41	[3]
CdTe	5.35	3.68	0.41	[4]
ZnTe	7.11	4.07	0.36	[5]

Table 5.1 A selection of elastic constants used in this study

The Poisson's ratio for (Hg,Mn)Te is assumed to be that of HgTe for calculations performed in this study.

Once the relaxed lattice parameter has been determined the composition is determined from Vegard's law applied to (Hg,Mn)Te (Chapter One):

$$a = 6.46\text{Å} - 0.121x \qquad 5.8$$

where a is the lattice parameter of the relaxed layer and x is the manganese mole fraction.

5.2.3 Layer Thickness

Consider the situation in Fig 5.5 where a (Hg,Mn)Te/CdTe/ZnTe/GaAs system is set so that the substrate is diffracting incoming x-rays in a symmetrical reflection. The diffracted x-rays follow the path ABC and are subject to absorption from the (Hg,Mn)Te, CdTe and ZnTe layers. Absorption of the x-rays in the GaAs will also occur, however to determine the thickness of (Hg,Mn)Te diffraction from an uncovered GaAs substrate was used as a

standard, thus only absorption from the layers covering the GaAs substrate needed to be considered.

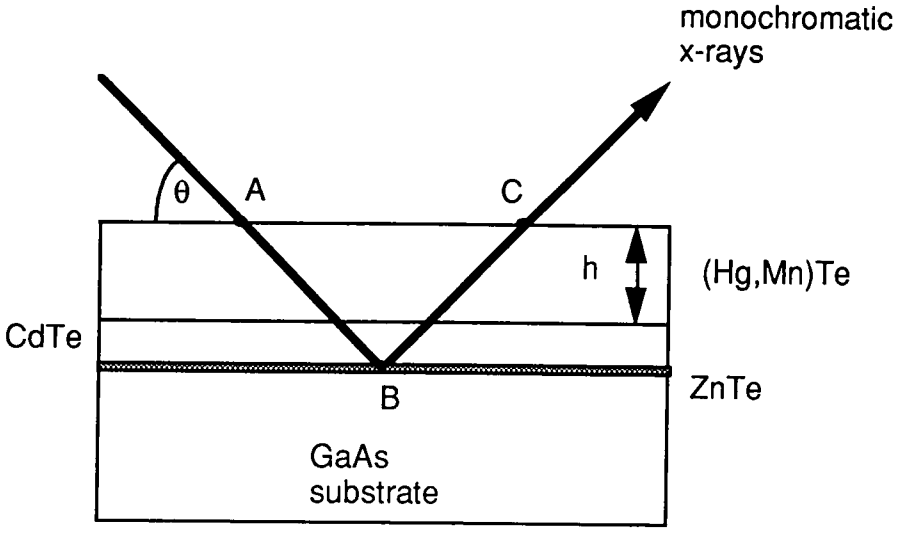

Fig 5.5 Calculation of layer thickness by diffraction from the substrate.

The path length can be calculated from simple trigonometry (equation 5.9) since the Bragg angle, θ_B, for GaAs can be calculated by Bragg's law for a known wavelength of x-rays.

$$ABC = 2h/\sin\theta_B \qquad 5.9$$

The integrated intensity of the substrate peak (the area under the peak) is related to the absorption coefficient and path length by equation 5.10 (Chapter Three).

$$I_L = I_0 \exp[-\mu\rho\, ABC] \qquad 5.10$$

where I_L and I_O are the integrated intensities of the x-ray diffraction peaks with and without an epitaxial overlayer, respectively, μ is the mean mass absorption coefficient and ρ is the density of the layer.

Experimentally it has been shown that for (Hg,Mn)Te epitaxial films of thickness greater than 1μm the ratio of the integrated intensities of the layer to substrate peaks was exponentially dependent on the combined thickness of the layer structure. This is expected from dynamical diffraction theory and the normal absorption of the x-rays diffracted from the substrate and agrees with equation 5.10. This is illustrated in Fig 5.6, which shows the variation of the substrate integrated intensity ratio (I_L/I_O) as a function of layer thickness, for several compositions. The thickness was measured independently by viewing a cleaved surface in the SEM.

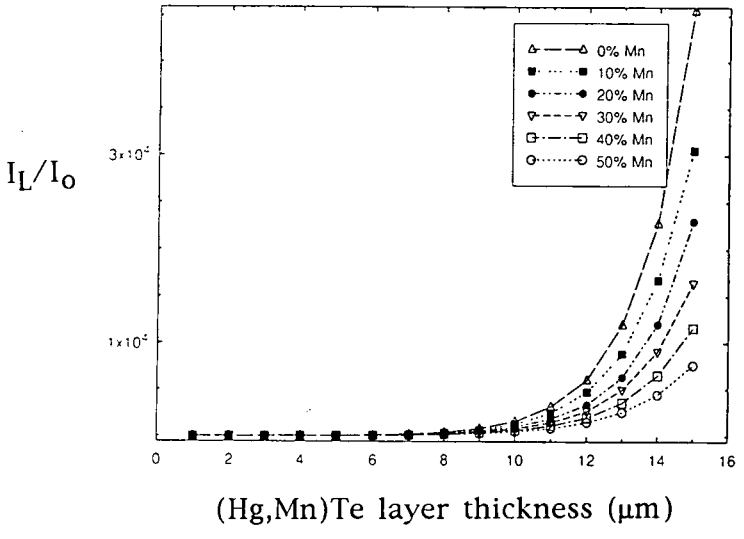

Fig 5.6 The dependence of I_L/I_O on (Hg,Mn)Te thickness.

Absorption within the layers can be calculated from the weighted sum of the mass absorption coefficients of the component elements as in equation 5.11.

$$\mu = \sum_j W_j \mu_j \qquad 5.11.$$

where W_j is the weighting factor for the j^{th} component.

The mass absorption coefficients for the elements encountered in the

(Hg,Mn)Te/CdTe/ZnTe/GaAs system are listed in Table 5.2 for the two wavelengths used in the course of the project (1.54056Å and 1.7905Å for $CuK\alpha_1$ and $CoK\alpha_1$ respectively), note the strong dependence of absorption on wavelength (see Chapter Three).

Element	Mass absorption coeffient (cm^2g^{-1})	
	$CoK\alpha_1$	$CuK\alpha_1$
Te	394	267
Mn	393	270
Cd	329	222
Hg	273	188
Zn	87.1	57.9

Table 5.2 X-ray mass absorption coefficients for the elements used in this study [6].

Densities of (Hg,Mn)Te, CdTe and ZnTe were calculated using equations 5.12 and 5.13 and the well established lattice parameters and atomic masses, m_{at}, as quoted in Table 5.3. The factor of 4 in equation 5.12 results from the zinc blende structure, which possesses four cations and four anions per unit cell.

$$\text{Unit cell mass} = \frac{\sum_j \left(4m_{at}\right)_j}{\text{AvConst}} \qquad 5.12.$$

where AvConst is Avagadro's constant (6.022×10^{23} $mole^{-1}$).

$$\rho = \frac{\text{mass}}{\text{volume}} = \frac{\text{unit cell mass}}{a^3} \qquad 5.13$$

For ternary alloys, calculation of the unit cell mass must take into account that two of the three elements are competing for the same sites in the lattice, so the composition must be considered. The density of (Hg,Mn)Te and its dependence on composition is presented in Fig 5.7 and equation 5.14.

Element	Atomic mass
Te	127.6
Mn	54.9
Cd	112.4
Hg	200.6
Zn	65.4

Compound	Lattice parameter (Å)	Density ($g.cm^{-3}$)
CdTe	6.481	5.86
HgTe	6.46	8.09
MnTe (cubic)	6.334	4.77
ZnTe	6.1037	5.64
GaAs	5.653	

Table 5.3 Lattice parameters, atomic masses and densities of elements and compounds used in this study [6].

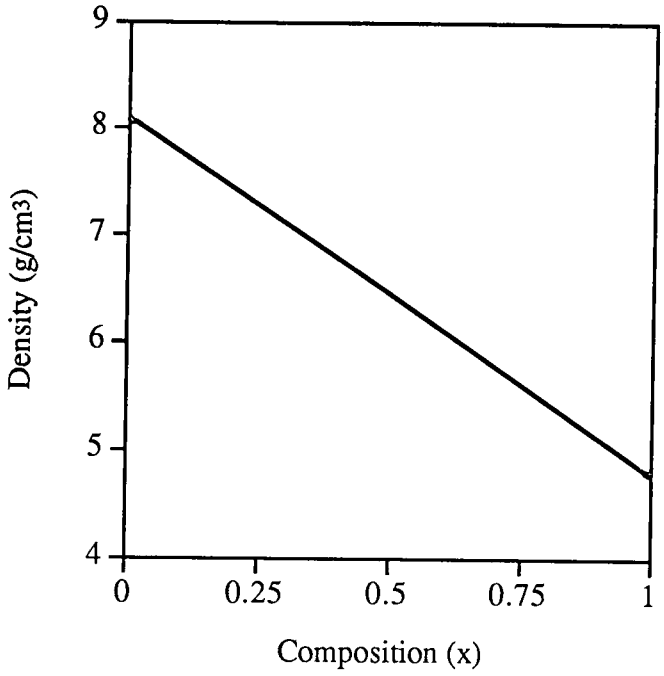

Fig 5.7 The calculated dependence of (Hg,Mn)Te density upon composition.

$$\rho = 8.09 - 3.32x \qquad 5.14$$

where ρ is the density in $g.cm^{-3}$ and x is the manganese mole fraction.

These densities were substituted into equation 5.11 to calculate the mass absorption coefficients for the principal binary compounds. The values are listed in Table 5.4.

Compound	Mass absorption coeffient (cm^2g^{-1})	
	$CoK\alpha_1$	$CuK\alpha_1$
CdTe	364	246
MnTe	394	268
HgTe	320	219
ZnTe	290	196

Table 5.4 Mass absorption coefficients of the principal binary compounds.

In the calculation of layer thickness, each component layer must be considered separately and the absorption of the (Hg,Mn)Te layer calculated once the composition is known, Fig 5.8.

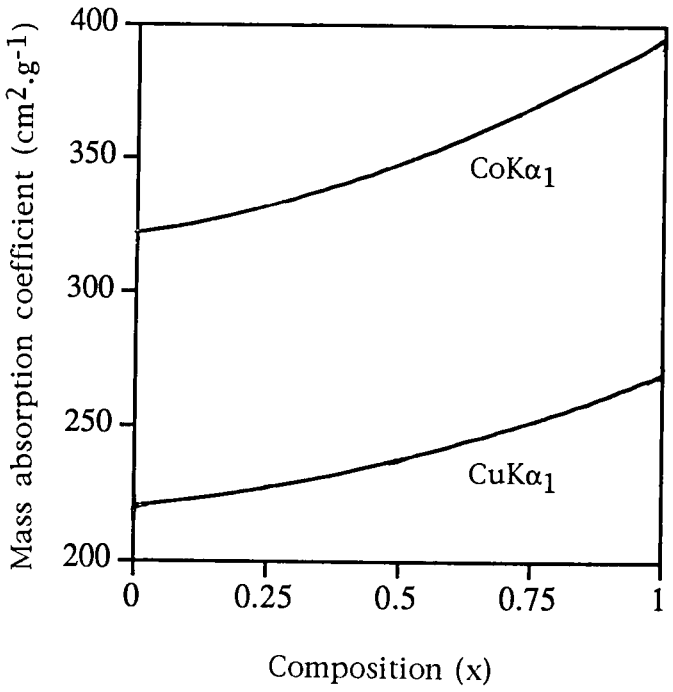

Fig 5.8 The calculated compositional dependence of the x-ray mass absorption coefficient for (Hg,Mn)Te.

The mass absorption coefficient (μ) for $CoK\alpha_1$ and $CuK\alpha_1$ in (Hg,Mn)Te are given in equations 5.15 and 5.16 respectively.

$$\mu = 41.943x^2 + 31.217x + 320 \qquad 5.15$$

$$\mu = 28.343x^2 + 20.457x + 219 \qquad 5.16$$

where (μ) is in cm^2g^{-1} and x in the manganese content of the layer.

Equation 5.17 is the thicknesses calculated by the integrated intensity ratio method (note that diffraction from the substrate occurs at 33.1° and 38.4° for $CuK\alpha_1$ and $CoK\alpha_1$ respectively).

$$h = \frac{\sin\theta_B}{2(\mu)\rho} \ln\left(\frac{I_o}{I_L}\right) \qquad 5.17$$

In practice, where the total layer thickness for the (Hg,Mn)Te/CdTe/ZnTe/GaAs system was 5μm or more, the ZnTe layer could be ignored in the calculation since it was less than 0.1μm thick. There was excellent correlation between the thickness of (Hg,Mn)Te layers measured by x-ray absorption, by viewing cleaved edges in the SEM [8] and by TEM [9]. It is of interest to note that polycrystalline films exhibited a very small substrate integrated intensity compared to single crystal films with a similar thickness.

5.3 The Dependence of X-ray FWHM on Layer Thickness for (Hg,Mn)Te Epitaxial Layers

The FWHM values were measured from the x-ray rocking curves taken from a range of layers of different thicknesses. Empirically, these values

were found to follow an inverse thickness dependence on the layer thickness, as shown in Fig 5.9. The FWHM of the 004, 111 and 224 symmetric reflections were used, to allow a proper comparison. Included in the graph are data from Brown et al [7] for CdTe layers on GaAs and results using $Cd_{0.96}Zn_{0.04}Te$ and GaAs substrates for (Hg,Mn)Te growth. At first glance it may be surprising that FWHM values for CdTe on GaAs lie on the same line of the FWHM vs inverse thickness plot as (Hg,Mn)Te on $Cd_{0.96}Zn_{0.04}Te$ where the lattice mismatches are 14.6% and 0.2% respectively.

However, in terms of a coincidence lattice site model for the interface [8], seven lattice sites of CdTe map closely onto eight GaAs sites, with an "effective mismatch" of only 0.245%, i.e. rather similar to that of the (Hg,Mn)Te/$Cd_{0.96}Zn_{0.04}Te$ system.

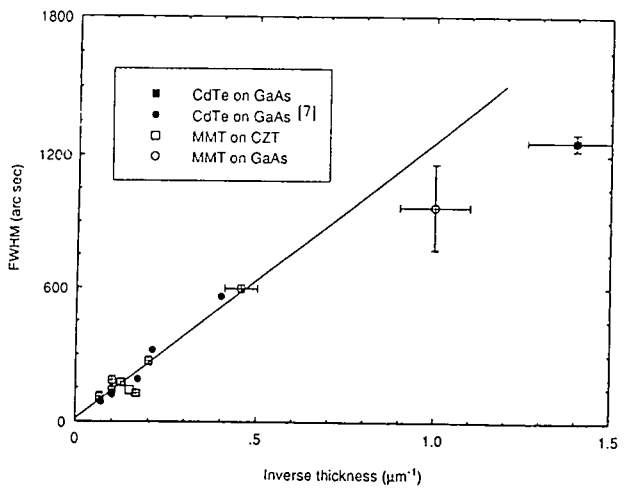

Fig 5.9 FWHM as a function of inverse layer thickness for (Hg,Mn)Te and CdTe on a variety of substrates

The principal uncertainties in the FWHM vs inverse thickness graph lie in the thickness measurements. An under-estimation of the CdTe buffer layer thickness would result in an increase in the integrated intensity of the

substrate peak and would account for the occurrence of the points below the fitted line. Equally, over-estimation of the thickness of CdTe would explain the points above the fore-mentioned line. Another possible reason for points lying above the line would be a loss of extinction due to strain within the grains but would not account for the scattering of points below the line. A more detailed analysis of the dependence of FWHM on thickness, using a larger number of data points, has ben presented in Fig 5.10.

Substrate orientation and type seemed to have little effect on the thickness dependence of (Hg,Mn)Te FWHM.

Keir et al [10] presented results for double crystal x-ray diffraction from (Hg,Cd)Te on GaAs, grown by MOVPE, where the layer was repeatedly etched to reduce the thickness. Their results indicated a sharp increase in the FWHM near the substrate interface, tending towards a constant value for thick layers. This would be in qualitative agreement with the FWHM dependence on thickness for (Hg,Mn)Te. However, Brown et al [7] using etch pit counting on CdTe and (Hg,Cd)Te on GaAs, determined an empirical relationship where the FWHM was proportional to the square root of the dislocation density.

Ayers et al [11] proposed a model to explain the observed FWHM behaviour, based on dislocation density. In their model the dislocation density was taken to be inversely proportional to the thickness. This was based on data from GaAs grown on Si, where half loops were formed by the interactions of misfit dislocations. Due to the presence of the CdTe buffer layer the Ayers model cannot be applied directly to the (Hg,Mn)Te/CdTe/GaAs system. The high dislocation density and the Bragg peak position indicated that the CdTe buffer layer was almost totally relaxed. Hence, although Ayers et al predicted that the gradient of the dislocation density vs inverse thickness

plot was proportional, to a first approximation, to the lattice mismatch, the (Hg,Mn)Te layers have a stronger than expected dependence on thickness.

Using a model where dislocations produce a mosaic structure, Gay et al [12] proposed that it was the tilt between sub-grains which was responsible for the broadening of the rocking curves for epitaxial films. They also proposed that the threading dislocation density, D_h, can be related to the x-ray rocking curve FWHM (in radians) and the Burger's vector, **b**, as:

$$D_h = \frac{FWHM^2 - B^2}{9\mathbf{b}^2} \qquad 5.18$$

where B is the FWHM for a dislocation free crystal and may be considered to be of the order of 10 arc secs.

Applied to a 0.5μm thick layer of $Hg_{0.9}Mn_{0.1}Te$ containing dislocations of Burger's vector a/2<011> equation 5.18 predicts a dislocation density of $7 \times 10^{11} cm^{-3}$, which is two orders of magnitude greater than the dislocation density $10^9 cm^{-3}$ observed by TEM for a layer of similar thickness [9].

When the numerator of equation 5.18 was calculated as a function of the thickness of the (Hg,Mn)Te layer (found by x-ray absorption for the same position on the layer) two exponential regions were observed, Fig 5.10, with a transition between the two regions occurring at a thickness of about 2μm.

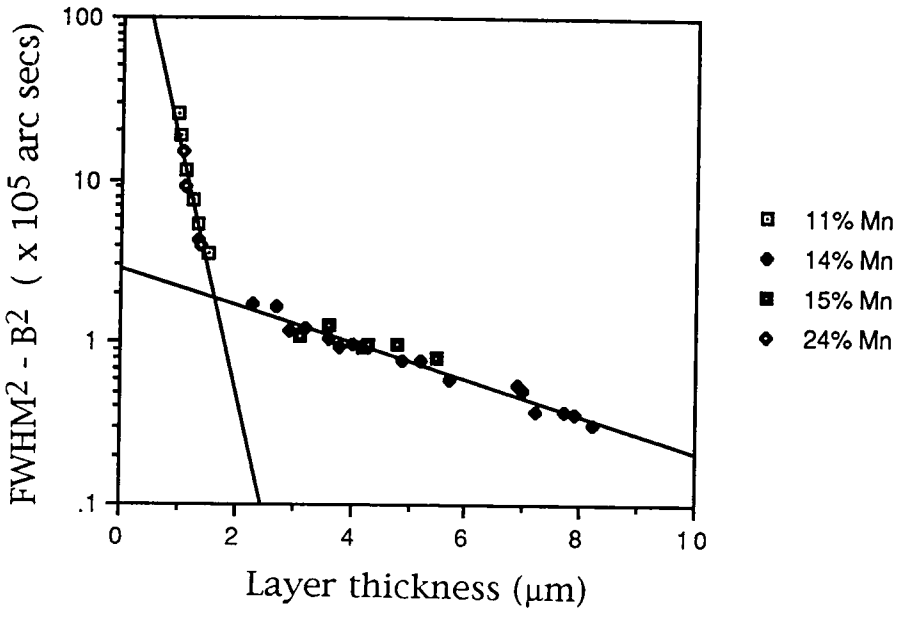

Fig 5.10 Dislocation density as a function of the thickness of (Hg,Mn)Te layers.

Supposing that the rate of change of the dislocation density, D_h, at a particular layer thickness, l, is proportional to the dislocation density at that thickness, thus:

$$dD_h(l)/dl = - A.D_h(l) \qquad 5.19$$

where A is a constant.

Integrating equation 5.19 yields:

$$D_h(l) = D_h(0).\exp(-\zeta l) \qquad 5.20$$

where $D_h(0)$ and ζ are the dislocation density at zero thickness and the rate constant respectively.

Since ζ governs the rate of the reduction of dislocation density with thickness it may be reasonable to speculate that ζ is an annihilation rate constant. This presumes that the rate at which dislocations annihilate is

proportional to the number of dislocations.

The existence of two slopes, 52.6 x 10^6 and 1.4 x 10^6 Arc secs.m^{-1} respectively, in Fig 5.10 would imply either that two annihilation mechanisms or two types of dislocation occur. Studies made on the (Hg,Mn)Te layers by TEM [9] supported the argument for the existences of two types of dislocations, determined by contrast experiments to be predominant along {111} planes and in the [110] direction respectively, see section 5.5.2.

5.4 Investigation of Surface Uniformity

It was shown in Chapter Two that the manganese concentration increased exponentially and the layer thickness decreased in a linear manner along the direction of gas flow due to depletion of the DIPTe precursor. This was a consequence of the difference in the pyrolysis characteristics of the manganese and tellurium precursors and resulted in an increase in the TCMn/DIPTe partial pressure ratio along the direction of the gas flow. Non-uniformity of the deposited layer is undesirable as device performance will be heavily dependent on the position along the surface. In order to understand the growth process more fully, a more thorough analysis of the uniformity of growth was performed using double axis x-ray diffraction. Scans were made of the 004 symmetrical reflections from the substrate and layer at different positions on the layer surface at regular spatial intervals of 2 or 3mm using $CuK\alpha_1$ or $CoK\alpha_1$ radiation with a beam diameter of 1mm. The composition, thickness and FWHM of the layer at these points was entered into Surfer™ in a spreadsheet format and used to fit regularly spaced contours to the data [13]. Fig 5.12 a, b and c shows the spatial variations of composition, thickness and FWHM over a typical layer. The direction of gas flow was from left to right.

For experiments performed on the Bede model 150 diffractometer the composition was first determined for a known position on the layer surface using EDAX then the values of composition at other positions calculated from their Bragg peak separation from that of the EDAX position This was necessary because the model 150 was not designed to analyse such large Bragg peak separations as occurred between (Hg,Mn)Te and GaAs. Profiles were taken along the centre line, in the direction of the gas flow, for (Hg,Mn)Te layers of differing composition and thickness.

The x-ray FWHM was found to increase by between 15" and 60" per mm down the gas flow direction. The manganese content had no noticeable effect on the FWHM for surface positions with similar thicknesses. However the rate of increase of x-ray FWHM with distance down the gas stream was more prominent in larger manganese content layers, Fig 5.11. A reduction in the FWHM was usually observed at the downstream edge for layers containing greater than 20% manganese, presumably a result of edge effects.

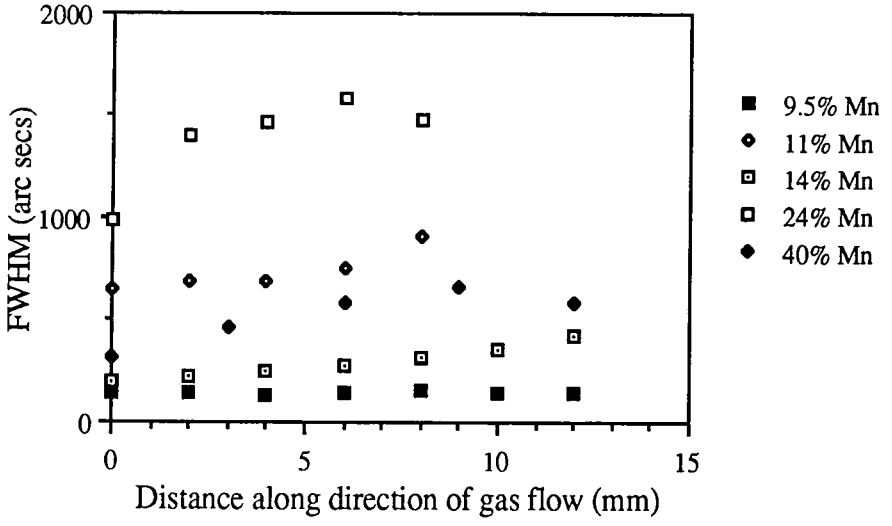

Fig 5.11 Variation in the x-ray FWHM along the direction of gas flow (compositions measured in the centre of the specimens).

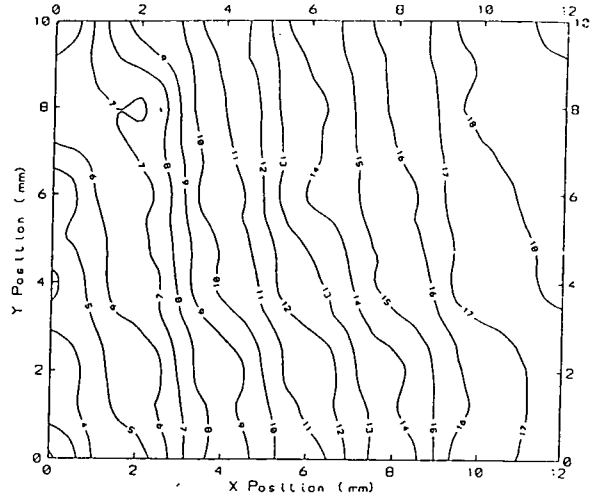

(a)

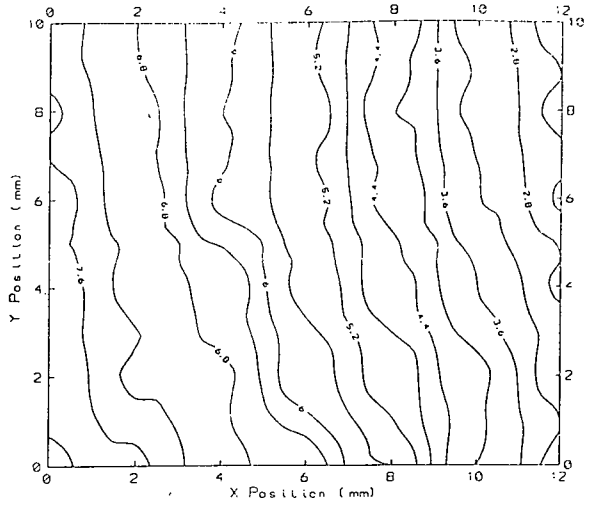

(b)

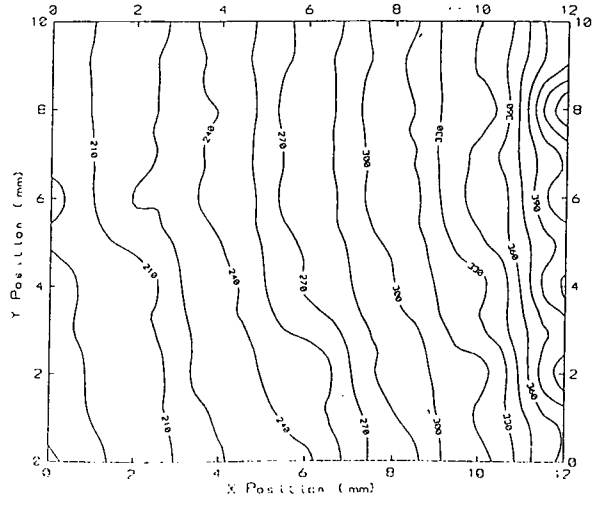

(c)

Fig 5.12 Maps of (a) manganese content, % (b) thickness, μm and (c) FWHM, arc secs, for a (Hg,Mn)Te/CdTe/ZnTe/GaAs structure grown by DAG.

The increase in x-ray FWHM along the direction of the gas flow appears to be a consequence of of the reduction in layer thickness, Fig 5.13. In Chapter Two this was attributed to the depletion of the tellurium precursor. For layers containing in excess of 10% manganese the reduction in thickness was reasonably linear with a change in the order of five percent of the composition of the upstream edge per mm. For compositions containing less than 10% manganese the reduction in thickness was very much less (around twenty times less for $Hg_{0.905}Mn_{0.095}Te$ layers). This implied that the degree of manganese inclusion into the growing (Hg,Mn)Te layer was a dominant factor in determining the growth rate, since the DIPTe would have been fully pyrolysed at the growth temperature.

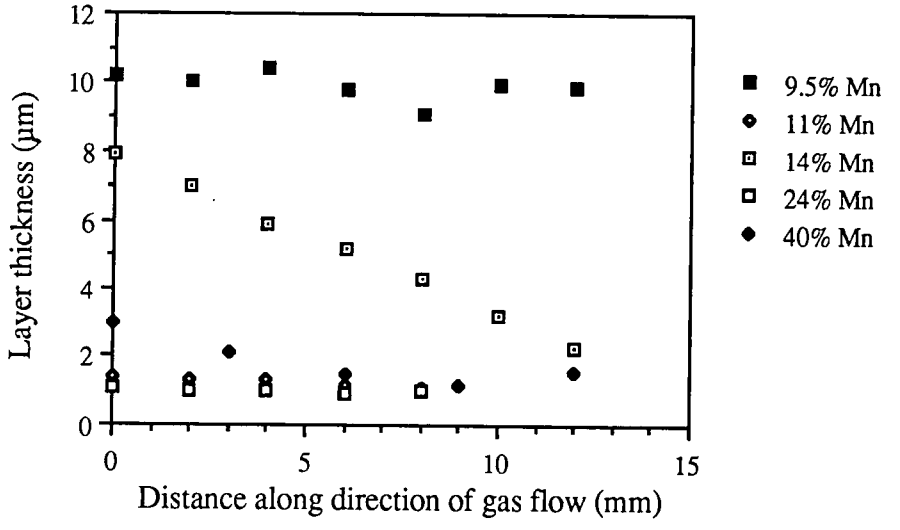

Fig 5.13 Variation in the (Hg,Mn)Te layer thickness along the direction of the gas flow (compositions measured in the centre of the specimens).

Along the direction of the gas flow the manganese content increased by typically between 1 and 3% manganese per mm with particularly thick or high manganese concentration layers exhibiting a reduction in the manganese content on the downstream edge, Fig 5.14.

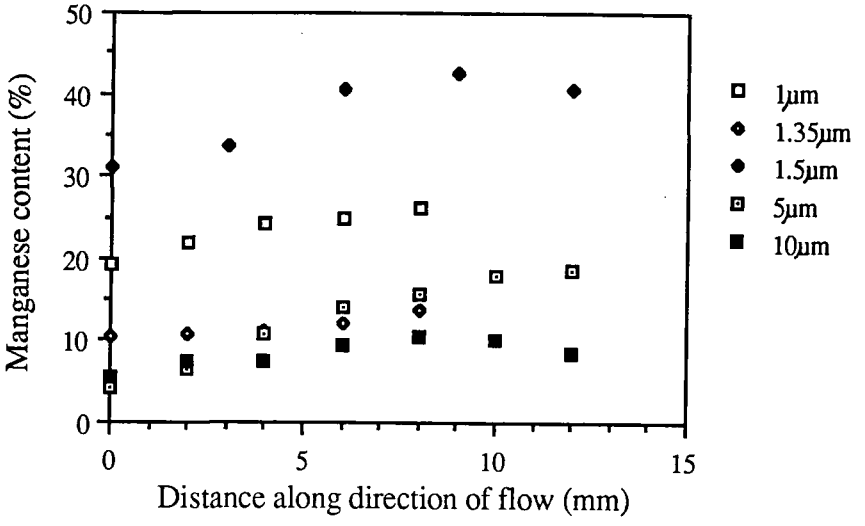

Fig 5.14 Variation in the manganese content of (Hg,Mn)Te along the direction of the gas flow (thicknesses measured in the centre of the specimens).

5.5 Sub-grain Structure

5.5.1 Analysis by X-ray Topography

Double crystal topography revealed a clear subgrain structure with a mean grain diameter dependent on the thickness (and hence dislocation density) of the (Hg,Mn)Te layers but which was found to be independent of the layer composition, Fig 5.15. A dependence on inverse thickness might be expected, since the dislocation density reduced with thickness most rapidly in the first two microns from the interface with the buffer layer, Fig 5.10.

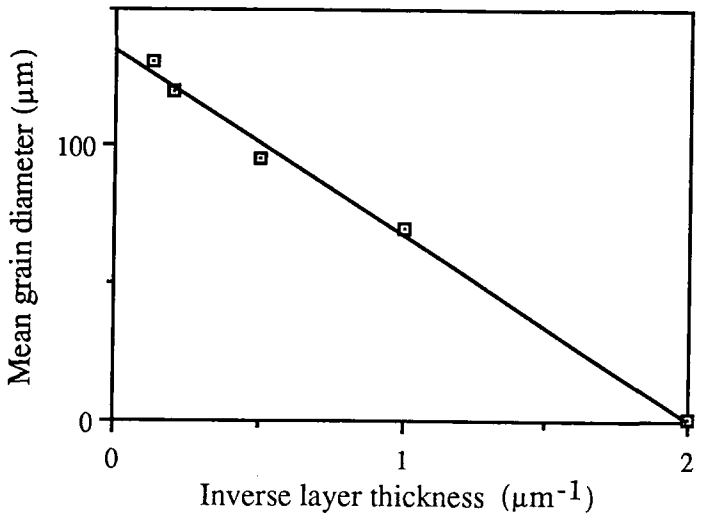

Fig 5.15 Dependence of the sub-grain size on the layer thickness.

A sequence of double crystal x-ray topographs are shown in Fig 5.16. Only a fraction of the grains satisfied the Bragg condition at any one angle and these were distributed evenly over the layer surface. Initially under low magnification the grain boundaries appeared rather straight but high magnification showed this to be far from true. No long range contours due to macroscopic wafer curvature were observed, indicating almost total relaxation. Taking topographs of the same area of an 8μm thick layer of $Hg_{0.95}Mn_{0.05}Te$ but at different angles, in particular at maximum diffraction on the Bragg peak and at half intensity on either side of the peak revealed a distribution of tilted grains such that ten micrographs, at different angles of x-ray incidence, were needed to cover all the tilted subgrains. (Fig 5.16). Grains which remained in contrast at different diffraction plane angles had large internal strain whereas those tilted out of contrast had smaller internal strain. The need for such a large number of micrographs to cover the entire range was not because of the large misorientation of many grains, as this was not mirrored by a large FWHM, but was thought to be the result of the small magnitude of strain within

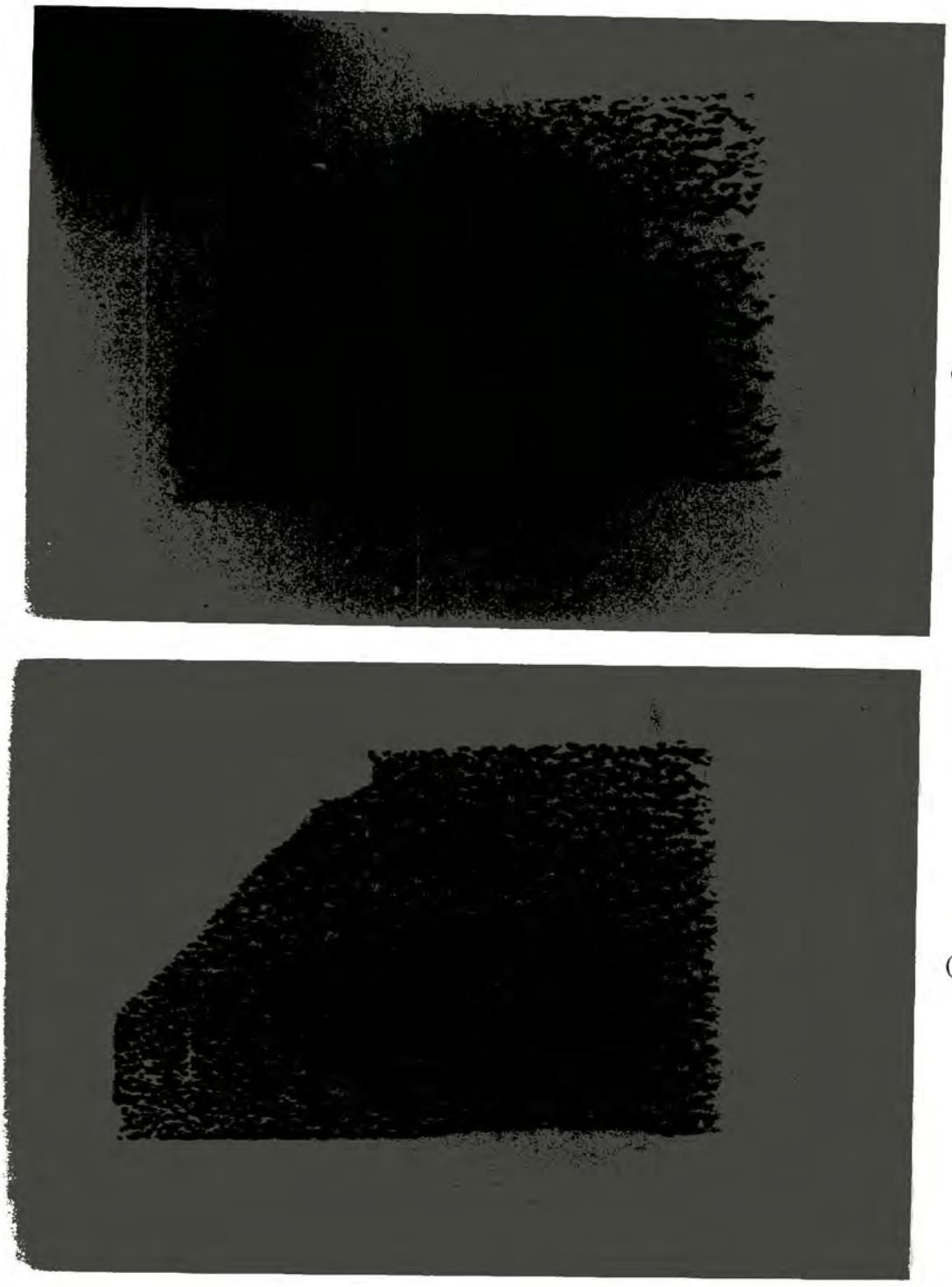

Fig 5.16 Double crystal topographs of a $Hg_{0.95}Mn_{0.05}Te$ layer: (a) -100" on negative flank; (b) +100" on the positive flank of the rocking curve.

the majority of grains. This means that because intrinsically the FWHM was about 12", the sampling range of each topograph was small.

Dislocation densities in the layers were too large for individual dislocations to be resolved.

The number of diffracting grains within five areas of $1mm^2$ at identical distances down the gas flow for the upstream, centre and downstream positions on the surface were counted and averages taken. The distribution of grains as a function of angular position is shown in Fig 5.17. At the upstream position the dominant diffracting sub-grains correspond to a larger lattice parameter than those diffracting from the centre "band" feature which occurred more predominantly on the positive flank of the rocking curve. This distribution of lattice parameter along the direction of gas flow corresponded well with the increase in manganese concentration (and hence a reduction in the lattice parameter of a relaxed layer) reported in section 5.4.

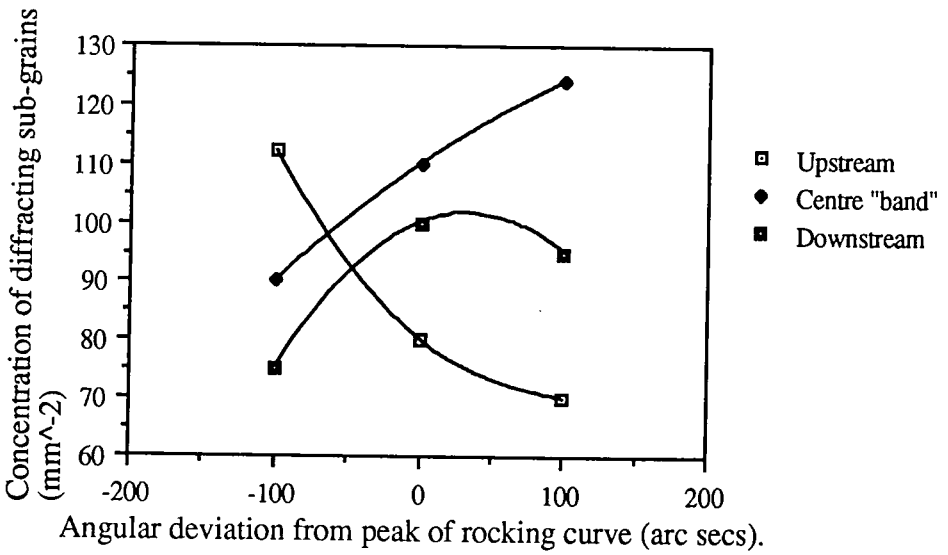

Fig 5.17 Distribution of diffracting grains in an x-ray topograph for an 8μm thick layer of $Hg_{0.95}Mn_{0.05}Te$

5.5.2 Analysis by TEM

Selected specimens were examined in TEM by H.Tatsuoka. Sections perpendicular to the substrate plane were produced by cleaving along orthogonal {110} planes. Epoxy resin was then used to bond slices face to face such that both orthogonal {110} orientations could be viewed [12] and mechanical polishing and Ar^+ ion milling used to thin the specimens. Plan view sections were produced by thinning the specimens from the substrate side and imaged in a JEOL 100CX TEM operated at 100kV. The TEM images provided clear evidence that the CdTe buffer layer considerably reduced the dislocation density in the (Hg,Mn)Te layer, caused by lattice mismatch with the substrate.

At the (Hg,Mn)Te/CdTe interface interdiffusion of Cd and Hg or Mn during growth, produced a region of around 0.15μm thickness, as calculated using data from Leute et al [14], where the lattice parameter varied. This region also contained a three dimensional misfit dislocation array thought to be the result of dislocations climbing during growth. Such arrays have also been observed by Abraham et al [15] in graded hetroepitaxial (In,Ga)P layers. Also present were relatively straight $[1\bar{1}0]$ dislocations. Two main categories of threading dislocations were determined from contrast experiments. The first type were dislocations extending from the interface to the surface predominantly along {111} planes The second category consisted of irregularly shaped dislocations extending in the $[1\bar{1}0]$ direction, with a Burger's vector of $\mathbf{b}$ = 1/2a<011> lying in {111} planes.

A dislocation density of the order of 10^9 cm^{-2} at the surface was found in plan view TEM. However many dislocations were bent near the (Hg,Mn)Te/CdTe interface. The sub-grain nature of the layers, first seen

by x-ray topography, was also clearly apparent in plan view TEM images. The diameters of the grains were about 1μm which was in good agreement with estimates obtained from layers of similar thickness by x-ray topography. Diffraction pattern analysis indicated a tilt between sub-grains of the order of 0.7°. This was in good agreement with the FWHM of the rocking curve obtained by double crystal diffraction results, which was 2580" (0.72°), indicating that the dilation component in the broadening of the rocking curve was insignificant at these smaller thicknesses.

5.6 Triple Axis x-ray Diffraction

Triple axis diffraction [16] showed no conditioner or analyser streaks, because the diffuse scattered intensity remained high at relatively large distances from the 004 point in reciprocal space. Fig 5.18 shows an isointensity contour plot in reciprocal space about the 004 point for a 8μm thick layer of $Hg_{0.945}Mn_{0.055}Te$ grown on (001) GaAs. Tilts dominate and elongate the plot in the Q_y direction, in agreement with the TEM data. A scan in the Q_y direction through the maximum intensity position in reciprocal space gave a FWHM of 168", which corresponded to the tilt of the sub-grains. Dilations are shown as a slight asymmetric distribution in the Q_z direction. The corresponding FWHM was significantly smaller (44") than the contribution of tilt in the layer.

Double crystal x-ray diffraction operates with the window of the detector integrating the scatter over a wide angular range. A rocking curve in this arrangement represents a scan in the Q_z direction integrated along a line inclined at the Bragg angle to the Q_y axis.

Keir et al [17] obtained similar results for CdTe on GaAs although full reciprocal space maps were not plotted. They found for a θ-2θ (Q_z) plot

FWHMs of 40" and 44" were obtained with 277" and 580" for specimen (constant Q_z) scans; these results are very comparable to the (Hg,Mn)Te results.

Fig 5.19 shows the isointensity contour plots for $Hg_{0.95}Mn_{0.05}Te$ on a $Cd_{0.96}Zn_{0.04}Te$ substrate. There is significant asymmetry present in the Q_z direction, corresponding to regions of expansion in the lattice which cause local increases in the lattice parameter. FWHMs, taken through the maximum intensity position in the Q_z and Q_y directions, were 68" and 207" respectively. From this result it was clear that the substrate type and orientation had little effect on tilt or dilation distribution, when a buffer layer was used, despite differences in the layer to substrate mismatch. Only layers of thicknesses of 4μm or more were analysed using the triple axis technique since insufficient diffracted intensity was obtained using thinner layers, to produce a reasonable isointensity plot after passing through the analyser.

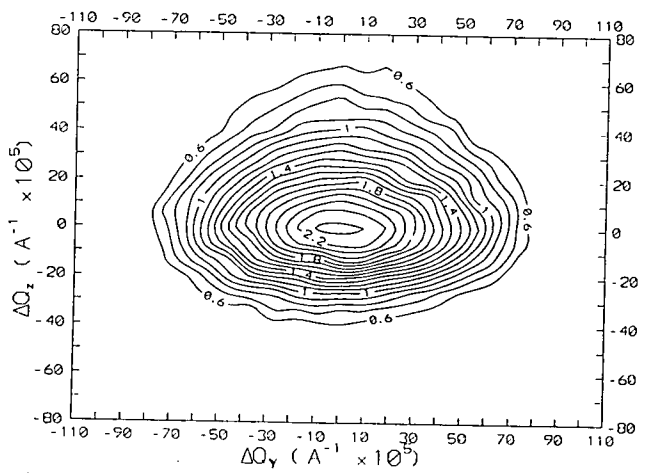

Fig 5.18 Triple axis isointensity contour plot around the 004 reciprocal lattice point for $Hg_{0.95}Mn_{0.05}Te$ grown on (001) GaAs.

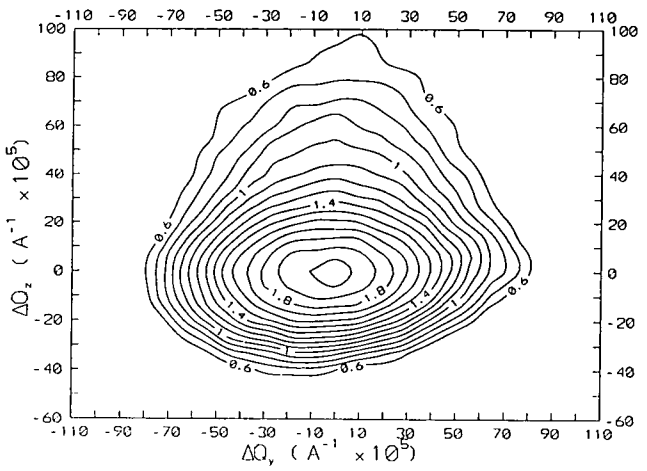

Fig 5.19 Triple axis isointensity contour plot around the 004 reciprocal lattice point for $Hg_{0.95}Mn_{0.05}Te$ grown on (001) $Cd_{0.96}Zn_{0.04}Te$.

5.7 Morphology

The surface morphology of (Hg,Mn)Te layers was investigated by M.Funaki using SEM (Cambridge Instruments S600). Morphology was affected by poor substrate preparation and unoptimised growth conditions as well as substrate orientation. Whereas the surface morphology of (Hg,Cd)Te has been widely reported [18,19] there has been little similar work performed on (Hg,Mn)Te [20].

Initially the dependence of surface morphology on the growth temperature was investigated, with the other growth conditions kept constant, Table 5.5, using CdTe buffered (100) GaAs substrates.

Layer	ZnTe	CdTe	(Hg,Mn)Te
Susceptor temperature (°C)	350	350	350-410
Total flow rate (cc/min)	7200	7200	1400
DipTe flow rate (mmol/hr)	1.3	1.3	3.69
DMZn feed rate (mm/hr)	3.1		
DMCd feed rate (mm/hr)		1.94	
TCMn feed rate (mm/hr)			2.67
Hg temperature (°C)			215

Table 5.5 Growth conditions.

The principal findings were [20]:

- At 350°C it was thought that the temperature was insufficient to promote surface migration of atoms, resulting in the observed rough and angular surface.

- At 380°C, elongated hexagonal hillocks typically 40μm long on a tortoise shell pattern background were observed in the films.

- Epitaxial growth did not occur for growth temperatures greater than 390°C and the layers became polycrystalline with grain sizes of around 5μm. EDAX confirmed that the $Hg_{1-x}Mn_xTe$ relationship was conserved. However it should be noted that the transformation from epitaxial to polycrystalline growth at 380°C only occurred for GaAs substrates and not for (Cd,Zn)Te substrates.

- At temperatures greater than 400°C the surface appearance was similar to that of sintered ceramics.

The dependence of surface morphology on substrate orientation was then

investigated for layers grown at the optimum growth temperature of 380°C. The main results were as follows:

- Growth on CdTe buffered (100) GaAs substrates resulted in elongated hexagonal hillocks sitting on a tortoise shell background, as mentioned previously.

- On unbuffered (100) 2° off to the nearest (110) $Cd_{0.96}Zn_{0.04}Te$ substrate the background became slightly rippled although hillocks were still present.

- On (211)B $Cd_{0.96}Zn_{0.04}Te$ substrates a strongly faceted growth occurred with developed (100) facets.

- On (111)B $Cd_{0.96}Zn_{0.04}Te$ substrates the surface was divided into islands by numerous "crevasses".

These results indicated that buffered (100) GaAs was probably the preferred orientation of substrate in terms of obtaining good morphology.

5.8 Summary

Double crystal x-ray diffraction has been used to accurately determine (Hg,Mn)Te composition, from analysis of the Bragg peak separation between substrate and layer, and layer thickness, from the absorption of x-rays in the (Hg,Mn)Te layer. Layers of (Hg,Mn)Te layers over 1μm thick were almost 100% relaxed, with an x-ray FWHM that was essentially independent of composition.

It was found that dislocation density decreased most rapidly with thickness at the (Hg,Mn)Te/CdTe interface. Models have been proposed by Ayers and

Gay for the dislocation density dependence on thickness based on dislocation half loops and mosaic structures respectively. Analysis by the Gay model revealed a distinct change in the thickness dependence at a thickness of around 2 μm with two corresponding rate constants. Interestingly TEM studies of the same sample by Tatsuoka et al showed that there were two main types of dislocation present in the layers. The first type were dislocations extending from the interface to the surface predominantly along {111} planes and the second were dislocations extending in the $[1\bar{1}0]$ direction. For a thickness of 0.5μm a dislocation density of $10^9 cm^{-2}$ was measured penetrating the surface, however many dislocations were bent away at the interface. This could explain the two annihilation rate constants. However, the Gay analysis gave dislocation densities two orders of magnitude greater than that observed in TEM for layers of similar thickness and this leads to some uncertainty in the interpretation of the FWHM vs thickness data.

Surface uniformity studies were performed by DCXRD using an x-y scanning stage. The manganese concentration in (Hg,Mn)Te increased by 1-3%Mn per mm, thickness decreased by 5% per mm and FWHM increased by 15" to 60" per mm along the direction of gas flow. The largest non-uniformity was observed in high manganese content layers.

Topography revealed clear sub-grains whose grain diameter decreased in a linear manner with inverse thickness. Tilting of the layer brought different areas of sub-grains into contrast revealing a possible increase in lattice parameter towards the upstream edge which was consistent with the increase in manganese composition along the gas flow direction. No long range strain contours caused by wafer curvature were observed.

Tilts were shown to be the cause of rocking curve broadening by

isointensity contour plots from triple axis x-ray diffraction experiments. However plots from layers grown on GaAs and $Cd_{0.96}Zn_{0.04}Te$ showed little difference despite the large difference in lattice mismatch.

References

[1] T.D. Hallam, S.K. Halder, J.M. Hudson, C.R. Li, M Funaki, J.E. Lewis, A.W. Brinkman and B.K. Tanner. (1993) J.Phys. D: Appl. Phys. **26** A161.

[2] P.F. Fewster (1986) Philips J. Res. **41** 268.

[3] Y.K. Vekilow (1971) Sov. Phys. Sol. Stat. **13** 956.

[4] H.J. McSkimin (1961) J. Appl. Phys **33** 56.

[5] B.H. Lee (1970) J. Appl. Phys. **41** 2984.

[6] International Tables of Crystallography (1992) vol **C** Kluwer Academic Publishers, Ed, A.J.C. Wilson 201-204.

[7] G.T. Brown, A.M. Kier, M.J. Gibbs, J. Giess, S.J.C. Irvine and M.G. Astles (1989) Electrochem. Soc. Symp. Proc. **89**-5 171.

[8] M. Funaki, Private Communication.

[9] H. Tatsuoka, K. Durose and M. Funaki. Inst. Phys. Conf. Ser. No.**135** Chapter 9.

[10] A.M. Keir, A. Graham, S.J. Barnett, J Giess, M.G. Astles and S.J.C. Irvine (1990) J. Crystal Growth **101** 572.

[11] J.E. Ayres, L.J. Schowatter and S.K. Ghandhi. (1992) J. Crystal Growth. **125** 329.

[12] P. Gay, P.B. Hirsch and A. Kelly (1953) Acta Metallurgica **1** 315.

[13] B.K. Tanner, T.D. Hallam, M. Funaki and A.W. Brinkman. (1993) Mat. Res. Soc. Symp. Proc. **280**.

[14] V. Leute, H.M. Schiddtke, W. Stratmann and W. Winking (1981) Physica Status Solidi **67**(a) 183.

[15] M.S. Abrahams, C.J. Buiocchi and G.H. Olsen (1975) J. Appl. Phys. **46** 4259.

[16] B.K. Tanner and D.K. Bowen. (1992) J. Crystal Growth **126** 1.

[17] A.M. Keir, S.J. Barnett, J. Giess, T.D. Walsh and M.G. Astles (1991) Appl. Surf. Sci. **50** 103.

[18] M.J. Bevan, N.J. Doyle and T.A. Temofonte. (1992) J. Appl. Phys **71**(1) 204.

[19] R.J. Koestner, H.Y. Liu and H.F. Schaake. (1989) J. Vac. Sci. Technol. **A7**(2) 517.

[20] M. Funaki and A.W. Brinkman (1994) J. Crystal Growth **139** 211.

Chapter Six

Transport Properties

6.1 Introduction

In this chapter the results of the investigation of carrier behaviour in (Hg,Mn)Te epitaxial films is reported and the dependence on crystal parameters, such as composition and thickness etc., discussed. The carrier transport properties were obtained from the analysis of temperature dependent Hall and resistivity data, as described in Chapter Four.

Although it has been widely reported that (Hg,Mn)Te possesses novel magneto-transport properties [1], it was the intention here to concentrate on studies of Hall and resistivity measurements for an investigation of fundamental carrier behaviour. Electrical stability of the layer over a period of years is vital for successful device fabrication. Spicer et al [2] suggested that cadmium was responsible for destabilising the Hg-Te bond in (Hg,Cd)Te leading to loss of mercury from the surface. Therefore it was also decided to investigate the stability of (Hg,Mn)Te epitaxial films, with a view to determining whether similar problems of instability existed for manganese.

6.2 Transport Dependence on Crystal Parameters

The majority of layers grown exhibited n-type behaviour as determined from the sign of the Hall voltage. Consequently to ensure that the contacts were ohmic, evaporated indium was chosen as the contact material. Where the (Hg,Mn)Te was p-type, gold was used. Light incident on the surface of (Hg,Mn)Te layers had the effect of reducing the resistivity, perhaps due to carrier excitation into the conduction band. However no extensive studies

were performed and all the results presented here were for dark currents.

The carrier mobility for n-type (Hg,Mn)Te increased with layer thickness up to 8μm presumably as the number of sub-grain boundaries was reduced, Fig 6.1a, and hence the quality of the crystal improved (Chapter Five). For thicknesses greater than 8μm the mobility exhibited no clear dependence on thickness. When the mobility was considered as a function of x-ray FWHM a better correlation was obtained. As discussed in Chapter Five, x-ray FWHM provides a measure of the crystalline quality of the layer and hence the consideration of the FWHM in this section may provide an insight into the relationship between the dislocation density in the layer and the electrical transport properties.

Gay et al [3] have proposed that the FWHM is proportional to the square root of the dislocation density. In that case, if the mobility were to be proportional to dislocation density, then a graph of mobility verses $FWHM^2$ should give a straight line. However, when mobility was plotted as a function of the FWHM squared, the fit to a straight line was poor and it transpires that a much better straight line is obtained when the mobility is plotted on semilogarithmic axes against the square root of FWHM.

Implicit in the Gay model is the assumption that dislocations are randomly distributed throughout the layer. This was clearly not the case here (section 5.5.1) and most of the dislocations were concentrated into sub-grain boundaries, with the implication that the FWHM was more dependent on tilts than on dislocation density. It may then be the case that the mobility is related to scattering from sub-grain boundaries and is determined by the probability per unit distance travelled of encountering a grain boundary. However, the relationship between FWHM and sub-grain size/tilt was unknown, thus this observation must remain tentative.

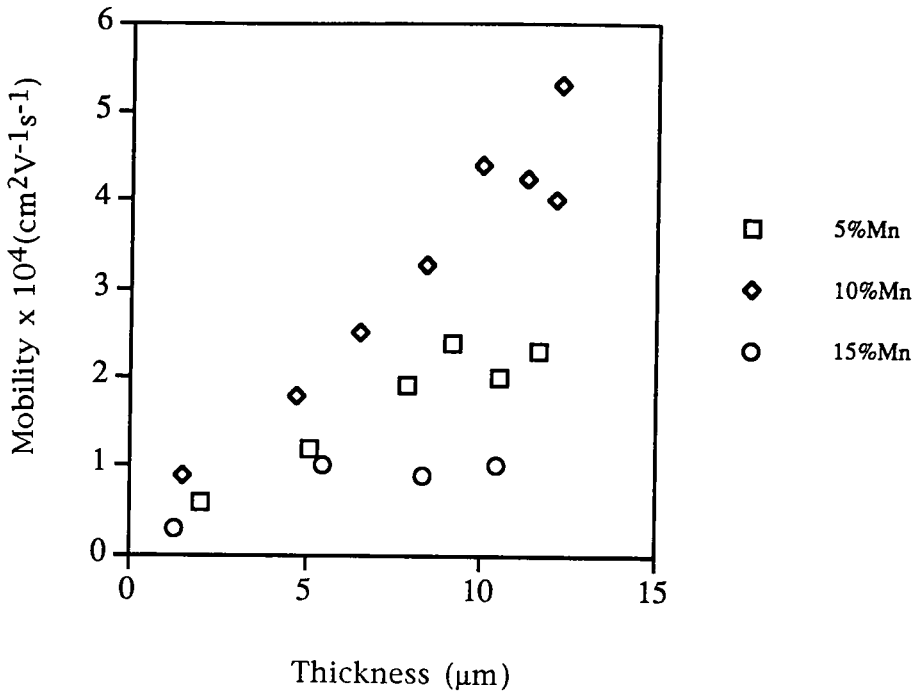

Fig 6.1a Thickness dependence of mobility for n-type (Hg,Mn)Te at room temperature.

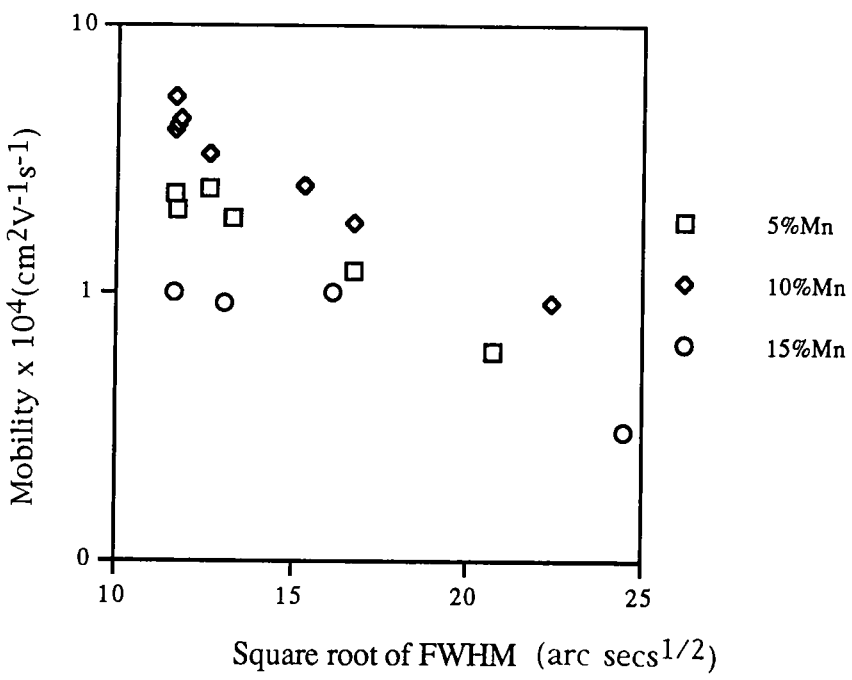

Fig 6.1b FWHM dependence of mobility for n-type (Hg,Mn)Te at room temperature.

Carrier concentration increased in a non-linear fashion with layer thickness, Fig 6.2, but tended to saturate at about 1.8 x 10^{17} cm^{-3} for layer thicknesses exceeding 10μm, suggesting a common carrier concentration for bulk crystal (Hg,Mn)Te. The carrier concentrations lie within a factor of four for a variation in manganese of 5 to 15%, when the corresponding bandgaps vary from 40meV to 350meV. Interestingly the carrier concentration converged at large thicknesses to the same value, suggesting that at room temperature the material was extrinsic with some common level of donor dopant. Nishino et al [4] reported Ga autodoping in (Hg,Cd)Te grown on GaAs by MOVPE. Using SIMS Nishino found no Ga the CdTe buffer layer and attributed the Ga incorporate in the (Hg,Cd)Te to the GaAs back surface reacting with mercury and metalorganic precursors during the growth. This reaction, it was suggested, produced volatile organic-gallium which acted as a Ga source. To investigate this Nishino coated the GaAs back with Si_3N_4 which reduced significantly the Ga incorporation in the (Hg,Cd)Te layer. The buffer layers used in this study are approximately 1μm compared to that of 8μm used by Nishino, therefore addition diffusion through the CdTe may have occurred during the (Hg,Mn)Te growth.

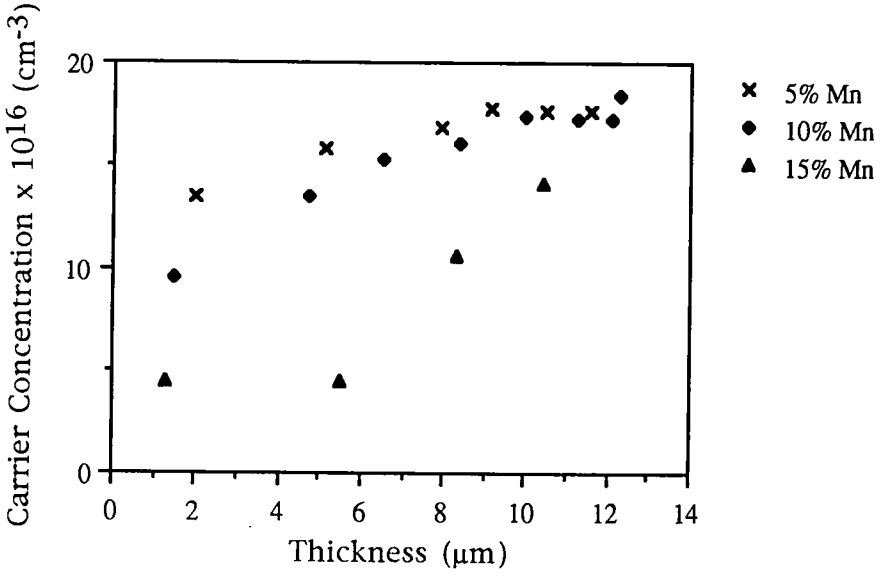

Fig 6.2 Dependence of carrier concentration on layer thickness for n-type (Hg,Mn)Te at room temperature.

The resistivity was found to reduce exponentially with increasing layer thickness up to thicknesses of 10μm as shown in Fig 6.3. The resistivity appeared to be independent of thickness for layers that were thicker than 10μm. The change in resistivity was obviously a result of the changes in carrier concentration and mobility with thickness.

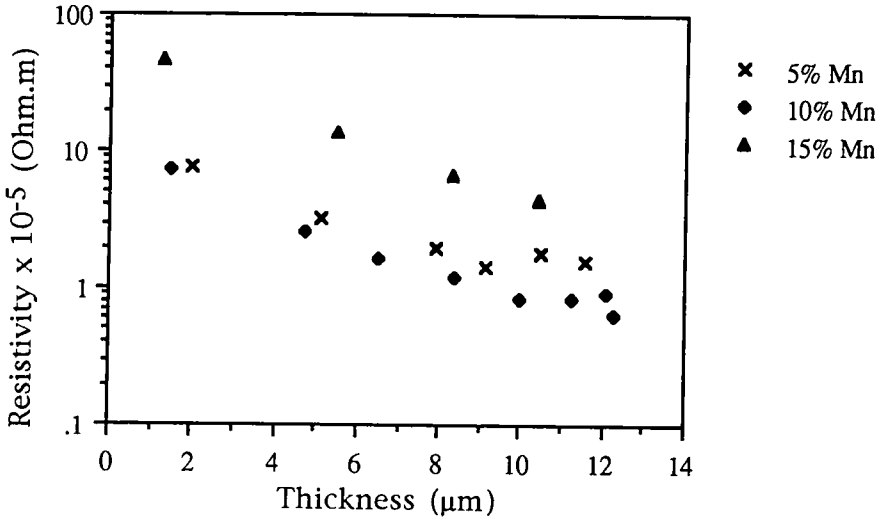

Fig 6.3 Dependence of the resistivity of n-type (Hg,Mn)Te on layer thickness at room temperature.

6.3 Temperature Dependence of Carrier Behaviour of Semimetallic (Hg,Mn)Te

6.3.1 Introduction.

The bandstructure of (Hg,Mn)Te has been studied in detail by Bastard [5] etc. For compositions below 4% at room temperature band overlap occurs between valence and conduction bands resulting in semimetallic behaviour due to the low concentration of carriers, compared to those found in metals, in the region of band overlap [5]. Hence semiconductor statistics based on a positive bandgap model cannot be applied to these

compositions and they must be considered separately. For semiconductors with a positive bandgap less than 300meV narrow gap conditions exist and at room temperatures intrinsic electrons contribute to conduction. When bandgaps greater than 300meV are considered, the probability of thermal excitation of carriers across the bandgap is very much reduced and extrinsic conduction usually dominates.

6.3.2 Semimetallic Behaviour of HgTe

At room temperature the Hall coefficient of HgTe layers was found to be in excellent agreement with electrical data obtained by Harman et al from bulk HgTe, annealed under a pressure of 14.6 atm mercury [6]. However it was a factor of three lower than the corresponding value at 77K, Fig 6.4. This suggested there was either a higher donor concentration in epitaxial HgTe or conversely a lower mercury vacancy concentration than is normally the case in as-grown bulk HgTe. For the epitaxial HgTe considered here, the Hall coefficient was increased by a factor of five on cooling from 290K to 100K (Harman et al [6] noted an increase of an order of magnitude over this range), below this temperature the Hall coefficients of both the epitaxial and bulk (Harman) HgTe levelled off to steady values. As stated earlier the temperature dependence of carriers in HgTe cannot be modelled by the usual narrow gap semiconductor statistics, due to the overlap of conduction and valence bands. Interestingly the carrier concentrations, found using equation 6.1 (Chapter Four), at 300K and 77K were found to be in excellent agreement with those calculated theoretically for HgSe (4.1 x 10^{17} cm^{-3} and 1.5 x 10^{17} cm^{-3} respectively) [7].

$$R_H = \frac{1}{n_e|q|} \qquad 6.1$$

where n_e is the free electron concentration and q is the electronic charge.

It should be noted that HgSe and HgTe have almost identical bandgaps over the temperature range considered [8].

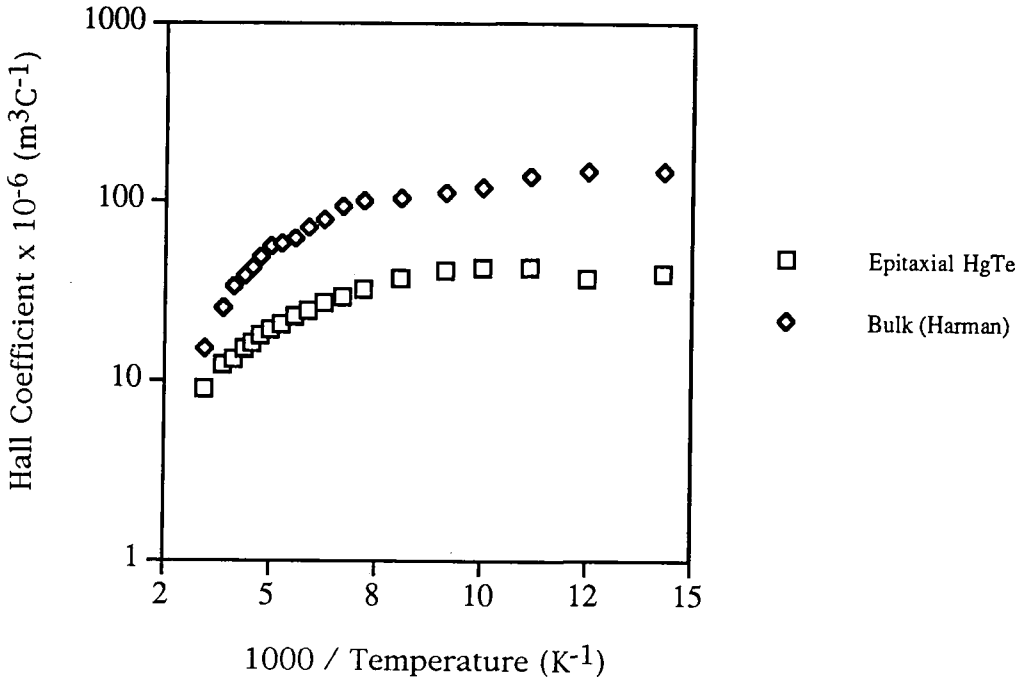

Fig 6.4 Dependence of Hall coefficient on inverse temperature for a) 6μm thick layer of n-type HgTe, b) bulk HgTe after Harman [6].

The resistivity of Durham grown epitaxial HgTe is shown in Fig 6.5 together with values obtained experimentally by Harman. This shows that the resistivity of Durham grown epitaxial HgTe was a factor of two lower than that reported for bulk HgTe by Harman at 300K and a factor of five lower at 77K, Fig 6.5. Both types of material displayed a similar dependence of resistivity on temperature with the resistivity decreasing exponentially as the temperature was raised from 77K to 200K, while for temperatures above 200K the resistivities levelled off.

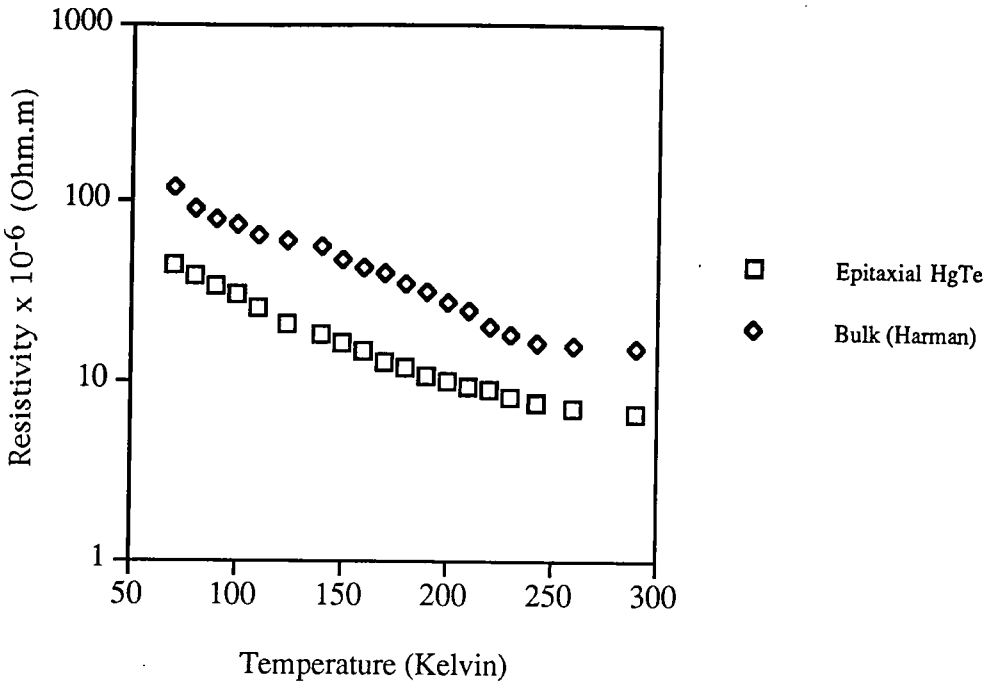

Fig 6.5 Dependence of resistivity on temperature for a) 6μm thick layer of n-type HgTe, b) bulk HgTe (Harman) [6].

The temperature dependence of the electron mobilities in epitaxial and bulk HgTe were in good agreement with each other. However epitaxial HgTe had a slightly higher mobility for temperatures in excess of 250K and fell below those quoted by Harman for temperatures below 250K, Fig 6.6. Lagrenaudie reported mobilities in the range 0.6 x 10^4 $cm^2V^{-1}s^{-1}$ to 2.5 x 10^4 $cm^2V^{-1}s^{-1}$ for epitaxial HgTe at 20°C [9].

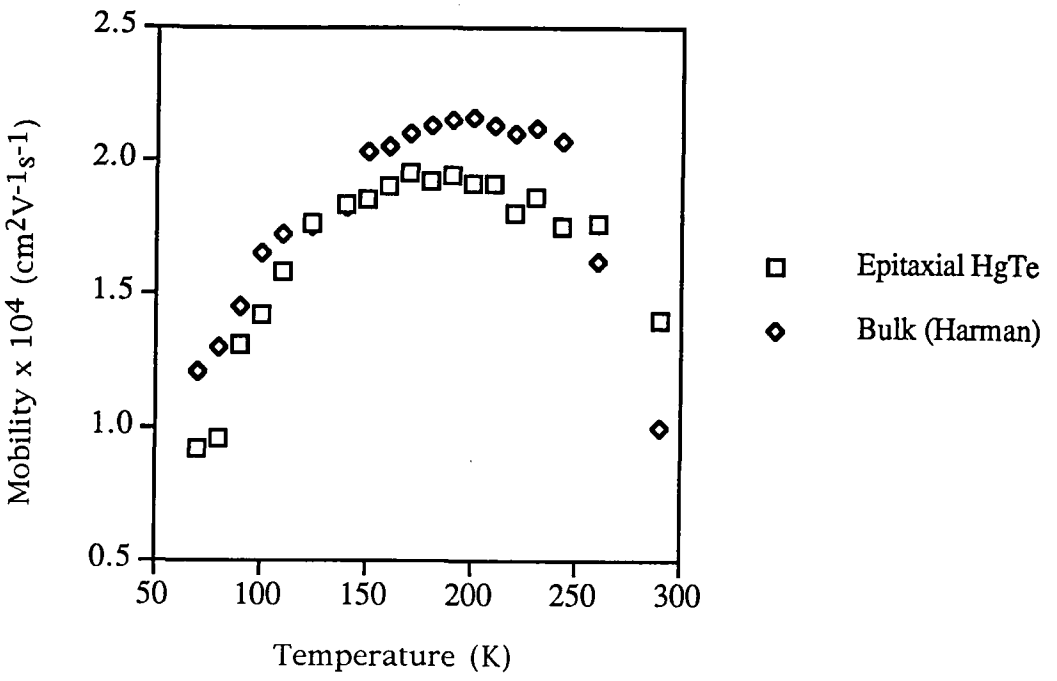

Fig 6.6 The mobility of 6μm thick epitaxial HgTe compared to that of bulk HgTe.

When mobility was plotted as a function of Temperature$^{3/2}$, the characteristics suggested ionised impurity scattering was the dominant scattering process for temperatures below 130K, Fig 6.7.

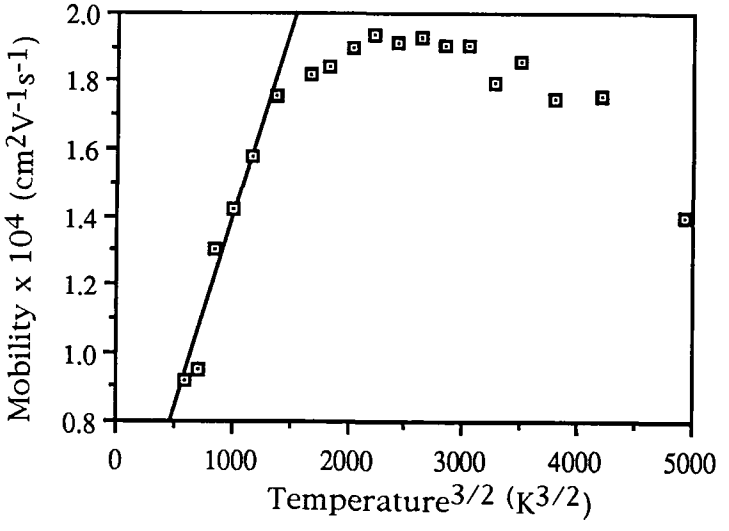

Fig 6.7 Mobility of 6μm thick epitaxial HgTe considered as a function of temperature$^{3/2}$.

At temperatures greater than ~240K the mobility was found to decrease with increasing temperature. The mobility characteristics in this range can be described by a $T^{-1/2}$ dependence (although the fit was far from conclusive due to the small number of data points above 240K) , Fig 6.8, implying that piezoelectric scattering was becoming more important.

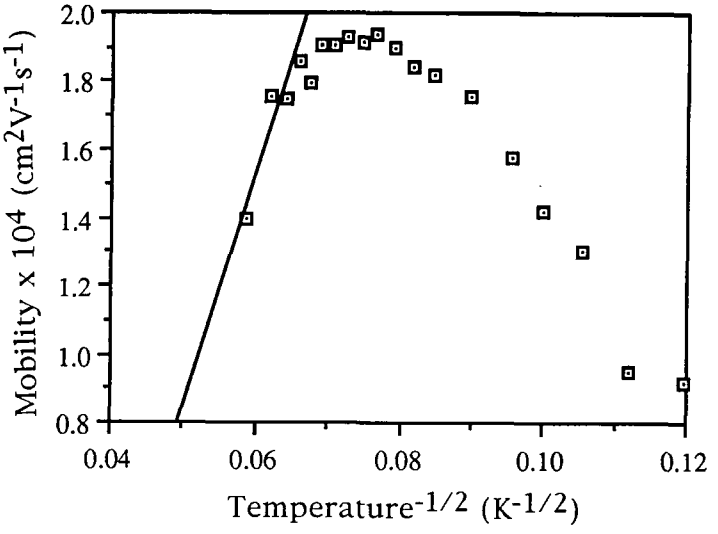

Fig 6.8 Mobility of a 6μm thick sample of epitaxial HgTe as a function of $T^{-1/2}$.

To investigate the scattering mechanisms more thoroughly detailed calculations were made assuming various scattering processes to identify those mechanisms which were operative in the present case. Calculations of mobility limited by ionised impurity scattering, μ_{II}, were made using equation 6.2 (see Chapter Four) assuming singly ionised electron donors with a concentration, N_D, of 1.5 x 10^{17} cm^{-3}, found from the extrinsic Hall data, Fig 6.4. Values for the effective mass, m^*_e, of $0.03m_0$ [10] and the static dielectric constant, ε_s, of 1.77 x 10^{-10} $F.m^{-1}$ [10] were used. The calculated μ_{II} vs T characteristics are plotted in Fig 6.9 where they are compared with the experimental points. The calculated values were observed to be in

excellent agreement with the experimental data below 120K.

$$\mu_{II} = \left[\frac{2^7(\kappa T)^3}{\pi^3 m^*}\right]^{1/2} \frac{\varepsilon'_s{}^2}{q^3 N_I}\left\{\log_e \frac{6m^*\varepsilon'_s(\kappa T)^2}{q^2h^2n'(2-n'/N)}\right\}^{-1} \qquad 6.2$$

$N_I = z_A N_D^+ + z_B N_A^-$, where z_A and z_B are the effective charges of the acceptors and donors respectively. Also n' is the number of free carriers per unit volume and $N = N_D^+ - N_A^-$.

The mobility limited by piezoelectric scattering in zinc blende structures is given in equation 6.3 [12]. The longitudinal acoustic wave velocity, C_L, and the piezoelectric electrochemical coupling constant, C, were unknown. However Harrison [12] has presented results for zinc blende (i.e cubic ZnS) and indium antimonide which suggested that the former was proportional to the square root of the longitudinal elastic constant. Hence using values of the elastic constants for HgTe and assuming the same behaviour [10], $d.C_L^2$ for HgTe was estimated to be 3.4 x 10^6 $Kg.cm^{-1}$.

$$\mu_{pie} = \frac{0.044dC_L{}^2\hbar^2\varepsilon'_s{}^2}{qC^2\left(m^*_e{}^3\kappa T\right)^{1/2}} \qquad 6.3$$

When the calculated values of mobility limited by piezoelectric, μ_{pie}, scattering were plotted against temperature, Fig 6.9, the calculated values exceeded the experimentally measured mobilities by a factor of four at room temperature. This suggested that there was at least a third scattering mechanism present at high temperatures.

Scattering by optical phonons is commonly found in II-VI semiconductors

and was probably occurring in HgTe. The mobility limited by polar optic phonon scattering is given by equation 6.4.

$$\mu_{opt} = \frac{8|q|}{6\alpha\omega_1 m^*_e \sqrt{\pi Z}} \psi(Z)\left(e^z - 1\right) \qquad 6.4$$

where ω_1 is the optical phonon frequency, q is the electronic charge, Z is the ratio of the Debye temperature (θ_D) to the lattice temperature, $\psi(Z)$ is a function that varies slowly between 0.6 and 1 over the temperature range 77K to 300K, and α is the coupling constant given by equation 6.5.

$$\alpha = \frac{q^2 m^*_e}{2\hbar^2\omega_1}\left[\frac{\varepsilon'_s - \varepsilon_\infty}{\varepsilon'_s \varepsilon_\infty}\right] \qquad 6.5$$

The terms ε'_s and ε_∞ are the static and optical dielectric constants respectively.

The optical phonon frequency was calculated from the Debye temperature, which for HgTe is 199K [5], using equation 6.6.

$$\theta_D = \frac{h\omega_1}{\kappa} \qquad 6.6$$

which gave a value of 2.6 x 10^{13} Hz. The coupling constant, α, was calculated to be 0.05 using values of ε'_s and ε_∞ of 1.77 x 10^{-10} Fm^{-1} and 1.24 x 10^{-10} Fm^{-1} respectively. This is a relatively low value, but is comparable to that of GaAs, 0.06. These values, together with $m^*_e = 0.03m_0$ were used in equation 6.4 to calculate μ_{opt} as a function of temperature. These are also plotted in Fig 6.9, and are found to be lower than μ_{pie} but still larger than the experimental values.

In situations where several scattering mechanisms are operative, the total mobility may be calculated from the individual mobilities using Mathiessen's rule, equation 6.7.

$$\frac{1}{\mu_{Total}} = \frac{1}{\mu_{opt}} + \frac{1}{\mu_{pie}} + \frac{1}{\mu_{II}} + \ldots\ldots \qquad 6.7.$$

The combined mobility, μ_{Total}, is compared with the experimental values over the measured temperature range in Fig 6.10. This shows excellent agreement, particularly given that the C_L and C were not known for HgTe. It therefore seems probable that the electron transport was limited by the combined effect of ionised impurity, piezoelectric and polar optic phonon scattering, and other scattering processes do not seem to be important.

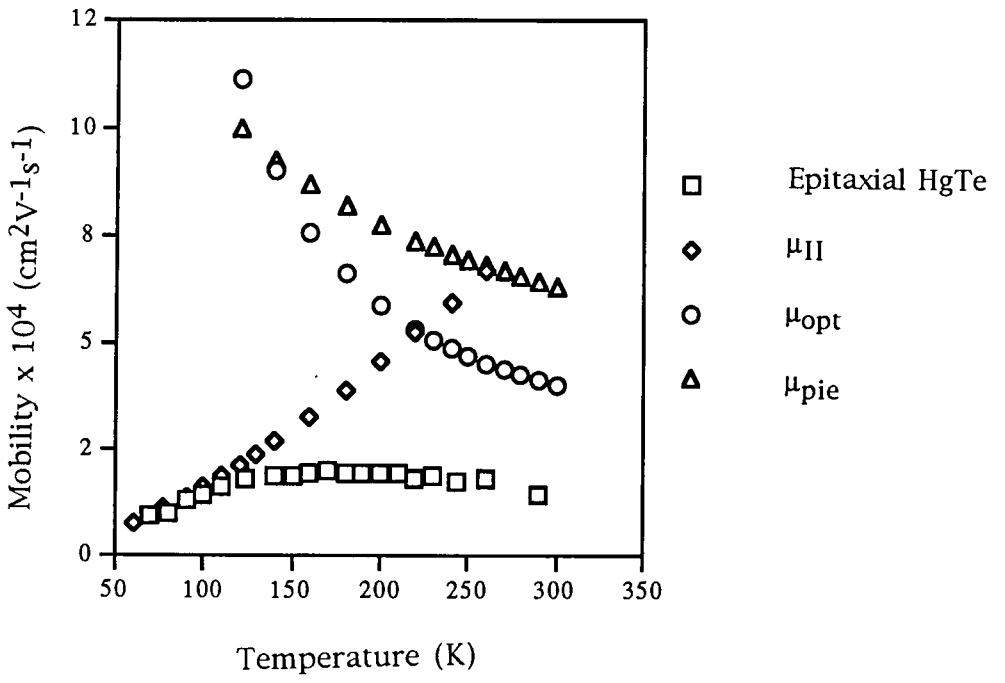

Fig 6.9 Scattering mechanism in n-type HgTe.

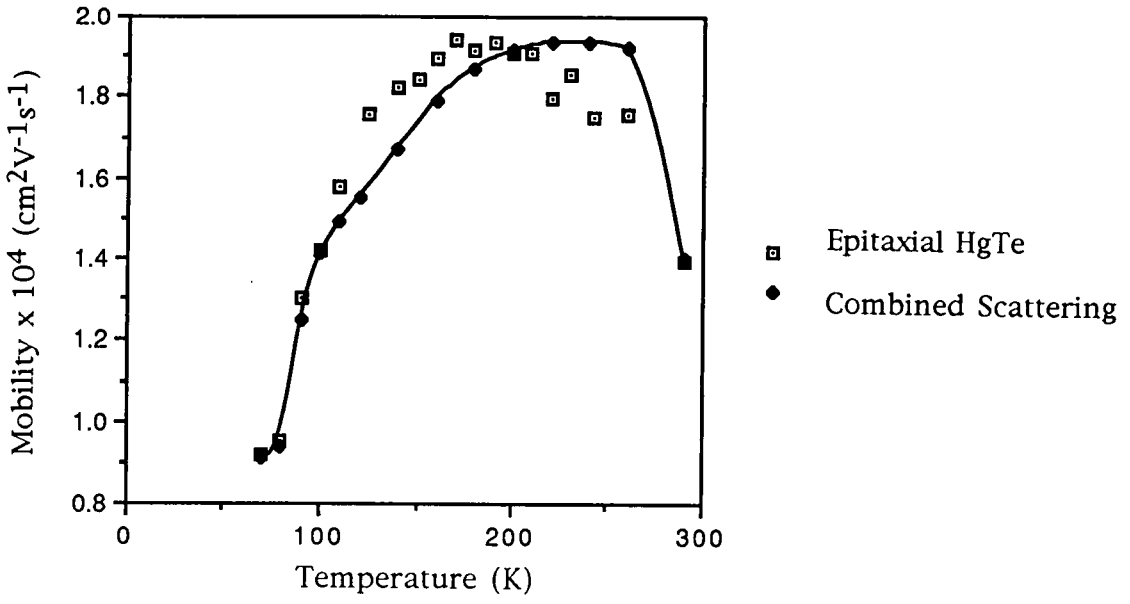

Fig 6.10 Combined effects of ionised impurity, piezoelectric and optical scattering mechanisms.

6.4 Temperature Dependence of Semiconducting n-type (Hg,Mn)Te

6.4.1 Semiconducting Behaviour

The majority of as-grown layers exhibited n-type conductivity, as seen by the direction of carrier deflection in an applied magnetic field. Layers containing 5% manganese had carrier concentrations and mobilities very similar to those reported for films grown by MBE [13] (2.8 x 10^{16} cm^{-3} and 4.8 x 10^4 $cm^2V^{-1}s^{-1}$ for a 2.5μm 7% manganese layer), Figs 6.1 and 6.2. However MOVPE epitaxial films containing 10% manganese were found to have larger carrier concentrations and mobilities than values reported for MBE grown layers [13] (1.1 x 10^{17} cm^{-3} and 4.3 x 10^4 $cm^2V^{-1}s^{-1}$ respectively compared to 1.1 x 10^{16} cm^{-3} and 1.2 10^4 $cm^2V^{-1}s^{-1}$ obtained for MBE).

6.4.2 Hall Data

The intrinsic electron concentration, n_i, of (Hg,Mn)Te has been measured by Rogalski [14] for $0<x<0.2$ and temperatures between 77K and 350K. The results were summarised into the compact form of equation 6.8.

$$n_i = \left(4.615-1.59x+0.00264T-0.017xT+34.15x^2\right)10^{14} \\ X\ Eg^{3/4}T^{3/2}\exp\left(\frac{-5802Eg}{T}\right) \qquad 6.8$$

where n_i is in cm^{-3}, T is the absolute temperature and Eg is the bandgap in eV.

This equation assumes a parabolic valence band with an effective mass for holes of $0.5m_0$ and that the influence of the light-hole valence band can be neglected. The temperature dependence of the bandgap for (Hg,Mn)Te has been discussed in Chapter One.

Once the intrinsic carrier concentration, n_i, has been calculated the total free electron concentration, n, can be obtained using the concentration of ionised donors found from the extrinsic Hall data, N_D^+, equation 6.9 [Chapter Four].

$$n \approx \frac{N_D^+ + \sqrt{\left(N_D^+\right)^2 + 4n_i^2}}{2} \qquad 6.9$$

For single carrier conduction the Hall coefficient data may be modelled as a function of temperature using equations 6.8, 6.9 and 6.10 [Chapter Four].

$$R_H = \frac{-r_H}{nq} \qquad 6.10$$

where R_H is the Hall coefficient, q is the electronic charge and r_H is the scattering factor, which has been taken as unity.

The calculated Hall coefficient values were consistently higher than the experimentally observed values, which was probably due to the surface (the area measured using EDAX) being more manganese rich than the underlying bulk material. This was possibly a result of mercury loss from the surface during the cooling down after growth.

Fig 6.11 shows experimental and calculated values of Hall data for a layer of $Hg_{0.95}Mn_{0.05}Te$ over the temperature range 77K to 300K. Calculated values were obtained using a donor concentration of 3.3 x 10^{16} cm^{-3} found from the extrinsic Hall data (T<77K). The composition (5%) was measured at the surface using EDAX. The results in the intrinsic region indicate that the bulk material contained less than 5% manganese since the onset of the intrinsic region occurred at lower temperatures.

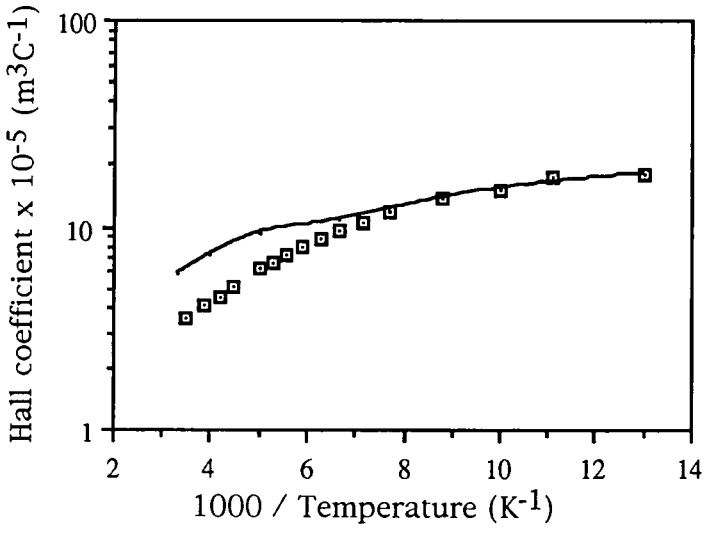

Fig 6.11 Dependence of Hall coefficient on inverse temperature for 10μm thick layer of n-type $Hg_{0.95}Mn_{0.05}Te$.

A similar analysis for a layer with a nominal (EDAX) composition of $Hg_{0.9}Mn_{0.1}Te$ is shown in Fig 6.12 as for the 5% manganese layer, the actual manganese content would appear to have been less than the value determined by EDAX. When a value of x=0.07 was used in the calculation instead, much better agreement was obtained between the measured and calculated values, In both instances a donor concentration of $1.2 \times 10^{17} cm^{-3}$ was assumed from the extrinsic region.

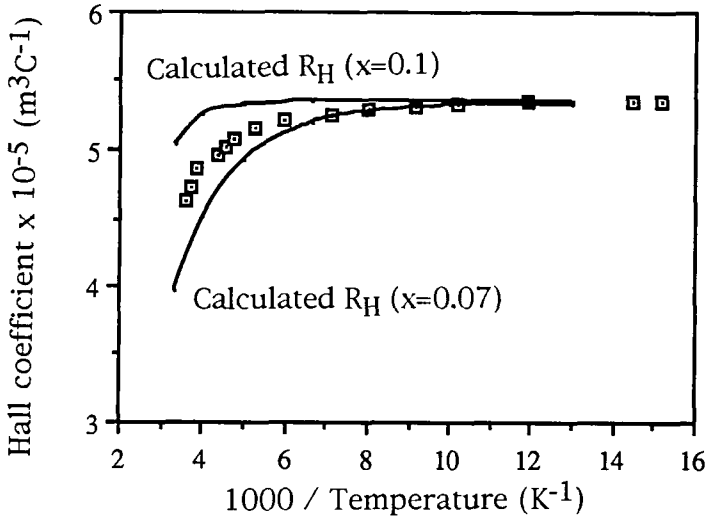

Fig 6.12 Dependence of Hall coefficient on inverse temperature for 5μm thick layer of n-type $Hg_{0.9}Mn_{0.1}Te$.

For the 15% manganese layers a "hump" was present in the Hall coefficient data at a temperature of about 150K. A possible explanation for this would be the presence of compensating acceptor levels deeper within the bandgap than the donor levels. The net density in the extrinsic region would then be $(N_D^+ - N_A^-)$. If the acceptor levels were not fully ionised at the temperatures in question, then their effect would be to reduce progressively $(N_D^+ - N_A^-)$, and hence n, as the temperature was increased until intrinsic conduction became significant. The best fit to the Hall data

without inclusion of any compensating acceptors, i.e. the "hump", is shown in Fig 6.13 and was obtained using the intrinsic calculation for $Hg_{0.9}Mn_{0.1}Te$ although the EDAX indicated a composition of ~15% manganese.

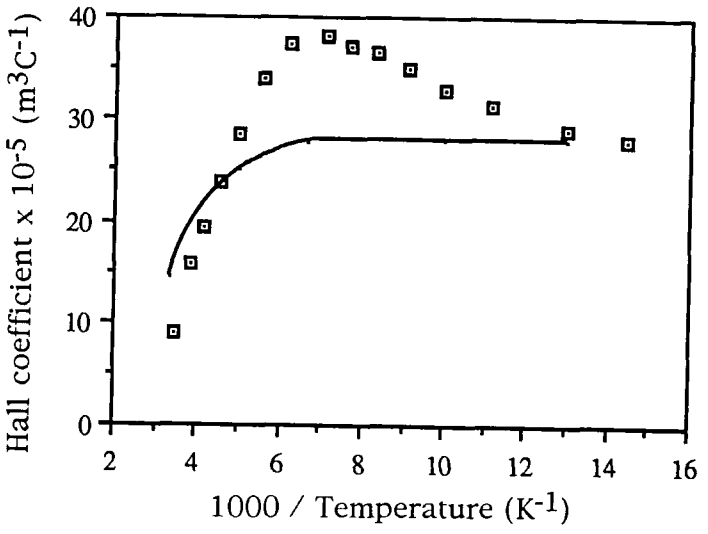

Fig 6.13 Dependence of Hall coefficient on inverse temperature for 5.5μm thick layer of n-type $Hg_{0.85}Mn_{0.15}Te$.

If acceptors are assumed to be present, then the difference between the combined value of the intrinsic electrons and the concentration of donors (i.e. the best fit line) and that of the experimentally measured carrier concentrations, for $Hg_{0.85}Mn_{0.15}Te$, may be considered to be equal to the density of ionised acceptor levels. The ionised acceptor density, in such a situation would be given by equation 6.10 [Chapter Four], therefore, a log plot of the difference (i.e acceptor concentration) multiplied by $T^{-3/2}$ as a function of inverse temperature, should give a straight line with slope given by the activation energy (equation 6.10) for the acceptors. This is plotted in Fig 6.14 for temperatures between 90K and 140K and does not show a very good fit, particularly at the higher temperatures. The "best fit" line would give a value for the activation energy of ~4meV.

$$n = 2\left[\frac{2\pi.m^*_e KT}{h^3}\right]^{3/2} \exp\left(\frac{-(E_a - E_v)}{KT}\right) \qquad 6.11$$

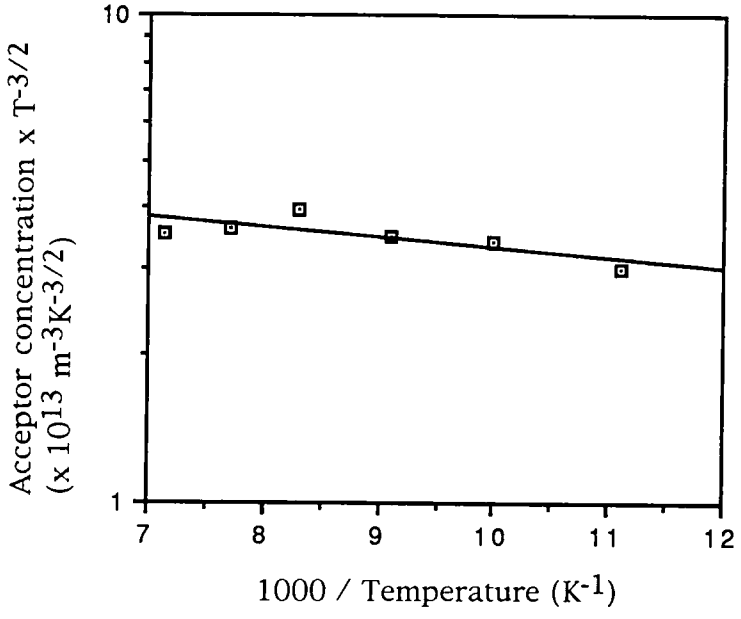

Fig 6.14 Determination of the activation energy of acceptor levels in $Hg_{0.85}Mn_{0.15}Te$.

It was possible to measure the transport properties of selected (Hg,Mn)Te layers at temperatures below 77K. Fig 6.15 shows the variation of R_H for a layer containing 15% manganese (as determined by EDAX). It shows a reduction in carrier concentration with reducing temperature as the donor levels are progressively frozen out. Analysis of the log carrier concentration-inverse temperature plot gives an activation energy of the order of 1meV for the donors. It is worth noting that this is considerably smaller than the postulated acceptor level energy (4meV).

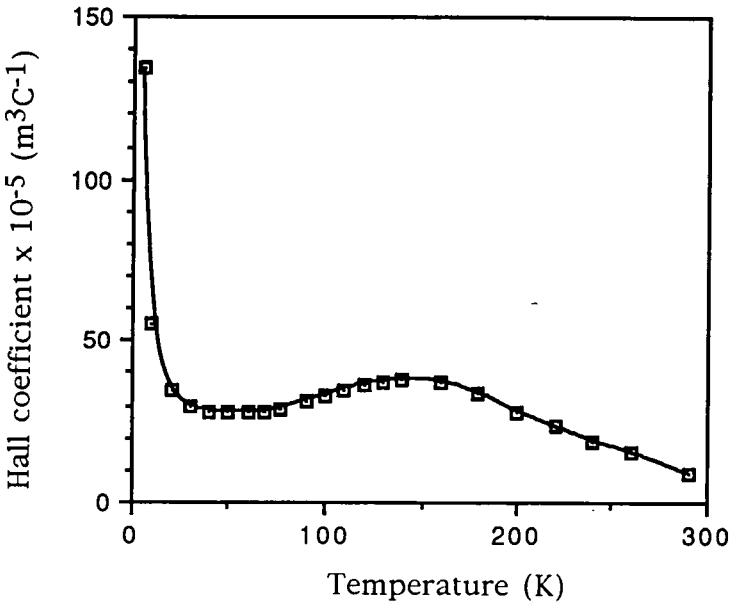

Fig 6.15 Freeze out of electrons was present at low temperatures for n-type $Hg_{0.85}Mn_{0.15}Te$.

Similar analysis of the carrier concentration as a function of temperature, in the extrinsic region, for the 5% and 10% manganese layers give donor activation energies of 0.8meV and 0.3meV respectively. A summary of values obtained in this section has been presented in table 6.1.

The bandgap energy can be determined from the temperature dependence of the Hall coefficient in the intrinsic region, equations 6.11 and 6.12 [Chapter Four]. A graph of $\ln(n_i T^{-3/2})$ is shown in Fig 6.16 as a typical example. According to equation 6.12, the slope in the intrinsic (high temperature) region is $(E_g/2\kappa)$.

$$n_i = \sqrt{N_c N_v}\exp\left(\frac{E_v - E_c}{2\kappa T}\right) \qquad 6.12$$

$$R_H = \frac{1}{n_i q} \qquad 6.13$$

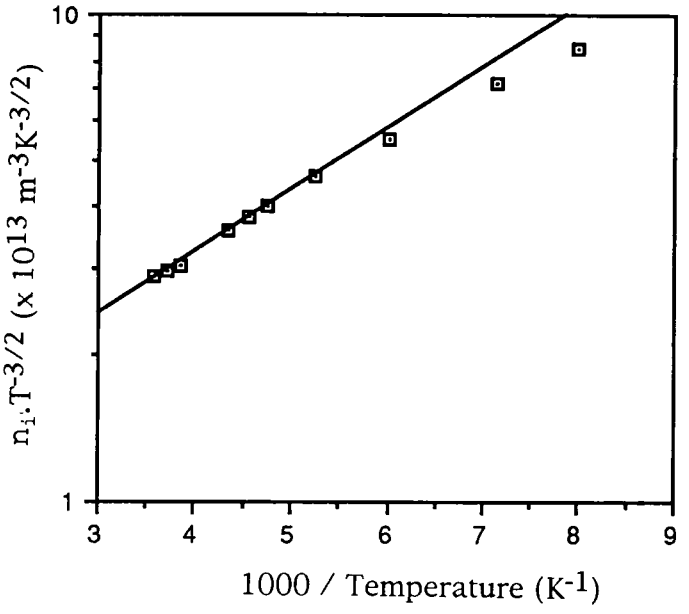

Fig 6.16 Determination of the bandgap of $Hg_{0.9}Mn_{0.1}Te$.

Some typical values of bandgap and carrier data for several layers of various thicknesses and compositions are given in Table 6.1. It was observed that the values of the bandgap were lower than expected for the surface composition but corresponded well to the underlying composition, as indicated by the Hall data fitting (i.e using equations 6.8 to 6.10). As noted before, thickness had a marked effect on all the parameters measured, and in the majority of cases decreasing the thickness reduced the value of the parameter. The highest values of donor concentration were found in thick layers containing ~10% manganese and the lowest donor activation energies were also found at this composition, although the latter appeared to be independent of the thickness for 10% manganese.

Mn (%) by EDAX	5		10		15	
Mn (%) by Hall Data	< 5		~ 8		~ 10	
Layer thickness (μm)	2	6	2	5	2	5
Donor concentration x 10^{16} (cm^{-3})	2.8	3.3	7.8	11.7	2.1	2.2
Donor activation energy (meV)	0.5	0.8	0.3	0.3	1.6	1
Bandgap (meV)	20	36	45	55	160	210

Table 6.1. Summary of bandgap and carrier behaviour with thickness and composition.

6.4.3 Scattering Mechanisms and Mobility in n-type Narrow Gap (Hg,Mn)Te.

A similar approach to that performed on the HgTe layer was taken in modelling the scattering processes. No values of Debye temperature, dielectric constants, longitudinal wave velocity or electrochemical coupling constants for cubic MnTe were known, so the values used for HgTe were adopted. Variations in electron effective mass with (Hg,Mn)Te composition were discussed in Chapter One and the variation in density was discussed in Chapter Five.

The mobility-temperature characteristics for a layer of $Hg_{0.95}Mn_{0.05}Te$ are shown in Fig 6.17. Calculated characteristics for optical phonon scattering and piezoelectric scattering are also shown for comparison. The graph clearly shows that the best agreement was obtained for $Hg_{0.95}Mn_{0.05}Te$ using a combination of piezoelectric and optical-phonon scattering mechanisms. However at around 70K the mobility appeared to level off

perhaps indicating the start of ionised impurity scattering.

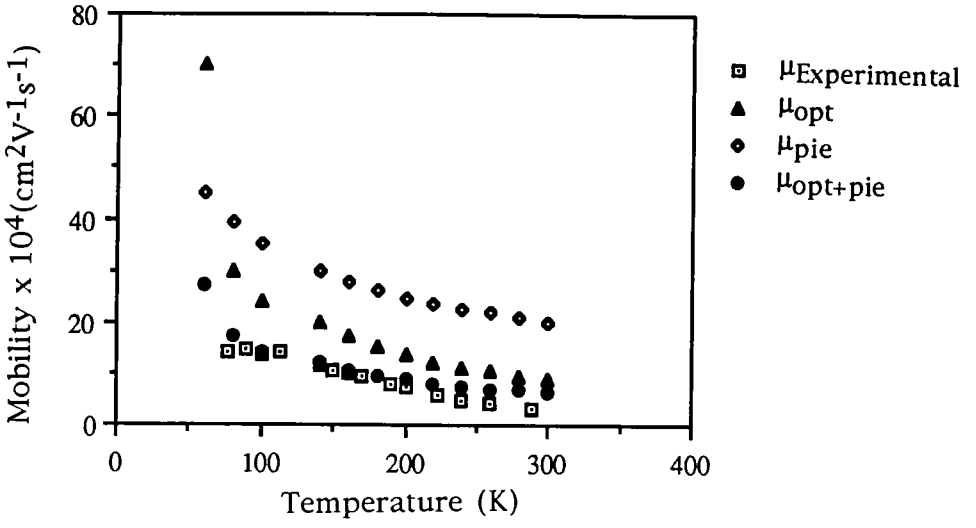

Fig 6.17 Scattering mechanisms in $Hg_{0.95}Mn_{0.05}Te$.

In the case of $Hg_{0.9}Mn_{0.1}Te$ the combination of piezoelectric and optical scattering gave a mobility which was two to three times that observed experimentally, Fig 6.18. Alloy scattering was then investigated since the introduction of manganese ions, above a certain concentration, into the HgTe lattice may have caused a deviation from the periodicity of the lattice. This would cause scattering of free carriers, as discussed in Chapter Four, and mathematically is represented as equation 6.14 [15].

$$\mu_{all} = \frac{4qN_{all}h^4\sqrt{\varepsilon}}{3\sqrt{2}\, m^*_e \pi x(1-x)(\Delta E)^2 (m^*_e)^{3/2} (\kappa T)^{1/2}} \qquad 6.14$$

where N_{all} is the density of alloy sites, ΔE is the depth of the scattering well and x is the fraction of manganese ions in the lattice.

The mobility defined by alloy scattering was taken to be the difference between the reciprocal values of mobility calculated using piezoelectric and optical-phonon scattering scattering and that observed

experimentally. When ΔE was calculated at 77K and 300K it was found to be 0.65eV±0.1eV. Harrison et al [12] interpreted ΔE as the difference in the electron affinities of the binary compounds constituting the ternary alloy. The electron affinity of HgTe and cubic MnTe was not known, but the value of ΔE obtained was slightly less than that of (Ga,In)As, which is reported to be 0.83eV.

However, the combination of all three scattering mechanisms results in an ill-fitting curve. Consideration of Fig 6.19 would suggest that perhaps the piezoelectric scattering may be more important than optical-phonon scattering, since the experimental data has a temperature dependence more similar to that of piezoelectric scattering.

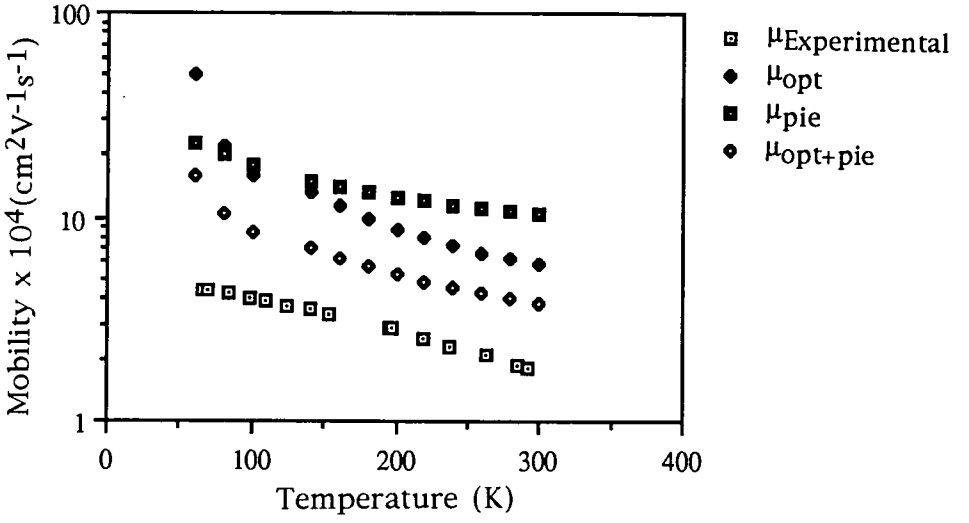

Fig 6.18 Scattering mechanisms in a 5μm thick layer of n-type $Hg_{0.9}Mn_{0.1}Te$.

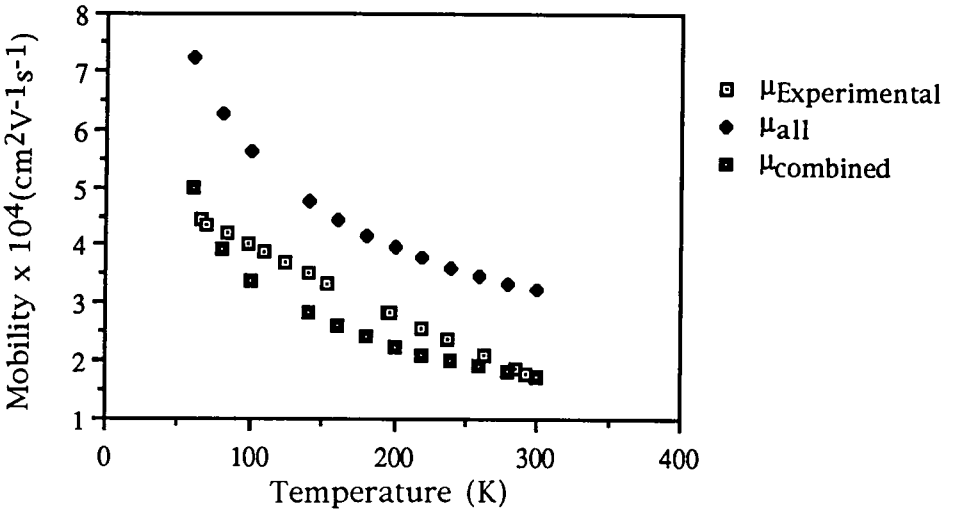

Fig 6.19 Scattering mechanisms, including alloy scattering, in a 5μm thick layer of n-type $Hg_{0.9}Mn_{0.1}Te$.

The mobility - temperature characteristics for a $Hg_{0.85}Mn_{0.15}Te$ layer are shown in Fig 6.20 and clearly shows the influence of ionised impurity scattering at T<140K. For analysis of ionised impurity scattering in $Hg_{0.85}Mn_{0.15}Te$ a donor concentration of 2.2 x 10^{16} cm^{-3} was obtained from the extrinsic Hall data. Fig 6.20 shows the modelling of the mobility data for a 15% manganese layer in terms of optical, piezoelectric and ionised impurity scattering and shows the total effect of these mechanisms. As for the 10% manganese layer the calculated mobility is higher (in this case by a factor of three). So an attempt was again made to introduce alloy scattering into the calculation, Fig 6.21.

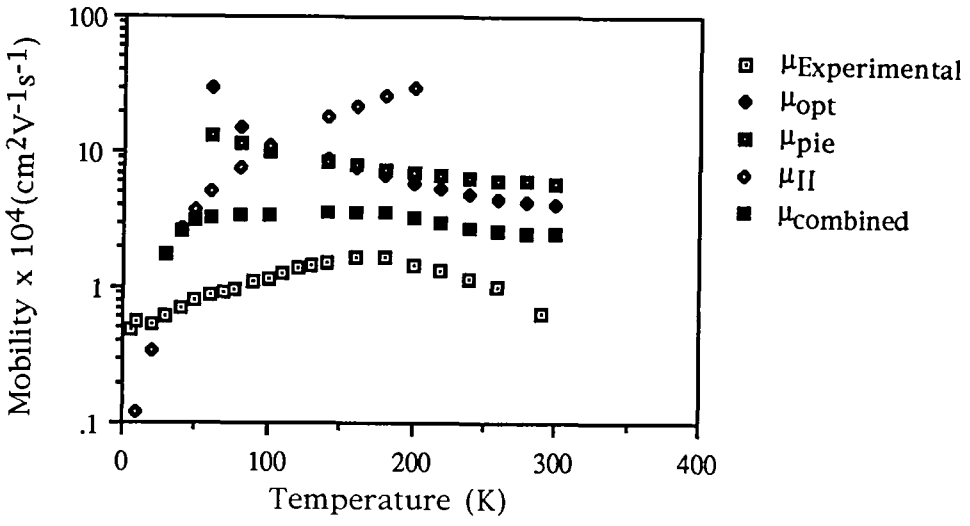

Fig 6.20 Scattering mechanisms in a 5.5μm thick layer of n-type $Hg_{0.85}Mn_{0.15}Te$.

From Fig 6.21 it was observed that the total of the four scattering mechanisms fits the mobility data in the region 150K to 250K but deviates severely below 150K, indicating that the ionised impurity scattering in reality was much greater than that modelled.

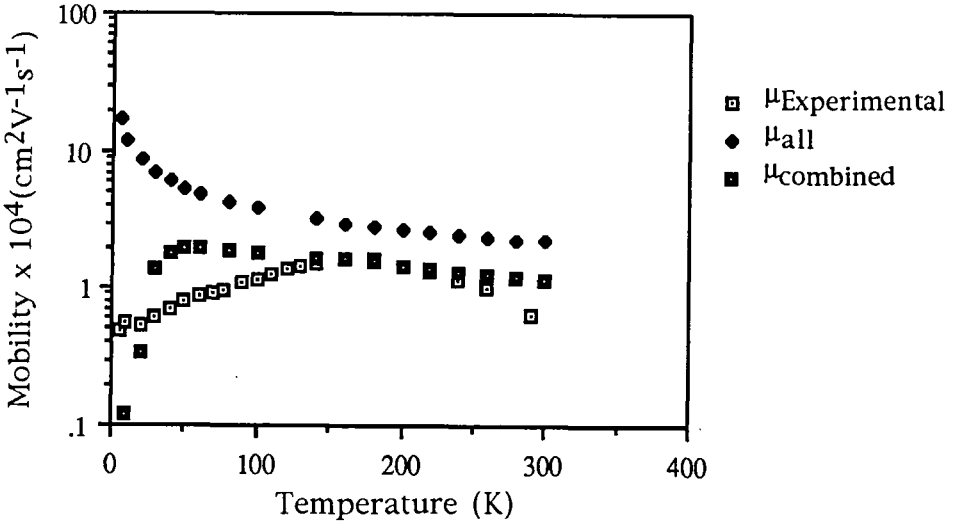

Fig 6.21 Scattering mechanisms including alloy scattering in $Hg_{0.85}Mn_{0.15}Te$.

6.4.4 Temperature Dependence of Resistivity for n-type Narrow Gap (Hg,Mn)Te

From the semiconductor statistics discussed in Chapter Four the resistivity of a semiconductor in a single carrier conduction regime, as for the case of the n-type (Hg,Mn)Te layers considered here, is such given by equation 4.28.

For $Hg_{0.95}Mn_{0.05}Te$ the resistivity below 180K was dominated by the reduction in intrinsic electrons. Above 180K the increase in resistivity was due to the mobility being limited by piezoelectric and optical phonon scattering, Fig 6.22.

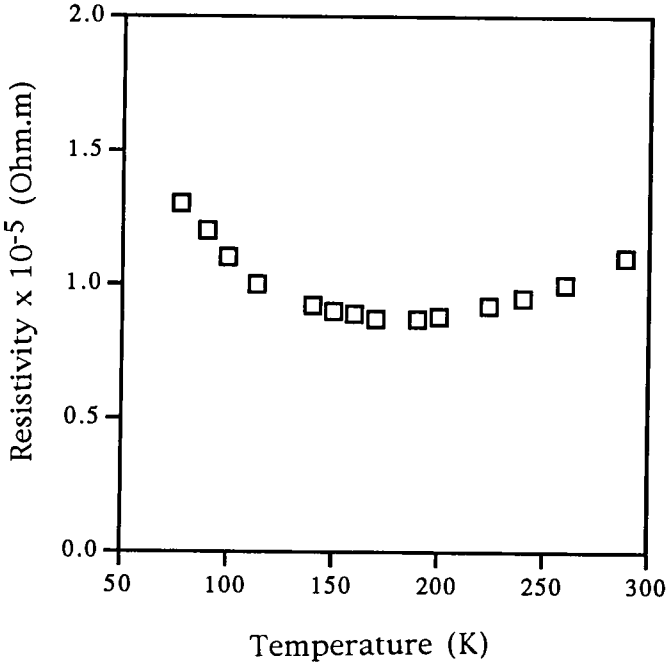

Fig 6.22 Dependence of resistivity on temperature for 10μm thick layer of n-type $Hg_{0.95}Mn_{0.05}Te$.

For $Hg_{0.9}Mn_{0.1}Te$ layers the resistivity was predominantly controlled by the piezoelectric, optical and alloy scattering mechanisms, Fig 6.23.

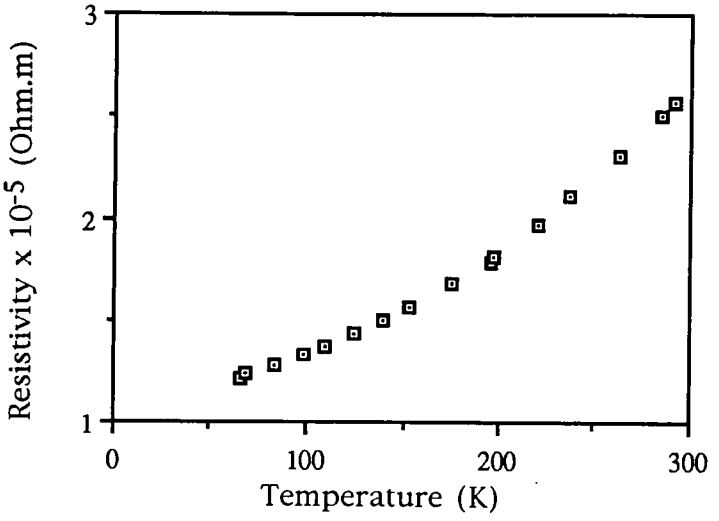

Fig 6.23 Temperature dependence of resistivity for 5μm thick layer of n-type $Hg_{0.9}Mn_{0.1}Te$.

The resistivity of some samples were measured down to 4.2K. Fig 6.24 shows the resistivity - temperature behaviour of a $Hg_{0.85}Mn_{0.15}Te$ layer. Carrier freeze out was observed at very low temperatures with a corresponding increase in the resistivity of two orders of magnitude. From 4.2K up to 77K the ionisation of donor levels controlled the resistivity and above this temperature the dominant factor was the increase in the electron concentration but this was limited by the reduction in mobility due to lattice scattering mechanisms.

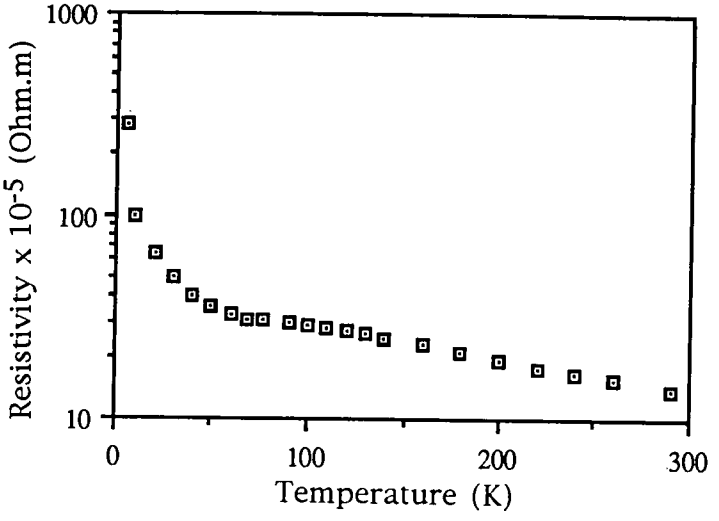

Fig 6.24 Dependence of resistivity on temperature for a 5.5μm thick layer of n-type $Hg_{0.85}Mn_{0.15}Te$.

6.5 Transport Properties of p-type Narrow Gap (Hg,Mn)Te

The majority of layers grown exhibited n-type behaviour, however p-type behaviour was found in some layers where the mercury pressure was lower than usual during growth due to the mercury boat being heated to only 180°C. One such layer of thickness 2μm and containing 10% manganese was found to have p-type conduction over the entire temperature range (4K to 300K) studied, Fig 6.25.

Below 100K this sample of $Hg_{0.9}Mn_{0.1}Te$ exhibited extrinsic p-type behaviour, and above this the increasing density of intrinsic electrons lowered the Hall coefficient towards the p to n transition. The extrinsic hole concentration, p, was found from the extrinsic Hall data to be $2.3 \times 10^{18} cm^{-3}$ and is related to the intrinsic electron density, n_i, [14] by equation 6.15 (Chapter Four).

$$n.p = n_i^2 \qquad 6.15$$

Once the electron and hole concentrations were known, assumed values for the mobilities of electrons and holes were taken from Figs 6.18 and 6.26 respectively for $Hg_{0.9}Mn_{0.1}Te$. Equation 6.16 was used to model the Hall coefficient for two carrier conduction and the resulting fit for $Hg_{0.9}Mn_{0.1}Te$ is shown in Fig 6.25. The carrier concentration was found to be slightly lower than that predicted by the model however this was easily accounted for in terms of the error in the value of composition and carrier mobilities.

$$R_H = \frac{p|q|\mu_h^2 - n|q|\mu_e^2}{\left(p|q|\mu_h + n|q|\mu_e\right)^2} \qquad 6.16$$

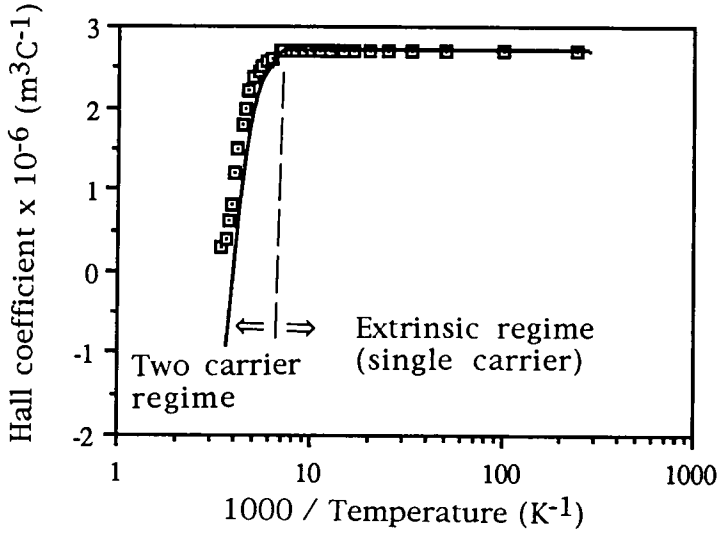

Fig 6.25 Dependence of Hall coefficient on inverse temperature for 5μm thick layer of p-type $Hg_{0.9}Mn_{0.1}Te$.

This analysis gave a value of the electron to hole mobility for p-type $Hg_{0.9}Mn_{0.1}Te$ of between 85 and 95 over the range 77K to 290K. Reported

values for the electron to hole mobility ratio in HgTe vary from 70 [16] to 100 [6].

The hole mobility - temperature characteristic was calculated from the Hall coefficient and resistivity data assuming (i) that in the extrinsic region (T<120K) the behaviour was effectively single carrier and (ii) a value of 90 for the electron mobility to hole mobility in the transition two carrier region (T>120K). The resulting characteristic (Fig 6.26) shows that at low temperature the hole mobility increased slowly with increasing temperature until a temperature of ~80K, between temperatures of ~80K and 200K the mobility decreased in an approximately exponential manner with a slope of 1.1×10^{-4} $cm^2V^{-1}s^{-1}T^{-1}$ while above ~200K the slope increased to 3.5×10^{-4} $cm^2V^{-1}s^{-1}T^{-1}$.

At temperatures below about 200K, the mobility was fairly well described by a combination of ionised impurity, polar optic and alloy scattering processes, where a value of $2.3 \times 10^{18} cm^{-3}$ was assumed for the ionised impurity centre density, based on the Hall coefficient data in the extrinsic region. The calculated mobility limited by each of these processes alone and in combination (Mathiessen's rule) are also shown in Fig 6.26. As indicated above, while these scattering processes could account for the shape of the characteristics at temperatures below 200K they over estimated the mobility at higher temperatures, where clearly some other mechanism became important. The approximately exponential dependence on temperature may indicate a second polar optic phonon mode, but this must remain speculative.

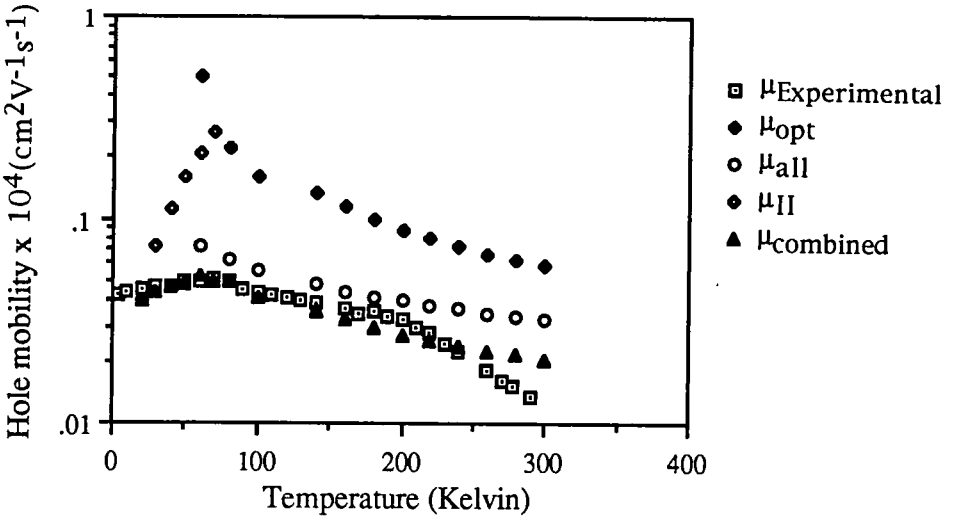

Fig 6.26 Scattering mechanisms in a 5μm thick layer of p-type $Hg_{0.9}Mn_{0.1}Te$.

6.6 Magnetoresistance in n-type (Hg,Mn)Te

Magnetoresistivity was measured in the van der Pauw configuration with a variable magnetic field of 0 to 0.38T applied perpendicular to the layer surface in both directions. A positive notation was given to magnetic fields directed through the samples from the layer side and a negative notation to those from the substrate side.

The change in the resistivity in response to an applied magnetic field was strongly dependent on the composition of the layer. HgTe layers possessed a resistivity which increased in a linear manner with an increasing magnetic field and with only a slight asymmetry with respect to the direction of the applied magnetic field, Fig 6.27. An offset of the order of 0.04 Tesla of the minimum resistivity with respect to zero magnetic field was present in all the HgTe layers examined. The magnetoresistance observed for Durham grown HgTe was larger than that reported for epitaxial HgTe by Aven et al [17]. Magnetoresistance results from the imbalance of the Lorentz force and the Hall fields acting on the carriers,

since only the Lorentz force is dependent on the carrier velocity whereas the Hall field is not. A well established model [17] for a single carrier type and spherical energy surfaces gives:

$$\frac{\Delta\rho}{\rho_o} = M\mu_H{}^2B^2 \qquad 6.17$$

where ρ_o is the zero field resistivity, $\Delta\rho$ is the change in resistivity, M is a magnetoresistance coefficient which is dependent on the scattering mechanism and B is the magnetic field strength.

Neither the results reported by Aven [17] or the Durham grown (Hg,Mn)Te exhibited a B^2 dependence perhaps due to multicarrier conduction or non-spherical energy surfaces.

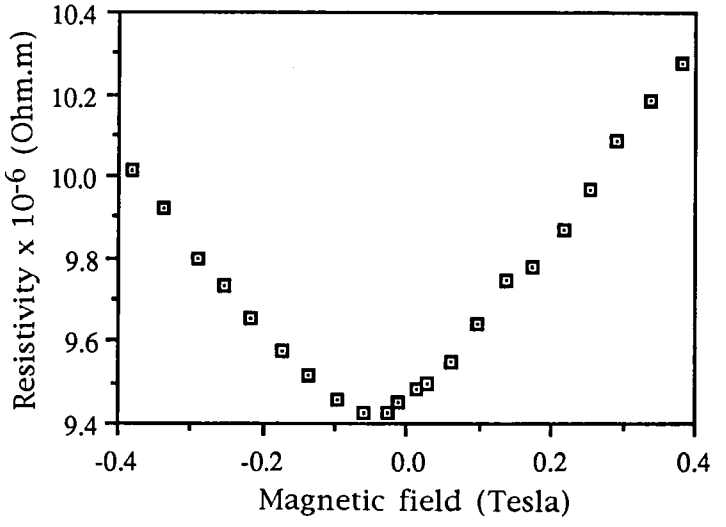

Fig 6.27 Magnetoresistivity characteristic for a 5μm thick layer of HgTe.

As the manganese content was increased to 10% the response became increasingly asymmetrical about the zero field value and the offset of the minimum resistivity from the zero field, increased, Figs 6.28 and 6.29.

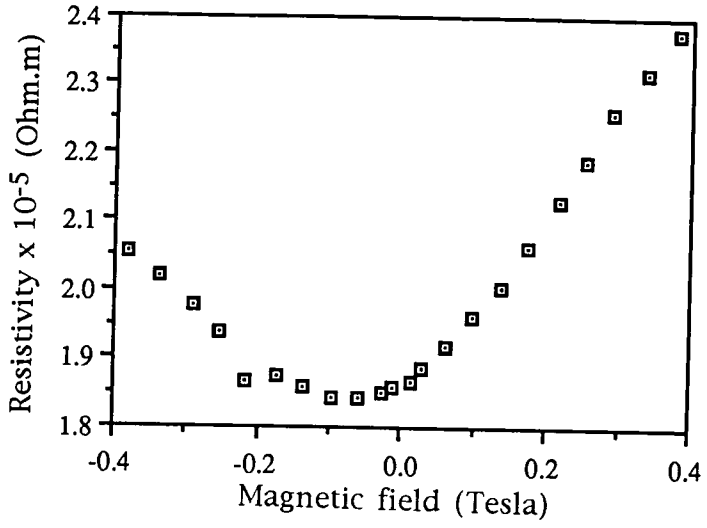

Fig 6.28 Magnetoresistivity characteristic for a 6μm thick $Hg_{0.95}Mn_{0.05}Te$ layer.

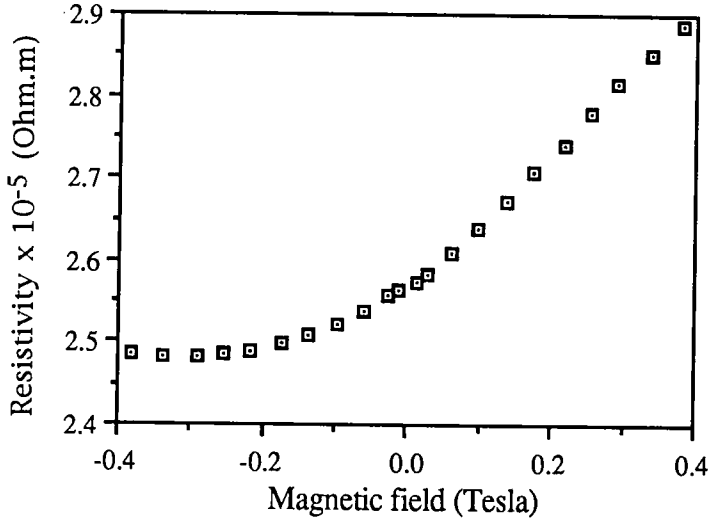

Fig 6.29 Magnetoresistivity characteristic for a 5μm thick $Hg_{0.9}Mn_{0.1}Te$ layer.

A near linear response of resistivity to magnetic field strength in both directions was achieved around compositions of 15% manganese, Fig 6.30.

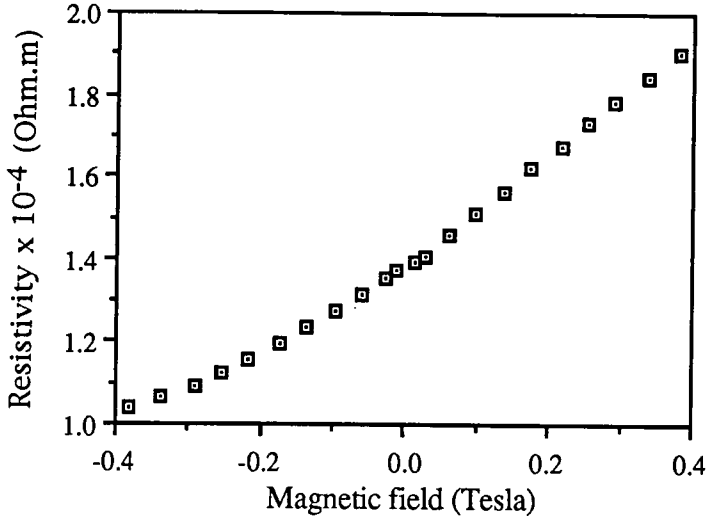

Fig 6.30 Magnetoresistivity characteristic for a 6μm thick $Hg_{0.85}Mn_{0.15}Te$.

The asymmetry in the magnetoresistance characteristics was represented by an asymmetric factor, defined as the ratio of the magnetoresistance measured with a 0.2T field applied in the positive direction to that measured with the same field in the reverse (-) direction. The asymmetry showed no strong or clear dependence on thickness (although the magnitude of the magnetoresistance did show a pronounced effect, see later) but did show a systematic trend with composition as shown in Fig 6.31.

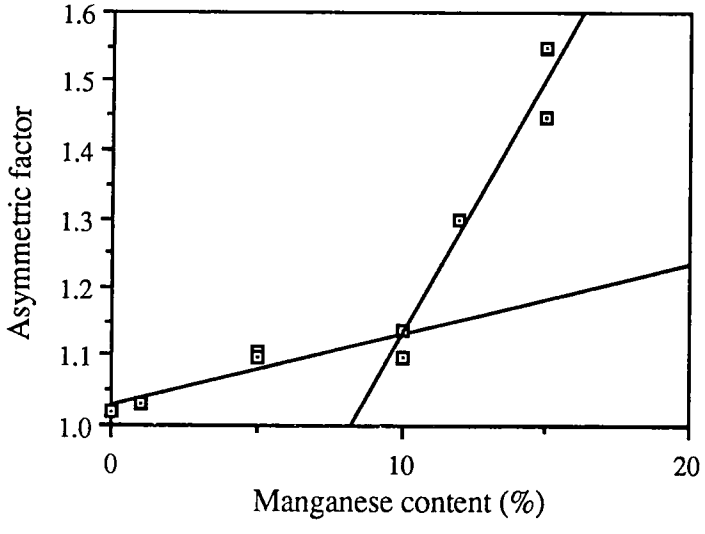

Fig 6.31 Dependence of magnetoresistance asymmetry on composition.

Analysis of the magnetoresistivity characteristics revealed that for small applied magnetic fields (relative to the field giving the minimum resistivity, i.e. allowing for the offset from zero field) the magnetoresistance varied as the square of the applied field. At larger fields, the dependence appeared to be linear. The transition field, B_2, at which the magnetoresistivity changed from a B^2 to B^1 dependence, was found to increase linearly with manganese concentration, Fig 6.32.

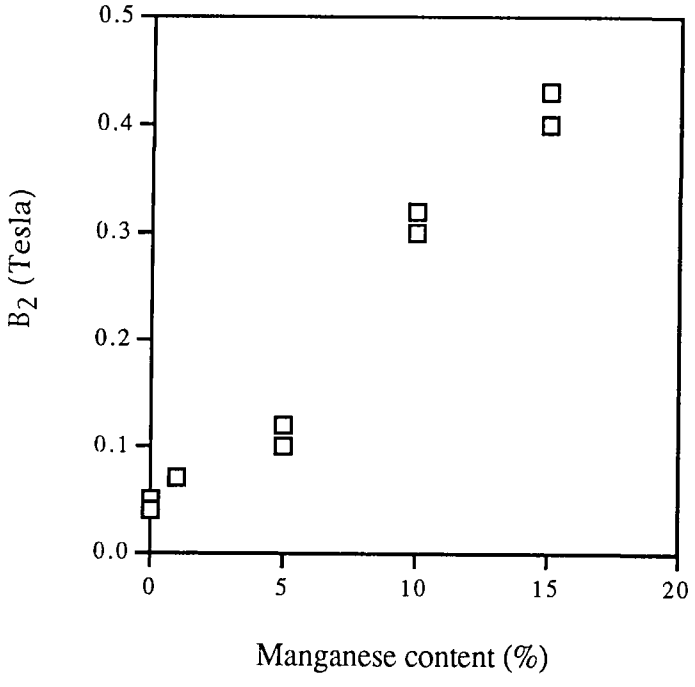

Fig 6.32 Variation in the transition field, B_2, with manganese concentration.

It should be noted that applying the field from the layer side i.e. in the positive sense would deflect electrons to the edge nearest the contact, for the configuration of currents and voltages used. Application of the field

from the substrate side (i.e. negative direction) would deflect the electrons across the surface to the opposite edge, thus depleting the electron concentration near the contact surface. This may provide an explanation for the observed asymmetry in the magnetoresistance, and was consistent with the magnetoresistance obtained by reversing the current direction. The increase in asymmetry with increasing manganese content may result from the self magnetisation of the manganese ions along the direction of the applied magnetic field effectively enhancing the magnitude of the asymmetry.

The free electron theory predicts that the electric field produced by the Hall effect will produce zero transverse current. However, since there is a difference in the mean velocities of conduction electrons, magnetoresistance will result from the curved paths of individual electrons. This magnetoresistance is present in a wide variety of materials [18], and has a quadratic dependence on small magnetic fields and a linear dependence on fields which result in the mean free path of electrons being larger than the radius of the electron orbits.

Giant negative magnetoresistance has been observed, by Mycielski et al [19], in p-type $Hg_{0.92}Mn_{0.08}Te$ at 4.2K on the application of large (7 Tesla) magnetic fields. No negative magnetoresistance, even at 4.2K using layers with compositions corresponding to the semimetal-semiconductor transition, was observed in this study for the range of magnetic fields ($-0.38T \leq B \leq 0.38T$) available. For layers of manganese content greater than 20% a small reduction in the resistivity was obtained on applying a magnetic field from the layer side of the sample (which was more pronounced in high manganese content layers), Fig 6.33. It was unclear as to whether this was an artefact of the contact due to the high resistivity of

the layer (~1.3 ohm.m) or whether it occurred as a result of the increasing radius of the acceptor wave function, although this is more commonly associated with p-type narrow gap (Hg,Mn)Te [5].

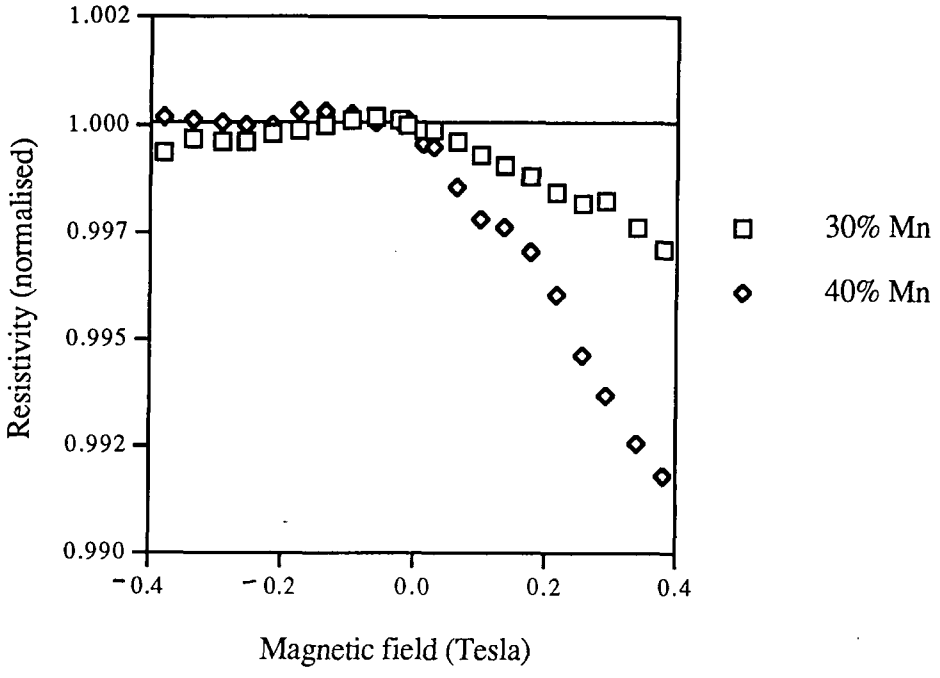

Fig 6.33 Magnetoresistivity characteristics for 2μm thick samples of $Hg_{0.7}Mn_{0.3}Te$ and $Hg_{0.6}Mn_{0.4}Te$.

The largest magnetoresistance was seen in narrow band gap layers containing of the order of 15% manganese. In addition, the magnetoresistance increased with layer thickness. The dependence of the magnetoresistance upon layer thickness for a 0.38T field, where the magnetic field direction is from the layer side, is given in Fig 6.34. However as previously noted, thickness had no noticeable effect on the shape of the magnetoresistance characteristic.

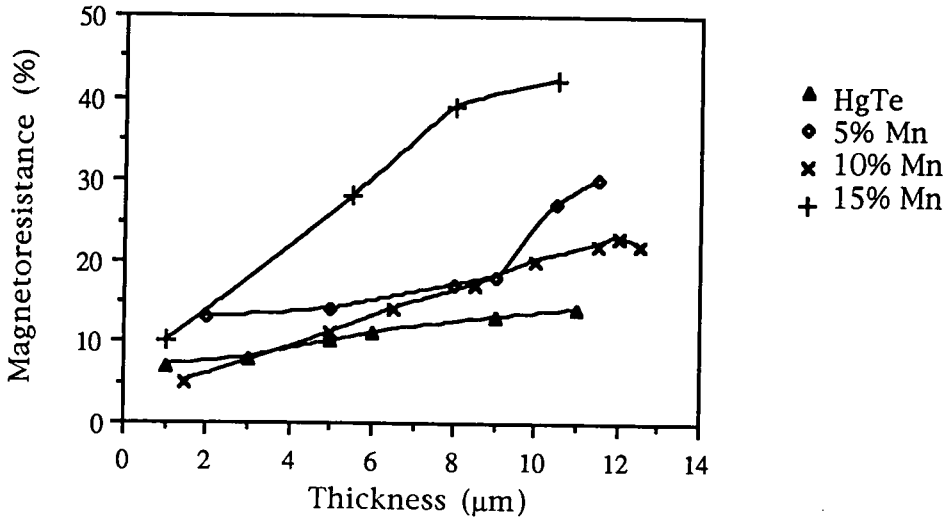

Fig 6.34 The effect of layer thickness on the magnetoresistivity at an applied magnetic field of 0.38T.

Lowering the temperature increased the effective change in resistivity with magnetic field due to the reduced thermal lattice vibrations, Fig 6.35.

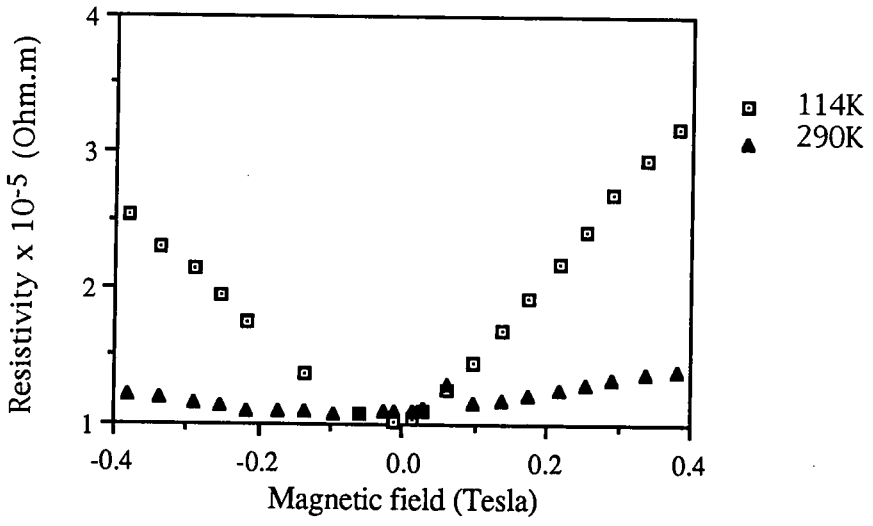

Fig 6.35 Magnetoresistance in $Hg_{0.95}Mn_{0.05}Te$ at 290K and 114K.

When a study was made of the temperature dependence of the magnetoresistance for magnetic fields directed from the layer side of the

sample a linear relationship was observed, Fig 6.36. At 77K the 5% manganese layers possessed a larger magnetoresistance than the 15% manganese layers.

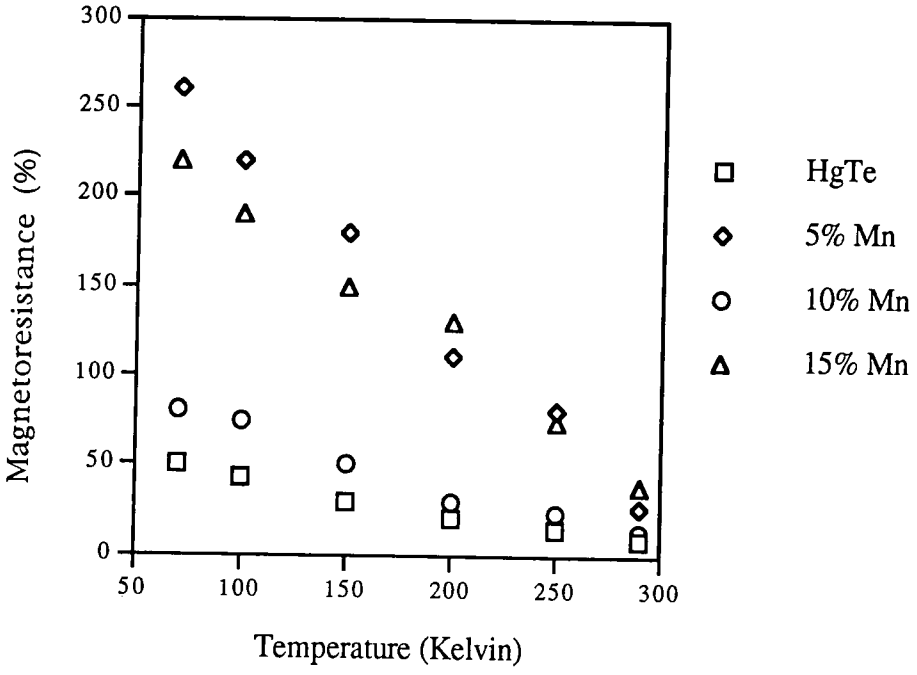

Fig 6.36 Dependence of magnetoresistance on temperature.

The above dependence of magnetoresistance on temperature can be approximated to a linear relationship and the slope of the "best fit" can be considered as a measure of the strength of that dependence. Initial indications are that compositions corresponding to a zero bandgap (i.e. ~5% Manganese) exhibited the largest dependence of magnetoresistance on temperature.

6.7 Surface Instabilities of n-type Narrow Gap (Hg,Mn)Te

All the transport measurements discussed above were made within a week or so, from the date of growth. Subsequently these measurements were repeated at monthly intervals to assess the stability of the layers when

stored in air in the laboratory with no precautions having been taken, for example, to exclude moisture, etc. Care was taken to avoid surface contamination or damage due to repeated soldering of the wires to the sample holder.

Figs 6.36 to 6.38 show the effect ageing in air had upon the transport behaviour in layers of n-type $Hg_{0.87}Mn_{0.13}Te$ of various thicknesses. Both the carrier concentration and mobility changed in a linear manner for the first five months (decreasing by 3 x 10^{15} cm^{-3} per month and $1000 cm^2V^{-1}s^{-1}$ per month respectively for a layer of ~1μm thickness), suggesting that the outdiffusion of mercury was a possible cause, but where the loss was still very much less than the total amount of mercury remaining in the layers. After five months the transport data appeared to vary as a function of the square root of time, suggesting a diffusion limited mechanism. EDAX measurements showed that there was no noticeable change in overall composition, again indicating that any outdiffusion was on a microscopic scale. For compositions corresponding to a positive bandgap the resistivity of n-type (Hg,Mn)Te layers increased with ageing, Fig 6.36, and that of compositions corresponding to semimetallic material decreased, Fig 6.39. For all n-type layers investigated the carrier concentration and mobility decreased with time.

Spicer et al [2] proposed that the stability of (Hg,Cd)Te depends on crystal quality to a depth of many microns. This statement seems to be the case for (Hg,Mn)Te when the change in transport properties with time is considered for layers of comparable compositions but differing thicknesses (and hence FWHMs), Figs 6.36 to 6.38. However the differences observed for (Hg,Mn)Te may also be a result of the thicker layers having a smaller surface area : volume ratio, and therefore change at the surface would

have less impact in thicker layers.

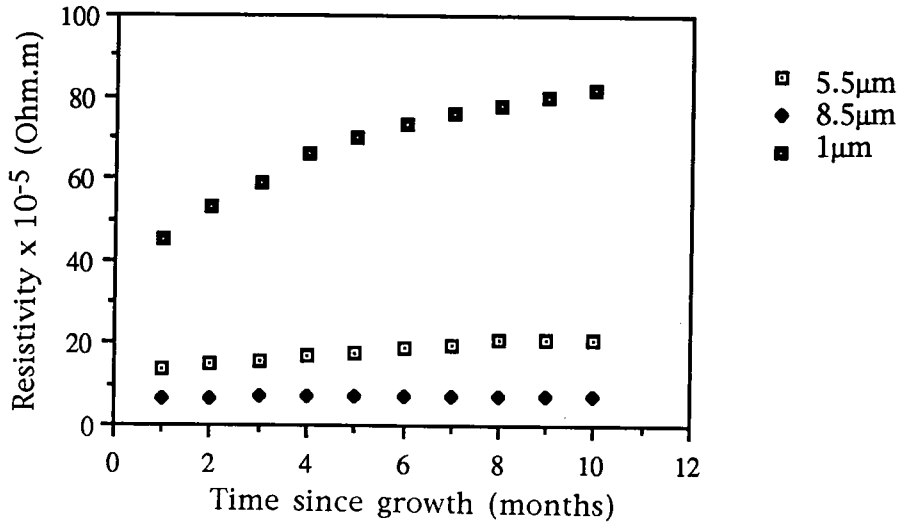

Fig 6.36 The change in resistivity of $Hg_{0.87}Mn_{0.13}Te$ with time.

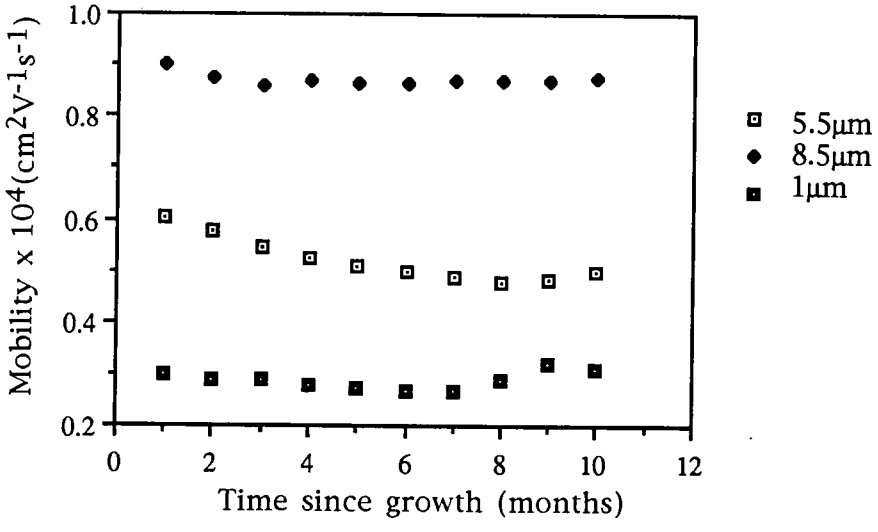

Fig 6.37 The change in carrier mobility of $Hg_{0.87}Mn_{0.13}Te$ with time.

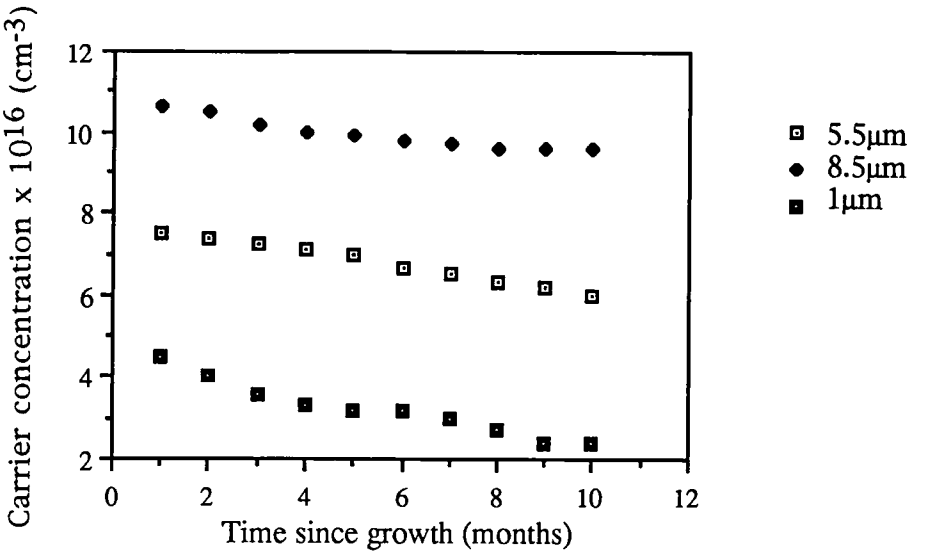

Fig 6.38 The change in carrier concentration of $Hg_{0.87}Mn_{0.13}Te$ with time.

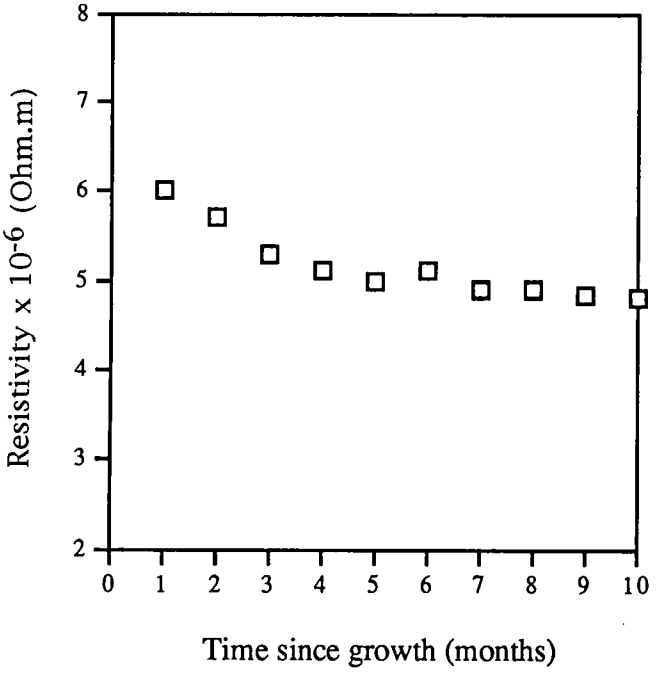

Fig 6.39 Change in resistivity of 6μm thick HgTe with time.

No type inversion with time was observed as proposed by Spicer et al [2], who suggested that acceptor defect levels might "pin" the Fermi level at the surface and thus deplete or invert the surface. Spicer attributed the

creation of mercury vacancies and dislocations to "the difference in binding energy of the Hg $6s^2$ and Cd $5s^2$ valence levels contributing to the weakness of the Hg bonds in the lattice" [2]. Therefore, to prolong the life of a layer of (Hg,Mn)Te, the thickness should be greater than 5μm and a passivation layer used. Clearly, such a passivation layer should adhere well to the layer, provide good thermal and environment protection, be stable itself and introduce minimal defects or interaction with the layer it is intended protect. Various passivation layers have been investigated for (Hg,Cd)Te, such as anodic oxides, ZnS and SiO_2, all of which would be of interest for (Hg,Mn)Te.

6.8 Summary

The majority of (Hg,Mn)Te layers grown exhibited n-type behaviour. Carrier properties were found to be thickness dependent, where electron mobility and concentration increased with thickness which resulted in a reduction in resistivity.

The temperature dependency of the Hall coefficient and electron mobility of epitaxial HgTe was found to be similar to that reported for bulk crystal HgTe [6] , although the magnitude of the values differed by up to a factor of three (in the case of Hall coefficients at 77K), possibly due to differences in residual impurity concentrations. Alternatively, this difference could be due to intergranular strain modifying the bandstructure as discussed in Chapter One, although at this stage this remains to be demonstrated. The electron concentrations for epitaxial HgTe at 300K and 77K corresponded well to those calculated by Harman et al [7] for HgSe, which has an almost identical bandstructure to HgTe. The temperature variation of the electron mobility in epitaxial HgTe was explained in terms of optical-phonon,

piezoelectric and ionised impurity scattering, with an excellent fit being obtained using published values of effective masses, dielectric constants etc. for HgTe.

When modelling the temperature dependency of electron concentration for n-type narrow gap (Hg,Mn)Te was attempted using the two band model with the semiconductor statistics, discussed in Chapter Four, ill fitting curves were obtained for the surface compositions. This it was suggested to be due to the underlying material having a lower manganese concentration than that of the surface. The determination of the bandgap from intrinsic Hall data substantiated this suggestion. In the n-type layers investigated, the activation energy of the electron donors was between 0.5meV and 1meV and the concentration of these donors was in the range 10^{16} to 10^{17} cm^{-3}. Acceptor levels with an activation energy of 4meV were found in $Hg_{0.85}Mn_{0.15}Te$. Piezoelectric and optical-phonon scattering were present in all the n-type (Hg,Mn)Te layers considered; however alloy scattering was also present in layers containing in excess of 5% manganese.

Layers of $Hg_{0.9}Mn_{0.1}Te$ grown using a lower mercury temperature (180°C) were found to be p-type, and displayed extrinsic behaviour at T<100K. The Hall data was successfully modelled using two carrier semiconductor statistics and unlike the n-type material the surface composition was in good agreement with the underlying material. Electron to hole mobility ratios for $Hg_{0.9}Mn_{0.1}Te$ were found to be in the range 85 to 95 for temperatures in the range 77K to 300K. The variation in mobility with temperature was attributed to ionised impurity scattering below 77K and a combination of optical and alloy scattering for temperatures between 77K and 200K. Above 200K a secondary optical scattering mechanism may have been responsible for the lower than expected mobilities.

The magnetoresistance, for n-type (Hg,Mn)Te, observed using magnetic fields up to 0.38T was proportional to the square of the magnetic field for low fields, but exhibited a linear dependence at larger fields. The range of magnetic fields for which the former condition applied increased with manganese content as did the asymmetry of the magnetoresistance with respect to the direction of the magnetic field. For compositions exceeding 20% manganese the resistivity was lowered by applying a magnetic field from the layer side of the sample. However this effect was very small and it was unclear whether it originated from a contact effect or was a genuine negative magnetoresistance effect. As the layer thickness was increased the magnitude of the magnetoresistance also increased. Lowering the temperature increased the magnetoresistance due to the reduction in the thermal lattice vibrations.

When transport measurements were repeated on n-type, positive bandgap (Hg,Mn)Te at monthly intervals electron mobility and concentration were observed to reduce with time. These changes were linear with time for the first five months beyond which a dependence on the square root of time became apparent. This suggested a loss of mercury from the surface by a diffusion mechanism which was more pronounced in thinner layers.

References

[1] R. Reifenberger and D.A. Schwarzkopf (1983) Phys. Rev. Lett. **50** 907.

[2] W.E. Spicer, J.A. Silberman, I. Lindau, A.B. Chen, A. Sher and J.A. Wilson (1983) J. Vac. Sci. Technol. **A1(3)** 1735.

[3] P. Gay, P.B. Hirsh and A. Kelly (1953) Acta Metallurgica **1** 315.

[4] H. Nishino, S. Murakami, H. Ebe and Y. Nishijima (1995) J. Crystal Growth **146** 619.

[5] G. Bastard, C. Rigaux and A. Mycielski (1977) Phys. Status Solidi **B79** 585.

[6] T.C. Harman, M.J. Logan and H.L. Goering (1958) J. Phys. Chem. Solids **7** 228.

[7] T.C. Harman and A.J. Strauss (1961) J. Appl. Phys. **32**(10) 2265.

[8] R. Zallen, G. Lucovsky, W. Taylor, A. Pinczuk and E. Burstein (1970) Phys. Rev. **B1** 4058.

[9] J. Lagrenaudie (1958) J. Chim. Phys. **55** 175.

[10] "Semiconductors and Semimetals" ed. R.K. Willardson and A.C. Beer (1977) **Vol 10** pub. Academic Press Inc p85.

[11] "Semiconductors" R.A. Smith (1978) Cambridge University Press p101-110.

[12] W.A. Harrison (1956) Phys. Rev. **101** 903.

[13] J. Reno, I.K. Sou, P.S. Wijewarnasuriya and J.P. Faurie (1985) Appl. Phys. Lett **47** (11) 1168.

[14] A. Rogalski (1991) Infrared Phys. **31**(2) 117.

[15] J.W. Harrison and J.R. Hauser (1976) J. Appl. Phys. **47** 292.

[16] W.D. Lawson, S. Nielsen, E.H. Putley and A.S. Young (1959) J. Phys. Chem. Solids **9** 325.

[17] "Physics and Chemistry of II-VI Compounds" ed M. Aven and J.S. Prener (1967) pub. North Holand Pub. Co., Amsterdam.

[18] "The Physical Principles of Magnetism" by A.H. Morrish (1966) pub. J.Wiley and Sons, London p100-143.

[19] A. Mycielski and J. Mycielski (1980) J. Phys. Soc. Japan **49** 809.

Chapter Seven

The Interdiffused Multilayer Process

7.1 Introduction

Due to the non-uniformity of DAG grown (Hg,Mn)Te layers it became clear that an alternative growth procedure was required. For device applications it has been generally acknowledged that (Hg,Cd)Te must have a composition which varies by less than 0.5% over a distance of ~1cm, but standard DAG grown (Hg,Cd)Te varied by about 5% over this distance. To solve this problem the Interdiffusion Multilayer Process (IMP) was developed by Tunnicliffe et al [1]. It involved depositing alternate HgTe and CdTe layers of small thicknesses and allowing interdiffusion to occur, Fig 7.1. It was found that for thicknesses of 0.1μm or less, diffusion will be complete within a 10 minute anneal at the growth temperature in a flow of hydrogen and under a mercury overpressure. Rapid interdiffusion of mercury and cadmium at lower temperatures is preferable, in order to reduce the possibility of crossdiffusion from the substrate or from other structures deposited. If the diffusion is complete, then since HgTe and CdTe have similar lattice parameters, the Cd content of the resulting CMT layer can be determined from the ratio of the thicknesses of HgTe and CdTe layers deposited:

$$x = t_2/(t_1+t_2) \qquad 7.1$$

where t_1 is the thickness of HgTe layers, t_2 is the thickness of CdTe layers and x is the cadmium fraction in the resultant layer.

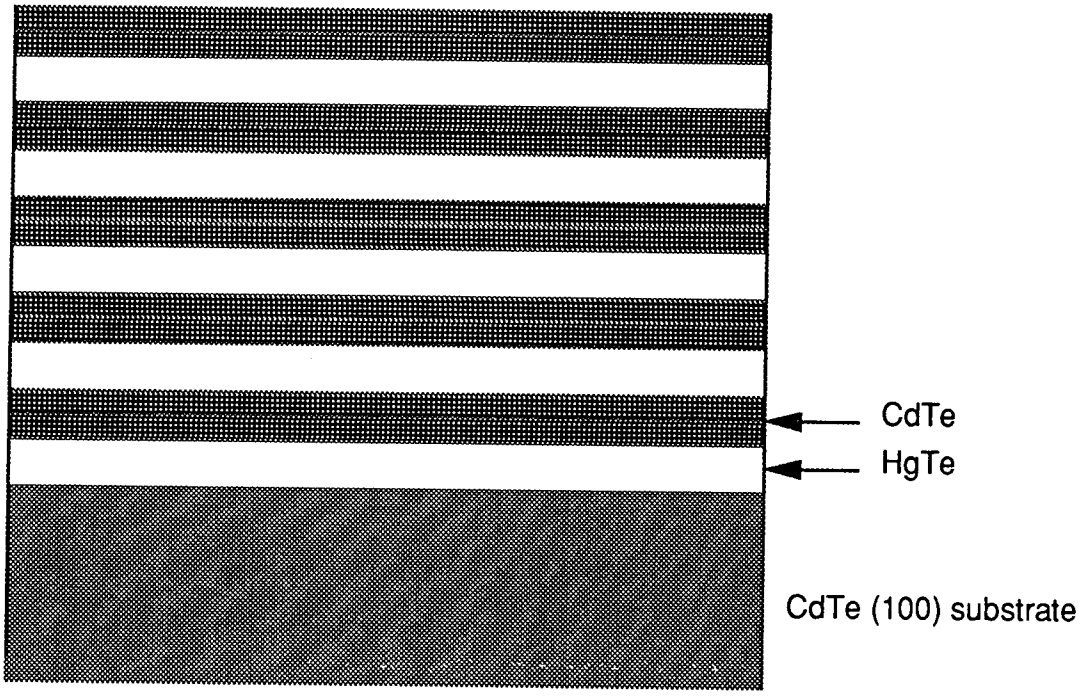

Fig 7.1 The Structure Grown For Improved CMT Uniformity By Tunnicliffe et al [1]

7.2 Adaptation of the IMP Process to Growth of (Hg,Mn)Te.

Before IMP growth can be attempted the conditions for MnTe and HgTe deposition must first be optimised and zinc blende growth of the binary layers ensured. For this condition to be satisfied for MnTe a Mn/Te ratio of unity has to be achieved. The effect of altering the TCMn/DIPTe partial pressure ratio on the Mn/Te ratio was investigated by growing layers on GaAs (100) substrates whilst keeping all other growth conditions constant, Table 7.1. The Mn/Te ratio was assessed using EDAX at three positions 10mm apart.

Substrate	CdTe buffered GaAs (100)
Substrate Temperature	370, 380 and 390 ^{o}C
Total Flow Rate	1750 cc/min
DIPTe Bubbler Temperature Carrier Gas Flow Rate	15^{o}C 25-450 cc/min
TCMn Bubbler Temperature Carrier Gas Flow Rate	75^{o}C 400 cc/min
Hg Boat Temperature	215^{o}C when Ts=370,380^{o}C 250oC when Ts=390^{o}C

Table 7.1 Growth conditions used for the optimisation of MnTe growth [2].

The results are summarised in Fig 7.2, which shows the Mn/Te ratio as a function of TCMn/DIPTe feed rate ratio. Susceptor temperatures less than 380^{o}C required a TCMn/DIPTe feed rate ratio that was impractically large. It is clear from these results that a susceptor temperature of 380^{o}C gave layers

with a Mn/Te ratio of one over the whole layer for TCMn/DIPTe feed rate ratios of between 5 and 8. At 390°C the TCMn/DIPTe feed rate ratio changes too steeply along the gas flow direction to obtain a uniform growth of MnTe. For the growth of HgTe the carrier gas flow rate for the DIPTe was increased to 600cc/min to obtain a higher growth rate. Unlike MnTe there are no other phases for HgTe and such a preliminary study was not required.

Typically 100 cycles of the HgTe/MnTe structure were grown, at a susceptor temperature of 380°C and using the flow rates given in Fig 7.3, onto GaAs (001) substrates with a 1μm CdTe buffer layer overlaying a 0.1μm ZnTe layer. Due to the finite response times of the gas flow control system a transition time of 39 seconds was allowed in the flow rates to change between HgTe and MnTe growth, Fig 7.3. A constant partial pressure of mercury (75 Torr) was maintained as mercury inclusion into the layer could easily be controlled by the DIPTe flow rate. To allow smooth switching between MnTe and HgTe the TCMn carrier gas was diverted to bypass around the bubbler. To determine the effect of post growth in-situ annealing duplicate layers were grown with and without a one hour anneal under the same mercury vapour pressure, susceptor temperature and total flow rate as that had been used during the growth. After growth the substrate required 45 minutes to cool to room temperature compared to 10 minutes for the mercury boat. Therefore no unintentional mercury annealing occurred. To vary the composition of the layers the ratio of the HgTe growth time to that of the MnTe layer was altered.

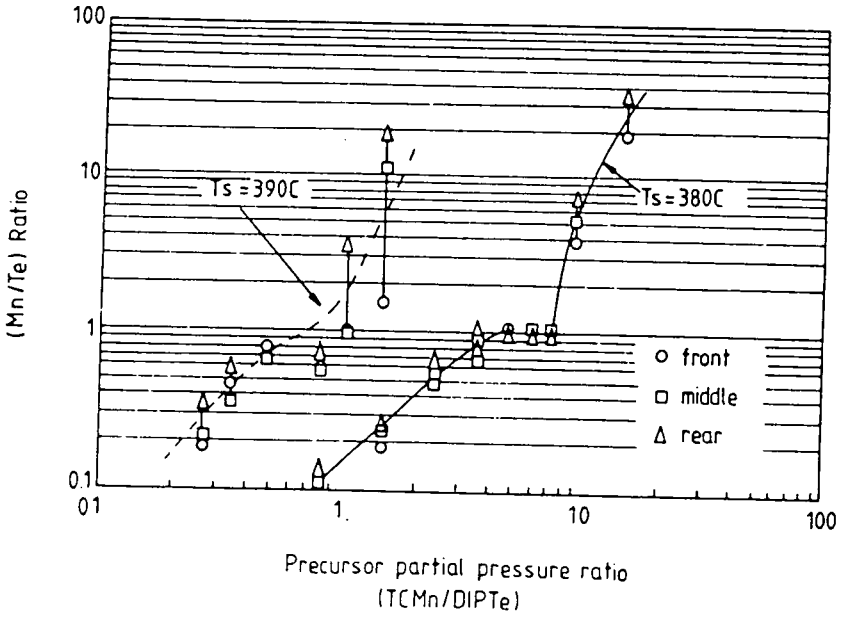

Fig 7.2 Determination of conditions required for MnTe growth.

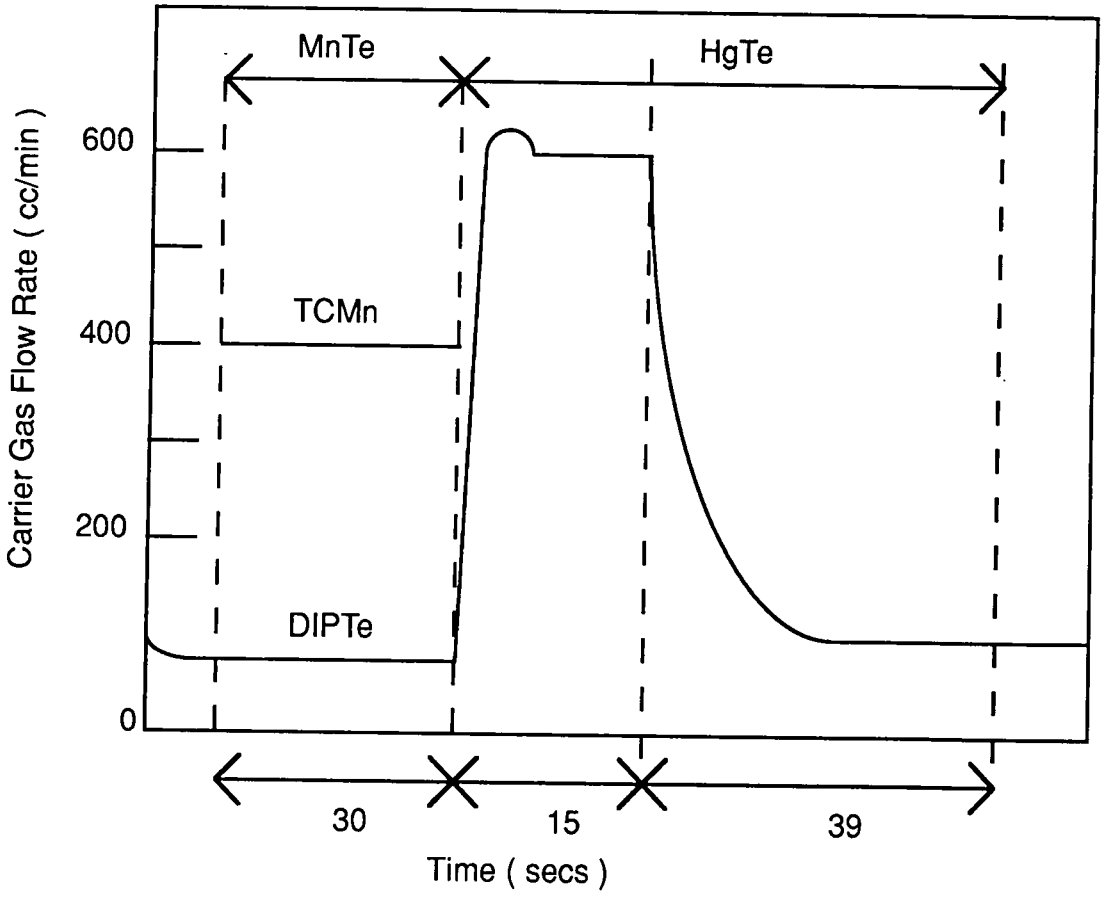

Fig 7.3 Typical carrier gas flow rates for one cycle of MnTe/HgTe growth.

7.3 Structural Analysis of (Hg,Mn)Te Layers Grown by IMP

7.3.1 Thickness Dependence of Crystal Quality.

Typical double crystal x-ray rocking curves for 4μm thick layers of $Hg_{0.87}Mn_{0.13}Te$ grown by IMP and DAG respectively are presented in Fig 7.4. These were obtained using $CuK\alpha_1$ radiation in the 004 reflection. The broad peak on the low angle side corresponds to the CdTe buffer layer and no significant difference was detected between this peak for layers grown by IMP or DAG of similar thicknesses. Similarly the integrated intensity (see chapter four) of the substrate rocking curve was found to give an estimate for the thickness of IMP layer, using the x-ray absorption calculations developed for DAG layers, which was in excellent agreement with that measured by cross sectional SEM. Hence it was deduced that the absorption of x-rays in (Hg,Mn)Te was of similar magnitude in IMP and DAG layers of comparable composition and thickness.

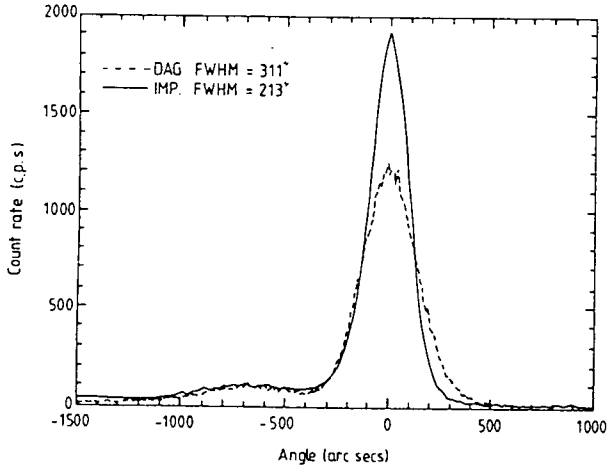

Fig 7.4 Rocking curves of 4μm $Hg_{0.87}Mn_{0.13}Te$ grown by IMP and DAG respectively [2].

The most striking difference between the x-ray rocking curves from IMP and DAG layers was that for similar thicknesses the FWHM of the DAG layer was 50% larger than that of the IMP layer. This improvement in layer quality was probably a result of the alternate growth of HgTe and MnTe bending the threading dislocations at the interfaces, due to the difference in lattice parameters (6.46Å and 6.334Å respectively). The bending of dislocations should increase the probability of interaction between dislocations and hence their annihilation [5]. To analyse the relationship between FWHM and thickness, rocking curves were taken at regular intervals on the surface to obtain a good collection of data points. The composition was calibrated from EDAX results and the layer thickness calculated from the integrated intensity of the substrate peak, as for DAG layers. The FWHM of all the IMP layers considered were less than those of comparable thickness layers grown by DAG. However the difference in FWHM between the two growth techniques reduced with increasing thickness, Fig 7.5. It is unclear at present whether IMP or DAG layers have superior FWHM for thicknesses in excess of 10μm.

Another important observation was that, in contrast to DAG layers, the FWHM for IMP layers was dependent on the composition (with larger manganese concentrations having larger FWHMs for similar thicknesses). This suggested that the mechanism of dislocation bending was stronger in lower manganese content layers, where the ratio of HgTe to MnTe thicknesses was larger (7.5 for 13% manganese and 14.8 for 6.3% manganese).

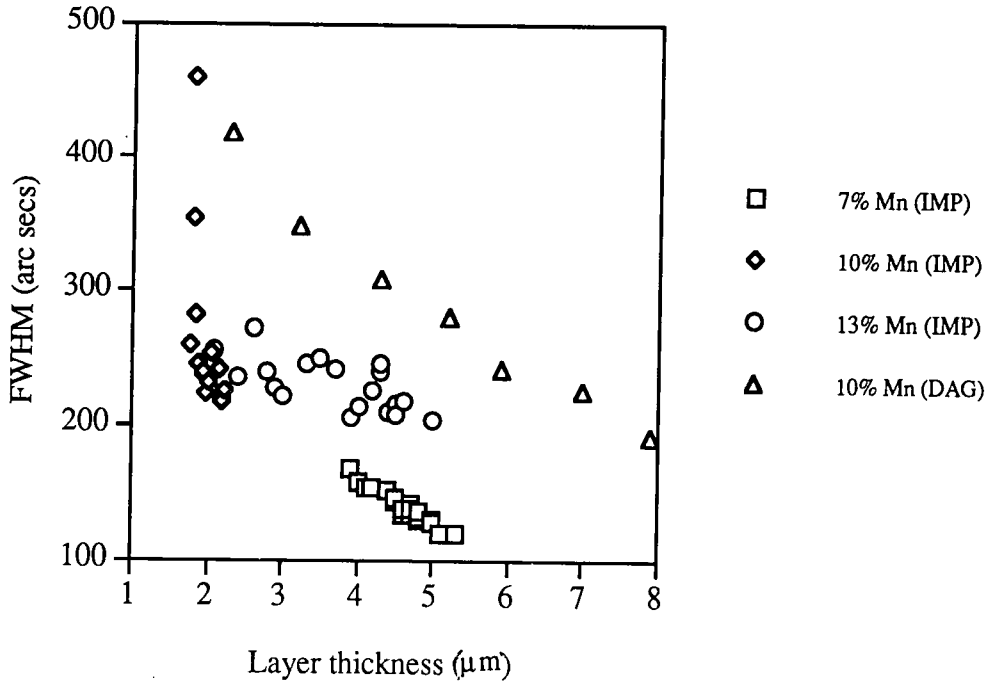

Fig 7.5 FWHM dependency upon layer thickness for IMP and DAG grown layers.

Calculated values of composition for central positions in the IMP layers from the growth time of binary layers, equation 7.1 (growth rates of HgTe and MnTe were calculated to be $7\mu m.hr^{-1}$ and $1.7\mu m.hr^{-1}$ earlier in this study) corresponded well to that measured by EDAX.

However thickness calculations using these growth rates implied that the IMP layers should have been of the order of five times the thickness. The reason for this discrepancy is not known, but may indicate that there was a significant induction phase in the nucleation in the MnTe and HgTe cycles.

7.3.2 Surface Uniformity of (Hg,Mn)Te Grown by IMP.

An identical approach to that detailed in Chapter Five was used to record rocking curves of the layer and substrate, at 2mm intervals, in order to assess the surface uniformity of (Hg,Mn)Te grown by IMP. The adoption of the IMP process produced a significant improvement in uniformity in the central region of all the IMP layers considered [3], Fig 7.6. Edge effects were more prominent for IMP growth, however this may have been a result of this growth having been performed on smaller substrates.

As a qualitive investigation of surface uniformity the variation of layer thickness, FWHM and composition along the centre line, in the direction of gas flow, was considered for each layer. The increase in the manganese concentration along the direction of gas flow observed in DAG layers [3] was also present for those grown by IMP, Fig 7.7. However IMP layers of comparable composition and thickness possessed superior uniformity to DAG layers, Fig 7.6. Initial studies indicated that compositional uniformity was improved with increasing thickness and manganese concentration.

The IMP layer thickness diminished along the direction of the gas flow except for $Hg_{0.93}Mn_{0.07}Te$ layers, Fig 7.8. This would suggest that the ratio of the thicknesses of the MnTe and HgTe deposited varies along the direction of the gas flow but the sum of the deposited thicknesses is less dependent upon the position on the substrate. However the thickness uniformity was superior to that obtained by DAG.

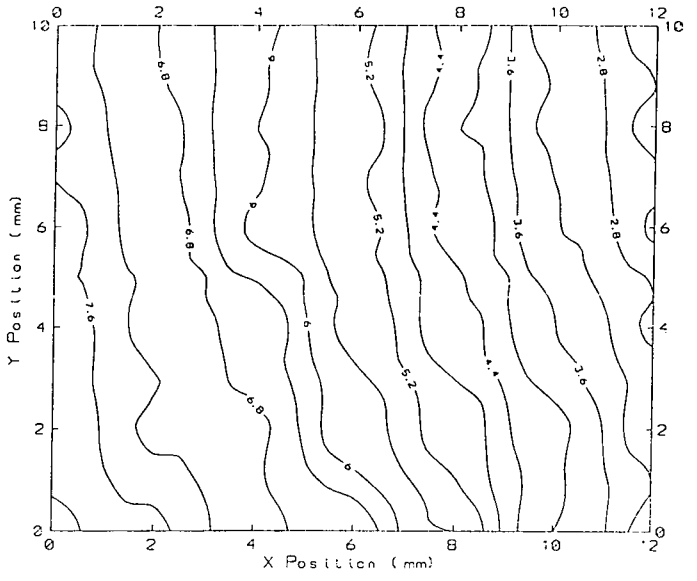

Thickness, μm (DAG)

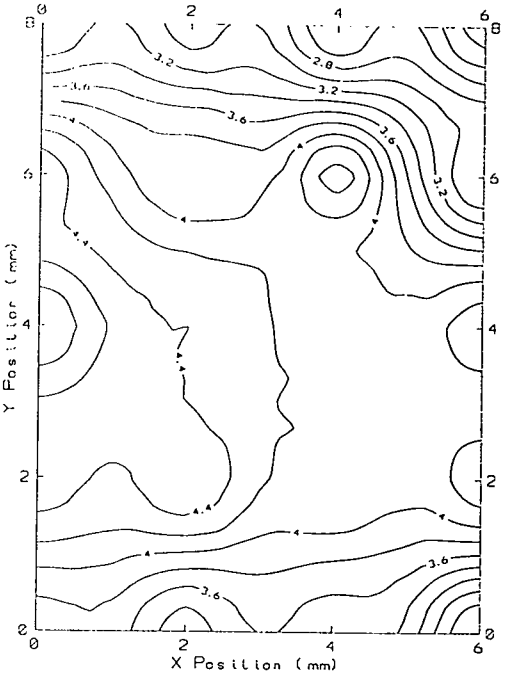

Thickness, μm (IMP)

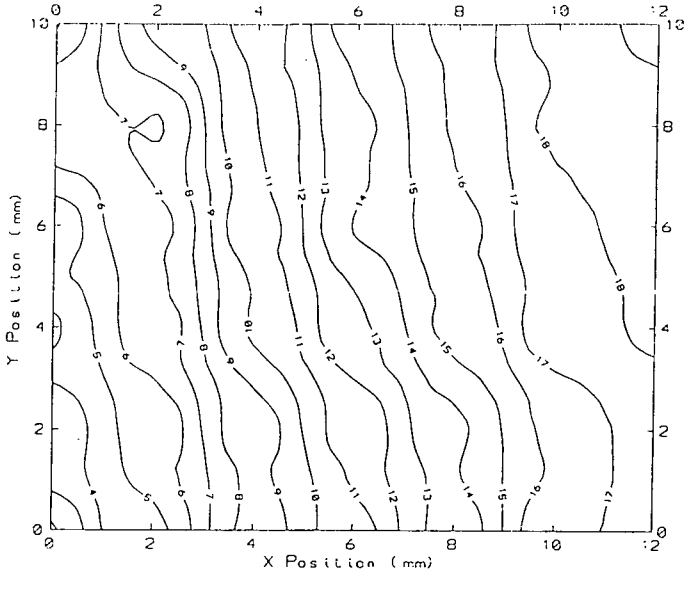

Manganese Concentration, % (DAG)

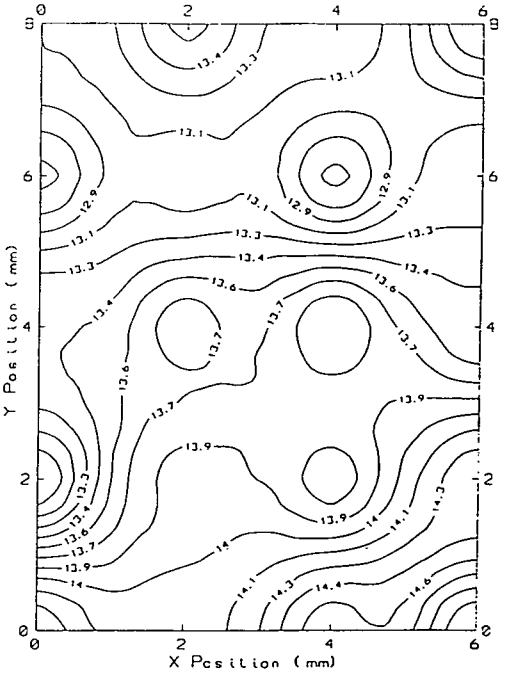

Manganese Concentration, % (IMP)

Fig 7.6 Layer thickness and compositional variations over the surface of comparable DAG and IMP layers (gas flow was from left to right).

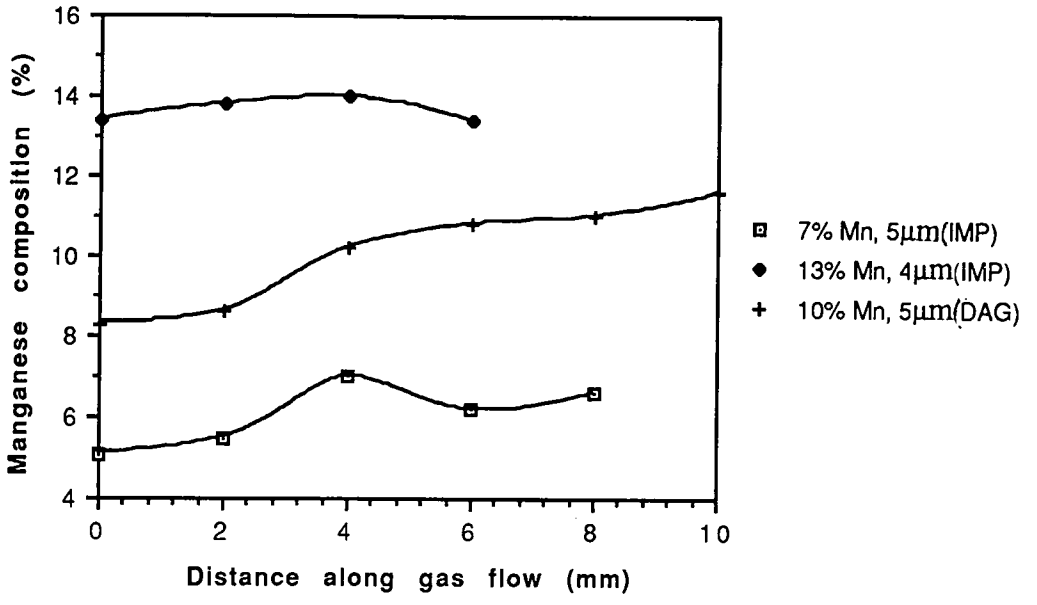

Fig 7.7 Variations in layer composition along the direction of gas flow for IMP and DAG layers.

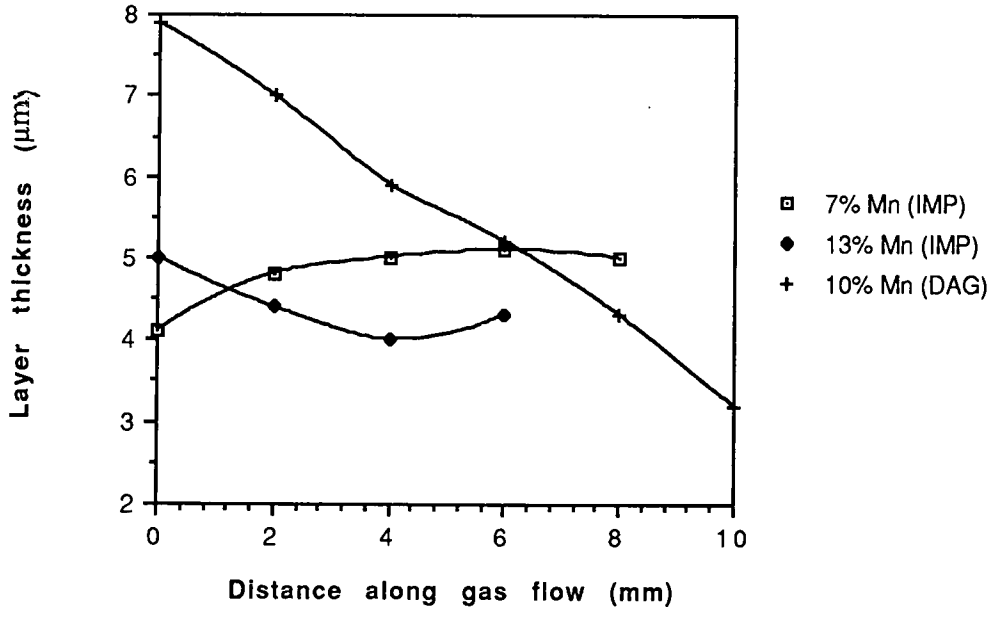

Fig 7.8 Variations in layer thickness along the direction of gas flow for IMP and DAG layers.

7.3.3 Analysis of Dislocation Networks in (Hg,Mn)Te Grown by IMP

Double crystal x-ray topography was performed by J.M.Hudson and C.Moore at Durham on IMP grown (Hg,Mn)Te using $CuK\alpha_1$ radiation in the 224 reflection. The angle of incidence was around 0.5 degrees, in order to provide wide surface coverage. Unlike DAG layers (Chapter Five), the IMP layers exhibited no sub-grain structure, even for thicknesses of less than 4μm and the majority of the surface of IMP layers diffracted x-rays onto dental film when set to the Bragg angle, Fig 7.9. The latter result would substantiate the claim of improved compositional uniformity (and hence lattice parameter) obtained by IMP.

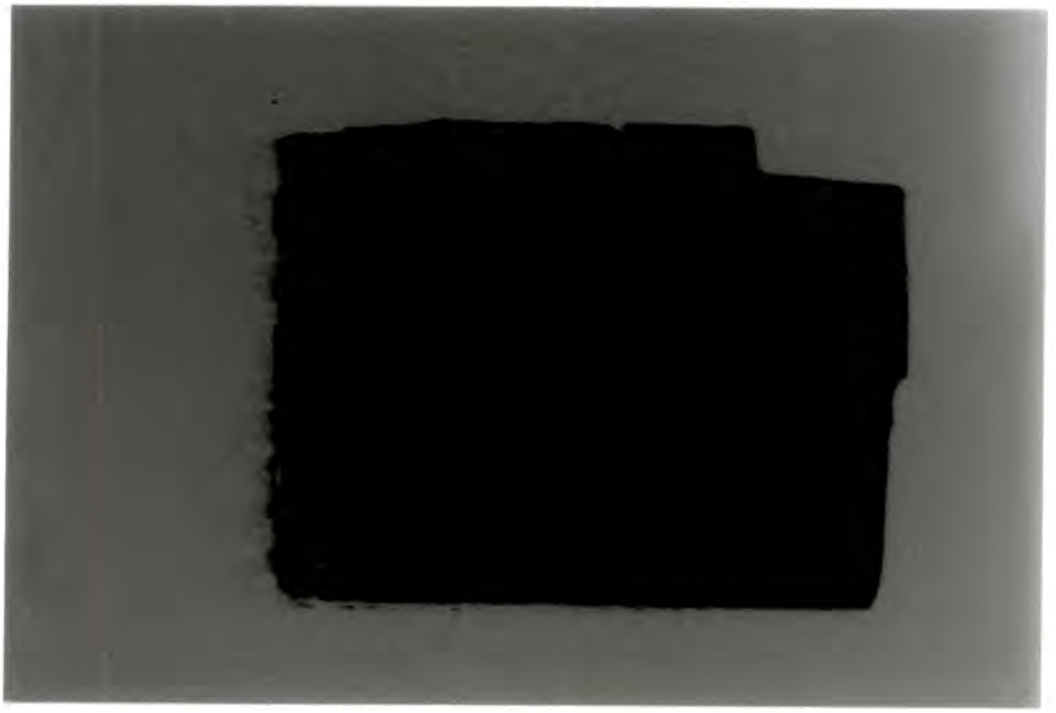

Fig 7.9 Double crystal topograph of a 4μm layer of IMP grown $Hg_{0.87}Mn_{0.13}Te$, taken using $CuK\alpha_1$ radiation in a 224 grazing incidence setting [4].

TEM investigations by Tatsuoka et al [5] confirmed that the interdiffusion between the binary layers in the IMP growth of (Hg.Mn)Te was complete, without the need for a post growth anneal. The high threading dislocation density within the CdTe buffer layer was dramatically reduced at the (Hg,Mn)Te/CdTe interface and dislocations extending from the interface to the surface were eliminated [5]. When DAG layers were considered (Chapter Five) a dislocation array existed near the interface where the dislocations were anisotropic and lay in the $[1\bar{1}0]$ direction. However for the IMP layer considered, TEM revealed no stacking faults, dislocation pairs or sub-grain boundaries, all of which were present in the DAG layers examined. A plan view, bright field image revealed a dislocation density of $\sim 10^{7} cm^{-3}$. Tatsuoka [5] explained the more pronounced bending of dislocations in IMP layers, compared to DAG, in terms of the lattice mismatch between the alternately deposited binary layers (HgTe and MnTe).

7.3.4 Surface Morphology of IMP Grown (Hg,Mn)Te

SEM and optical microscopy were used by M.Funaki [6] to investigate the surface morphology of IMP grown (Hg,Mn)Te. When a comparison with the surface morphology of layers grown by DAG was made for a layer thickness of 4μm, it was discovered that whilst the hillocks found on the DAG layers still persisted the background was considerably improved, becoming flatter. As reported in Chapter Five the facets found in DAG layers developed with layer thickness and this would suggest that the repetition of very thin alternate layers in IMP may have resulted in the improved surface morphology.

7.3.5 The Effect of Post Growth Annealing

To determine whether a post growth anneal was necessary to obtain complete diffusion between the binary layers (although subsequent DCXRD and TEM studies revealed that it was not), two layers were grown under identical conditions, except that one was subjected to a post growth anneal. This was performed for one hour at the susceptor temperature, mercury vapour pressure and total flow rate used during the growth. This post growth anneal had the effect of broadening the x-ray rocking curve by ~50%, Fig 7.11.

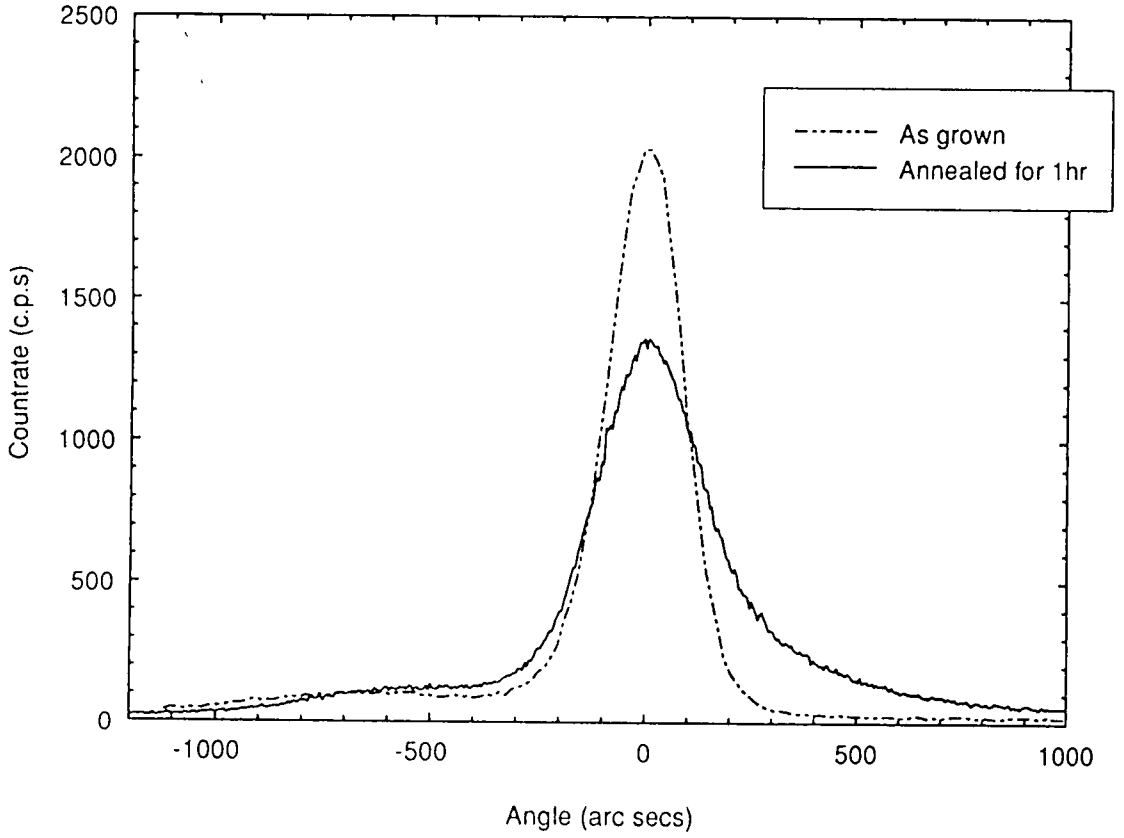

Fig 7.11 The influence of the post growth anneal upon the FWHM.

The dependence of FWHM on layer thickness for the layer subjected to the anneal lay in the range observed for DAG, Fig 7.12. This broadening was attributed to a loss of mercury from the surface by M.Funaki. Optical reflectance and EDAX measurements performed by J.Lewis and M.Funaki respectively are presented in Table 7.2. The table clearly indicates a mercury depleted surface layer, since EDAX and optical reflectance have penetration depths of the order of 3μm and 0.5μm respectively. The values of the FWHM for given layer thicknesses for the annealed IMP layer was similar to those obtained for DAG, Fig 7.12. However there was a substantial spread in the FWHM obtained for a given thickness, and as a consequence the dependence on thickness was less pronounced.

Interestingly, the annealed IMP layer had a superior surface morphology to that of comparable DAG layers. Although annealing had the effect of roughening the surface when compared with unannealed IMP layers.

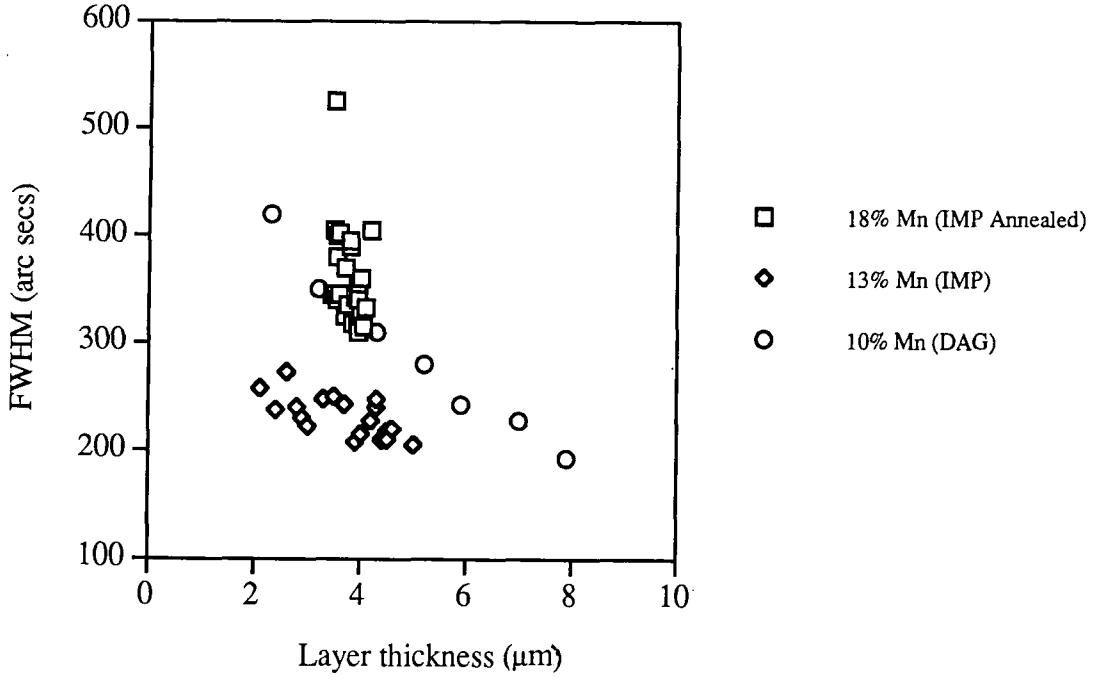

Fig 7.12 The x-ray FWHM dependence upon layer thickness for an annealed IMP layer.

	Manganese fraction (x)	
Method	IMP (unannealed)	IMP (annealed)
Optical reflectance	0.18	0.40
EDAX	0.13	0.18

Table 7.2 The composition of annealed and unannealed IMP layers, determined by optical reflectance and EDAX.

The annealed and unannealed layers had similar uniformity of composition, Fig 7.13, however the annealed layer appeared to have superior thickness uniformity, Fig 7.14. This may suggest that the annealing process redistributed surface species. However the variation between growth runs must also be considered before any conclusions can be made.

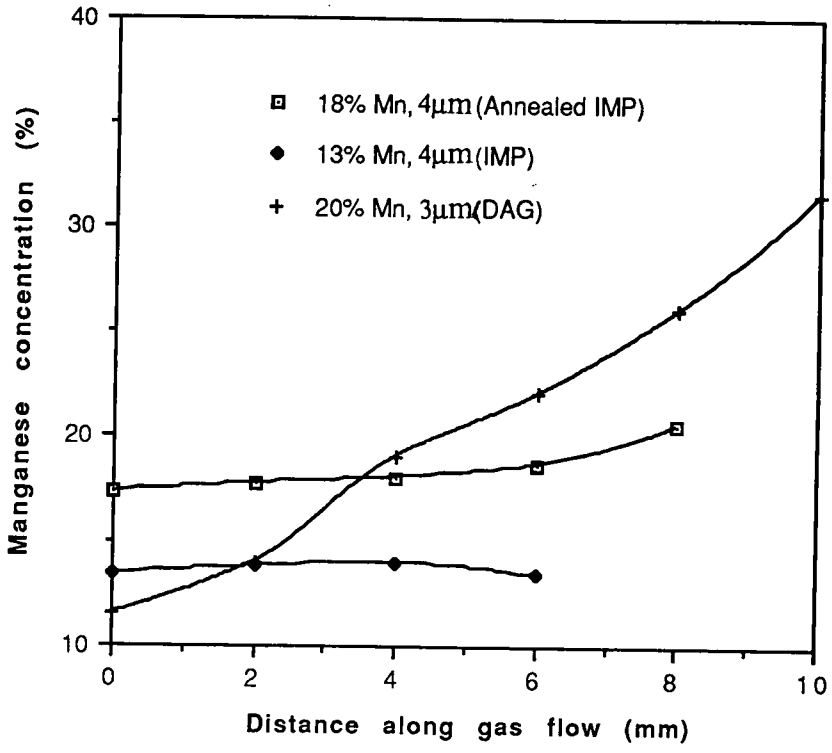

Fig 7.13 Variations in layer composition along the direction of gas flow for annealed and unannealed IMP layers (DAG layers are included for comparison).

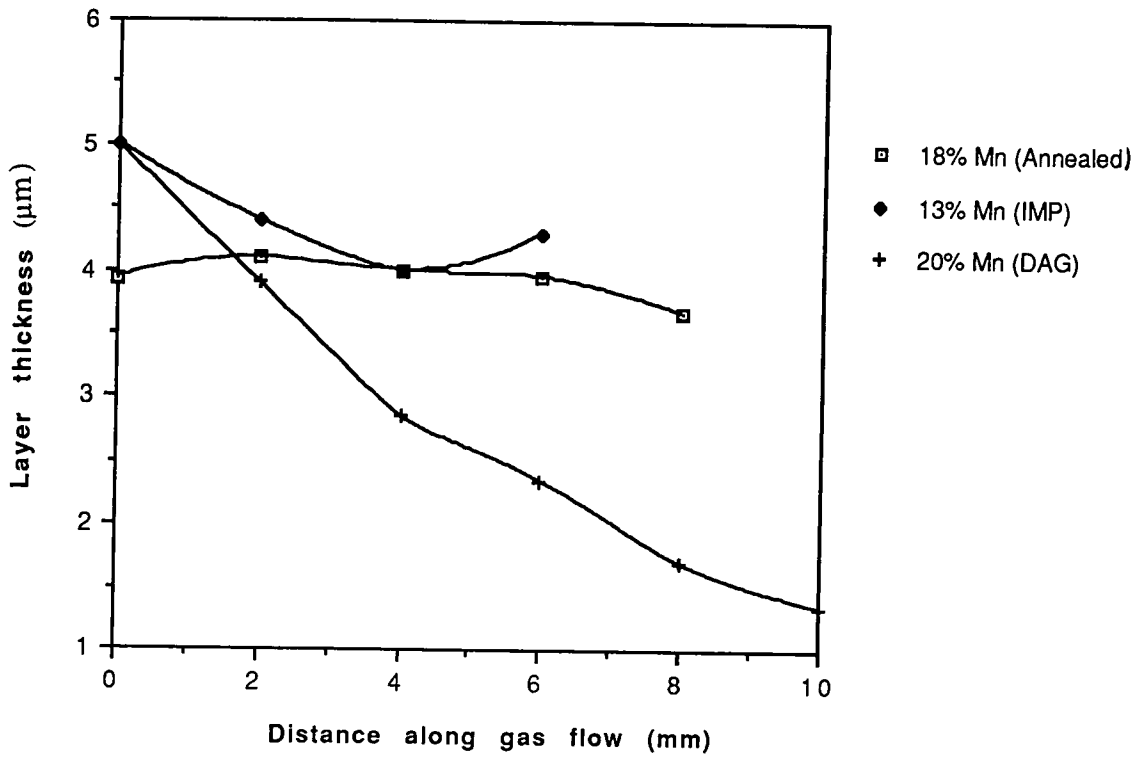

Fig 7.14 Variations in layer thickness along the direction of gas flow for annealed and unannealed IMP layers (DAG layers are included for comparison).

7.4 Summary

The growth of alternate layers of HgTe(~0.1μm) and MnTe (~0.01μm) during the IMP process required no post growth anneal for complete interdiffusion (as shown by DCXRD and TEM) to occur. Layers grown by this technique possessed superior x-ray FWHMs (for a given thickness) and improved uniformity when compared to layers grown by DAG. The improvement in FWHM was attributed to increased bending of threading dislocations at the HgTe/MnTe and MnTe/HgTe interfaces. The improvement in uniformity was thought to be a result of the growth of the

binary layers (HgTe and MnTe) under more optimum conditions. Unlike layers grown by DAG, the IMP layers possessed FWHMs which were dependent upon composition. This was suggested that the bending of the dislocations varied with the ratio of the thicknesses of the two binary layers. Double crystal x-ray topography and TEM revealed that no sub-grains were produced during the IMP growth. In addition stacking faults and dislocation pairs were found to be eliminated in IMP. Surface morphology was also improved in IMP, although the hillocks were found to be still present. Post growth annealing was discovered to cause an extensive loss of mercury from the surface, broadening the x-ray rocking curve and roughening the surface. However, annealed IMP layers still possessed a superior surface uniformity when compared to that of DAG layers.

References

[1] J. Tunnicliffe, S.J.C. Irvine, O.D. Dosser and J.B. Mullins (1984) J. Crystal Growth **68** 245.

[2] M. Funaki, A.W. Brinkman, T.D. Hallam amd B.K. Tanner (1993) Appl. Phys. Lett. **62** (23) 2983.

[3] T.D. Hallam, S. Oktik, M. Funaki, C. Moore, A.W. Brinkman, K. Durose and B.K. Tanner (1995) J. Crystal Growth **146** 604.

[4] J.M. Hudson (1993) PhD Thesis, Durham University.

[5] H. Tatsuoka, K. Durose and M. Funaki (1993) Inst. Phys. Conf. Ser. No**135** Chapter 9 339.

[6] M. Funaki and A.W. Brinkman (1994) J. Crystal Growth **139** 211.

Chapter Eight

Electrical Characterisation of Epitaxial (Hg,Mn)Te Grown by the Interdiffused Multilayer Process.

8.1 Introduction

The improvement in crystalline quality observed in (Hg,Mn)Te layers grown by IMP has been described in Chapter Seven, and it was therefore important to examine how this affected the carrier behaviour. The IMP layers were characterised using the same electrical techniques, i.e Hall and resistivity measurements, that were employed with the DAG samples, as described in Chapter Six. Comparisons have been made between the carrier behaviour in layers grown by IMP and DAG.

8.2 Dependence of Carrier Behaviour on Layer Parameters

All the IMP layers considered exhibited n-type behaviour over the temperature range 77K to 300K (the details of the growth process has been discussed in Chapter Seven [1]). The dependence of electron mobility on layer thickness for 5%, 10% and 13% manganese IMP layers is presented in Fig 8.1. The data taken from similar DAG layers has been included in the graph for comparison. The carrier mobility of these layers at room temperature was generally greater than layers of similar thickness and composition grown by DAG, the increase in mobility was most pronounced in layers with very narrow bandgaps (5% manganese). One exception was the case of an IMP layer containing 13% manganese and with a thickness of two microns, where the mobility was less than half that of corresponding DAG layers. A possible explanation for this exception may be the presence of half loops [2] which are more concentrated in thin

layers grown by IMP due to bending of the dislocations by the alternate layers of HgTe and MnTe during growth. The conditions of growth of 13% manganese IMP layers may extend this dislocated region to 2μm from the interface. It is surprising however to observe that IMP layers have a remarkably similar mobility-thickness dependence to DAG layers, since the dislocation density in the IMP process is reduced more rapidly with thickness. This suggests that the mobility is less dependent on dislocation density than previously thought. For bandgaps greater than 150meV, the mobility increased as the manganese content was reduced and for (Hg,Mn)Te with a positive bandgap less than 150meV the mobility lay in the range of values between that of 10% and 13% manganese layers.

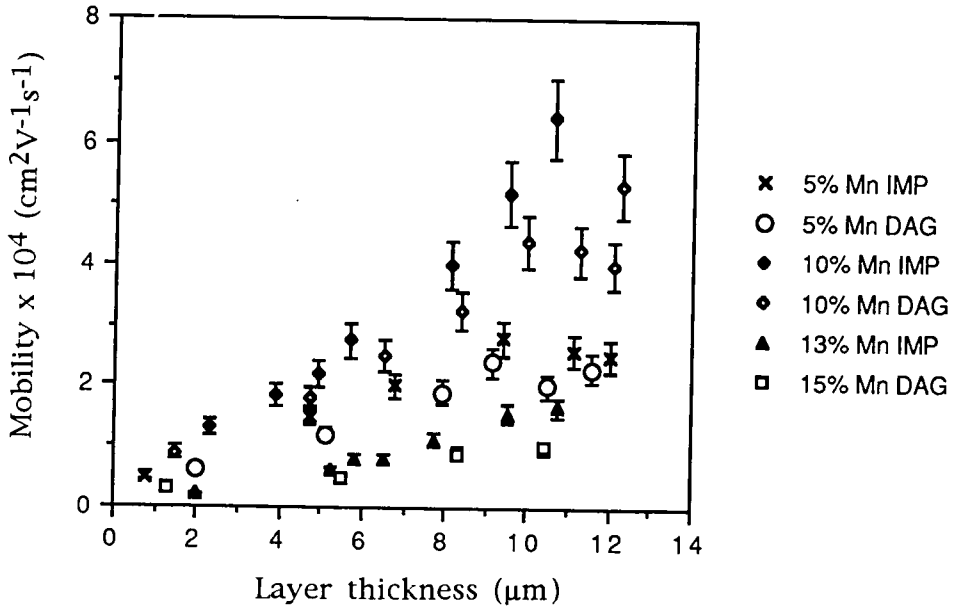

Fig 8.1 Dependence of carrier mobility on layer thickness and composition.

The carrier concentrations of IMP and DAG layers as a function of layer thickness is given in Fig 8.2. The IMP layers considered (with manganese concentrations between 5% and 13%) possessed a positive bandgap and layers containing in excess of 5% manganese had a smaller carrier concentration by around 25% than the corresponding DAG layers.

However $Hg_{0.95}Mn_{0.05}Te$ grown by IMP and DAG had similar magnitudes of carrier concentration. Again the thickness dependence of IMP and DAG are very similar and the increase in electron concentration may imply a reduction in p-type donors e.g mercury vacancies, present in a sub-layer or competing against electron donors introduced accidently as impurities. The increase in electron concentration with reducing manganese content was most prominent in layers of less than 8μm, which may suggest that the intrinsic electrons are more dominant in thinner layers.

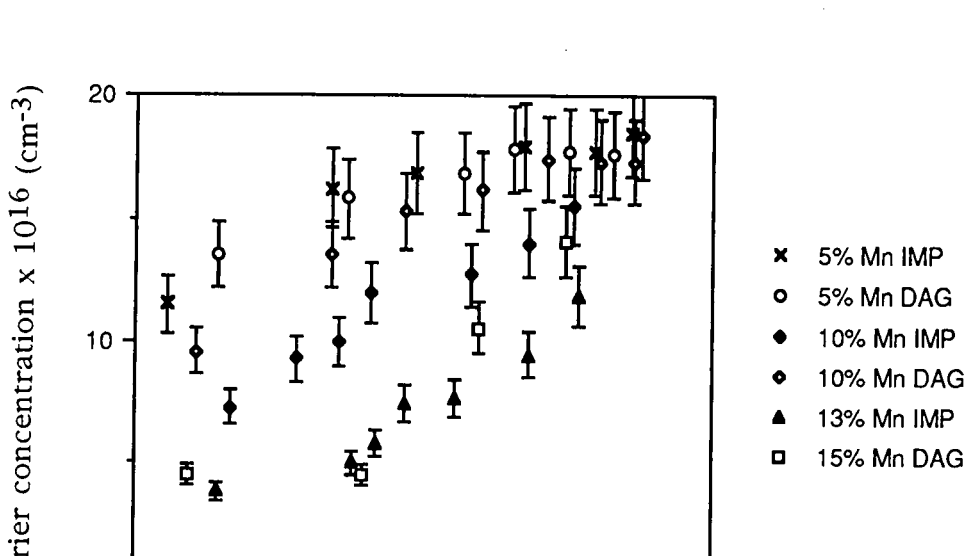

Fig 8.2 Dependence of carrier concentration on layer thickness and composition.

The resistivity was found to decrease exponentially with increasing thickness, for thickness up to 8μm for all the IMP and DAG layers considered. For thicknesses greater than 8μm the resistivity appeared to approach a steady value which was less dependent on composition than that found for thinner layers. For compositions corresponding to very narrow bandgaps (5% manganese) the resistivity in layers grown by IMP

was typically 30% lower than similar layers grown by DAG. This was a result of the higher carrier mobility which was more important than the reduction in carrier concentration in the IMP layers. For larger manganese compositions (and hence the wider bandgap energies) no appreciable difference was observed between IMP and DAG layers.

Thin 13% manganese layers exhibit a large resistance due to the small mobility discussed earlier in this chapter.

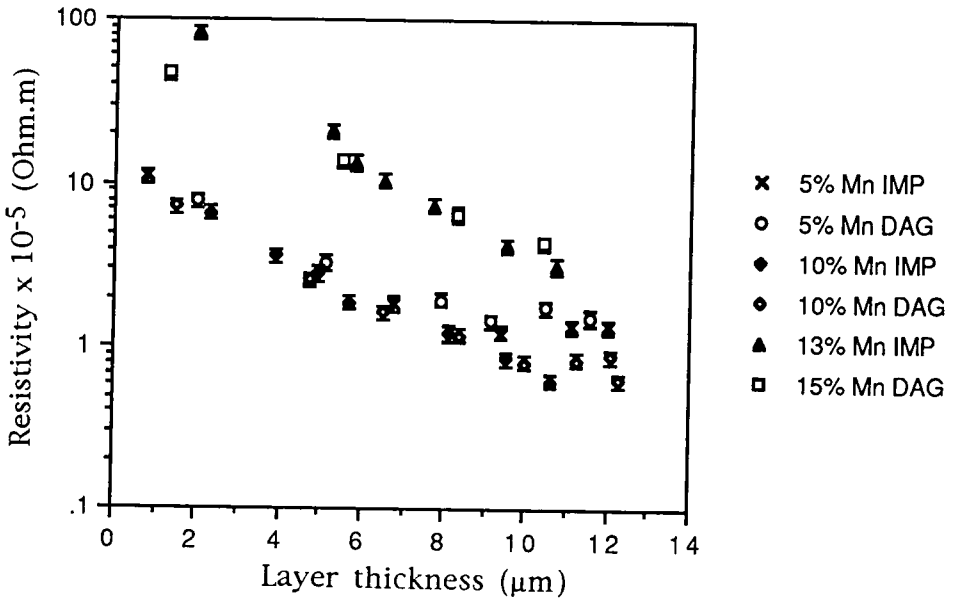

Fig 8.3 Dependence of resistivity on layer thickness and composition.

8.3 Temperature Dependence of Carrier Behaviour

8.3.1 Modelling of Hall Data

The Hall data was modelled in a similar manner to that described in Chapter Six, and transport data from samples with compositions between 7% and 13% manganese in the temperature range 77K to 290K were considered [3]. The donor concentration, N_D, was determined from the Hall data in the extrinsic region and was found to increase in a linear manner with the

manganese content, x, Fig 8.4. A least squares fit to the line is given in equation 8.1 but note that the relationship is only applicable for manganese concentrations between 7% and 13%. This relationship was not observed for DAG layers where donor concentrations were considerably larger (with a maximum for 10% manganese).

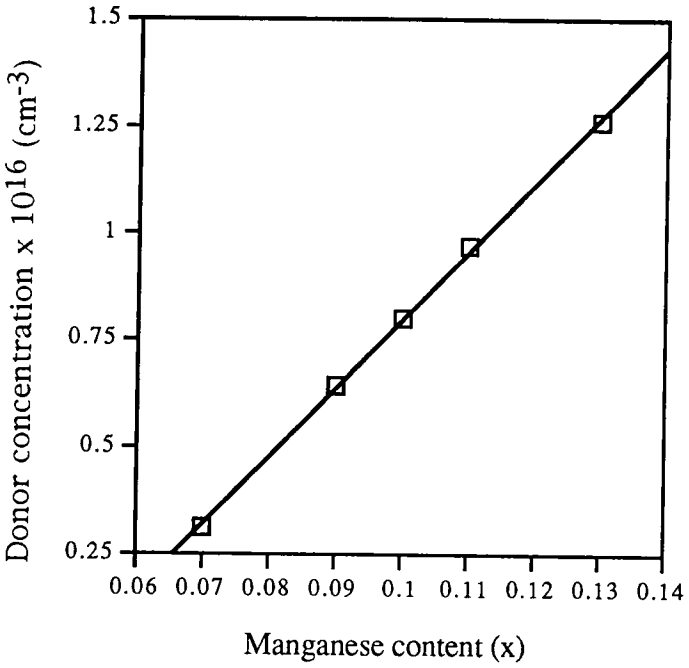

Fig 8.4 Electron donor concentration dependence on composition for 2μm thick n-type (Hg,Mn)Te grown by IMP.

$$N_D = (15.6x - 0.770)10^{16} \qquad 8.1$$

where N_D is in cm^{-3} and x lies in the range 0.07 to 0.13

Examples of Hall data for IMP layers are given in Figs 8.5 to 8.7. In general good correlations were obtained between experimental data and the calculated curves for compositions of 10% manganese or below. This was not observed in DAG layers where the underlying material had a lower

manganese concentration than that of the surface. However in IMP layers less than than 5μm thick with manganese concentrations below 10% the carrier concentrations were less than that predicted by the model and the differences were greater than the 10% allowed in the model. This may suggest the presence of traps or recombination centres within the bandgap.

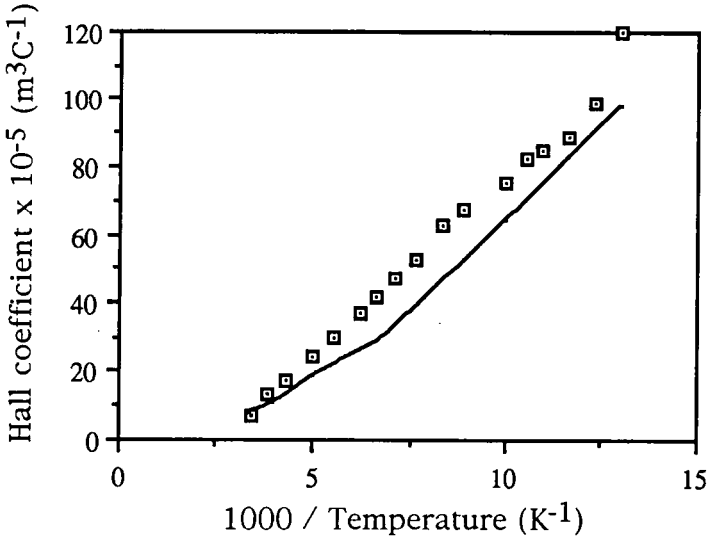

Fig 8.5 Hall data fitting for a 2μm $Hg_{0.93}Mn_{0.07}Te$ IMP layer.

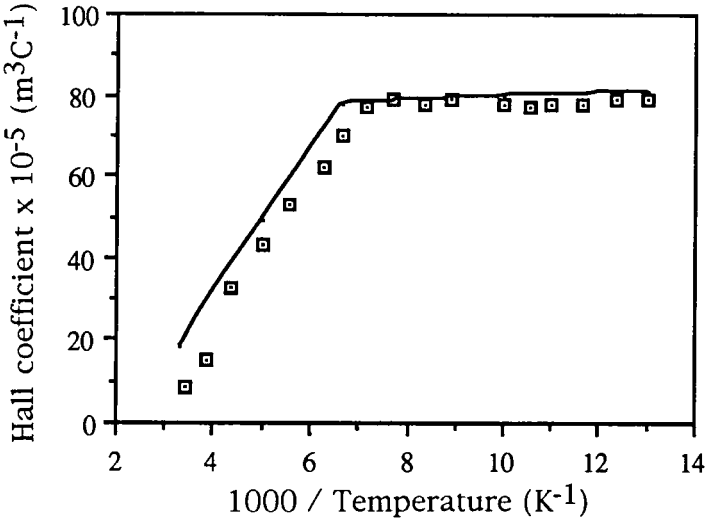

Fig 8.6 Hall data fitting for an 2μm thick $Hg_{0.9}Mn_{0.1}Te$ IMP layer.

For compositions in excess of 10% manganese the experimental electron concentrations were greater than values predicted by the model and the onset of intrinsic conduction. This suggested that the compositions measured by EDAX (the top micron or so) is not typical of the entire layer and a sub-band or graded region with less manganese was present (as for DAG).

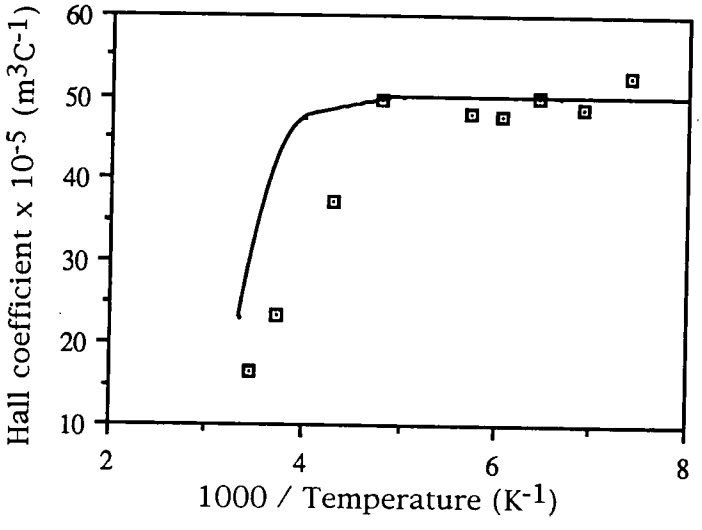

Fig 8.7 Hall data fitting for a 2μm $Hg_{0.87}Mn_{0.13}Te$ IMP layer.

When the Hall data for layers of the same surface composition (measured by EDAX) but differing thicknesses was investigated thicker layers were found to have higher concentrations, as illustrated in Fig 8.8. More detailed study suggested there was a logarithmic change in donor concentration, Fig 8.9. This implies that a saturation of the donor concentration occurs at large layer thicknesses. A least square fit is presented as equation 8.2, which is applicable to $Hg_{0.93}Mn_{0.07}Te$ for the thickness range 2μm to 9μm. When the donor concentrations were considered as a function of the FWHMs of the layer, and also of the dislocation densities present, non linear dependences were observed. This suggests that the donor concentrations in the layers are not related to the layer quality but instead to the layer thickness.

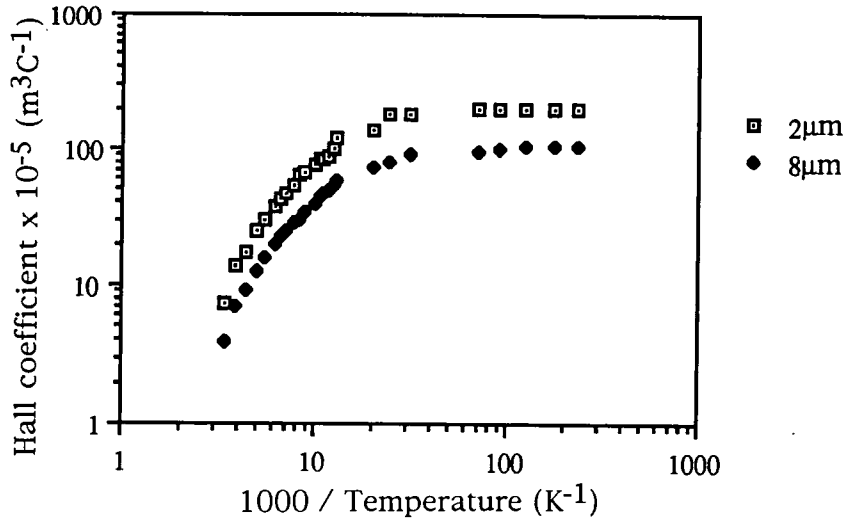

Fig 8.8 Hall data dependence on layer thickness for $Hg_{0.93}Mn_{0.07}Te$.

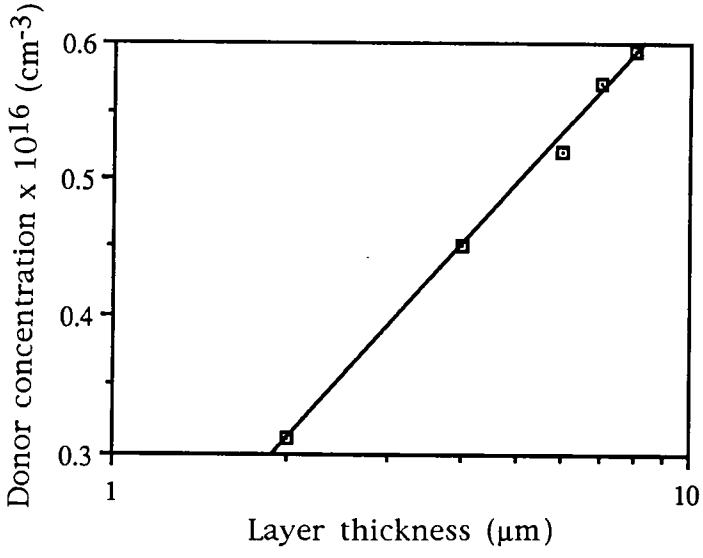

Fig 8.9 The donor concentration of $Hg_{0.93}Mn_{0.07}Te$ as a function of thickness.

$$N_D = 0.170 + 0.466\log_{10}t \qquad 8.2$$

where N_D is the electron donor concentration (x $10^{16}cm^{-3}$) and t is the thickness of $Hg_{0.93}Mn_{0.07}Te$ in μm.

The dependence of intrinsic carrier concentration on temperature in

$Hg_{0.93}Mn_{0.07}Te$ was also found to be a function of thickness, Fig 8.10. Below a thickness of 5μm the experimentally measured carrier concentration was less than that of the predicted by the model and above 5μm became progressively greater than the predicted value, Fig 8.10.

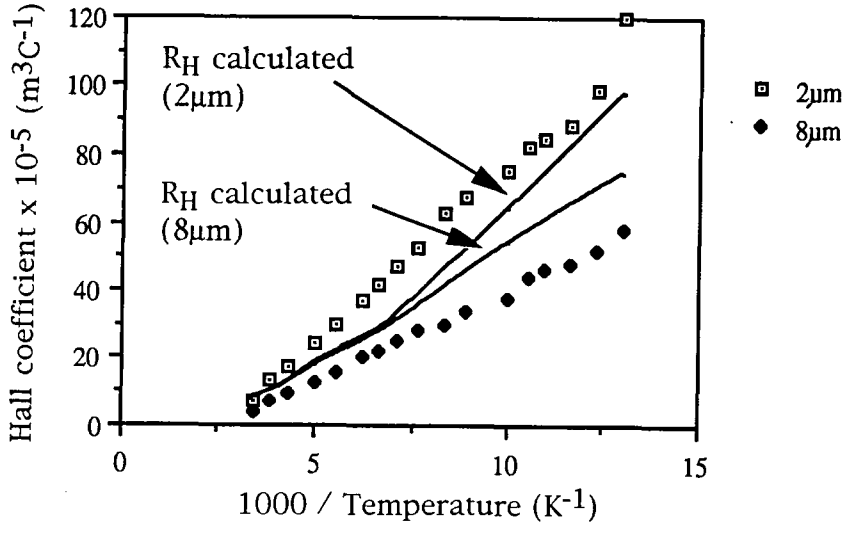

Fig 8.10 Fitting the Hall data of 2μm and 8μm thicknesses of $Hg_{0.93}Mn_{0.07}Te$.

Determination of the activation energy of the donors was done by consideration of the variation of carrier concentration with temperature in the extrinsic region. The slope of the ln(n) vs 1/T characteristic in the extrinsic region (if the $T^{3/2}$ dependence is neglected due to its small magnitude) is $-E_D/\kappa$ (equation 8.2), where E_D is the activation energy (Ec-Ed) of the donors and κ is Boltzmann's constant.

$$n = 2\left[\frac{2\pi.m^{*}_{e}\kappa T}{h^3}\right]^{3/2} \exp\left(\frac{-(E_c - Ed)}{\kappa T}\right) \qquad 8.2$$

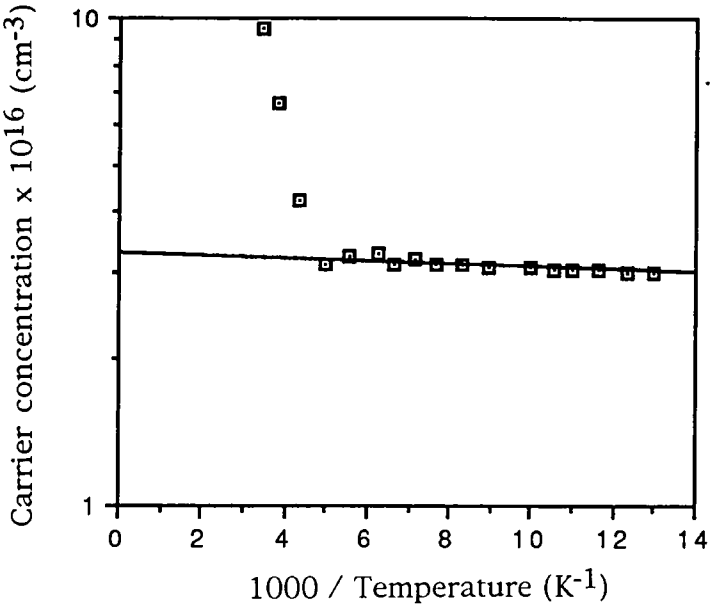

Fig 8.11 Determination of donor activation energy from Hall data for a 2μm thick IMP layer of $Hg_{0.87}Mn_{0.13}Te$.

Similarly the bandgap can be determined from the intrinsic Hall data, equation 8.3 [Chapter Four]. However since high temperatures are being considered the $T^{3/2}$ term must be included. The slope of the high temperature end of Fig 8.12 is $Eg/2\kappa$, where Eg is the bandgap and κ is Boltzmann's constant.

$$n_i = \sqrt{N_C N_V}\exp\left(\frac{E_v - E_c}{2\kappa T}\right) \qquad 8.3$$

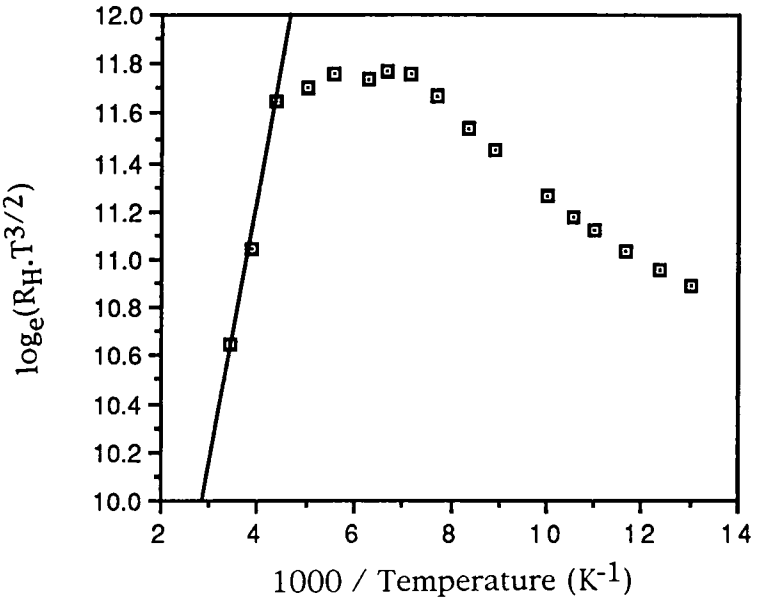

Fig 8.12 Determination of the bandgap from Hall data for a 2μm layer of $Hg_{0.9}Mn_{0.1}Te$.

A brief summary of the compositional and thickness dependence of the carrier and bandgap behaviour is presented in Table 8.1. The increase in donor concentration with layer thickness for IMP layers was more pronounced than that of corresponding DAG layers. IMP layers also possessed a larger donor activation energy and smaller donor concentrations than DAG layers of similar thickness and composition.

Manganese content (%)	7		10		13	
Layer thickness (μm)	2	8	2	8	2	8
Donor concentration x 10^{16} (cm^{-3})	0.32	0.6	0.77	1.3	1.25	2.2
Donor activation energy (meV)	1.3	1.5	1.6	1.4	2	1.8
Bandgap (meV)	120	105	200	220	215	240

Table 8.1 Carrier data for n-type (Hg,Mn)Te grown by IMP.

8.3.2 Carrier Mobility

For the 2μm thick $Hg_{0.93}Mn_{0.07}Te$ layer grown by IMP, electron mobility at temperatures above 77K was governed by polar optic scattering. However, to obtain a good fit to the experimental data the coupling constant, α, was required to be twice that of similar composition DAG layers. This would suggest that, if the effective mass was comparable for DAG and IMP layers, then the dielectric constants of (Hg,Mn)Te were reduced by the IMP growth process by typically a factor of 1.6. This reduction is rather large and may be due to residual strain in the layers, that the variables were calculated in the literature for bulk crystal (Hg,Mn)Te or the compositional non-uniformity of epitaxial (Hg,Mn)Te, or indeed a combination of all three factors. Below 77K the mobility was temperature independent which suggests that neutral impurity scattering occured, Fig 8.13. For similar composition layers grown by DAG piezoelectric scattering was also evident.

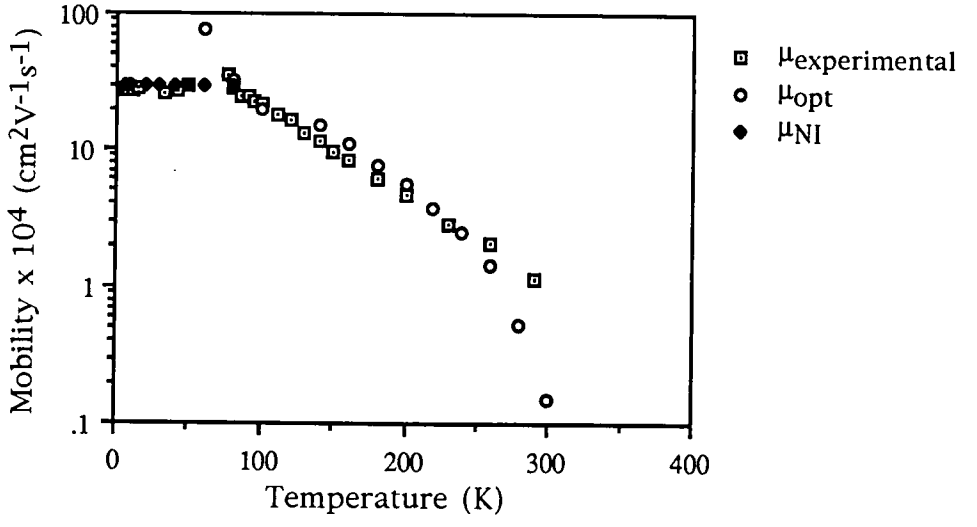

Fig 8.13 Mobility dependence on temperature for a 2μm thick $Hg_{0.93}Mn_{0.07}Te$ layer grown by IMP.

When layers with higher manganese concentrations were considered, ionised impurity scattering was increasingly evident below 120K, Fig 8.14.

Neutral impurity and optical scattering were also still present, the latter calculated using the coupling constant found for $Hg_{0.93}Mn_{0.07}Te$ grown by IMP and the former calculated using a static dielectric constant of 15, but the experimentally measured mobility was less than expected for these scattering mechanisms for temperatures above 220K. For similar composition DAG layers both alloy and piezoelectric scattering were also evident. This may suggest that for temperatures above 220K piezoelectric scattering may be present in $Hg_{0.9}Mn_{0.1}Te$ grown by IMP.

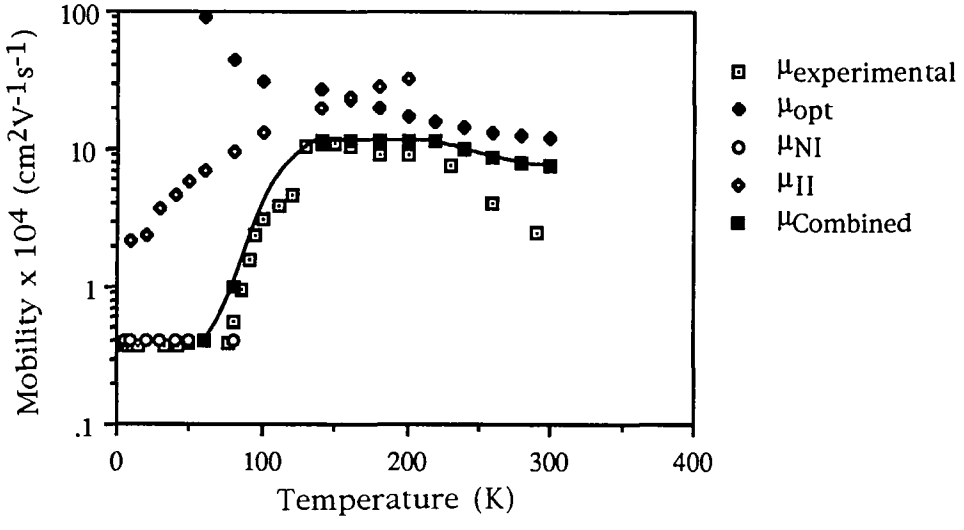

Fig 8.14 Mobility dependence on temperature for a 2μm thick $Hg_{0.9}Mn_{0.1}Te$ layer grown by IMP.

When $Hg_{0.87}Mn_{0.13}Te$ was considered using the adjusted dielectric constant and an effective mass of $0.02m_0$ [3] the calculated mobility, using values determined from DAG layers, was of the order of 25 times larger than that observed experimentally for temperatures over 200K, Fig 8.15. The variation of mobility in this temperature range was best fitted using an inverse square root dependency on temperature. This suggested either alloy scattering, piezoelectric scattering or a combination of both was present in the layers. Since the variables used to calculate the alloy

scattering were well known it was assumed that the discrepancy was a result of the ratio of the longitudinal wave velocity to the electrochemical coupling constant being reduced by a factor of around five for IMP layers (compared to DAG).

Below 150K scattering became temperature independent suggesting neutral impurity scattering.

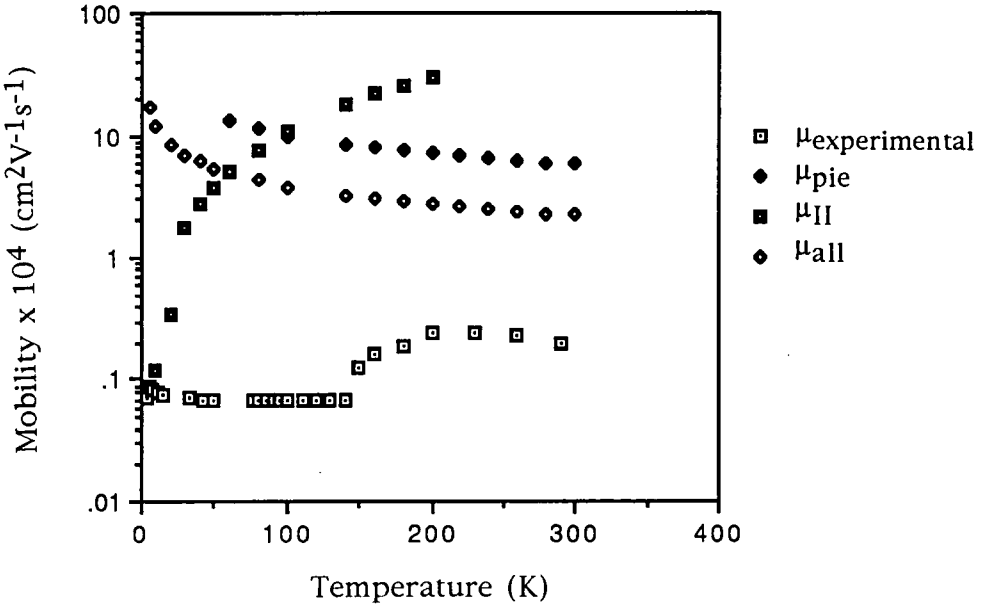

Fig 8.15 Mobility dependence on temperature for a 2μm thick $Hg_{0.87}Mn_{0.13}Te$ layer grown by IMP.

As the thickness of IMP grown layers was increased, impurity scattering was reduced for all compositions and lattice scattering dominated down to 50K for 8μm thick layers, Fig 8.16.

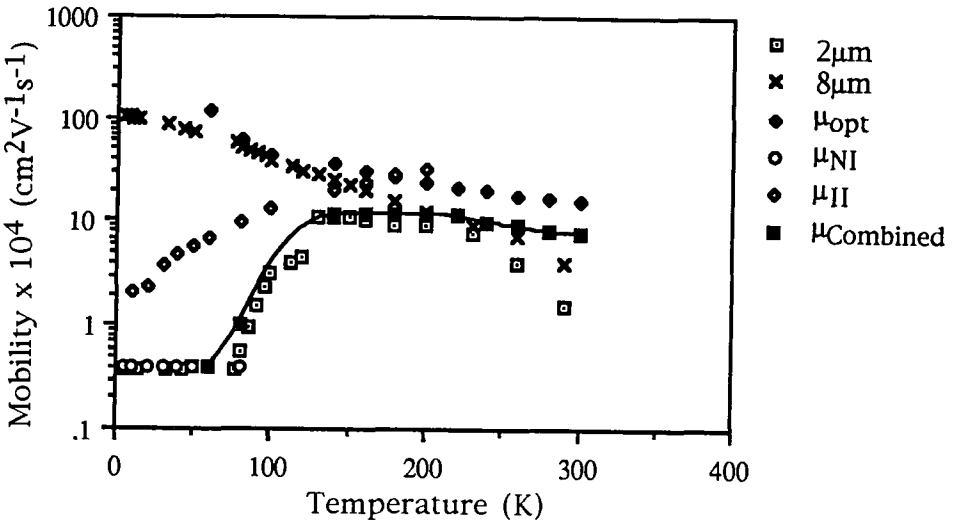

Fig 8.16 Mobility dependence on temperature and thickness for a $Hg_{0.9}Mn_{0.1}Te$ layer grown by IMP.

When the concentration of neutral scattering centres (N) was calculated, Equation 8.4, from the neutral scattering mobility (μ_{NI}) [Chapter Four] using a static dielectric constant of 15 [3] and effective masses as obtained by Jaczynski et al [4] a strong dependence was found on layer composition, Fig 8.17 and equation 8.5.

$$N = \frac{m^*_e}{20\mu_{NI}\varepsilon'_s}\left[\frac{q}{\hbar}\right]^3 \qquad 8.4$$

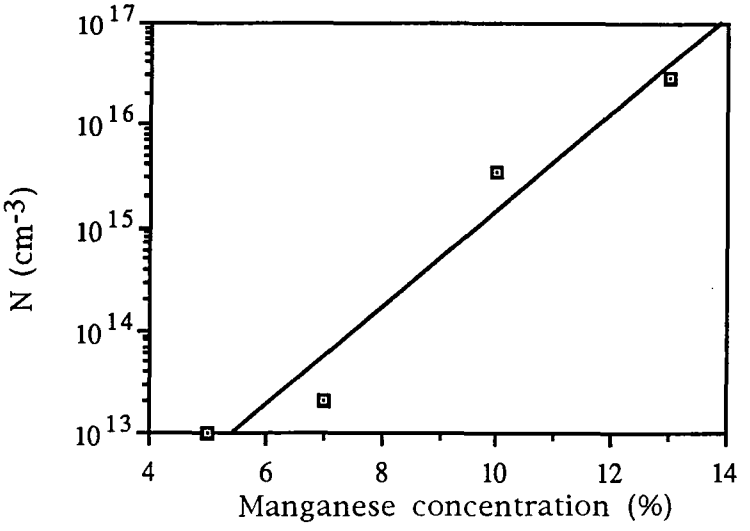

Fig 8.17 Concentration of neutral impurity atoms in 2μm thick n-type (Hg,Mn)Te grown by IMP.

$$\log_{10}N = 0.48Mn(\%) + 10.4 \qquad 8.5$$

where N is the concentration of neutral impurity atoms in cm^{-3}.

8.3.3 Resistivity Data.

The behaviour of the carrier mobility governed the resistivity of $Hg_{0.93}Mn_{0.07}Te$ for temperatures above 77K. Whereas below this temperature the concentration of carriers was the dominant factor, Fig 8.18. This was broadly similar to the behaviour of DAG layers of comparable thickness and composition.

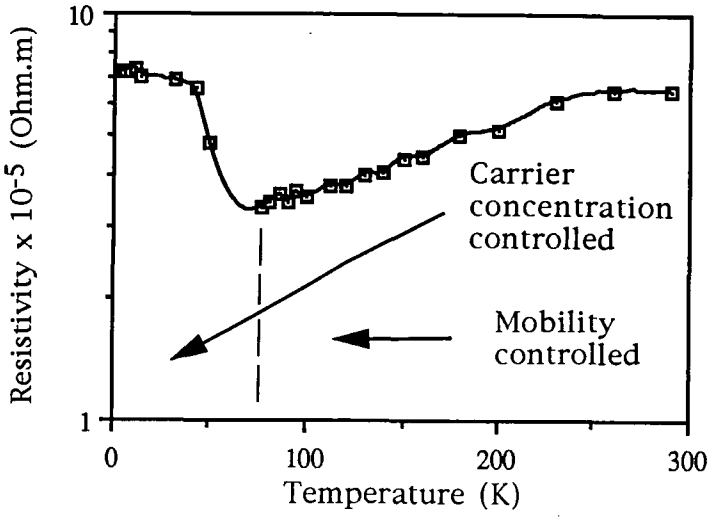

Fig 8.18 Resistivity data for 2μm thick $Hg_{0.93}Mn_{0.07}Te$.

At temperatures below 77K both the carrier concentration and mobility vary insufficiently in $Hg_{0.9}Mn_{0.1}Te$ layers to dramatically alter the resistivity, which remained essentially constant, Fig 8.19. When similar layers grown by DAG were considered at temperatures below 77K the resistivity increased with increasing temperature as a result of the mobility being lowered.

On raising the temperature from 77K to 150K the resistivity of the IMP $Hg_{0.9}Mn_{0.1}Te$ layers dropped by 15 times due to the corresponding increase in mobility.

Above 150K the intrinsic carrier concentration, in these IMP layers, reduced the resistivity as the temperature was increased.

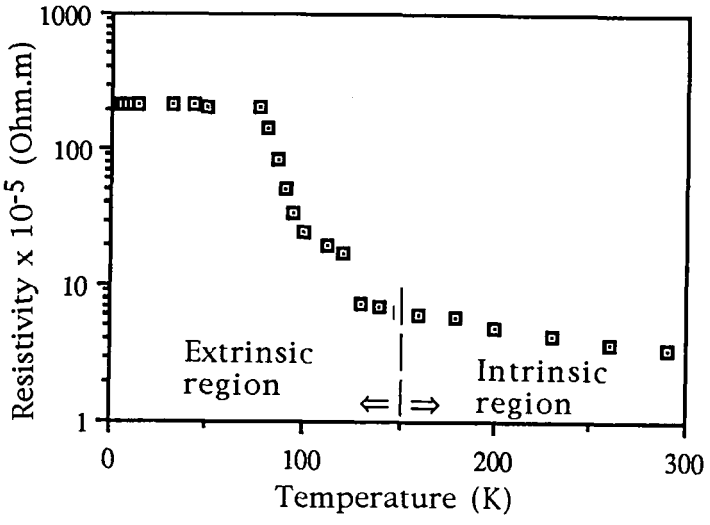

Fig 8.19 Resistivity data for 2μm thick $Hg_{0.9}Mn_{0.1}Te$ IMP layers.

The resistivity of a 2μm thick IMP layer of $Hg_{0.87}Mn_{0.13}Te$ was predominantly determined by the carrier concentration. Freeze out of the electrons was displayed below 10K. Between 10K and 200K a region of extrinsic conduction of donors existed with an activation energy of ~2meV. Intrinsic conduction became significant above 200K. Similar behaviour was observed in corresponding DAG layers.

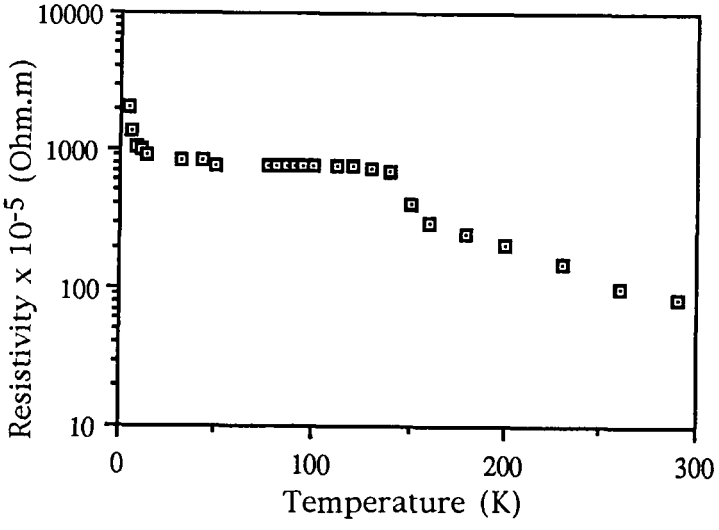

Fig 8.20 The temperature dependence of the resistivity of a 2μm $Hg_{0.87}Mn_{0.13}Te$ IMP layer.

8.4 Magnetoresistance in n-type (Hg,Mn)Te Grown by IMP.

The magnetoresistance was investigated using the techniques outlined in Chapter Six, where a positive value of magnetic field indicated that the magnetic flux lines originated from the layer side of the sample.

The compositional dependence of magnetoresistance for IMP layers [5] was the inverse of that observed in DAG layers, in that it was less asymmetrical with field direction as the manganese concentration increased. $Hg_{0.93}Mn_{0.07}Te$ grown by IMP had a highly asymmetric magnetoresistance Fig 8.21. Similarly Figs 8.22 and 8.23 show the magnetoresistances of the IMP layers $Hg_{0.9}Mn_{0.1}Te$ and $Hg_{0.87}Mn_{0.13}Te$ which show progressively less asymmetry as the manganese concentration increased.

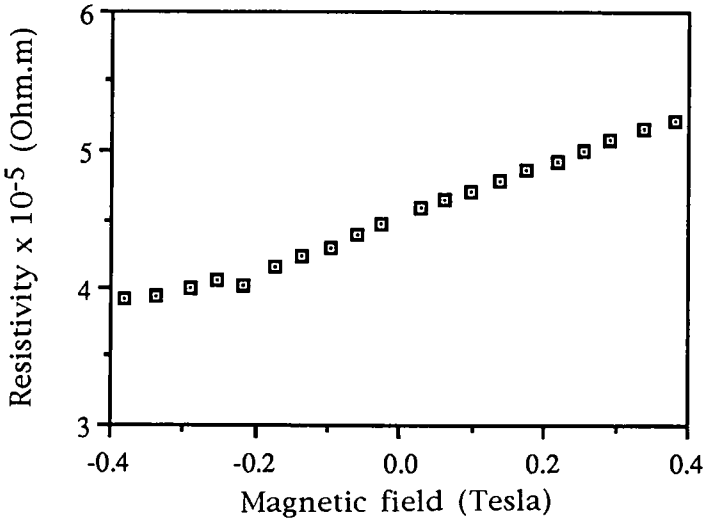

Fig 8.21 Magnetoresistance of $Hg_{0.93}Mn_{0.07}Te$ grown by IMP.

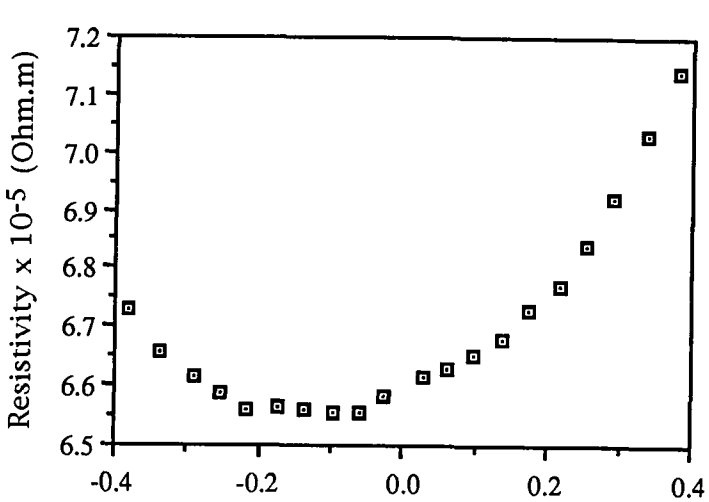

Fig 8.22 Magnetoresistance of $Hg_{0.9}Mn_{0.1}Te$ grown by IMP.

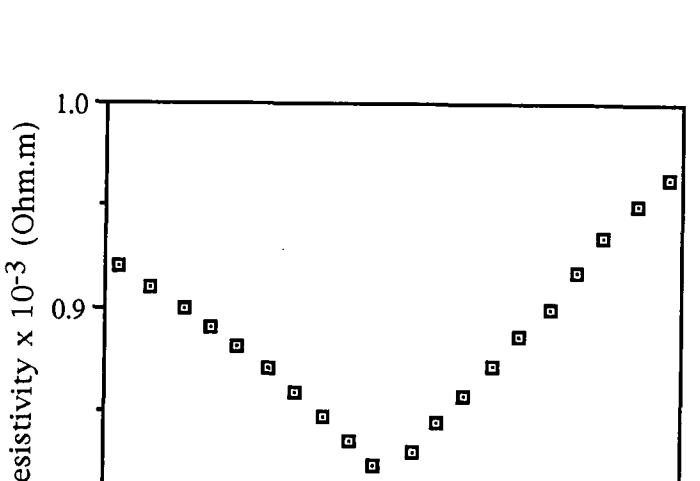

Fig 8.23 Magnetoresistance of $Hg_{0.87}Mn_{0.13}Te$ grown by IMP.

When the ratio of the resistivities obtained by applying a 0.2 Tesla field from each direction perpendicular to the layer surface in turn (the asymmetry factor, see section 6.6) was considered as a function of the composition a clear dependence was observed, Fig 8.24.

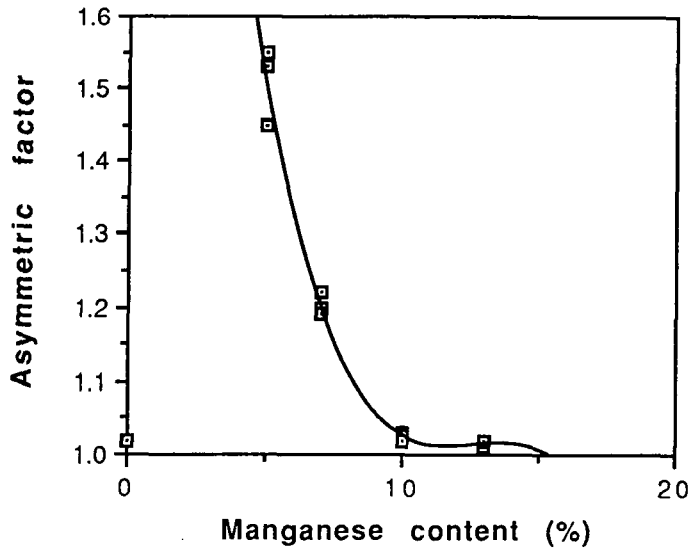

Fig 8.24 Dependence of magnetoresistance asymmetry on layer composition for IMP layers.

The magnitude of the asymmetry for IMP layers was comparable to that of DAG with a distinct change in the dependence occurring around 8μm. There was no noticeable dependence of asymmetry on layer thickness for IMP (or DAG) layers.

The magnitude of the magnetoresistance (measured using a +ve magnetic field), however, in IMP layers was larger than that observed in DAG layers of similar compositions for most compositions, thicknesses and temperatures, Fig 8.25 and 8.26. The magnetic field for this study was applied from the layer side of the sample and the percentage change in resistivity from the zero field condition recorded. The change of magnetoresistance with increasing thickness was most prominent in the first six microns for IMP layers, after which the magnetoresistance tended towards a value independent of the thickness, Fig 8.25. For DAG layers the magnetoresistance increased in a more uniform manner with thickness. This may be related to the dislocation density reducing more rapidly with

the distance from the buffer layer interface in IMP layers.

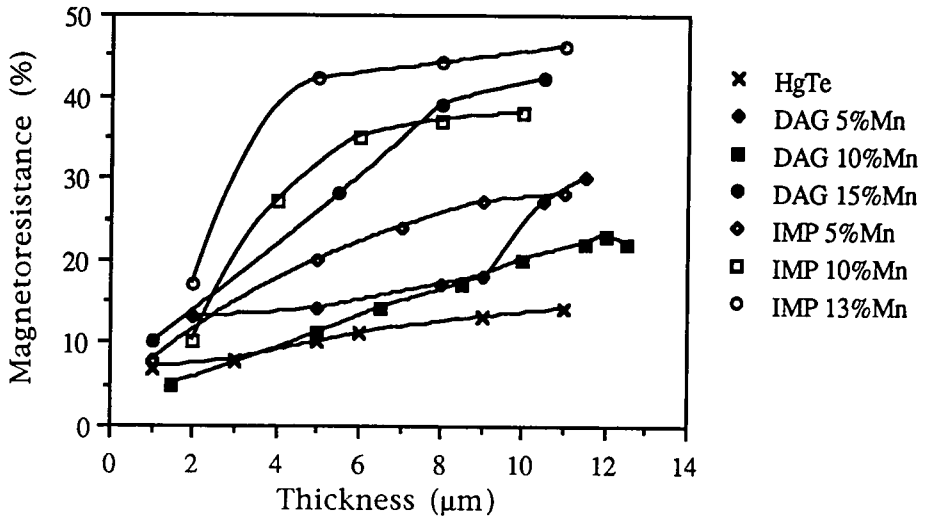

Fig 8.25 Thickness dependence of magnetoresistance, using a 0.38 T magnetic field, at room temperature.

Both IMP and DAG layers had magnetoresistances which increased with reducing temperature, Fig 8.26.

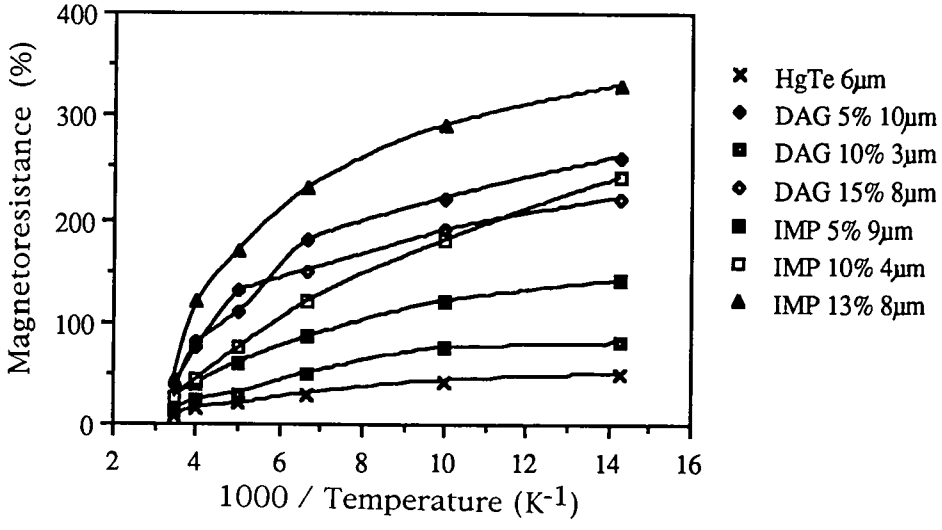

Fig 8.26 The temperature dependence of magnetoresistance, using a 0.38T magnetic field.

8.5 Stability of the Electrical Properties of n-type (Hg,Mn)Te Grown by IMP

The stability of DAG layers with respect to time was reported in Chapter Six and was found to be best in thick layers where the crystal quality was good. $Hg_{0.87}Mn_{0.13}Te$ layers grown by IMP, of various thicknesses, were subject to Hall and resistivity measurements at room temperature at monthly intervals after their growth. The results are presented in Figs 8.27 to 8.29. The mobility of 8μm $Hg_{0.87}Mn_{0.13}Te$ grown by IMP increased by ~10% on aging in air for five months. However the mobility of thinner IMP layers were more stable than either DAG or thick IMP layers.

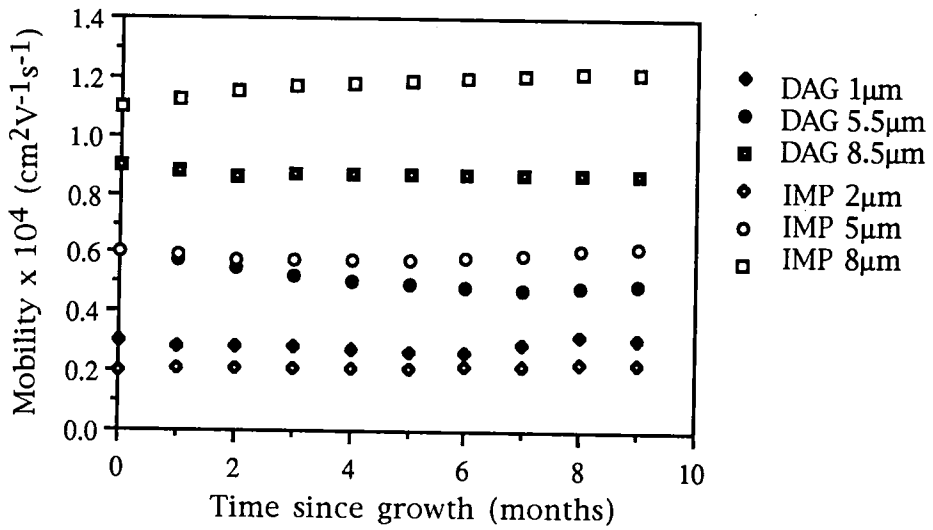

Fig 8.27 The variation of the electron mobility of n-type $Hg_{0.87}Mn_{0.13}Te$ with time.

The carrier concentration was reduced in all the layers considered upon ageing, Fig 8.28. The most marked change on adopting the IMP process with respect to carrier concentration stability was in thin (2μm) layers. In this case the change in carrier concentration over a five month period was decreased from 50% to 30% on changing from the DAG to the IMP process.

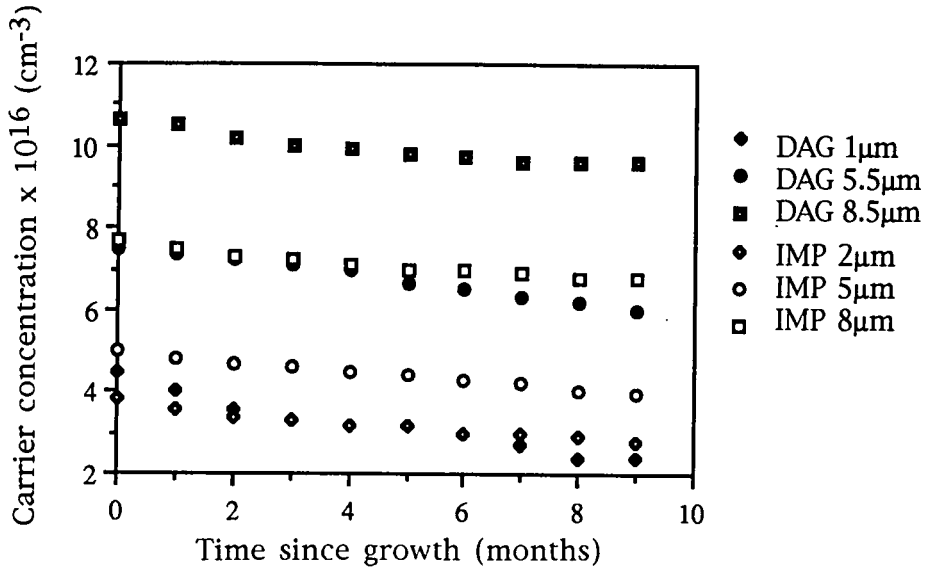

Fig 8.28 The variation of the carrier concentration of n-type $Hg_{0.87}Mn_{0.13}Te$ with time.

The most significant improvement obtained by using the IMP process was the increase in the stability of the resistivity, where the resistivity of IMP layers increased at only half the rate of equivalent DAG layers, Fig 8.29.

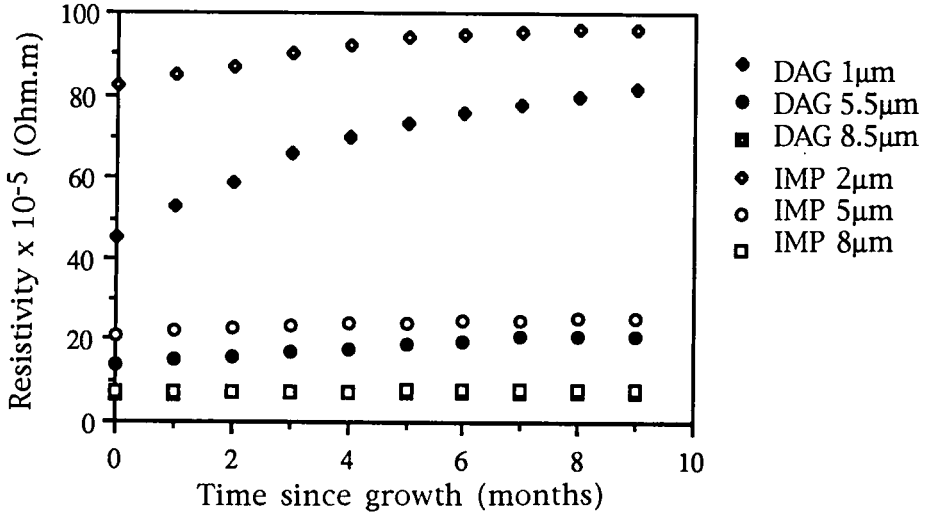

Fig 8.29 The variation of the resistivity of n-type $Hg_{0.87}Mn_{0.13}Te$ with time.

The improvement in the stability of electrical measurements with respect to time suggest that, if (as suggested in Chapter Six) an outdiffusion of mercury was responsible for the electrical degradation, then the IMP process helped to reduce this unwanted process. Whether this was a result of the reduction in the dislocation density is at present unclear. EDAX analysis showed that the overall composition was unaltered with time for either IMP or DAG layers. This would suggest that the outdiffusion of mercury was on a microscopic scale thus creating mercury vacancies which act as electron acceptors.

8.6 Summary.

Electron mobilities were higher and carrier concentrations lower in layers grown by the IMP process compared to those of equivalent compositions and thicknesses grown by DAG. This resulted in IMP layers possessing lower resistivities to the corresponding DAG layers except for compositions of the order of 5% manganese where the resistivities were similar. The thickness dependence of room temperature transport measurements were very similar, despite the variation in dislocation density with thickness discussed in Chapter Seven. This would suggest that dislocation density played a relative insignificant role in limiting the electron mobility and lattice-phonon interaction was dominant. The ratio of carrier concentrations between different compositions of (Hg,Mn)Te were small which would suggest extrinsic conduction was dominant, even at room temperature. Electron donor concentrations were found to increase linearly with the manganese content of layers and logarithmically with layer thickness for IMP layers. No such clear trends were observed using DAG layers but a maximum in donor concentration was observed in DAG layers containing 10% manganese. Higher donor activation energies and lower donor concentrations were found for IMP layers compared to DAG.

Modelling of the temperature dependence of Hall data revealed good agreement between the surface composition and that of the underlying material for IMP layers containing 10% or less manganese. However IMP layers containing more than 10% manganese had surface compositions that were more manganese rich than the material below (as was the case for all DAG layers considered).

On analysing the electron mobilities as a function of temperature it was discovered that for $Hg_{0.93}Mn_{0.07}Te$ optical scattering and some neutral impurity scattering was present for IMP layers and the coupling constant was twice that of similar layers grown by DAG. Piezoelectric scattering which was an additional process for $Hg_{0.93}Mn_{0.07}Te$ grown by DAG was not observed in similar IMP layers.

On increasing the manganese content to 10% neutral scattering became more evident and ionised impurity scattering was evident. Analysis of the optical scattering revealed that the static dielectric constant was probably reduced by a factor of 1.6 on going from DAG to IMP layers. For similar DAG layers piezoelectric and alloy scattering were also present. When IMP $Hg_{0.87}Mn_{0.13}Te$ was considered the dominant scattering mechanism was piezoelectric. However calculations using values determined from DAG layers, gave mobilities twenty five times larger than those observed suggesting that the ratio of the longitudinal wave velocity to the electrochemical coupling constant was five times larger for IMP layers than those grown by DAG.

On analysis of the neutral impurity scattering it was found that the concentration of neutral impurity centres was exponentially dependent on composition, increasing several orders of magnitude with an increase in

the manganese content of a few per cent.

Less asymmetry of the magnetoresistance to the magnetic field direction was displayed as the manganese content of IMP layers was increased. This was the opposite relationship to that found for DAG layers. For comparable thicknesses and compositions IMP layers had larger magnetoresistances to those grown by DAG although similar dependences on thickness and temperature were found.

The stability with respect to time was better in IMP layers, with the largest improvements being observed for resistivity. Whether the improvement was solely due to the reduction in dislocation densities in IMP layers, thus limiting the outdiffusion of mercury, is at present unclear.

References

[1] M. Funaki, A.W. Brinkman, T.D. Hallam and B.K. Tanner (1993) Appl. Phys. Lett. **62**(23) 2983.

[2] H. Tatsuoka, K. Durose and M. Funaki (1993) Inst. Phys. Conf. Ser. No**135** Chapter 9 339.

[3] A. Rogalski (1991) Infrared Phys. **31(2)** 117.

[4] M. Jacznski and W. Dobrowolski (1980) Physica Status Solidi **102(b)** 195.

[5] S. Oktik, T.D.Hallam, A.B. Horsfall, C.D. Moore, A.W. Brinkman, B.K. Tanner and I. Terry (1995) accepted for II-VI conference, Edinburgh 13th-18th August 1995.

[6] W.E. Spicer, J.A. Silberman, I. Lindau, A.B. Chen, A. Sher and J.A. Wilson (1983) J. Vac. Sci. Technol. **A1(3)** 1735.

Chapter Nine

Summary and Conclusions

9.1 Introduction

The main themes of the work reported in this thesis have been the characterisation of the MOVPE growth process for (Hg,Mn)Te, assessment of the structural quality of the layers and Hall and resistivity measurements made in the temperature range 4.2K to room temperature.

9.2 Surface Uniformity and Structural Quality of DAG (Hg,Mn)Te

Direct alloy growth of epitaxial (Hg,Mn)Te using TCMn, DIPTe and elemental mercury in a horizontal atmospheric pressure MOVPE reactor was assessed for differing growth conditions. Layer composition was strongly dependent on the susceptor temperature, mercury vapour pressure and TCMn/DIPTe feed rate ratio. For the former the pyrolysis of TCMn was reviewed and the possible presence of manganese species with pyrolysis temperatures lower than that of TCMn considered.

The compositional and thickness uniformity of layers grown by DAG was generally poor and one possible explanation was proposed in terms of the difference in pyrolysis rates between DIPTe and TCMn. This led to depletion of the Te precursor along the susceptor with a variation in the effective TCMn/DIPTe feed rate ratio, and to corresponding variations in thickness and composition.

Double crystal x-ray diffraction has been used to determine accurately layer composition, thickness and crystalline quality (FWHM). X-ray diffraction mapping enabled spatial uniformity to be assessed over the

layer. Epitaxial (Hg,Mn)Te layers of thickness greater than ~1μm were shown to be almost totally relaxed, using symmetric and asymmetric reflections. There was a reduction in the dislocation density with increasing layer thickness (as inferred from FWHM), This was considered in terms of the Gay model and revealed a distinct change in the thickness dependence at ~2μm with two corresponding rate constants.

Double crystal x-ray topography revealed a clear sub-grain structure where the grain diameter decreased in a linear manner with inverse thickness. Tilts between the sub-grains were shown, by triple axis x-ray diffraction, to be the primary cause of rocking curve broadening in (Hg,Mn)Te.

9.3 Transport Properties of (Hg,Mn)Te

The majority of (Hg,Mn)Te layers grown exhibited n-type behaviour and electron mobility and concentrations were found to be dependent on layer thickness. The temperature dependence of Hall coefficient and electron mobility in epitaxial HgTe were found to be similar to that reported for bulk crystal HgTe. Optical-phonon, piezoelectric and ionised impurity scattering mechanisms were successfully combined to model the experimental temperature dependence of mobility for epitaxial HgTe.

Piezoelectric and optical-phonon scattering were present in all the n-type (Hg,Mn)Te layers considered, however alloy scattering was also present in layers containing in excess of 5% manganese.

In contrast, attempts to model the temperature dependence of carrier concentration in narrow gap (Hg,Mn)Te using a two band model was less successful. Ill fitting curves were obtained for the surface compositions. This, it was suggested, was due to the underlying material having a lower

manganese concentration than that of the surface. Estimates of the bandgap from intrinsic Hall data substantiated this suggestion. In the n-type layers investigated, the activation energy of the electron donors was between 0.5meV and 1meV and the concentration of these donors was in the range 10^{16} to 10^{17} cm^{-3}. Acceptor levels with an activation energy of 4meV were found in $Hg_{0.85}Mn_{0.15}Te$.

When a lower mercury boat temperature was used during growth the (Hg,Mn)Te layers exhibited p-type behaviour with a typical acceptor activation energy of ~4meV. The variation of hole mobility and temperature was attributed to a combination of ionised impurity, optical-phonon and alloy scattering mechanisms.

The magnetoresistance, for n-type (Hg,Mn)Te, observed using magnetic fields up to 0.38T was proportional to the square of the magnetic field for low fields, but exhibited a linear dependence at larger fields. The range of magnetic fields for which the former condition applied increased with manganese content. Considerable asymmetry was observed in the magnetoresistance characteristics with applied field direction. The magnitude of the asymmetry appeared to increase the manganese concentration. The reason for the asymmetry was unclear. Carriers would have been deflected either towards or away from the contacts depending on the field direction. This may have given rise to asymmetry, but this remains speculation.

When transport measurements were repeated on n-type, positive bandgap (Hg,Mn)Te layers at monthly intervals, electron mobility and concentration were observed to reduce with time. These changes were linear with time for the first five months after which a dependence on the square root of time became apparent. This suggested a loss of mercury

from the surface coupled with mercury diffusion to the surface from within the layer. This was obviously more pronounced in thinner layers, where the surface comprised a greater proportion of the layer volume.

9.4 Structural Quality of (Hg,Mn)Te Grown by IMP

To improve the compositional and thickness uniformity of (Hg,Mn)Te the interdiffused multilayer process was employed. In this technique alternate layers of HgTe and MnTe were deposited and allowed to interdiffuse. It was found, by x-ray diffraction, that no post growth annealing was required for complete interdiffusion to occur. Layers grown by this technique possessed superior x-ray FWHMs (for a given thickness) and improved uniformity when compared to layers grown by DAG. The improvement in FWHM was attributed to increased bending of threading dislocations at the HgTe/MnTe and MnTe/HgTe interfaces. Unlike layers grown by DAG, the IMP layers possessed FWHMs which were dependent upon composition. It was suggested that this because the bending of the dislocations varied with the ratio of the thicknesses of the two binary layers. Since layer composition was determined by the relative thicknesses of the constituent binary layers.

Double crystal x-ray topography and TEM revealed that no sub-grains were produced during the IMP growth. Post growth annealing was discovered to cause an extensive loss of mercury from the surface, broadening the x-ray rocking curve and roughening the surface. However, annealed IMP layers still possessed a superior surface uniformity when compared to that of DAG layers.

9.5 Transport Properties of (Hg,Mn)Te Grown by IMP

Electron mobilities were higher and carrier concentrations lower in layers grown by the IMP process compared to those of equivalent compositions and thicknesses grown by DAG. Modelling of the temperature dependence of Hall data revealed good agreement between the surface composition and that of the underlying material for IMP layers containing 10% or less manganese. However IMP layers containing more than 10% manganese had surface compositions that were more manganese rich than the material below (as was the case for all DAG layers considered).

On analysing the electron mobilities as a function of temperature it was discovered that for $Hg_{0.93}Mn_{0.07}Te$ optical scattering and some neutral impurity scattering was present for IMP layers and the optical phonon coupling constant was twice that of similar layers grown by DAG. On increasing the manganese content to 10% neutral scattering became more evident and ionised impurity scattering became evident at low temperatures. When IMP $Hg_{0.87}Mn_{0.13}Te$ was considered the dominant scattering mechanism was piezoelectric. However calculations using values determined from DAG layers, gave mobilities twenty five times larger than those observed in the IMP layers. This suggested that estimates for the ratio of the longitudinal wave velocity to the electrochemical coupling constant from analysis of the DAG samples underestimated the true values (not known) by a factor of about five times.

On analysis of the neutral impurity scattering it was found that the concentration of neutral impurity centres was exponentially dependent on composition, increasing several orders of magnitude with an increase in the manganese content of just a few per cent.

Less asymmetry of the magnetoresistance to the magnetic field direction

was displayed as the manganese content of IMP layers was increased. This was the opposite relationship to that found for DAG layers. For comparable thicknesses and compositions IMP layers had larger magnetoresistances to those grown by DAG although similar dependences on thickness and temperature were found.

The stability with respect to time was better in IMP layers than for comparable DAG layers, with the largest improvements being observed in resistivity. This may well have been a consequence of the superior crystal quality resulting in a reduction in pipe diffusion of mercury.

9.6 Future Work

To produce (Hg,Mn)Te suitable for device fabrication the surface compositional and thickness uniformity would have to be improved. This could be achieved by improving the growth technology either through use of a rotating susceptor or improved reactant distribution. Once this problem had been addressed, production of p-n junctions could be investigation using mercury annealing to suppress the mercury vacancies in p-type (Hg,Mn)Te to provide selective area n-type doping. Alternatively doping with group III (e.g. Indium) or group VII (e.g. Iodine) may be considered. The device potential for (Hg,Mn)Te is large due to the bandgap being adjustable with composition and with fine tuning being possible using an applied magnetic field. The heavy nature of the component elements (mercury and manganese) make (Hg,Mn)Te a candidate for x-ray detection and the magnitude of the band gap is ideal for detection of infra-red radiation.

Further investigations into the asymmetry of the magneto resistance in (Hg,Mn)Te layers are required to establish whether it is just a Hall effect or

if it is a genuine asymmetry in the material. Also of interest would be high magnetic field studies of the negative magnetoresistance, since the magnetic fields used in this study were limited to a maximum of 0.38 Tesla.

This study has established the main structural and transport properties of epitaxial (Hg,Mn)Te and has provided a foundation on which more specialist measurements can be based in the future.